REMOTE CONDITION MONITORING OF STRUCTURAL INTEGRITY OF RAILS AND CROSSINGS USING ACOUSTIC EMISSION TECHNIQUE

by

Shengrun Shi

A thesis submitted to the University of Birmingham for the degree of

DOCTOR OF PHILOSOPHY

School of Metallurgy and Materials

College of Engineering and Physical Sciences

University of Birmingham

October 2018

SYNOPSIS

Today, rail networks worldwide are becoming increasingly busy. Rolling stock operates at faster speed and deals with heavier load than before. The operating conditions can cause wear and fatigue damage under cyclic loading and generate different types of rail defects, such as shelling crack, rail-end-bolt hole crack, split head and head check defects.

At present, depending on the severity of damage, a defective rail or crossing can still remain in service with or without repairs being performed or replaced within a standardized time-schedule ranging from immediately to up to 1 week after applying Emergency Speed Restriction (ESR). Therefore, inspection and assessment of the growth of these defects in service is critical in making maintenance decisions and ensuring the smooth operation of the rail network. Various non-destructive testing (NDT) techniques have been used for structural integrity evaluation in rail sector. Acoustic emission (AE) technique is a passive NDT technique and its application in rail sector is still very limited.

In this research, the possibility of using AE technique to monitor structural integrity of rails and crossings in real time has been investigated. AE technique has been used to monitor the damage evolution process of three different types of sample including:R260 grade rail steel samples (precracked and without precracking), Hadfield steel samples (precracked and without precracking), and a reference carbon steel sample during low and high frequency bending fatigue crack growth tests. A commercial AE system manufactured by Physical Acoustics Corporation (PAC) and a customised AE system developed by researchers at the University of Birmingham and Krestos Limited, UK have been used for data collection.

AE parameters including amplitude, energy, risetime, duration, count and average signal level (ASL) have been used to correlate crack length with AE hits for the commercial system. For all R260 rail steel samples, the occurrence of brittle cleavage fracture at certain crack lengths has been shown in the fractographs and the resulting sudden increase in crack length has been successfully detected by AE. The waveform based analysis has been carried out on the data captured by the customized system. Various signal processing algorithms including FFT (Fast Fourier Transform), moving RMS, moving crest factor, moving kurtosis, moving skewness are employed for the in-depth analysis of the acquired raw AE waveforms captured during the fatigue tests. All the algorithms show the capability to reflect the severity of damage accurately. However, the results obtained by various algorithms should be interpreted based on the principal of each algorithm. In addition, SK has been employed to analyse the signals. Although SK values can reveal the damage progression, the frequency ranges at which SK attain the peak values vary considerably at different stages. This is due to the influence of noise caused by crack faces rubbing during crack opening and closing. Field trials have been carried out on two different crossings on the west coast mainline. Template-based cross-correlation analysis has been employed to analyse the data captured from the instrumented crossing and proved to be effective in evaluating the health state of the monitored crossings. Overall, this research has shown that AE can be used as a tool to effectively evaluate the structural integrity of rails and Hadfield steel crossings online.

Acknowledgements

First and foremost, I would like to thank my deceased father , Guibo Shi, who passed away on August 26th ,2017, and my mother, Pengqing Gao for their continuous support they have given to me throughout my study and their numerous sacrifices for the family. I could not have done it without them. Many thanks to my brother Shengwei and my sister Lishuang for their support.

I would like to express my heartfelt thanks to my supervisor Dr Mayorkinos Papaelias for providing me the great opportunity to carry out the research under his supervision and for his dedicated guidance, encouragement, continuous support through the course of the research. It was my great privilege and honour to work with him.

I would like to thank Prof Clive Roberts and Dr Sakdirat Kaewuruen for their support during the research. My sincere thanks also go to my industrial supervisor, Dr Slim Soua from TWI Ltd, for providing me the opportunity of performing the research in an industrial environment and for his kind support during the study. I also gratefully acknowledge the scholarship provided from the National Structural Integrity Research Centre (NSIRC).

I would also like to show gratitude to Mr Patrick Vallely from Network Rail for providing the opportunities for performing the field trials at Cropredy. My sincere thanks also go to Dr Arash Amini, Dr Zheng Huang, Dr Jinlong Du, Dr Zhiyuan Han,Dr Jun Zhou ,Dr Nikolaos Angelopoulos Mr Zipeng Liu for their assistance and support in the research.

Last but not the least, my warm thanks to Dr Timothy Doel and Mr David Price for their valuable assistance during fatigue testing.

Publications

Journal Papers

Shi, S., Han, Z., Liu, Z., Vallely, P., Soua, S., Kaewunruen, S & Papaelias, M. (2017). "Quantitative monitoring of brittle fatigue crack growth in railway steel using acoustic emission", Proceedings of the Institution of Mechanical Engineers, Part F: Journal of Rail and Rapid Transit. Available at https://doi.org/10.1177/0954409717711292

Conference Papers and Presentations

Shi,S., Soua, S., Kaewunruen, S & Papaelias, M "Online structural integrity monitoring of railway infrastructure using acoustic emission"NSIRC conference,Cambridge, 27-28 June 2016

Shi,S., Huang Z., Kaewunruen,S, Vallely,P., Soua,S & Papaelias,M."Remote Condition Monitoring of Structural integrity of Rails and Crossings" First World Congress on Condition Monitoring-WCCM 2017,London, 13-16 June,2017

Valley,P., Papaelias,M., Huang,Z., **Shi,S**., Kaewunruen,S & Davis,J "Development of novel acoustic emission techniques for monitoring the structural health of cast manganese crossings",Stephenson Conference 2017,London, 25-27 April 2017 (Won Prize for Best paper)

Shi,S."Acoustic emission monitoring of flaws in rails and cast manganese crossings" Researcher Links Workshop in RCM for Railway,Istanbul,Turkey, 22-24 March 2016

Shi, S., Papaelias ,M., Kaewunruen, S., Roberts, C & Soua, S., “Acoustic emission monitoring of flaws in rails and cast manganese crossings”,Next Generation Rail Conference 2016,Derby

TABLE OF CONTENTS

LIST OF FIGURES

LIST OF TABLES

LIST OF ABBREVIATIONS

ΔK	Stress intensity factor range
AE	Acoustic emission
ASL	Average Signal Level
ACFM	Alternating Current Field Measurement Inspection Technique
BCC	Body-centred Cubic
CT	Compact Tension
CWT	Continuous Wavelet Transform
DFT	Discrete Fourier Transform
DWT	Discrete Wavelet Transform
DCPD	Direct Current Potential Drop
ESR	Emergency speed restriction
EMATS	Electromagnetic acoustic transducers
EPFM	Elastoplastic Fracture Mechanics
FT	Fourier Transform
FCC	Face-centred Cubic
FCG	Fatigue Crack Growth

FFT	Fast Fourier Transform
FIR	Finite Impulse Response
GCC	Gauge Corner Cracking
HDT	Hit Definition Time
HLT	Hit lockout time
IIR	Infinite Impulse Filter
IMC	Infrastructure Maintenance Contractors
K_{Ic}	Plane-strain Fracture Toughness
LEFM	Linear Elastic Fracture Mechanics
MFL	Magnetic Flux Leakage
MIT	Magnetic Induction Testing
MARSE	Mean Area under the Rectified Signal Envelope
NDT	Non-Destructive testing
PDT	Peak Definition Time
PLB	Pencil Lead Break
PSB	Persistent Slip Bands
PSD	Power Spectral Density

PICC	Plasticity-induced Crack Closure
RCF	Rolling Contact Fatigue
RCM	Remote Condition Monitoring
RMS	Root Mean Square
SK	Spectral Kurtosis
SCF	Stress Concentration Factor
SFE	Stack Fault Energy
SFT	Stress Free Temperature
SIF	Stress Intensity Facor
SHM	Structural Health Monitoring
STFT	Short-time Fourier Transform
TWIP	Twinning-induced Plasticity
UT	Ultrasonic Testing

Chapter 1:

Introduction

CHAPTER 1 : INTRODUCTION

In-service rails and Hadfield crossings may develop structural defects due to the stresses and environmental conditions they are subjected to. The railway networks have been accommodating high traffic densities during the past decade. Currently, depending on the severity of damage, a defective rail or crossing can remain in service with or without repairs being carried out or replaced within a standardised time-schedule ranging from immediately to up to 1 week after an Emergency Speed Restriction (ESR) has been imposed. For certain defects, the application of fish plates or clamps may be necessary to ensure that at least theoretically the defect is not growing further during passage of the trains even though the ESR has been imposed.

During emergency repairs, normal operation of the railway line affected can be seriously disrupted resulting in delays and unnecessary costs. Outsourcing the majority of maintenance activities to Infrastructure Maintenance Contractors (IMCs) has contributed greatly to the reduction of cost for maintaining the railway during Control Period 3 (CP3) and Control Period 4 (CP4) for Network Rail. The total maintenance cost in 2015-2016 for Network Rail is £1.3bn，which accounts for 18% of total Network Rail expenditure as shown in Figure 1-1.

Railway infrastructure managers including Network Rail have been gradually shifting their maintenance strategy from conventional reactive modes to condition-based and predictive approaches [1]. The importance of Remote Condition Monitoring (RCM) in terms of reducing maintenance costs has been gradually realized since CP4 in part through the deployment of intelligent infrastructure has been carried out for some assets. During CP5，focus has been given to the deployment of intelligent infrastructure to other assets

to further reduce maintenance cost. In order for predictive and prognostic modes to be applied efficiently and reliably in the railway context, accurate identification of the type of defect and evaluation of its severity are necessary. Accurate prediction of the remaining life time of in-service rails and Hadfield crossing would enable better allocation of available resources and improved scheduling of repairs overall leading to minimal disruption and reduced cost of maintenance. Moreover, techniques which could confirm the status of the in-service components being monitored, i.e. whether a defect is propagating or not could allow higher ESRs to be applied instead or the requirement of an ESR to be imposed removed all together [2-4].

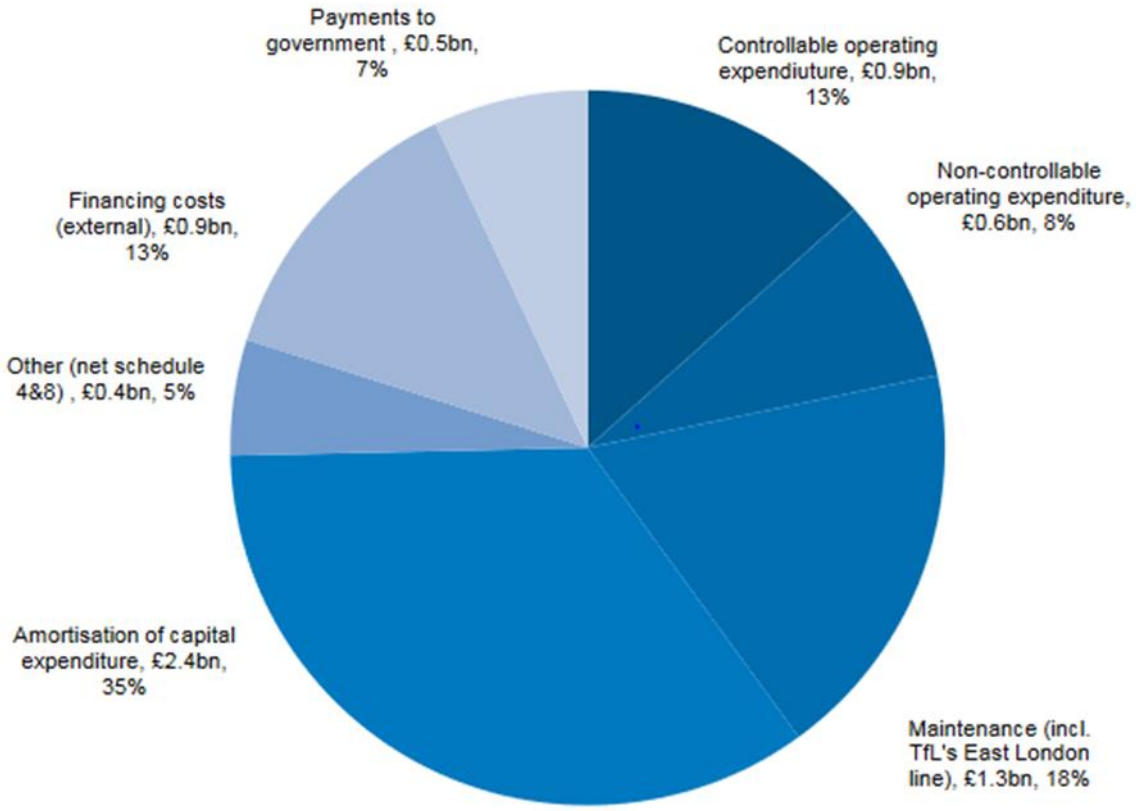

Figure 1-1: Gross Network Rail Expenditure 2015-2016 [5]

AE testing is a dynamic condition monitoring technique which is extensively used for online Structural Health Monitoring (SHM) and evaluation of critical structural components. AE has the potential of being employed as an efficient tool in the real-time monitoring of the structural integrity of rails and crossings. However, an inherent limitation associated with AE is that it is very sensitive to unwanted external noises and it is highly essential that some specific analysis be employed to discriminate the signals correlated with defects from the noises or at least weaken the influence of the noises on the useful signals, especially when the AE inspection is performed in noisy environments.

In this project, the applicability of using AE to monitor structural integrity of rails and crossings online has been investigated. A commercial AE system manufactured by Physical Acoustics Corporation (PAC) and a customised AE system developed by researchers at the University of Birmingham and Krestos Limited, UK have been used for data collection.AE data captured during fatigue crack growth tests performed on different rail and Hadfield steel samples have been based on different AE signal related parameters and signal processing algorithms such as Fast Fourier Transform (FFT) and Spectral Kurtosis (SK). The aim of the analysis was apart from identifying the crack growth events to quantify the severity of damage in the specimens at least in a semi-quantitative way. One of the key objectives of the project was to evaluate appropriate filtering algorithms in order to minimise the influence of unwanted noise on the AE signals and increase the accuracy of the results acquired. Field tests have also been carried out to evaluate the effect of rolling stock noise on the AE measurements. The main results from this research are shown in the following chapters along with the methodology used. The main conclusions and recommendations for future work are shown in final chapter.

Chapter 2:

Manufacturing Processes and Mechanical Properties of Rail and Cast Manganese Steel Grades

CHAPTER 2 : MANUFACTURING PROCESSS AND MECHANICAL PROPERTIES OF RAIL AND CAST MANGANESE STEEL GRADES

2.1 Rail steel

The manufacturing process of modern rail steel bloom comprises three key stages. It includes the molten pig iron production, the continuously casting process and the cutting into blooms. The final microstructure of different rail steel grades is dependent on the chemical composition and cooling profile. The vast majority of rail steels have a predominantly pearlitic microstructure with little ferrite present. The iron-carbon (Fe-C) phase diagram can be used as reference for the quick estimation of the microstructure of steels dependent on the amount of carbon present at different temperatures and equilibrium as shown in Figure 2-1. At higher temperatures, austenite is the only phase in the microstructure present. Austenite has a face-centred cubic (FCC) crystal structure, allowing a higher solubility of carbon. As the steel cools down the crystallographic structure changes to body-centred cubic (BCC) due to the gradual phase transformation of austenite to ferrite and pearlite, or cementite and pearlite depending on the carbon content. The BCC crystal structure allows lower solubility of carbon than FCC. The insoluble carbon results in the formation of cementite (Fe_3C) and ferrite (Fe) lamellae or pearlite as this phase is otherwise known [6].

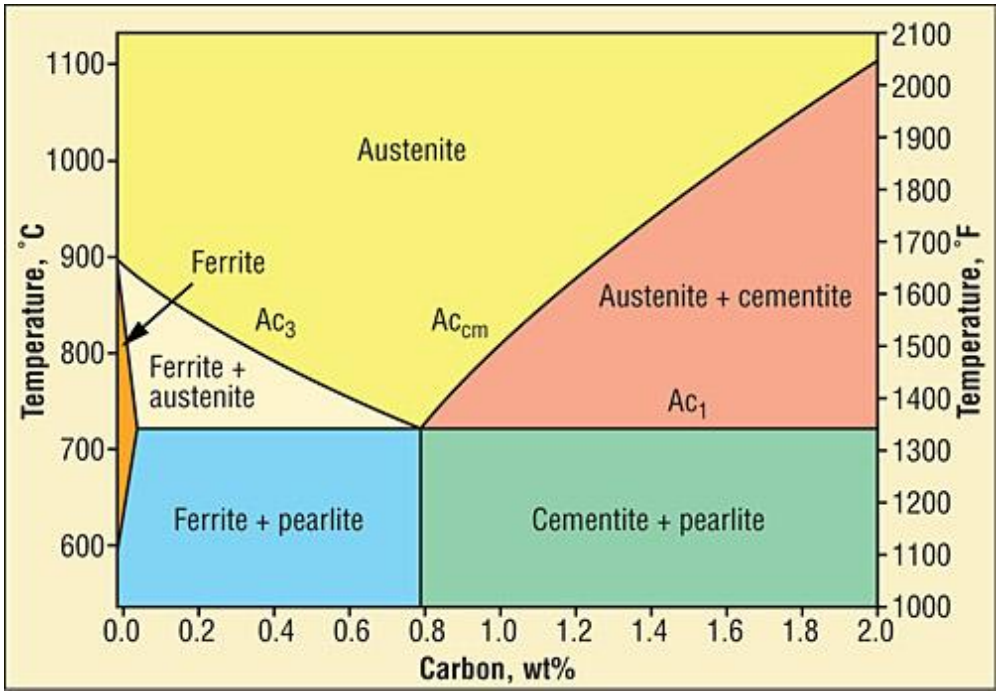

Figure 2-1: The Fe-C phase diagram [7].

Modern pearlitic steel grades such as the R220 and R260 grade are the most widely used in rail manufacturing. Pearlitic steel grades have low production cost and relatively high resistance to wear thanks to the higher level of hardness they exhibit. Older rail steels due to their lower hardness used to wear at a much higher level in comparison with modern rail steel grades and hence surface defects due to rolling contact fatigue effects were quite rare.The carbon content in pearlitic rail steels is normally between 0.5 wt. % to 0.8 wt. % with small amounts of Mn and Si added during the steel-making process to increase hardness and improve toughness. If the carbon content exceeds the eutectoid point, some extra brittle cementite will form. Hence, carbon content needs to be kept below the eutectoid composition. Cracking of the harder cementite lamellae results in more energy being released and hence higher levels of AE activity arises in comparison with the softer ferrite grains during damage evolution.

The mechanical properties of pearlitic rail steels, especially the yield strength and hardness, are largely influenced by the interlamellar spacing. Normally, the yield strength and hardness are inversely related to the interlamellar spacing which is similar to the relationship between yield strength and grain size for steels with austenite or ferritic structures. Finer interlamellar spacing can be obtained by increasing the cooling rate, but the rate should be smaller than the upper limit for the martensitic transformation [8, 9].

Bainitic steel grades are promising materials to be used for improving the fatigue crack growth resistance of rails. Bainite is composed of ferrite and insoluble cementite resulting from higher cooling rates during the steelmaking process. Depending on the processing procedure and composition, the microstructure of bainitic steels can vary greatly. Bainitic steel grades normally contain 0.15-0.45 in wt. % C, 0.15-0.2 in wt. % Si, 0.3-2.0 in wt. % Mn, 0.5-3.0 in wt. % Cr and other alloying elements. Bainitic steels can be classified into two types, the upper bainite and lower bainite. Upper bainite contains lath-shaped ferrites with the carbides distributed in between the laths. In lower bainite the carbides are distributed within the laths. Excellent mechanical properties can be acquired if no carbides come out of the solution through the addition of appropriate alloying elements such as B. Oxidising elements are needed to prevent B from being oxidized, thus keeping it an effective alloying element. Tests have been carried out to compare the mechanical properties between carbide-free bainitic steel and premium pearlitic steel. It has been seen that carbide-free bainitic steels are exhibit better resistance to RCF in comparison with pearlitic rail steels [6, 10].

The R260 rail steel grade has become the most commonly used steel grade for rail manufacturing around the world. It has a predominantly pearlitic microstructure with very small amounts (>1%) of ferrite present along the pearlite grain boundary. The chemical

composition and material properties for the R260 steel grade are shown in Table 2-1&Table 2-2 respectively [11].

Table 2-1: Chemical composition of R260 steel grade (in wt. %)

C	Si	Mn	P	S	Cr	V	Al	N
0.60-0.82	0.13-0.60	0.65-1.25	<0.030	0.008-0.030	<0.15	<0.030	<0.004	<0.008

Table 2-2: Material properties of R260 rail steel grade

Minimum UTS(ultimate tensile strength)/MPa	Minimum elongation / %	Hardness / BHN
880	10	220-260

Apart from the mechanical properties shown in Table 2-2, other parameters of interest such as fatigue crack growth rate, fatigue strength, fracture toughness and the level of residual stresses should also meet the requirements required by the relevant rail manufacturing industrial standards which need to be upheld at all times[12] .

El-shabasy and Lewandowski investigated the effect of changes in R-ratio on the fatigue crack growth behaviour of a fully eutectoid pearlitic steel. Fatigue crack growth (FCG) tests were carried out on separate three-point bending samples with different R-ratios, 0.1, 0.4 and 0.7 respectively at room temperature. They found that as the R-ratio increases, the threshold value ΔK_{th} decrease and the magnitude of the slope in the Paris-

Erdogan regime increases. Furthermore, the percentage of static fracture, i.e. cleavage fracture in the fracture surface increases with the R-ratio for the same ΔK value.

Maya-Johnson et al. in their study evaluated the influence of interlamellar spacing on FCG characteristics for two different types of pearlitic rail steels, R260 and 370CrHT. The interlamellar spacing of pearlite in R370CrHT steel is smaller than that in R260. It was found that 370CrHT shows slower crack growth rate than R260 in the Paris-Erdogan regime. They argued that most of the energy needed for the crack to grow is consumed for the same increment in crack length for 370CrHT when compared with the R260 grade. The smaller interlamellar spacing means more interfaces between ferrite and cementite exist within the same volume. It was also found that for ΔK values smaller than 11MPa·$m^{1/2}$ no crack initiation occurs whilst the fracture toughness ranges at approximately 35MPa·$m^{1/2}$ [13] .

2.2 Cast manganese steels

For switches and crossings due to the high dynamic impact loads they are subjected to, steel grades which show superior impact resistance and fracture toughness to standard ones need to be used. The preferred material in this case is the cast manganese steel grades or Hadfield steel. The content of Mn in this type of steel is much higher than normal pearlitic rail steel. Mn is an austenite stabiliser, thus facilitating the formation of an FCC austenitic microstructure which has much higher toughness and impact resistance than conventional rail pearlitic steel grades. Hadfield steel has a low stack fault energy (SFE). The composition of the Hadfield used in this research is as shown in Table 2-3

Table 2-3: Chemical composition of Hadfield steel grade (in wt. %)

C	Si	Mn	P	S
1.2	0.15	11-14	0.02	0.02

Hadfield steel becomes much harder with time after it is put into use due to work hardening [6]. The exceptional strain hardening property of Hadfield steel is closely related to its low SFE and high concentration of carbon atoms in interstitial solid solution. Low SFE makes it more difficult for cross-slip to happen but favours the twinning formation in Hadfield steel.

The nominal composition for Hadfield steel grades is 1-1.4% carbon and 10-14% Mn with a Mn/C ratio of roughly 10:1. Manganese increase the ductility of the steel contributing to the resistance to abrasive action from train wheels. It is the excellent combination of these properties that makes Hadfield steel widely used in many engineering applications, especially in rail crossings. As-cast Hadfield steels normally have carbides, it is common that solution treatment and water quenching are applied in order to generate a fully austenitic microstructure before they are put into use [14, 15]. To enhance the wear and deformation resistance of Hadfield steel at the early stage of its service life, pre-hardening treatment should be performed on the surface. Explosive hardening is considered the best pre-hardening method for Hadfield steel [16].

Kang et al. investigated the cyclic deformation and fatigue behaviours of Hadfield steel under laboratory conditions. They did strain-controlled low cycle and stress-controlled high cycle fatigue tests. Severe plastic deformation occurred near the fracture surface

during the high cycle fatigue. The fracture surface was characterised by quasi-cleavage. They found that the main reason for work hardening in cast manganese steel is the interaction between dislocations and carbon atoms in the C-Mn clusters [17].

Niendorf et al. studied the crack growth behaviour of a high-manganese TWIP (Twinning Induced Plasticity) steel. They used miniature CT specimens with stress ratios R=0.1 and R=0.5 during testing. The surface in the crack wakes became rougher once the crack growth enters into the unstable stage. The same could be observed if stepwise ΔK increase was applied during the stable stage [18]. The effect of different grain sizes on fatigue strength of high-Mn TWIP steels has been reported by Hamada et al. They used thermodynamic modelling to calculate the SFE and they proved that the SFE values of the investigated steels are within the range that twinning formation during plastic deformation is facilitated. Although most cracks initiate from grain boundaries, they mostly grew transgranularly during the process [19].

The repeated contact stresses between the train wheels and crossing nose can harden the surface layers of the nose to a certain depth. However, when the increase in the hardness cannot offset the wear resulting in different defect to form. Fatigue cracks normally initiate where the shear stress is maximum. After the initiation, the crack will grow internally following arc paths and then grow parallel to the running surface at a larger depth [20, 21]. The susceptibility of rails and cast manganese crossings to crack initiation and propagation is determined not only by external loading, but also their fatigue resistant properties. The fundamentals of fatigue and fracture of rails and cast manganese crossings are shown in the following chapter. Various types of loads and stresses in rails and crossing have also been introduced.

Chapter 3:

Fundamentals of Fatigue and Fracture of Rails and Cast Manganese Crossings

CHAPTER 3 : FUNDAMENTALS OF FATIGUE AND FRACTURE OF RAILS AND CAST MANGANESE CROSSINGS

3.1 Introduction

Rails and cast manganese crossings are exposed to harsh operational and environmental conditions which with time can result in the structural degradation of these valuable railway infrastructure assets. Therefore, it is imperative that the condition of the structural integrity of both rails and cast manganese crossings is known in order to make effective and cost-efficient maintenance decision leading to higher safety and reliability levels as well as minimal disruption to normal railway operations. In heavily used railway networks any delays or disruption are highly undesirable as they result in higher operational costs, loss of valuable time for the rail network users and hence further costs to the national and international economy and a growing resistance to use rail transport more in comparison with road transport. In the present chapter, the effects of fatigue and environmental-based degradation are discussed together with fracture.

3.2 Fatigue

Fatigue refers to the repetitive loading process leading to gradual structural deterioration and eventually final failure that a material undergoes when it is subjected to external stresses (normally below the yield strength of the material) varying with time [22, 23]. The earliest research on fatigue can dated as early as the beginning of 1800 and interestingly has been partly related to the railway industry [24]. To characterise the fatigue resistance of any material, the stress intensity threshold value (K_{th}) above which fatigue crack can initiate and subsequently propagate along with Fatigue Crack Growth (FCG) rates need to be evaluated. When a cracked metallic structure is loaded, three possible types of crack tip displacement based on the relative movements of the opposing

crack surfaces can be observed. These include mode I, mode II and mode III, as shown in Figure 3-1 and relate to the types of stresses to which the structure has been exposed to. Mode I relates to the movement of the surfaces in the opposite directions. Fatigue cracks in metals grow mostly in mode I as long as the elastic conditions are strictly met. In Mode II, the opposing crack surfaces move over each other in the direction that is perpendicular to the crack tip. In Mode III, the two surfaces move relative to each other in the direction that is parallel to the crack tip [22].

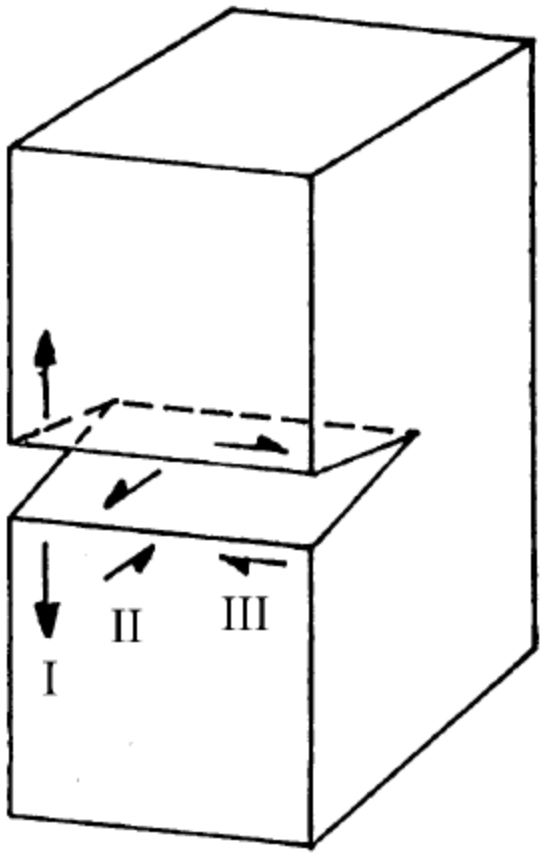

Figure 3-1: The different modes of crack surface displacement [25]

In order to characterise the stress and displacement fields (Figure 3-2) in the vicinity of the fatigue crack, the stress intensity factor K （mode I） is employed as shown in Equation 3-1.

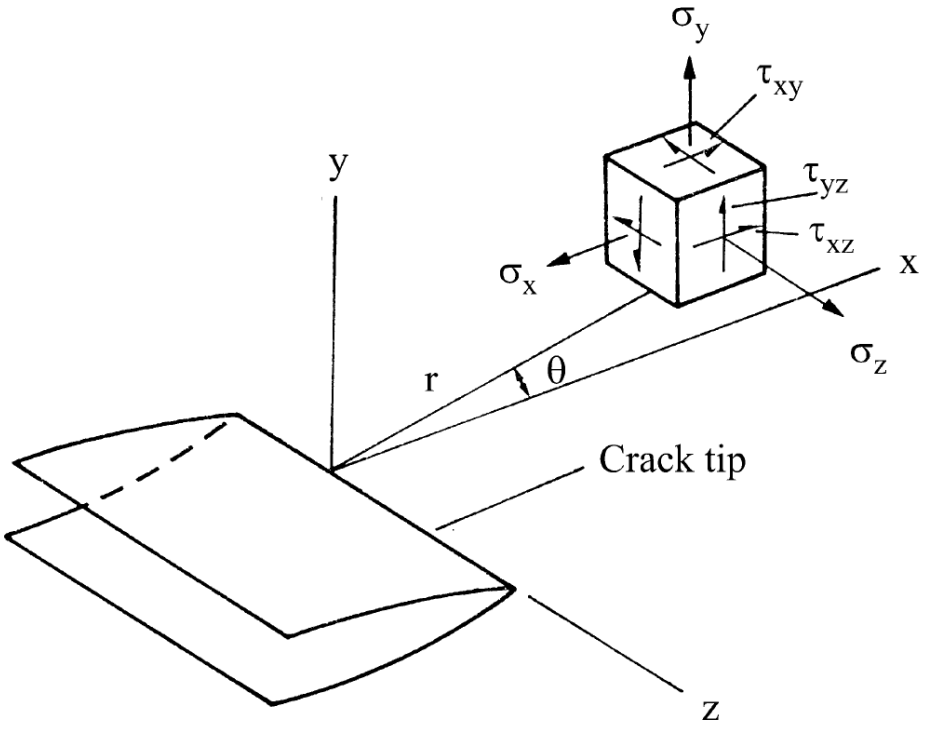

Figure 3-2: Illustration of stress state at a point ahead of the crack tip [25]

$$K = \lim_{r \to 0} \sigma_y \sqrt{2\pi r} \qquad (3\text{-}1)$$

Where r is the distance to the crack tip, σ_y is the stress perpendicular to the crack tip, $\sqrt{2}$ is the commonly used numerical constant, although different values can also be found, leading to different K values.

For the other two modes, the equations have the same form as the above one, but the shear stress should be used instead. It is also noteworthy to point out the difference between the stress intensity factor (SIF) and stress concentration factor (SCF). Stress

concentration will arise if the cross-sectional area of the structure show abrupt changes, such as a notch for example. A notch is a common typical stress raiser and small cracks tend to initiate from it under sufficient loads. However, it should be noted that discontinuities in the material or inclusions can also act as stress concentrators, so it is not only a macroscopic geometrical related factor. SCF is used to characterize the intensity of stress concentration which is determined by the shape and size of the notch that exists in the structure, whereas SIF is inherent property of the material and needs to be calculated experimentally for different geometry and loading conditions [26]. For a through crack of width 2a in an infinite plate subjected to uniform tension σ, the SIF is :

$$K = \sigma \sqrt{\pi a} \tag{3-2}$$

The fatigue resistance of any material including rail and cast manganese steel grades is dependent on the stress amplitude and mean stress. There are four major phases that dominate the fatigue process, including cyclic hardening or softening, t, microcrack formation, macrocrack or dominant crack formation and dominant macrocrack growth. The percentage of each phase in the total fatigue process is determined by the stress amplitude and mean stress as shown in Figure 3-3 [24]. The number of cycles is represented by $N_{i,j}$ where the first subscript i (i=1,2,3,4) represents the phase and second j(j=f,1,2,3) the stress amplitude. The occurrence of cyclic hardening or softening is dependent on the magnitude of the cyclic stress amplitude. If cyclic stress amplitude is below the yield strength, then cyclic hardening will not happen.

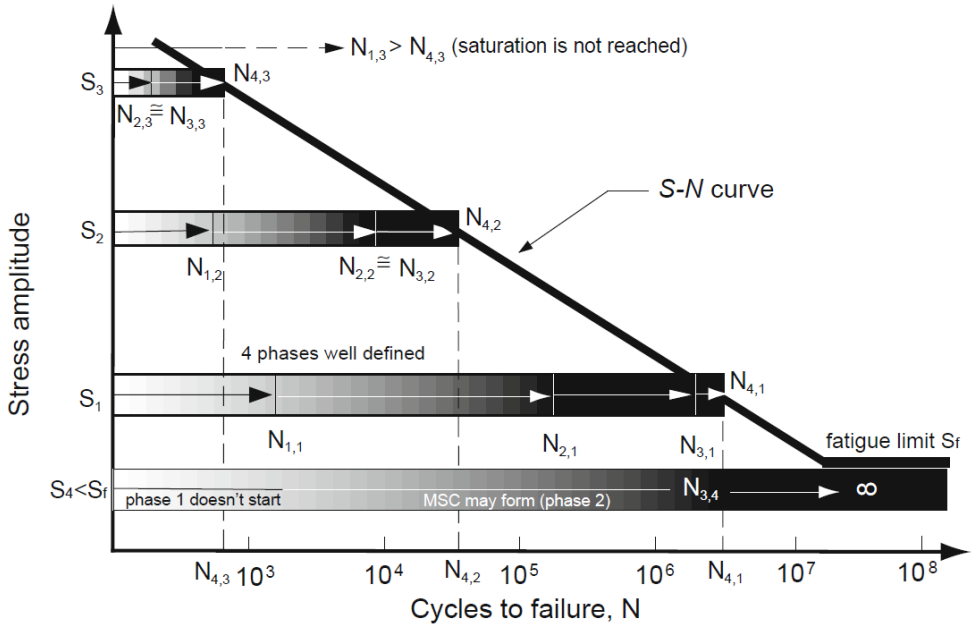

Figure 3-3: Typical S-N curve for a single mean stress value for a material exhibiting endurance limit [24].

The fatigue degradation process normally comprises three different stages. In the first stage, the crack initiates. This occurs when the stress intensity factor range, ΔK, reaches the threshold value, K_{th}. Subsequently initiated micro-cracks will grow at a fairly slow rate. Microscopically, the crack initiation is caused by the movement of slip bands or dislocations within the material. Persistent slip bands (PSB) can be formed due to the extrusion and intrusion over a few loading-unloading cycles. A microcrack can then nucleate at PSB or the edge of extrusion bands as shown in Figure 3-4. It is expected that the slip activity should be detectable using the acoustic emission technique.

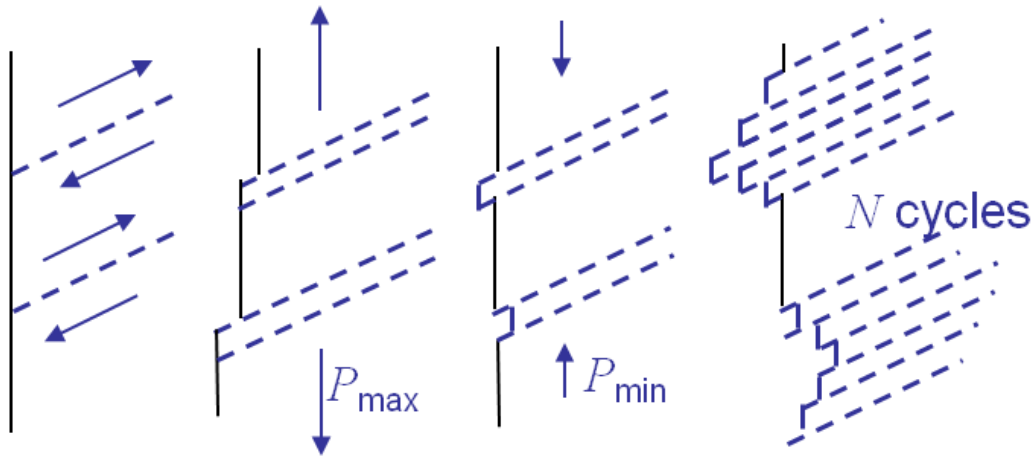

Figure 3-4: Dislocation glide during loading process and the corresponding PSB formation [27]

The fracture of inclusions or non-metallic phases can also cause the formation of microcrack. The crack propagates in the same direction as the slip bands, which is usually orientated at 45° with respect to the stress axis [28].It is noteworthy to point out that depending on the stress amplitude and mean stress, cyclic hardening or softening may also happen before. In the second stage, the crack growth rate satisfies the Paris-Erdogan law, in which the crack growth rate exhibits a logarithmic linear relationship with ΔK, which is quantified using Equation 3-3 below:

$$da/dn=C\Delta K^{m} \quad (3\text{-}3)$$

where da/dn represent the crack rate, C and m are material-related constants which are determined experimentally.

During the second stage cracks grow perpendicularly to the applied stress. The crack proceeds through a repetitive blunting followed by sharpening process, resulting in the formation of the so-called ‘striations’ on the fractured surface commonly observed using typical scanning electron microscopy[28]. Beach marks, which are caused by the change of the stress state during the fatigue process can be observed visually on the fracture

surface of the specimens. Beach marks may contain thousands of striations. They can also be caused by the differences in the degree of oxidation for different parts of the specimen produced by factors like temperature, pH, etc. In reality, the crack growth rate depends on numerous factors apart from ΔK like environment, loading frequency, etc.

It should be noted that the above equation only applies when the Linear Elastic Fracture Mechanics theory holds true. It can result in an underestimation of the crack growth rate when K_{max} approach the K_{Ic} of the material or overestimation when K_{max} is close to long crack threshold below which the crack does not grow or grow at an extremely small rate that cannot be detected under laboratory conditions [29]. It has been reported that short cracks, which are of similar size to grains in the microstructure, can even grow below the long crack stress intensity range threshold and the crack growth rate decrease continuously until the threshold is reached. More generally, short cracks should be taken into consideration in the following scenarios

(1) When the crack is similar to the local plastic zone in terms of the size.

(2) When the crack size is similar to the grain size of the material.

(3) When the crack is short physically, e.g., crack length $\leqslant$0.5-1mm.

For cracks initiating from the notch root, crack propagation is controlled by the notch tip plasticity in the early growth stage. When the crack grows inside the notch plastic zone, the shear plastic strain ahead of the crack tip is the combination of plastic deformation caused by notch plasticity and crack tip singularity. As the crack grows in the plastic zone, the contribution to the shear plastic deformation from notch plasticity decreases, whereas the contribution from crack tip increases. However, the decrease of the influence from notch tip plasticity is faster than the increase of influence of crack tip plasticity, hence,

the crack growth rate will decrease gradually after the crack initiation. Once the crack grows away from the notch plastic zone, crack arrest can even happen if the crack tip plasticity is not large enough, as crack tip plasticity is the only driving force in this case. Moreover, when the crack size is small, the influence of the microstructure of the materials cannot be neglected.

Another factor that needs to be taken into consideration when applying the Paris-Erdogan empirical law in order to characterise the crack propagation is the possibility of the occurrence of crack closure during the cyclic loading process. This process is known as Elber's rule. There are four major types of crack closure mechanisms, including plasticity-induced crack closure, roughness-induced crack closure, oxide-induced crack closure and phase transformation-induced crack closure. If crack closure occurs throughout the loading cycle then the crack will be arrested. This is a microstructural related effect which is applicable only to short cracks.

Plasticity-induced crack closure (PICC) is caused when there is residual compressive stress left behind on the fatigue crack wake. Crack closure can occur even when the external stress is tensile during the unloading process [30]. Roughness-induced crack closure can occur due to the zig-zag type crack growth path. This kind of crack closure is more commonly found near the threshold around which crack growth path is crystallographic and tortuous. Oxide-induced crack closure occurs due to the fretting action of the crack faces in air or operational atmosphere .Transformation-induced crack closure is caused by the increase in the material's volume due to phase transform ahead of the crack tip. It is similar to PICC in the sense that residual compressive stress was induced as a result of the dilation of the transformed area and the crack can be closed prematurely during the unloading process [31]. The factors influencing phase

transformation include strain rate, temperature, phase meta-stability, etc. It has been reported that strain-induced martensite transformation can decrease the crack growth rate in the initial to middle stages of crack propagation for metastable austenite stainless steel grades [32, 33].

Finally, at the third and last stage of crack growth, the crack becomes unstable growing at a very high rate which is followed by final brittle fracture. At this stage, the crack growth rate can reach 10^{-3} mm/cycle or above, depending on the material type. There are two basic fatigue crack growth modes; tensile mode and shear mode [28].

Actually, cracks tend to be subjected to mixed mode loadings rather than a single load type, in which case, both K_i and K_{ii} should be taken into consideration when fully characterising the crack growth properties of a certain material. Kim, J.-K. and C.-S. Kim investigated the influence of mixed mode loading on the crack growth behaviour of rail steel using laboratory-based experiments. They employed comparative stress intensity factor ranges ΔK_v combining both K_i and K_{ii} to characterise the stress condition that the specimen was subjected to under varying stress ratio and loading angle. They found that the crack growth rate was smaller for mix-mode loading when ΔK_v is in the low range. This was more obvious when the stress ratio became smaller. The lower crack growth rate may be caused by the asperity interlock mechanism brought about by K_{ii}, which does not exist in single K_i mode [34].

Conventional FCG is governed by the LEFM theory in which all the material is approximately elastic and is caused by the mutual competition of two mechanisms, intrinsic and extrinsic. Intrinsic mechanisms involve processes such as micro-cracking or creation of voids, whereas extrinsic mechanisms include crack deflection or crack

faces in contact through bridging, wedging, sliding or a combination of all [35]. Intrinsic mechanisms are dependent on mechanical properties of the material. However, it is worth noting that plastic deformation can be induced ahead of the crack tip during the FCG process. The size of the plastic zone is determined by the combined effect of the yield stress and K_{max} during the loading process. The LEFM theory can only hold if the plastic zone size is small enough in comparison to the size of crack. Once the plastic zone is large enough compared with the crack length, the Elastoplastic Fracture Mechanics (EPFM) should be used instead [36].

For a rail surface initiated crack, which will be described in detail later, both LEFM and EPFM theory need to be utilized during the crack evolution process. The surface-initiated crack goes through three different phases as shown in Figure 3-5. For crack growth in Phase (i), LEFM theory is valid and the crack initiates from the shear stress. After crack growth pass through Phase (i) into Phase (ii) [37], EPFM should be employed since the crack tip plastic zone is very large if compared to the crack length. Finally, the crack propagates deeper, being less influenced by the cyclic shear loading (Phase (iii)), hence LEFM is valid again. The crack growth is mainly driven by shear or tensile stress [38].

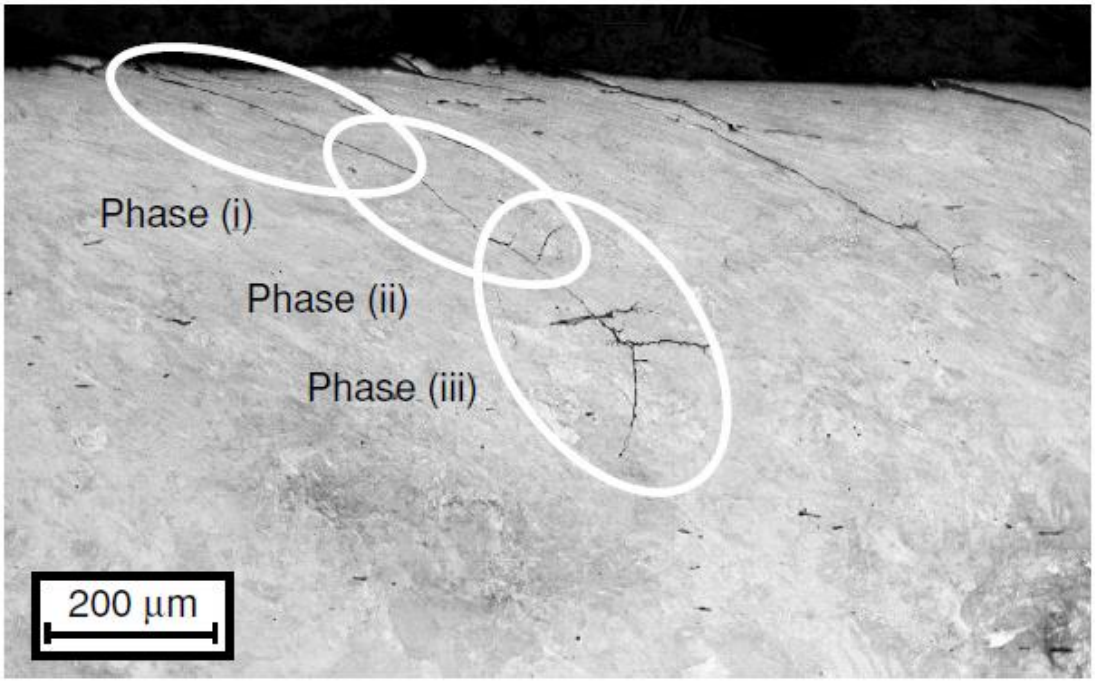

Figure 3-5: The three different phases of a surface-initiated (Rolling Contact Fatigue or RCF) crack [39].

There are four major factors that can influence the fatigue life of a steel structure. These include loading type and amplitude, microstructure, mechanical properties and environmental conditions [40].

When the external stress applied is higher than the yield strength, the material is subjected to plastic deformation. The ability of the material to bear plastic deformation is defined as ductility. It can be characterized quantitatively in the following equation:

$$\% \varepsilon = \left(\frac{l_f - l_0}{l_0}\right) * 100 \qquad (3\text{-}4)$$

where l_f and lo are the final and original lengths respectively.

Strain, ε, has a value lower than 5% in typical brittle materials. At room temperature, most steel grades show a considerable degree of ductility [41].To improve the resistance to ratcheting damage, it is fairly preferable that a steel grade with higher ductility should be used for rail manufacturing. Normally, the ductility decreases with increasing carbon content in rail steels due to the formation of cementite as discussed earlier. However, cementite and the formation of a predominantly pearlitic microstructure can improve the resistance of rails to wear thanks to the higher hardness achieved [42]. However, increased hardness may result in fatigue surface cracks (such as RCF) to initiate and subsequently propagate with time.

3.3 Ductile and brittle fracture

There are two possible fracture modes for metals, ductile and brittle. Examples of both fracture modes macroscopically are shown in Figure 3-6. In most situations, the ductile fracture mode is preferred to brittle mode due to the fact that a crack can be found before final failure occurs if appropriate inspection is carried out. The ductile fracture is accompanied by extensive plastic deformation ahead of the crack tip with the crack growing relatively slowly. This apart from allowing enough time for inspection, it also permits repair or replacement actions to be completed before final failure occurs unexpectedly which would be the case in brittle fracture.

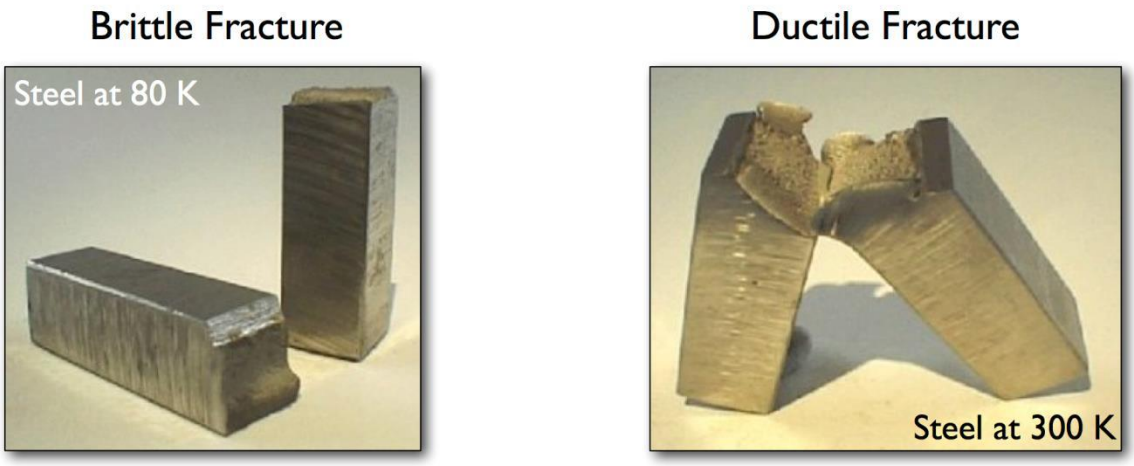

Figure 3-6: Brittle and ductile fracture of steel at low temperature (80K) and high temperature (300K) respectively [43].

Brittle fracture normally happens in an unnoticed way, giving very little if any indication before the sudden final catastrophic failure occurs. The crack grows very quickly with little plastic deformation being produced. Far more strain energy is required to facilitate the ductile fracture in comparison with brittle fracture. To characterize the materials resistance to brittle fracture, an important expression relating stress with facture toughness has been proposed as shown in Equation 3-5 below

$$K_c = Y\sigma_c\sqrt{\pi a} \tag{3-5}$$

where K_C is defined as fracture toughness, Y is a parameter related to specimen size and geometry as well as loading configuration, σ_C is the critical stress and α, is the crack length. Based on equation 3-5, the likelihood of brittle fracture increases with crack length for the same loading mode. The K_C value decreases with the thickness of the specimen for the same material. When the thickness reaches a critical value after which the K_C becomes constant, plane strain conditions start to occur. Kc under plane strain conditions

is commonly known as plane strain fracture toughness (K_{IC}) and it is more preferable than Kc in damage tolerant design and fatigue life prediction [23].

3.4 Types of loads and stresses in rails and crossings

The rail network infrastructure is subject to continuously increasing axle loads, higher rolling stock speeds and larger traffic density. A typical railway track consists of two major structures, the superstructure and substructure. Superstructures comprise the rails, rail pads, sleepers and fastening systems, whereas substructures comprise the ballast, sub-ballast and subgrade.

Rails and crossings are central to the whole railway track structure and they transfer the impact and vibrations caused by the moving rolling stock to the underlying sleepers. A schematic showing the cross section of a typical rail is shown in Figure 3-7

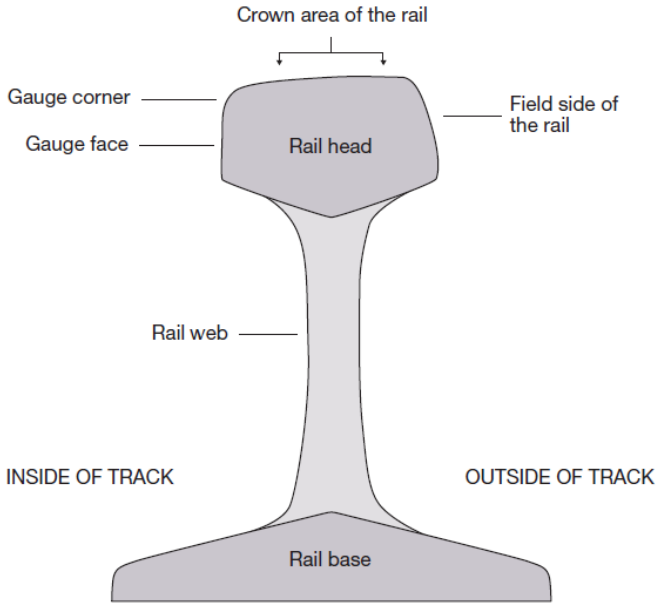

Figure 3-7: Schematic of typical rail cross section [44]

There are several major types of forces applied by the wheels on rails and crossings including, vertical, lateral and creep forces. Vertical loads are applied directly by the wheel tread on the rail head during normal operation. Vertical loads contain three components, including static, dynamic and impact loads. The static component is directly related to the weight of rolling stock sustained by each wheel, which should be constant over a relatively long period of time for a certain rail line. In curved track, the nominal wheel load applied on the high and low rails can be quite different, influenced by various factors such as train speed, superelevation, rail and wheel geometry, etc. The dynamic and impact component is induced by increases in speed, surface roughness, corrugation, height and gauge dimensional changes, and irregularities on rails such as joints or transitional regions from normal rails to crossings. The lateral component normally refers to the load exerted by the wheel flange on high rails during curving, although high lateral loads can also be generated due to the dynamic behaviour of wheelset and rolling stock, especially hunting. Creep forces are generated in a localised area due to wheel rolling on the rail. The longitudinal creep force is caused by the traction applied by the rolling stock on the rails, whereas the lateral creep force is due to the lateral oscillation of wheelset on the rails [45]. The wheel-rail interface contact problem is considerably complex. If the rail is considered as a rigid structure, then there will be two degrees of freedom for the wheelset, namely the lateral displacement, y, and the yaw angle α as shown in Figure 3-8.

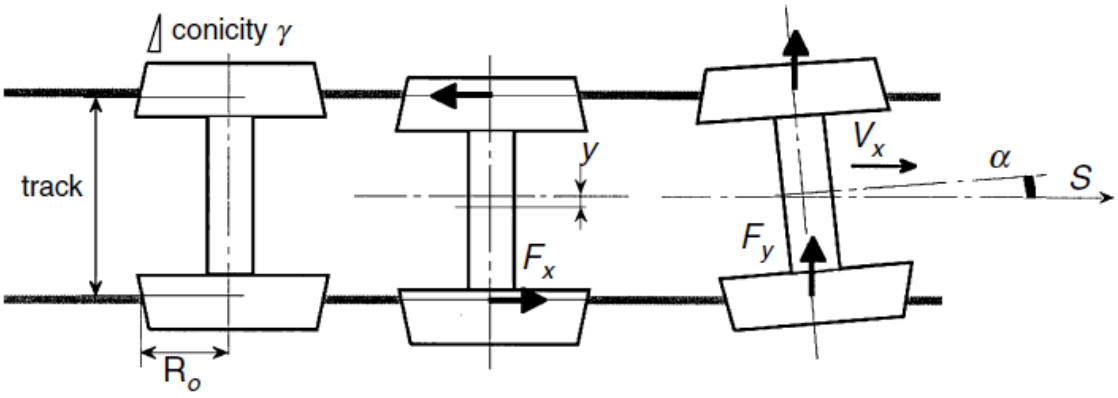

Figure 3-8: Degrees of freedom for wheelset [46].

Under ideal conditions, the magnitude of contact force between rails and wheels should be equal to that of static loading when both rails and wheels are free from any abnormalities and they are in perfect contact with each other. However, realistically, quasi-static loading is more often used when taking into account the influence of track support, curvature, superelevation, surface roughness, etc. Moreover, the deteriorating wheel and rail profiles can induce high frequency dynamic loading during a short period of time [47]. Rails and cast manganese steel crossings found in-service are subjected to five major types of stresses, including bending, shear, contact, thermal and residual stresses. The longitudinal stress state is shown as in Figure 3-9 [48, 49].

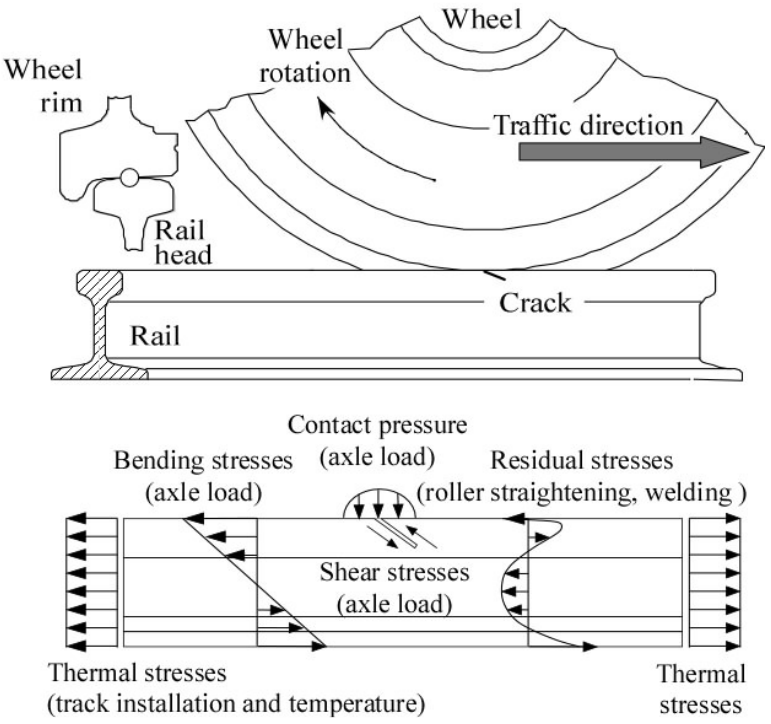

Figure 3-9: A wheel rolling on continuously welded rail and the longitudinal stress state on the rail [49].

3.4.1 Bending stresses

Bending stresses are caused by the vertical and horizontal component of the wheel load. These take the form of compressive stress in the rail head and tensile stress in the rail foot. The wheel lateral load can also cause the rail head to move laterally relative to rail foot, thus producing vertical tensile stress in the web plane. If off-centre vertical loading occurs, torsion of rail will take place. When evaluating the level of bending stress, the dynamic effects should be taken into account. The sleeper quality and wet beds influencing track stiffness may also have an important effect on the actual bending stress amplitude, although when calculating bending stress, it is normally assumed that the track rests on a continuous structure with constant modulus for simplicity. The irregularities on

the rail surface like dips, joints and on the wheel tread surface such as flats and out of roundness may also influence the bending stress amplitude.

3.4.2 Shear stresses

Shear stresses are mainly caused by surface imperfections and the vehicle acceleration and deceleration. Shear stresses are responsible for failures in the boltholes which are used for joining rail sections which are not continuously welded. Nowadays, more continuously welded rails are used to reduce the occurrence of bolthole failures, however, plates similar to fishplates are still in use today. Mode II and III loading of the vertical crack in the rails are triggered due to the shear stress generated by the passage of the wheel, as shown in Figure 3-10.

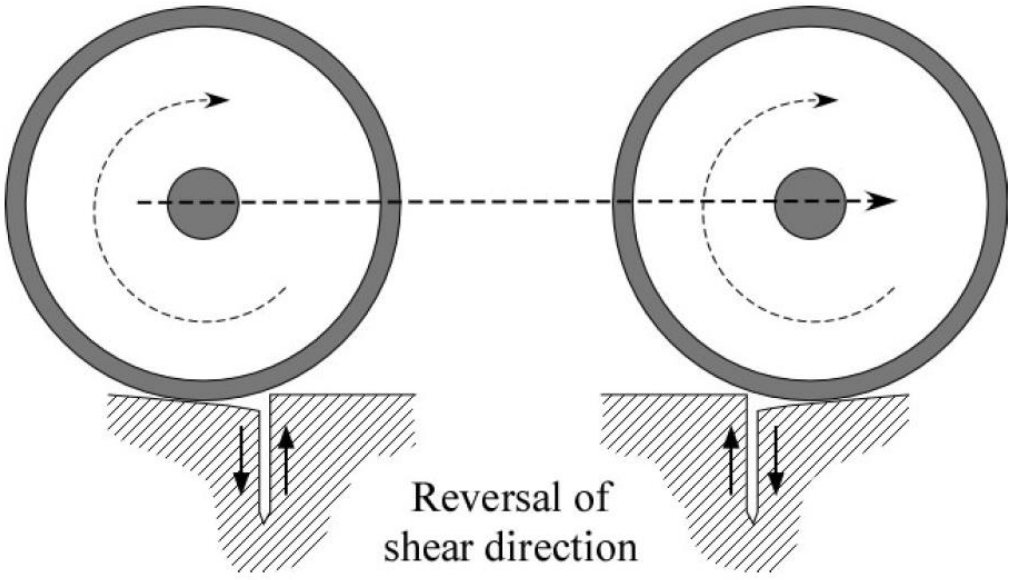

Figure 3-10: Shear loading of a vertical crack during the passage of a wheel [17].

3.4.3 Contact stresses

Stresses arising from the rail-wheel contact interactions are very high. Contact stresses can be predicted based on Hertzian analysis. Hertz assume that the contact area between two non-conforming bodies are elliptical in shape and the pressure distribution is of semi-ellipsoid shape. The formula for calculating the pressure at certain point is as follows,

$$\mathrm{p} = p_0\left(1 - \frac{x^2}{a^2} - \frac{y^2}{b^2}\right) \tag{3-6}$$

Here, p_0 is the maximum pressure at the origin of the coordinate (center of the ellipse), a and b is the length of major and minor semi-axis, respectively, x and y determine the location of the contact point. In the above equation, the values of p_0, a, b are determined by the geometry of contact bodies near the contact area and external normal compressive force.

For the Hertz theory to be valid, at least two conditions discussed below should be met.

1) The contact between the elastic bodies should be frictionless.
2) The size of the contact area should be much smaller than the radii of the curvature of the two elastic bodies.

The contact stresses are mainly determined from the wheel load and the forces in the plane near the wheel-rail interface [46, 50].

3.4.4 Thermal stresses

Thermal stresses occur predominantly as a result of the expansion or compression of continuously welded rails when the environmental temperature is lower or higher than the design Stress Free Temperature (SFT). The rail-sleeper system can buckle under

external compression increasing the derailment risk if the thermal stresses arising by high temperatures exceed the tolerance allowed or welds can break when the temperature drops far below the SFT. The movement of rolling stock as well as braking can be a contributor of thermal stresses at local and have a temporary effect. However, in cases where high ambient environmental temperatures prevail the extra heat generated by the wheels of rolling stock due to friction can be sufficient to cause the rail to buckle, likely resulting in derailment of the train itself. For this reason Emergency Speed Restrictions (ESRs) can be applicable.

To decrease the likelihood of buckling, rails are continuously welded using specially designed procedures to make sure they are in tension for most of time. When the temperature is high, compressive thermal stresses are produced to restrict the longitudinal expansion, whereas if the temperature is low, especially in winter, tensile thermal stresses are generated to avert rail shrinkage.

3.4.5 Residual stresses

Residual stresses are primarily produced during the manufacturing process, particularly the heat treatment and straightening processes. For head-hardened rails, longitudinal tensile residual stresses can be found on top of the rail head and foot, whereas in rail web, compressive longitudinal stresses tend to be dominant [45, 51]. As the bending stresses in the rail foot are tensile also, the combination of both bending and residual stresses expose the rail foot under higher risk of crack propagation [52].

3.4.6 Dynamic and other effects

Rails also sustain loads generated from acceleration, traction and braking of the train moving at a certain speed. During cornering, the lateral load allowing the train to follow

the curved route as well as the load distribution from low rail to high rail also needs to be taken into consideration. Force analysis becomes more complicated if dynamic loads are considered. Due to the irregularities on the rail and wheel surfaces, rail stresses can be increased greatly. The dynamic effect is more obvious in high speed conditions, which can lead to unexpectedly higher crack growth rates to occur. The dynamic loads can be obtained by multiplying the static load by a magnification factor, K, as shown in Equation 3-7 [49]:

$$F_{dynamic} = KF_{static} \tag{3-7}$$

The duration of the dynamic load is very short, for example, 2-10 ms. The most common source of the dynamic load is from the wheel-rail interface interactions caused by wheel shelling and wheel flat. It is generally believed that the magnitude of dynamic load is determined by the severity of the discontinuity, the axle load and the unsprung mass of the train[47, 53]. For switches and crossings, the inherent structural differences from plain track make it susceptible to both high static and dynamic load. The curves in switches and crossings have smaller radius in comparison with that for plain track. Thus higher lateral guiding forces are needed. Moreover, high vehicle jerk happens during the short transition from straight to curved section. Cant is rarely applied in the transition curve of switches and crossings, hence requiring more lateral force compared with plain track[54].A general switch & crossing unit can be found in Figure 3-11.

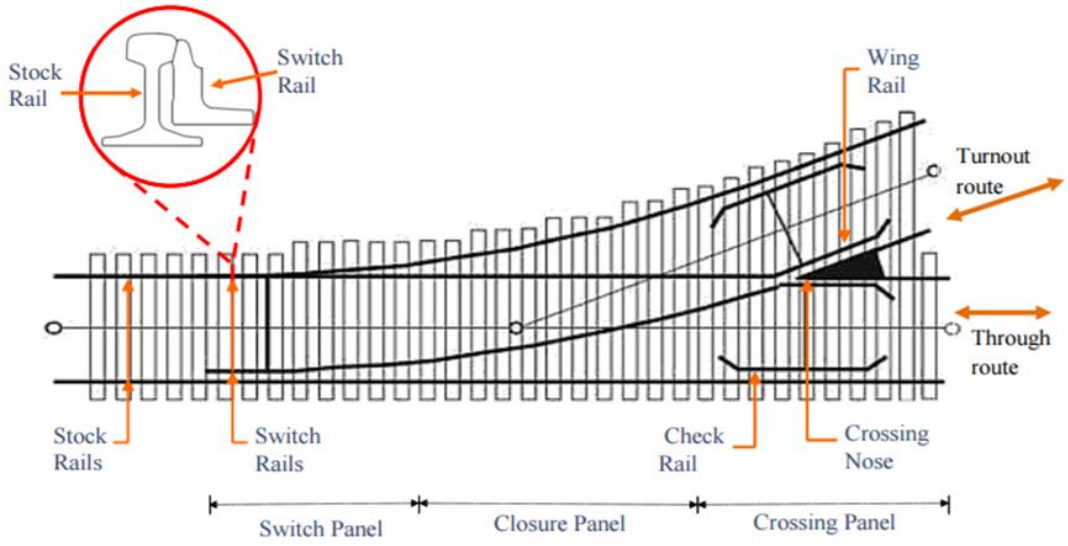

Figure 3-11: General switch & crossing unit [55].

High impact loads can be induced when the wheel transfer from stock rail to switch rail and from the wing rail to the crossing nose. Ideally, the contact force should not increase much during the transition. However, the actual force value shows a high deviation mainly due to the irregularities on the rail and wheel surfaces. More specifically, factors influencing the value of the impact load include the wheel speed, axle load and profile of the wheels and crossings. The wing rail deviates outwards before the frog entry, as does the contact point on the outer wheel with the rolling radius decreased. Hence, the vertical force for the rail before the crossing nose keeps decreasing until the wheel contacts the crossing nose, whereas the lateral force shows a reversal before and after the transition. Normally, the wheel passes the wing rail in a downward trend.

It is noteworthy to point out that if the nose is higher than the wing rail, then the induced impact load will be even larger. Hence, wear, plastic deformation or even crack growth can take place in both the wheels and crossings. It has been reported that defects in switches and crossings account for the largest percentage of all major faults found on the railway network [56, 57]. Defects in rails and crossings, if not detected in time, can pose

a significant threat to the safety and efficiency of the network. Therefore, inspection and assessment of the growth of these defects in service is critical in making maintenance decisions and ensuring the smooth operation of the rail network. Various NDT techniques have been used for structural integrity evaluation in rail sector. The different types of structural defects in rails and crossings and commonly used NDT techniques are presented in Chapter 4.

Chapter 4:

Structural Defects in Rails and Crossings

CHAPTER 4 : STRUCTURAL DEFECTS IN RAILS AND CROSSINGS

4.1 Introduction

Traditionally, there are three major types of defects found on the railway network, including manufacturing-related defects, improper usage-related defects and fatigue-related defects. Manufacturing-related defects refer to the damage type caused by hydrogen accumulation in the steel. For example during the steel-making process is not controlled properly, some hydrogen atoms or other inclusions such as manganese sulphides (MnS) can be left in the steel. Hydrogen atoms can combine to form molecular hydrogen, thus increasing the internal pressure within the microstructure vicinity causing crack initiation. Similarly Mn can react with S to form soft MnS inclusions from where RCF cracks and other defects can initiate and subsequently propagate. Improper usage-related defects refer to those caused by inappropriate operational activities, such as wheel-burns, accidental impacts, etc. Over the last 30 years, due to the improvement in manufacturing quality, defects related to steel quality are rarely found. Rail defects occurring due to fatigue, and the possibility of failures resulting from RCF defects in particular have been increasing in recent years due to the more wear resistant steel grades.

The derailment at Hatfield, UK (2000) is an example of the possible consequences that uncontrolled RCF damage can have on the railway network if it is not addressed in time [48]. Figure 4-1 shows the aerial view of the eight derailed coaches after the catastrophic train derailment at Hatfield.

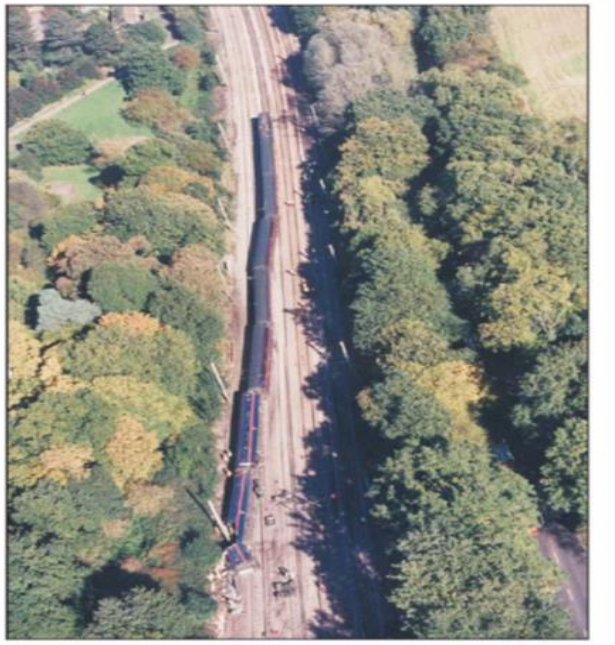

Figure 4-1: Aerial view of the eight derailed coaches in the Hatfield rail crash in 2000 [58].

4.2 Ratcheting behaviour

The rail surface deformation during wheel-rail contact is mainly determined by the level and nature of the rolling contact stress, as shown in Figure 4-2. If the stress level is low, the surface material behaves elastically with no accumulated deformation. Plastic deformation will start to occur only after a certain load level is exceeded.

The surface layer will accumulate deformation plastically as a result of the repeated friction loading that the rails are subjected to. Residual stress can be induced along with the occurrence of plastic deformation. At some point, the further plastic deformation will be prevented from the residual stress and the surface material will respond elastically again. This type of material behaviour is termed as elastic shakedown. If the load level exceeds the elastic shakedown limit value, the plastic shakedown theory will apply. If the plastic shakedown limit load is exceeded, the residual stress will not be big enough to

suppress further deformation and plastic strain will continue to accumulate. Figure 4-2 also shows the material responses due to different stress levels. Once the critical strain value is reached, cracking will initiate. The critical strain is much higher than that during tensile test due to the contribution of compressive loading. This sort of strain accumulation with each cycle is commonly known as ratcheting behaviour.

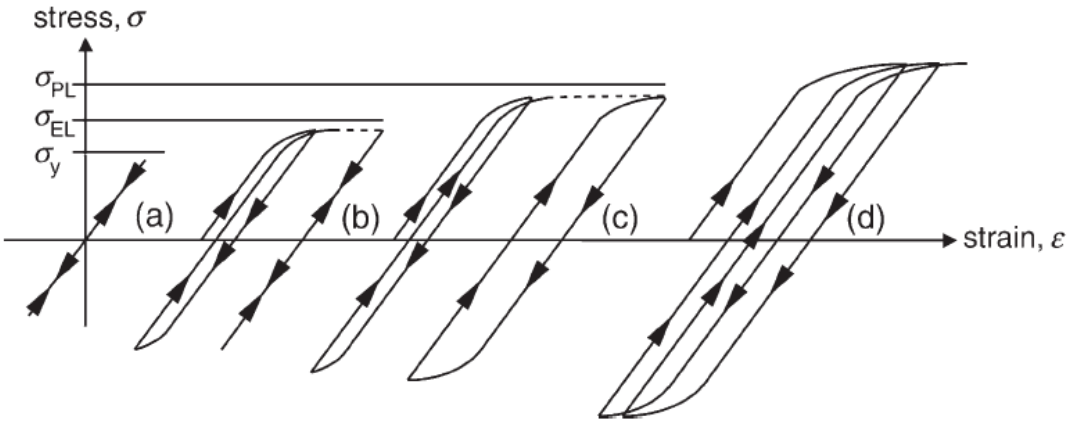

Figure 4-2: Material responses due to different stress levels and nature [59].

If the friction co-efficient is fairly small, it is very likely that the fatigue crack will initiate underneath the rail surface. Subsurface fatigue cracks mostly happen in the high rails of curves in some heavy haul lines. It has been reported that cracks can initiate 3mm to 15mm below the surface, resulting from the locally high tensile stress. Unlike surface initiated cracks, these cracks are more influenced by such factors like material microstructural defects (such as inclusions), residual stresses, thermal cooling and global bending[49].

4.3 Corrugation

Grassie [60, 61] made a thorough review of the characteristics, causes and treatments of rail corrugation. Corrugation refers to quasi-sinusoidal surface irregularities on either wheel or rail. If the corrugation wave length is smaller than one meter then it can be

normally observed by naked eye. It can add extra impact loads to the nominal wheel load and also reduce passenger comfort. Moreover, it can facilitate the RCF on high speed line and cause 'Belgrospi' type defects to form, although itself is not fatigue-related defect [62].

Based on the fixed waveform length and damage mechanisms, corrugations can be classified into six major types, namely 'heavy haul' and 'light rail' corrugation, 'pinned-pinned resonance' and 'rutting' corrugation, other P2 resonance corrugation and track form-specific corrugation. The detailed damage mechanism and corresponding treatments for each type can be found in Grassie's comprehensive review study [60]

4.4 Rolling contact fatigue

Normally, there are three different modes of RCF in the UK. The probability of RCF occurring is closely related with curve radius. Normally, the higher radius the curve is, the more possible the occurrence of RCF will be. In curves, the outer rail is more susceptible to wear and RCF, which is caused by:

(1) The smaller contact zone, which is equivalent to a pound coin sized area
(2) The dynamic load producing the centripetal acceleration and the axle oscillation when the train rounds the curve [63]

4.4.1 Head checking

In the British railway system, the most common type of RCF is head checking, which is also known as gauge corner cracking or GCC if it occurs at the gauge corner, as shown in Figure 4-3. Head checks and GCC initiate from the rail surface as small and fine cracks. Shelling defects initiate due to the fact that the shear stress exceeds the maximum allowable values for the rail. After the initiation, they grow at a shallow angle into the rail

before turning into a steeper angle at around 3 to 5mm deep. Normally, this type of defect can be found on highly canted curves with the curve radius and cant deficiency determining its location on the rail head [64, 65].

Figure 4-3: Heavy GCC present on the rail head surface [45] .

The angle at which the head checking cracks grow into the rail head is closely related to rail fracture. If the angle is approximate 15°, it is highly possible that multiple fractures could happen, leading to train derailment [66]. Four distinct regions can be identified during crack propagation process as shown in Figure 4-4. In Region A, the crack initiates on the surface and starts to grow. In regions B and C, the crack keeps growing under a certain angle until it reaches a depth of 3-5mm. As the crack grows its growth rate increases due to the continuously increasing stress ahead of the crack tip. However, once the crack length reaches a critical value, the rate starts to drop, as the influence of localised stress field caused by the rail-wheel contact has been greatly weakened due to the increasing distance between the crack tip and the stress field. In Region D, they continue to propagate branching vertically or horizontally and the crack growth rate increases

again. The crack growth rate is mainly controlled by the contact stress and global bending, both of which can greatly enhance the crack growth rate.

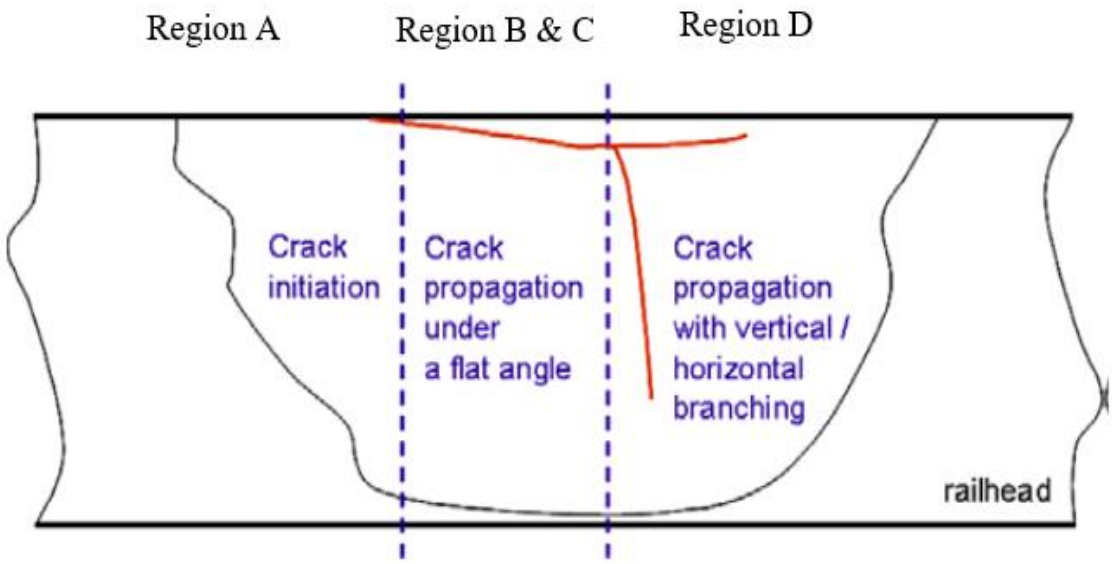

Figure 4-4: Different stages of Crack propagation in the railhead [67]

The actual crack length is determined not only by crack growth rate but also the wear rate, as shown in Figure 4-5. When the wear rate is very high (Level 1), the crack initiation can be prevented. The crack propagation can be retarded if the wear rate is at Level 2, since the wear rate exceeds crack growth rate once the crack reaches a length. If the wear rate is fairly small (Level 3), then the crack length is not restricted by wear rate at all.

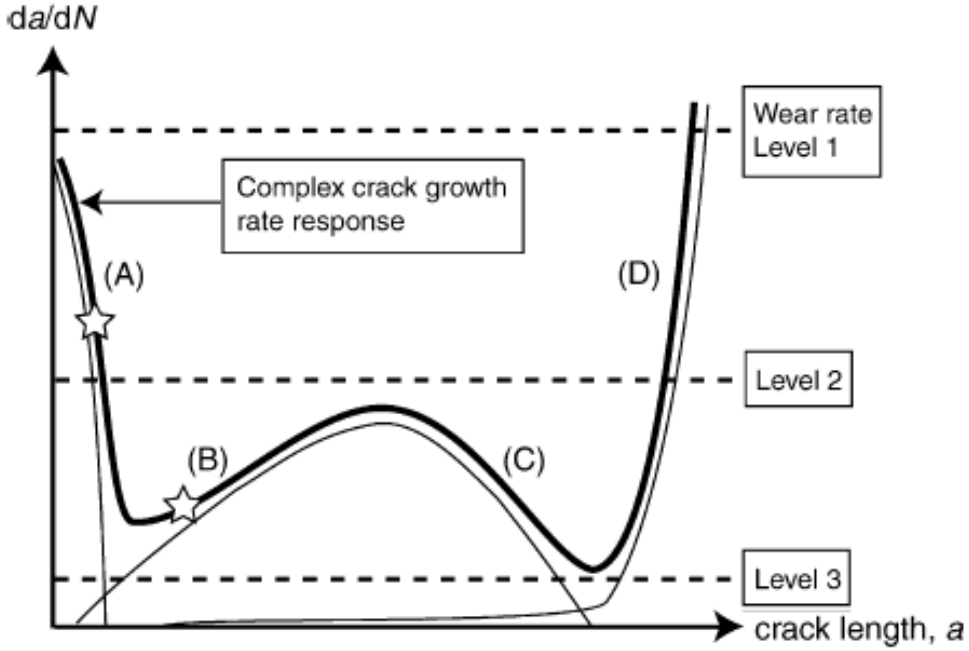

Figure 4-5: The life cycle of a crack in the railhead [68]

4.4.2 Shelling

This is one type of internal defects induced by the high shear stress, which is influenced by a combination of factors like wheel load, rail crown radius and traction force. They initiate at around 2-8mm below the rail surface and then grow longitudinally for some distance before either spalling out or turning into transverse defects. The difference between shelling and head checking in terms of crack initiation location is mainly because of the influence of the ratio of tangential force to normal force the maximum shear stress occurs, as shown in Figure 4-6.

Clearly, as the ratio increases, the maximum shear stress increases and the location for maximum stress is shifted closer the rail surface, thus facilitating the formation of surface cracks. Another factor explaining the different growth characteristics for shelling crack compared with head checking cracks is work hardening property of the rail materials. The

work hardened layer can be up to 8-10mm in depth and it can prohibit the shallow head checking cracks from growing into the rail head, whereas for shelling cracks, they may grow through the worked hardened zone and with the effect of other types of forces like bending develop into transverse defects [45].

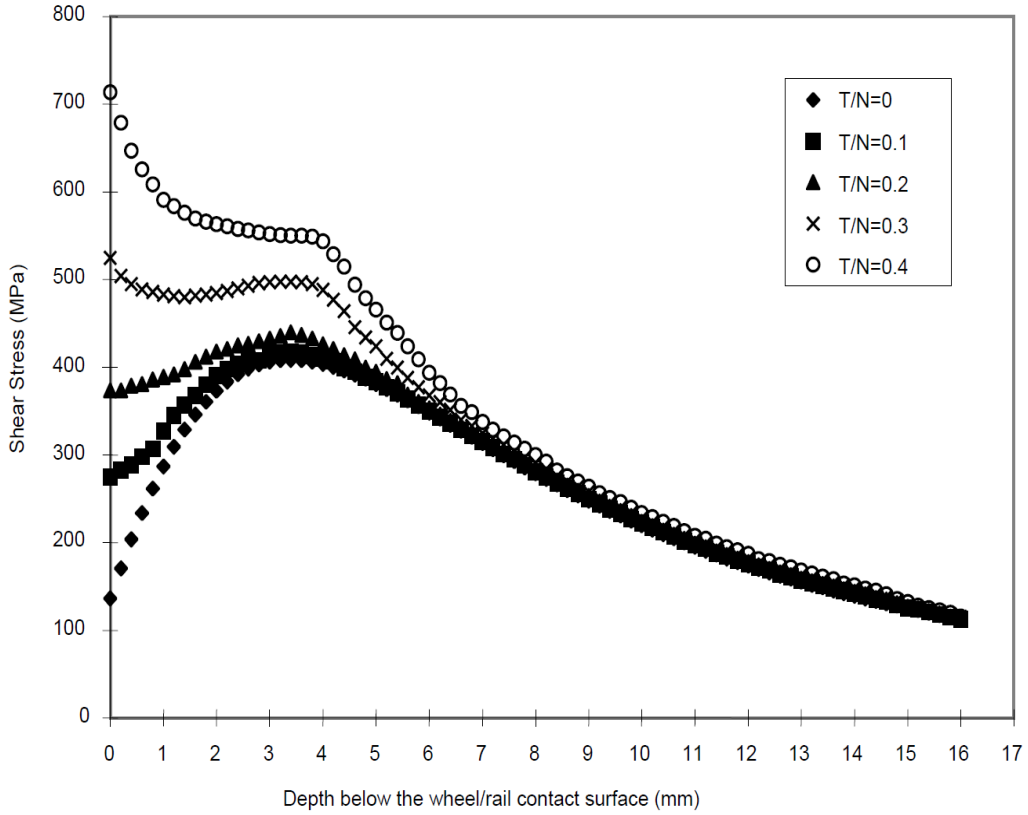

Figure 4-6: Correlation between the shear stress and depth below the contact surface [69]

4.3.3 Squats

Squats are another type of RCF damage. They occur in straight tracks or large curves and originate from the sheared surface layers of the rail head. Squats are characterised by darkening of the rail surface as well as an increase in the running band. They are normally shown as two lobes of similar size on the rail surface. Squats can cause initiation of transverse cracking underneath. They can be of two types: squats on the rail crown and those occurring at the gauge corner. They are accompanied by two cracks, one in the

direction of travelling and the other in the opposite direction [45, 70, 71]. The root cause for initiation and growth mechanism is still not fully understood up to now.

4.4.3 Tongue lipping

Tongue lipping, which is named for the extrusion of thin layers of material from the rail head, can result in the crack initiation under the extruded steel and the following propagation in nearly horizontal plane. The crack may deviate from the horizontal plane and if it grows towards the rail surface, it will finally break loose a piece of rail surface material, however, if the crack deviates towards the rail foot, it may cause complete rail failure [45].

4.5 Other types of defects

4.5.1 Vertical split defects

Vertical split head defects initiate near the central line of the rail head and as the name indicates, they can result in the separation of the rail head into two parts if not detected and controlled properly in time. They can initiate from the longitudinal seams, segregation, inclusion generated during the manufacturing process. The type of defects are more commonly found for rails produced from ingots rather than the current continuous casting.

Although some visual characteristics on the rail surface can be observed for very large defects, the detection of small to medium size defects have to be performed with the aid of non-destructive testing techniques. After the initiation, they can grow both longitudinally and vertically and it is not uncommon for one end to extend towards gauge side and the other end to extend towards field side.

4.5.2 Horizontal split defects

Similar to vertical split head defects in terms of source type， they can initiate from internal segregation, longitudinal seams and manufacturing-related inclusions. After the initiation, the defects develop longitudinally and horizontally in the rail head. Again, for small and medium-sized defects, there are no visual characteristics. Impact loads may be one of the factors responsible for the initiation and development of these defects. During the crack growth process, stress conditions may involve both shear and tensile stresses, as the white etching layer which indicate the rubbing between crack faces can be found.

The turnout or crossing is an important system used to divert train from one route to another in the railway network. It consists of different parts including the rails, rail pad, fastener, screw spikes, sleepers (concrete, timber, etc.), ballast and formation. A high percentage of track renewals happen in switches and crossings. The degradation of switches and crossings under service is detrimental to passengers' ride quality, hence it is crucial that effective and efficient maintenance strategy be employed for turnout systems. The types of degradation in switches and crossings include RCF defect, wear, impact damage, etc [28, 72].

4.6 Rail inspection techniques

Traditionally, rail inspection was carried out manually and qualified personnel walking along the railway network to check visually if there are any existing defects that could pose threat to the integrity of the rail track, hence requiring a huge amount of labour which is also cost inefficient. Moreover, the accuracy and consistency of the inspection could not be ascertained as it is highly subjective and dependent to the skills and attention of the individual as well as physical condition, including vision condition. To reduce the

amount of time and labour spent on rail track inspection, various techniques and related equipment have been employed.

4.6.1 Magnetic flux leakage

Currently, magnetic flux leakage (MFL) and ultrasonic testing (UT) are two commonly employed techniques in rail inspection. One inherent limitation of MFL is its insensitivity to the defects far from the surface. Moreover, the orientation of the defects can affect their detectability. More specifically, the size of the magnetic flux leakage field decreases with the angle between the cracks and magnetic flux. If the orientation of the cracks is parallel to the induced flux, then they cannot be detected. If the orientation is vertical to the flux, the size of leakage field attains a maximum and smaller defects can be detected [73]. Rails become part of the magnetic circuit through a high ampere current that is input into the rails through a brush making contact with the rail head. The route that the current passes through will be distorted if a defect gets in the way and the resulting disturbance of magnetic field can be detected by an array of sensors [74, 75].

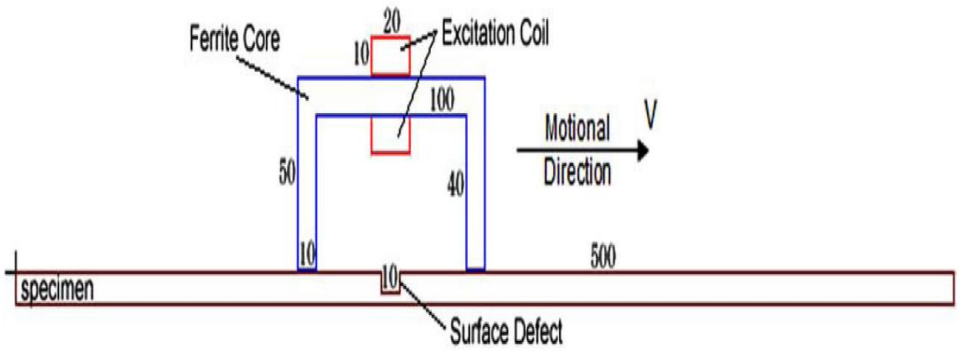

Figure 4-7: Schematic of the principle of MFL application on rails monitoring [76]

For MFL inspection on rails, sensing coils are placed a constant distance above the rails as shown in Figure 4-7. MFL is normally used as a complement to conventional ultrasonic testing to detect near-surface defects in a Sperry models. To get accurate results, the speed cannot be above 35km/h [76].

4.6.2 Ultrasonic testing

In ultrasonic testing, ultrasonic beams are input and transmitted through the rails at various angles. The ultrasonic waves are reflected back when they encounter defects in the rail structure. Based on the arrival time and amplitude, the location and severity of the defects can be determined together with its orientation. However, due to geometrical reasons, it is difficult to detect head checking cracks with this method and to determine the crack tip, which makes it impossible to calculate the crack length and give a reliable evaluation of the severity of damage present in the rails. Moreover, it is difficult to detect the defects in the rail foot using the ultrasonic technique as part of this rail region is obscured [77]. UT can be carried out manually by qualified personnel during the line closure period using special trolleys. The UT system can also be installed in hi-rail vehicles or test trains. The typical test trains are Sperry trains of models UTU1 and UTU2 and the maximum speed they can attain is 65km/h. The speed of deployment and resolution achieved by automated UT systems can be influenced by the way that the transducers are deployed, sled or wheel carriers. Sled carriers enable a shorter distance between the ultrasonic probes and the rail surface [78]. The inspection results of test trains and hi-rail vehicles need to be further confirmed by portable inspection units deployed manually [76]. However, some deeper cracks cannot be detected if the ultrasonic beams are reflected by the shallow cracks as shown in Figure 4-8 and this is one major disadvantage for ultrasonic inspection of rails.

Figure 4-8: Masking effect of a larger crack caused by a shallow crack in front [79]

The false detection of defects with ultrasonic means can occur if the threshold and time window are not set properly. Then the corresponding manual inspection will cause further delays to the railway network operation restoration until it is completed.

It is also noteworthy that UT is very sensitive to the environment. Under very cold weather, intervening interface forms due to the ice on the rails influencing the accuracy of detection. Leaf mould on the rails can also greatly undermine the sensitivity of the probe, which is a long-existing problem on UK railway lines.

4.5.3 Eddy current testing

Eddy current testing (ECT) is used as a complement to conventional UT testing especially for the detection of gauge corner cracks. It is one of the NDT techniques that employ the theory of electromagnetic induction. When an alternating current is input to a coil of conductive wire, a corresponding alternating magnetic field is generated. The eddy current can be induced once the wire is moved close enough to the rail surface and flow in opposite direction in close loops based on Lenz's Law. Once a crack exists, the eddy current will be disturbed and the resultant impedance change in the coil can then be

measured. Based on the level of impedance change the crack length can be correlated and analysed.

4.6.3 Visual inspection

Visual inspection should be carried out twice a year using photographs and video images and then the information is filled in the form for future reference [80]. It can be either portable or installed on the train. Extra attention should be paid to irregular track geometry like switches, rail weld zones, expansion joints and other irregular areas. Visual inspection can be easily influenced by the weather conditions prevailing at the time of the inspection. Lubrication and soiled rails can also adversely affect the quality of the visual inspection. The speed of the train needs to set properly to enable sufficient resolution.

4.6.4 Ultrasonic phase arrays

Ultrasonic phase array inspection is a type of ultrasonic testing method involving multiple sensing piezoelectric elements. Instead of conventional ultrasonic monocrystal or twin probes, ultrasonic phased arrays contain multiple elements in a single probe. The generated beam can be steered, swept and scanned by varying accordingly the excitation times of the elements resulting in different interference patterns. More specifically, the ultrasonic wave generated by each element can act constructively or destructively, resulting in the increase or decrease of the wave energy introduced in the rail. Compared with conventional ultrasonics, it has two advantages. Firstly, different inspections from the same location can be performed, hence enabling the accurate detection of cracks of different angles. Secondly, internal structure of the inspected object can be obtained [81]. However, ultrasonic phased arrays can only be used at slow speeds and need to be deployed manually.

4.6.5 Long range ultrasonic testing or guided waves

Long range ultrasonic testing or guided waves are a modified technique based on conventional UT which is better suited for the detection of transverse defects in the rail head. It employs much lower ultrasonic frequency range than conventional ultrasonic testing. In the low frequency range employed, the guided wave can easily penetrate alumino-thermic welds which can scatter the ultrasonic waves for conventional UT. However, the challenge for this technique is the data interpretation when the waves of different modes traveling at different velocities overlap [82].

4.6.6 Electromagnetic acoustic transducers

Electromagnetic acoustic transducers or EMATs based systems have the capability of generating and receiving ultrasonic waves without contact between the transducers and the rail surface (Figure 4-9). Its principle is based on the generation of ultrasonic oscillations arising from eddy current interactions with the microstructure of the material due to magnetostrictive and Lorenz force effects near the surface of the rail head. Both surface and bulk waves can be generated to assist the evaluation of the whole rail section. The intensity of the magnetic field will decrease rapidly with the increasing distance between the coil and the surface. The real challenge for EMAT is the low signal to noise ratio and the effective and accurate control of the probe's lift-off. EMATs are very sensitive to variations in the lift-off for both the generator and receiver part of the sensor. As a result of that, frequency domain rather than time domain should be looked into for the analysis, as the frequency content will hardly change over a standoff change of few millimetres.

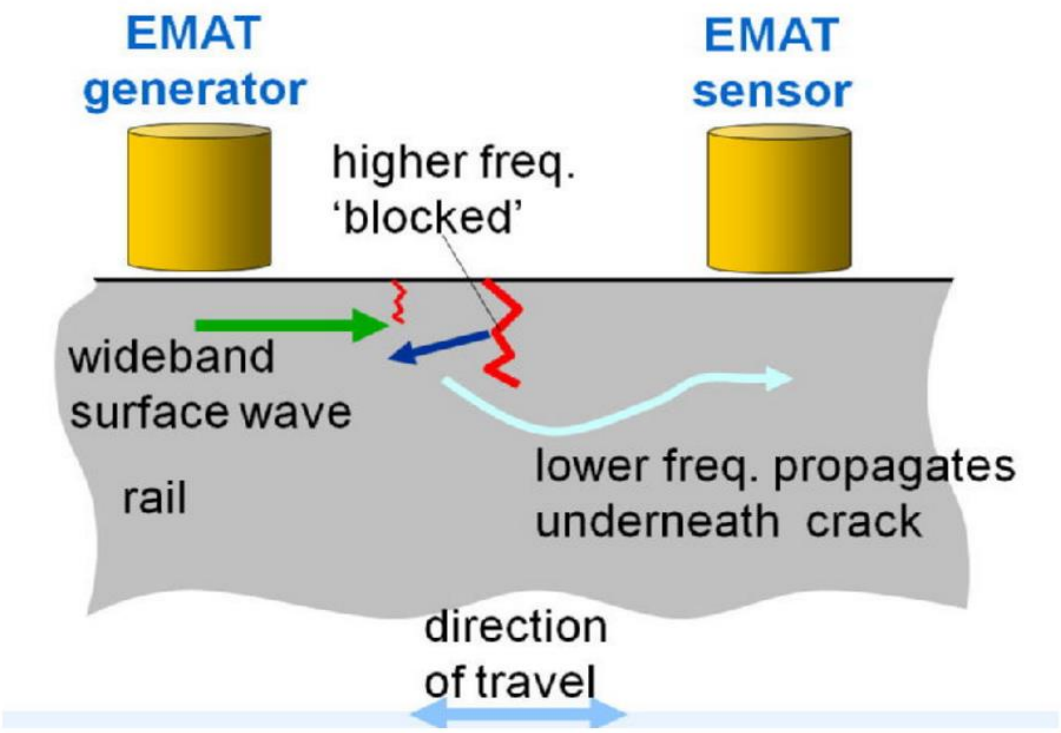

Figure 4-9: Schematic diagram showing the use of EMATS for measurement and detection of transverse cracks [83]

4.6.7 Alternating current field measurement

Alternating current field measurement (ACFM） was originally developed as a substitute to Magnetic Particle Inspection (MPI) for use in the oil industry. Its principle is based on the induction of a uniform alternating current within the thin layer at the surface of any conductor. If there is crack in the layer, the current will be redistributed around the ends and down the surface of the crack, causing the disturbance of the corresponding magnetic field associated with the current. The advantages of this technique over conventional ones, like UT, is its capability to capture the information regarding the depth as well as the length of the crack.

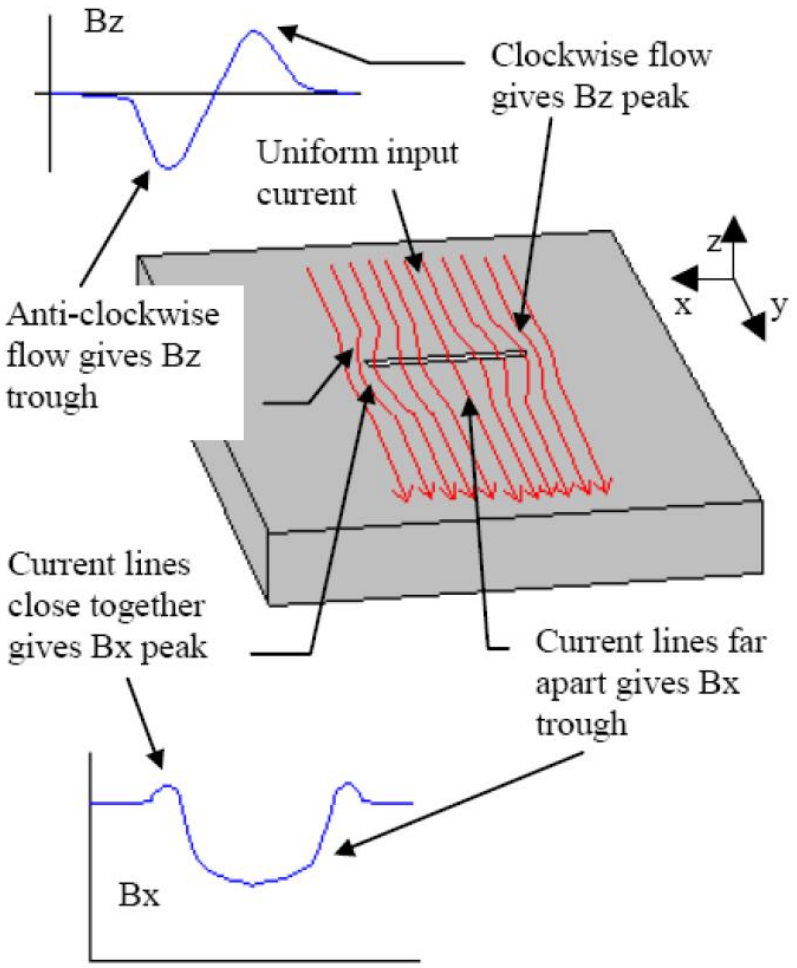

Figure 4-10: Principle of ACFM technique [84]

4.6.8 Probe vehicle

Kojima proposed the concept of probe vehicle which can detect track faults using a portable on-board sensing system. The system consists of accelerometers, microphones, an analogue input terminal, GPS receiver, a rate gyroscope. The accelerometers and microphones are used to measure track irregularities and corrugation, respectively. The system has successfully detected irregularities and corrugation on the commercial line in Japan using spectral peak calculation. The GPS receiver can locate the area where the track faults were found. Another system named RAIDARSS-3 has been installed on the in-service trains to check the car-body acceleration and longitudinal levels for Tokaido

Shinkansen. The repeatability of the measurements was confirmed and even minor changes in track irregularity could be detected. The information regarding the ability of both systems to detect the existence and growth of RCF crack has not been reported yet [85].

4.7 Damage tolerance concept and maintenance in railway

There are five approaches in assessing damage tolerance. First of all, the size and shape of existing cracks and other types of defects should be assessed correctly. The NDT techniques can be used to determine the size of the crack. The accuracy of the measurement depends on the used NDT techniques, the skills of the operators, etc. The crack shape can be determined based on the NDT results as well as past experience from experiments and failure analysis. After the determination of crack size and shape, the relationship between crack growth rate and effective stress intensity factor which takes into account factors such as variable load amplitude and mixed loading then needs to be obtained. For railway applications, the dominant mechanism for crack growth is fatigue, although sometimes corrosion-related damage evolution also needs to be accounted for. This is however more relevant to tunnels where moisture can accumulate for long periods of times under the rail foot. An inspection plan can then be made after the critical size of the crack is determined. It has to be ensured that the inspection interval is smaller than the remaining service lifetime of the damaged rail or crossing. However, if it can be proven that the crack does not grow between inspection intervals, then the number of inspections within a certain period of time can be potentially reduced [51].

As unplanned maintenance activities can cause severe disruption to the normal operation of the network with huge financial losses being incurred, the condition-based maintenance is becoming increasingly important for the realisation of more efficient and

high standard railway service. The concept of intelligent infrastructure has been put forward by Network Rail to enable the conversion from reactive to preventative maintenance for railway infrastructure. In Schöbel and Maly's work, interconnections between different faulty states have been established and the need for active monitoring of railway components using automated device has been clearly pointed out [86, 87].

SHM or RCM has been regarded as a promising way to enable more intelligent and efficient surveillance and management. It can minimise the disruption to normal operation of the railway network and provide continuous rather than intermittent monitoring of the infrastructure. Informed decision on the maintenance strategy employed can be made automatically based on the interpretation of the collected data in synthesis with historical data using appropriate algorithms. In the long run, the implication of SHM on safety and cost aspect of railway sector is immense. The above NDT techniques have their own advantages and disadvantages and a system integrated with different techniques seems a better solution to the infrastructure maintenance and management in the railway industry as mentioned in [77]. AE technique is another passive NDT technique and its application in rail sector is still very limited. The principles of AE technique and its application are presented in the following chapter. Some common algorithms for AE signal processing are also introduced.

Chapter 5:

Remote Condition Monitoring with Acoustic Emission and Data Analysis

CHAPTER 5 : REMOTE CONDITION MONITORING WITH ACOUSTIC EMISSION AND DATA ANALYSIS

5.1 Introduction

AE testing is gaining more popularity as a versatile means for SHM. The fundamental principles of the AE technique are visualised in Figure 5-1. The technique is based on the detection of elastic stress waves emitted during damage evolution while a structure is loaded structure. The elastic stress waves are detected by piezoelectric sensors mounted on the surface of the structure and converted into electric signal which can subsequently be digitised by an appropriate data acquisition card capable of high sampling rates.

One of the key advantages of AE over other NDT techniques is that it is passive in nature. Hence, it depends on capturing the energy released from the structure as damage evolves. The passive nature of AE increases its sensitivity to even extremely small defects that are growing (or otherwise are active) and hence infinitesimal small damage growth events are possible to be detected. However, it also makes quantification of damage far more difficult. Thus, although AE provides more flexibility when compared with other techniques, it is not under normal operation considered to be quantitative in its standard approach at least. Moreover, based on its principles, it can only work on dynamic processes such as crack growth and provide some indication regarding the severity of damage inside the structure. However, if the load exerted on the structure is not big enough to trigger AE activities, defects are not active and therefore, cannot be detected.

The piezoelectric sensors can be classified into two categories; resonant and wideband. Resonant sensors have the highest sensitivity at certain frequencies which is known as the sensor's resonant frequency, whereas wideband sensors show a stable response in wide frequency spectrum. The piezoelectric sensors will generate oscillating voltage at

the same frequency as the excitation causing them to vibrate like a bell[88] . Due to the lower cost and good sensitivity to signals from the preferred frequency range, resonant sensors are more commonly used in the field since they tend to cope better when dealing with filtering out unwanted noise sources. The selection of piezoelectric sensors is mainly based on their frequency response. The calibration curve of the sensors can be verified by inputting sinusoidal excitation. It is crucial that the sensors are coupled effectively with the surface of the monitored structure. Therefore, it is necessary to prepare the structure's surface in order to make sure it is smooth and clean before mounting the AE sensors. Wave direction and the type of medium can also influence the sensor's response [89].

Normally, before the signals are transmitted to an AE instrument for further analysis, they need to be amplified using appropriate amplification. This is achieved with the use of pre-amplifiers and amplifiers [90].

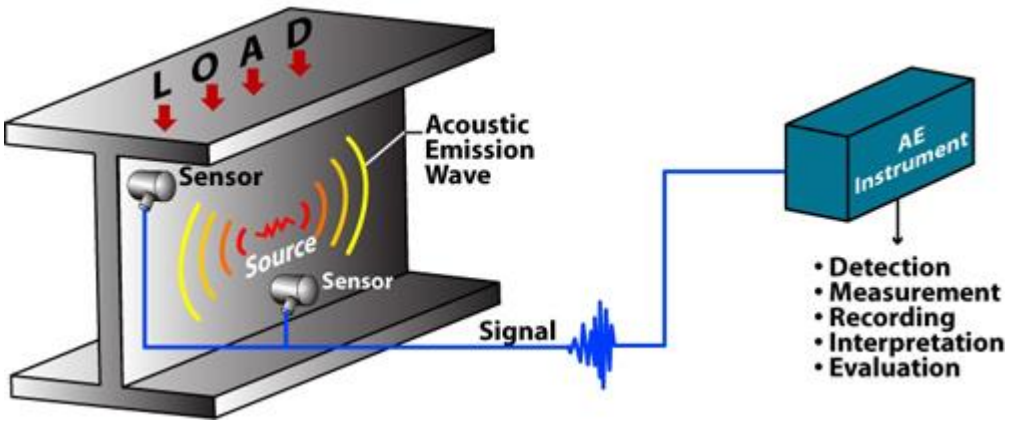

Figure 5-1: The principle of AE testing [91]

AE sources range from natural phenomena such as earthquakes to micro-crack initiation and subsequent propagation, dislocation slip and aggregation, impact, or phase transformation in metallic materials. In composite materials, AE signals can be generated from fibre breakage, delamination, debonding, etc. AE has also been reported to be applied in monitoring structures made of wood, concrete and polymer materials [92].

5.2 AE waveforms and measurement parametrisation

Normally, AE signals can be classified into two types of waveforms; continuous and burst-type as shown in Figure 5-2.

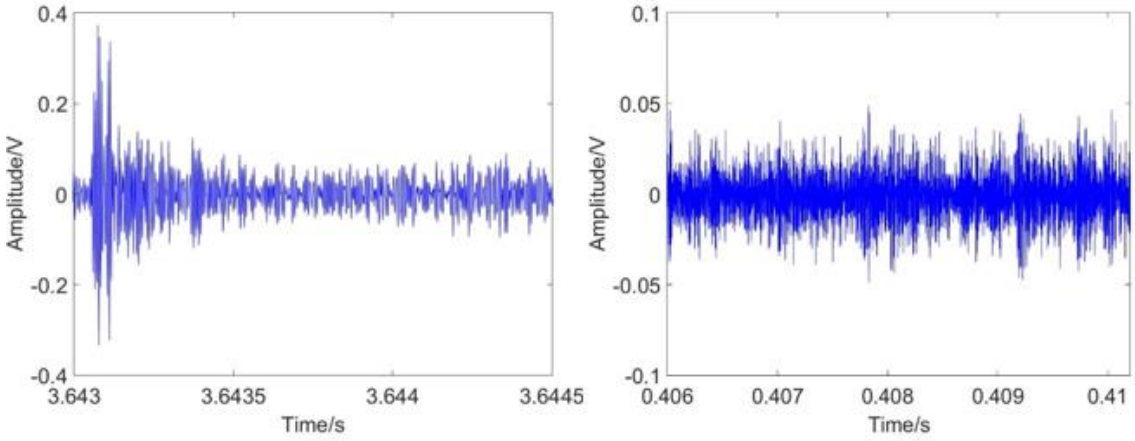

Figure 5-2: Typical burst-type (left) and continuous waveforms (right).

The type of AE waveforms captured during the test is mostly dependent on the source mechanism. In general, burst waveforms are related to damage degradation, such as crack growth, whereas continuous signals are more likely generated from unwanted noises, such as mechanical noise from the environment. In the case of crack growth in metallic materials, the signal intensity is determined by the crack growth rate. When the crack growth rate is below a certain limit, the burst signals related to crack propagation may be hidden within the noise signal level. This highlights the necessity to employ some

advanced signal processing methods for analysis and removing the influence of noise [93, 94].

Amplitude, duration, rise-time, MARSE energy, and threshold-crossing count are five major features extracted from a single AE hit, as shown in Figure 5-3.

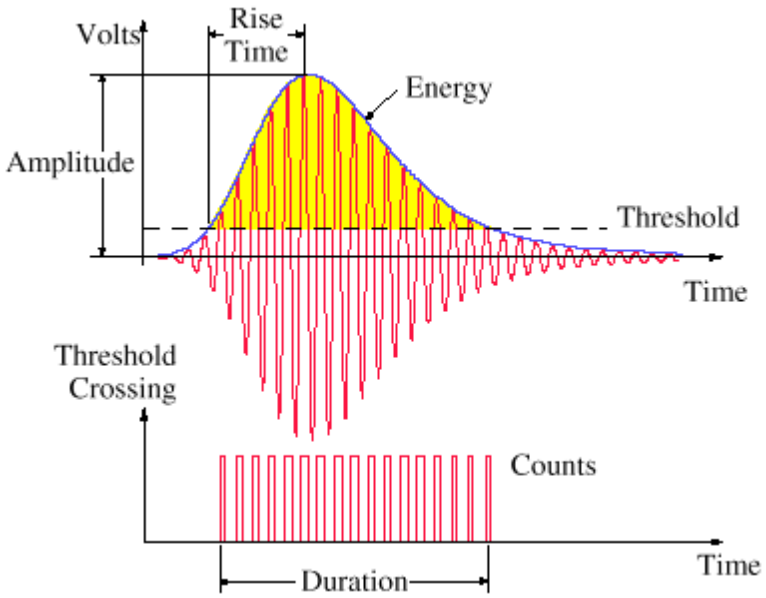

Figure 5-3: The major parameters measured in a typical burst AE waveform [37].

Amplitude refers to the maximum voltage in the captured AE waveform. Threshold-crossing counts represent the number of times the signal rises and exceeds the threshold value. Signal duration is defined as the time period during which the voltage is above the threshold value preset. Amplitude and duration are closely correlated. The time interval between the rising edge of the first count and the signal peak is defined as rise-time. The rise-time can characterise the frequency of AE sources. MARSE (Measured area under the Rectified Signal Envelope) energy represents the area under the envelope of the linear time voltage signal. Additionally, some other parameters can serve as useful complements to the above ones. Absolute energy is the ratio of the integral of the squared voltage over

the duration of one single AE hit to the reference resistance (1KSignal strength refers to the measured area of the rectified signal and it is related to the MARSE energy). ASL (average signal level) refers to the ratio of the integration of the absolute value of the amplitude of a rectified signal to its duration. Average frequency (counts/duration), initiation frequency and reverberation frequency are used to characterise the frequency of different parts of the single AE hit. As its name suggests, the average frequency can reflect the average frequency over the entire duration of an AE hit. Initiation frequency is the average frequency during the period between the first threshold crossing and the signal peak. Hence it can also be interpreted as the rise-time frequency. Reverberation frequency is essentially represented as the average frequency during the period between the signal peak and last threshold crossing and thus can be regarded as the ring down frequency. The formulae to calculate the above frequencies are shown in Equation 5-1 through Equation 5-3 [95]. Extra features can also be obtained by operation on two or more of the above features, including division, multiplication. Trend of cumulative sum of certain features like energy, count, etc. can give an indication of the condition

$$\text{Average frequency} = \frac{\text{Counts}}{\text{Duration}} \tag{5-1}$$

$$\text{Initiation frequency} = \frac{Counts\ to\ peak}{Risetime} \tag{5-2}$$

$$\text{Reveberation frequency} = \frac{(Counts - Counts\ to\ peak)}{(Duration - Risetime)} \tag{5-3}$$

It is very important to filter out any unwanted noises as much as possible during the data acquisition process. For a hit-based AE system, which will be described later, it is necessary to set an appropriate threshold prior to the tests. Any hits with amplitude lying lower than the threshold will be discarded. To determine a hit, three key parameters are employed which are set by the user, including the hit definition time (HDT), hit lockout

time (HLT) and peak definition time (PDT). HDT represents the maximum time between the first and last threshold crossing and it can prevent the merging of two different hits into one single hit. HLT specifies the time period during which the system is locked out after a hit has been captured and before a new hit can be detected. If the HLT value is set to be too low, then the reflections from the initially captured AE hit can also be logged. If the HLT value is set to be too high, then the system may miss some important signals. The PDT enables the correct determination of the signal peak and should be set as low as possible, however, if it is set too low, true peaks may be not identified [89]. Another important AE acquisition parameter is the sampling rate. If the sampling rate is set too low as shown in Figure 5-4, the true frequency contained in the original data cannot be revealed, which is known as aliasing as described in the Shannon theorem. The continuous signals can be properly sampled only when the sampling rate is higher than half of the maximum frequency contained in the original signal.

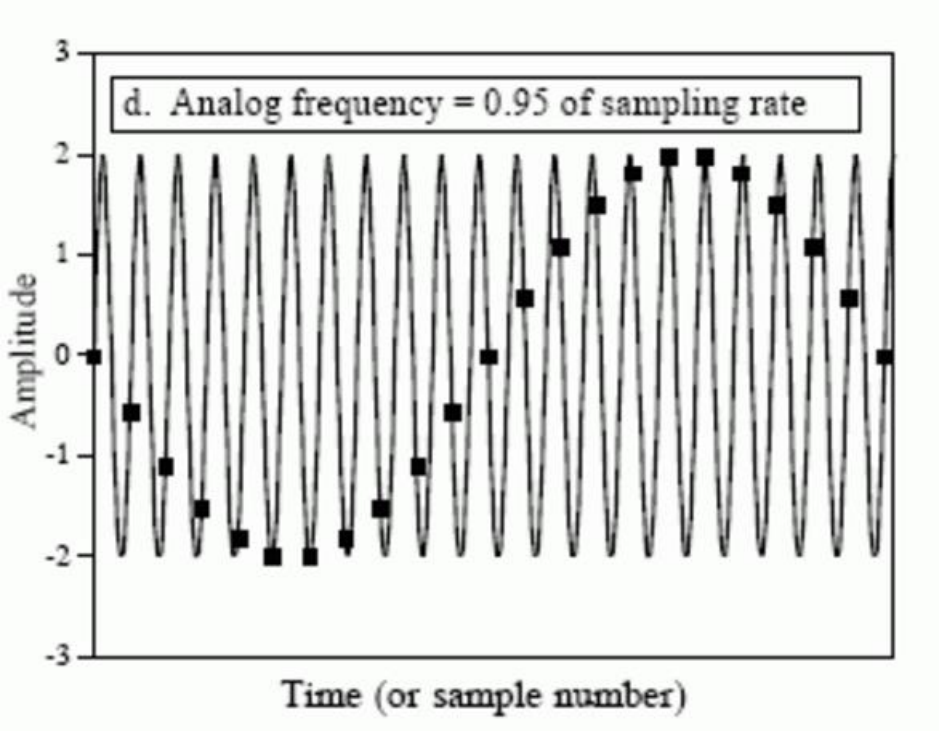

Figure 5-4:llustration of improper sampling [96].

There are two major methods to record and analyse AE signals. These are based on parameter-based or signal-based AE approaches. For the parameter-based AE method, a set of parameters rather than the original waveform is stored by the system. Post processing and analysis are based on the recorded parameters. The major merit of parameter-based technique is that it can save space and have higher data storing speed. However, sometimes it can be misleading to use only some parameters for characterising the actual signals. It is not easy to discriminate useful signals from noise and the parameters are highly dependent on various factors such as geometry of the structure, attenuation, etc. Statistical analysis focusing on the reduction of the influence of possible noise sources have therefore to be utilised for post-processing. In comparison with parameter-based approaches, the signal-based approaches enable more comprehensive and reliable analysis but generate a vast larger amount of data which may or may not be manageable. The signal-to- noise ratio can be visually evaluated from the captured

waveform. Moreover, the ratio can be significantly enhanced if some specific filtering algorithms are applied, which can be of great help to assess the severity of damage in the monitored structures accurately using AE. The limitation of the signal-based approaches is that they require much more computational and storage capacity for the AE system due to the larger amount of data generated and requiring processing and storage. The system can crash or run out of space if its specification cannot meet the requirements. A solution to this is to apply some triggering algorithms or take the measurement at a periodic interval depending on the type of application [97].

Certain types of filters need to be used to reduce the effect of background noise on AE signals, namely, low-pass, high-pass and band-pass filter. Traditionally, the way to apply these filters are through the use of analogue filters. Nowadays, digital filters are becoming increasingly popular due to the advantages they have. Digital filters are programmable and more precise. Moreover, they are free from the influence of temperature, manufacturing quality, etc. Finite impulse response and infinite impulse response filters are the most commonly used types of digital filters. As the names indicate, FIR filter has a finite response duration to the input signal， whereas that for IRF filter is infinite because the feedback added by the filter itself. Essentially, digital filtering is a type of calculation based on convolution technique and the number of source signal samples determines the order of the filter [98].

5.3 AE propagation mode and attenuation

AE signals can propagate in four major wave types, including longitudinal, shear, surface and Lamb or plate waves. If the source is internal to the structures and the sensors are close enough to it, then both longitudinal and shear waves can be detected. However,

when there is some distance between the sources and sensors, the surface and plate waves play a dominant role, as they are attenuated less than the other modes. It should be also noted that the wave detected by the sensors are often the results of the overlap of different modes and sources including the echoes and reverberation produced within the structures [94]. The energy released by AE sources can be transmitted to the sensors by different types of waves propagating through the solid depending on the shape of the medium and the source-sensor distance. When P or longitudinal waves strike the surface at the second critical angle, Rayleigh (Surface) waves can be generated. The attenuation loss of Rayleigh waves is less, which can be very helpful if the waves have to propagate long distances to reach the sensors. In plate-like structures, Lamb or plate waves dominate. There are two main differences between Lamb waves and bulk waves. Firstly, Lamb waves can travel in different types of modes, among which asymmetrical mode and symmetrical mode are the most common ones. Secondly, Lamb wave tends to be dispersive. The velocity is highly influenced by the frequencies and the thickness of the medium. The limitation of the Lamb waves and Rayleigh waves is that it is very difficult to derive the original form at the source based on the captured waves. Hence, the source depth cannot be determined accurately [94, 99]. For wave propagation in rails, there is a shift of frequency to lower components and this feature has been employed to detect break or partial break in the rail as reported in [100].

5.4 The Kaiser effect

The severity of damage can sometimes be inferred based on the AE response from the structure under different loading patterns. Normally, for a previously loaded structure, during re-loading process AE signals will be emitted only when the load level exceeds the previous maximum load level. This type of phenomenon was first investigated by

Joseph Kaiser and is known as the Kaiser effect to honour his contribution to this field of science and engineering [101, 102]. The Kaiser effect can be explained based on the AE-load curve displayed in Figure 5-5. Initially, as the load increases from A to B, the amount of cumulative emission accumulates. During CB segment, no signals are generated, in that the load level is lower than the level at point B. When the load at point B is exceeded, the AE activity resumes and increases as the load rises again. It is noteworthy to indicate that once the load is high enough (Point F), AE activities can be induced even the load is lower than the previous maximum load (Point D). This phenomenon is termed as Felicity effect. Felicity effect can be characterised by the Felicity ratio, which is defined as the ratio of the load at which AE activities reappear to the previous maximum load. The Felicity ratio can be regarded as a descriptive factor related to the extent to which the Kaiser effect has been violated. The higher the Felicity ratio deviates from unity, the more severe the damage in the monitored structure is [103].

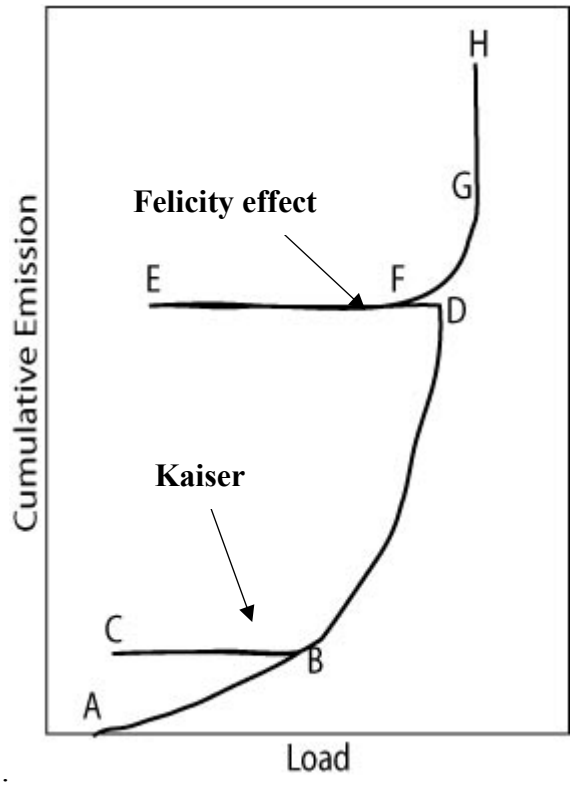

Figure 5-5: The Kaiser and Felicity effects [104]

5.5 Crack propagation monitoring using AE

Sinclair, A. et al performed AE analysis during fatigue crack growth in three steels with an ACEMAN system. The direct relationship between the event count (N) and the created crack area (A) was established as follows:

$$N = \gamma A \tag{5-4}$$

where γ is a constant determined by material properties and test conditions. The equation signifies that it is not the crack growth rate that determines the event count generated per unit crack length. However, the crack growth rate or ΔK can influence the amplitude spectra of the emissions. When ΔK increases to a greater value, a high energy emission mechanism can be activated.

Then they evaluated the possibility of three potential source mechanisms underlying AE generation during fatigue crack growth. The expansion of the plastic zone ahead of the crack tip was ruled out as the dominant source mechanism based on the measurements and calculations. A combination of micro-fracture processes ahead of the crack tip and crack closure unsticking are regarded as the main sources for AE generation, of which micro-fracture happens near the maximum load and unsticking normally happens in the earlier stage of the loading cycle [105].

Due to its sensitivity, the AE measurement can reveal the sub-stages of stable crack growth process during which FCG rate satisfies the Paris-Erdogan law (Equation 3-3) that can be hidden using conventional linear elastic fracture mechanics as reported in [106].It has been reported that the AE activity deteriorates during stage II_b of the crack growth test on austenitic stainless steel samples as a result of the reduced crack tip plastic zone size under plane stress condition. Cumulative count and crack growth rates were plotted against the stress intensity factor range on a log-log scale. A clear transition from II_a to II_b can be identified in the cumulative count plot whilst the crack growth rate plot showed a consistent trend. The relationship between the count rate and ΔK on a logarithmic scale should be expected to show similar trend as that for cumulative count and ΔK .However , due to the sensitivity of AE to microstructure features, for other types of steel, like pearlite steel, this trend may not be found [107].

The crack growth in pressure vessel steels has been monitored using both AE and direct current potential drop techniques. The displacement ahead the crack tip was also recorded. Three different types of compact tension (CT) samples in terms of the locations where fatigue pre-crack were induced, namely, base material, weld material and heat affected zone (HAZ) were used during tests for both 304L stainless and P265GH steels. The

microstructure of P265GH steel consists of ferrite and pearlite, whereas that of 304 stainless steel consists of austenite. AE sources during different stages of damage evolution have been identified and the ability of different AE signatures to separate each source mechanism was evaluated. More specifically, the maximum amplitude increases as the damage develops from plastic deformation stage to stable crack growth stage. It has also been shown that the value of maximum amplitude depends on not only the zone of propagation but also the type of steel. Counts are an identifier of plastic deformation, as the maximum count during plastic deformation is much smaller than that during other stages of damage evolution [108].

Roberts, T. and M. Talebzadeh used AE to monitor the fatigue crack growth in steel, welded steel CT and T-section girder test specimens. The AE signals generated from crack extension were separated from those from other sources by using the source location software in the system. The AE count rates during the top 100%, 10% and 5% of the load range were plotted as a function of ΔK on a log-log scale. It showed that the count rate for 10% and 5% of the whole load range had better correlations with the crack growth rate than 100% of the load range and increased regularly with the cycle number. The relationship between AE count rate and ΔK can be approximated as log-linear, which is similar to the Paris-Erdogan equation. Hence theoretically it is possible to predict the remaining life of a structure solely based on AE measurement [109].

Yu, J., et al., developed a model to correlate the absolute energy rate to the crack growth rate during the fatigue test on CT steel specimen. They tried to remove the false emissions completely through a combination of different methods. The waveforms generated from friction and pencil lead break (PLB) were used as reference to filter out false emissions. Then they employed a modified Swansong filter to further eliminate the friction signals

[110]. The principle behind Swansong II filter is that the duration of AE hits induced by fatigue crack growth should be directly proportional to their amplitudes. For a hit caused by friction or rubbing, the duration can be much higher than it should be if it is genuine emission.

Aggelis et al. used different parameters in AE waveforms to characterise the change in crack growth mode in aluminium specimens. When the crack growth changed from tensile mode to shear mode, the duration and rise-time of AE events exhibited an increase. Also the same happened to the the average frequency, but in a less obvious way. The change is attributed to the shift from longitudinal wave to shear wave in term of the dominant wave propagation type in the specimens, which is caused by the change in the crack growth mode [111].

Bassim et al. investigated the capability of AE to detect the onset of fatigue crack growth in four rail steels. Aside from AE acquisition, they also measured ΔK during four-point bending fatigue tests. The results demonstrated that AE could detect crack growth as small as 0.009 mm reliably and the fatigue stress intensity factor threshold was obtained based on the AE measurement. Furthermore, they found that fatigue crack mostly initiated near or in the inclusions in the rail steel samples using both optical and scanning electron microscope [112].

The earliest investigation on the potential of AE to detect rail track defects can date back to the research carried out by Kristoffer Bruzelius and D. Mba. They employed a test-rig to simulate the contact between wheel and track. They compared the AE original signals generated from the contacts between the rail wheel and track wheel with defects seeded on the track wheel and no seeded defects. Due to the natural wear between the contact

surfaces, it was impossible to discriminate the signals from the defect and those from the wear process. However, the number of AE bursts increase with time during a certain length of time window, consistent with the observation that the wear for both the wheel surface and track surface intensified with time. The observation of AE background activity (mostly from wear) during the test have been shown to be highly dependent on the load exerted on the track. It is noteworthy to mention that the material used during the test was carbon steel which is not typical of the rail head in actual conditions. Moreover, the rail head needs to go through a hardening process before being put into use, so the wearing problem may not as severe as shown in their research [113].

Kostryzhev, et al. employed AE to detect the signals released during the three point fatigue bending tests on pre-cracked and non-precracked R260 rail steel samples. They found that in a noisy environment, hit waveform and power spectrum are better choices to determine the onset of fatigue crack growth. Moreover, the peak frequencies for different fracture modes in the power spectrum are different. For fully pearlitic steels, the peak frequencies related to ductile fracture were observed to be smaller than 50 kHz, whereas those for brittle fracture were above 200 kHz [114].

Korenska, M., et al. used AE sensors to record the signals induced by the train passage. They compared the results from the loaded rail and those with the other unloaded rail using count rate versus time curve and frequency spectral diagram. When the train passed over the monitored section of the rail, the AE count increased continuously, in comparison to the isolated increase for that recorded by the sensors mounted on the unloaded rail. They used a high pass filter to remove a part of noise from the results. Moreover, they found the amplitudes in the frequency spectrum for the unloaded rail are smaller than those from the run-over (loaded) rail. From their experiments, it can be seen that not only

does the amplitude difference exist but the amplitude peaks are also in different location in the frequency spectrum. It might be helpful if they also did some analysis on the original signal to see if there are any spikes in the time-domain signal, thus determining whether there is damage evolution ongoing [115].

Murav'ev et al. investigated the possibility of using AE to monitor the rails on a bridge over the Ob River in Novosibirsk. They found that AE could detect the flaws which the ultrasound detector could not find when the defect size is small. They used linear source location to get the position of the flaw along the rails. However, the method became inefficient when the train ran over the inspected rail, as the signal was buried in the external noise. Hence it was only possible to capture the signals generated from the fault immediately before or after the train drove on the rail. It is highly essential that an alternative analysing method be employed to detect the flaw even when the train runs over the rail [116].

Zhang, X., et al., employed wavelet transform and Shannon entropy to detect defects. They used a test rig to simulate actual wheel-rail contact under lab condition and pencil lead breaks were carried out to simulate the AE source related to rail defects. They determined the frequency range that is typical of defect signals through frequency spectrum analysis. Based on the characteristic frequency range, the decomposition level of discrete wavelet transform was chose. The optimal wavelet was selected based on the Energy-to-Shannon entropy ratio. Finally, they used different time window to get the time-Shannon entropy result and confirmed this method can detect defects reliably. They found that the length of the time window has the decisive influence on discriminating the signals related to the defects from noises with this method. If the time window is set too

small, it will be extremely difficult to suppress the noise signals, however, if the window is set too big, the time resolution of the signals will be greatly lowered [117].

5.6 Analysis of AE signals

Convolution is one of the most important theoretical basis for digital signal processing and is the operation between two functions (*x* and *g*) as shown below:

$$(x * g)(t) \stackrel{\text{def}}{=} \int_{+\infty}^{-\infty} x(\tau) g(t-\tau) d\tau \tag{5-5}$$

Although *t* is used in the equation, it need not represent the time domain. But in that context, the convolution formula can be described as a weighted average of the function *x (τ)* at the moment *t* where the weighting is given by *g (–τ)* simply shifted by amount *t*. In linear system, convolution can be employed to show the relationship between the impulse signal, the input signal and the output signal. It shows both how each sample in the input signal contributes to the formation of the corresponding output signal and how each sample in the output signal gets the contribution from the input signal.

5.6.1 Root mean square

Root mean square (RMS) is closely related to the energy of the signal. Given a set of n samples $\{x_1, x_2, \cdots, x_n\}$, the RMS X_{RMS} is :

$$X_{RMS} = \sqrt{\frac{1}{n}({x_1}^2 + {x_2}^2 + \cdots + {x_n}^2)} \tag{5-6}$$

A more efficient way to characterise RMS is to divide the signal into overlapping segments and calculate the RMS in each segment. Balance should be made between

amplifying the useful and false signals by choosing the optimum window size. If the window size is set to be too big, then the ability of RMS to show sudden change in the waveform will be weakened, whereas if it is set to be too small, then some random noise may be amplified by mistake. The optimum window size is normally determined by trial and error.The RMS value is influenced by frequency and shape of the waveform [118]. Al-Balushi, K.R. and B. Samanta characterised the severity of damage for gear teeth using the energy index (EI), which is defined as the square of the ratio of the RMS of a segment to the overall RMS. It could enable successful early detection of embryonic gear failure. One desiring benefit of this feature is that its insensitivity to the variation of operation conditions of gearbox like machine load, speed, etc.[119]. To obtain more information from the signal, they employed overlapping mode for RMS calculation. An important consideration when using overlapping mode is to decide the ratio of step to sample. They tried to use different ratios of step to sample and compare the corresponding influences on the delay of detection when catastrophic tool failure occurred. It showed that within a certain range, the delay was reduced with decreasing step, however, when the step was set too small, the processing time would be longer and as a result, the delay would increase again [120].

5.6.2 Fourier transform

Fourier Transform is a powerful algorithm when it comes to frequency domain analysis and it decomposes any function into the sum of sinusoids. For a function *x(t)*, its Fourier Transform is defined as follows [120]:

$$S(\omega) = \int_{-\infty}^{+\infty} x(t)\exp(-i\omega t)dt \tag{5-7}$$

Actually, only a finite number of samples are employed to compute a discrete set of frequency range, commonly known as Discrete Fourier transform (DFT).The output frequencies are integer multiples of the fundamental frequency that is determined by the sampling interval. Actually, DFT is the only type of Fourier Transform that a digital computer is capable of performing. FFT is a fast algorithm to implement the DFT via a computer. When performing FFT, the number of samples used in time domain ideally should be a power of two [96]. One inherent limitation of FFT is that the variation of frequency distribution with time cannot be obtained, as the time t in the exponential basis exp(-iwt) cover the whole duration of the analysed signal [121]. If time frequency information is also preferred, Short Time Fourier Transform or Wavelet Transform should be used instead [122].However, in this case, uncertainty principles apply as shown below:

$$\Delta t \Delta w = 1/2 \tag{5-8}$$

Another problem that can be commonly encountered when using the Fast Fourier transform is spectral leakage. It is caused by the signal which is not time limited and hence frequency spectrum can be smeared out. Harmonics caused by periodic loading conditions can also be found in DFT, but their amplitudes are normally very small and sometimes can even be neglected during analysis.

Short time Fourier transform is proposed initially to overcome the drawback of no time-dependence information for FT. A window function is employed to multiply the original signal and FT is then calculated in each chunk of samples determined by the window function. The simplest window is the rectangular window and it replaces all but N values in a data sequence with 0. The mathematical formulae for STFT are as follows:

$$X(\tau, \omega) \triangleq \int_{-\infty}^{+\infty} x(t) w(t-\tau) e^{-j\omega t} dt \tag{5-9}$$

Where *w(t)* is the window function, commonly a Hann window or Gaussian window centered around zero, and *x(t)* is the signal to be transformed.

5.6.3 Crest factor

Crest factor is defined as the ratio of the peak amplitude to the RMS of the signal as shown in Equation 5-10.

$$\text{Crest factor} = \frac{Peak\ amplitude}{RMS} \tag{5-10}$$

It can serve to identify abnormal spikes related to damage evolution in the signals and normally high crest factor values indicate damage developing in the structure. As shown in Figure 5-6，although the two current waveform has the same RMS value，their crest factor values are obviously quite different, due to the differences in peak currents and this is exactly what crest factor is capable to detect. However, one inherent limitation of crest factor is its sensitivity to loading noise, as the increase in load will inevitably cause the increase of RMS. If the increase in RMS is higher than that for the damage-related peak,

then a decrease in the Crest Factor value will be anticipated as reported in the previous study [123].

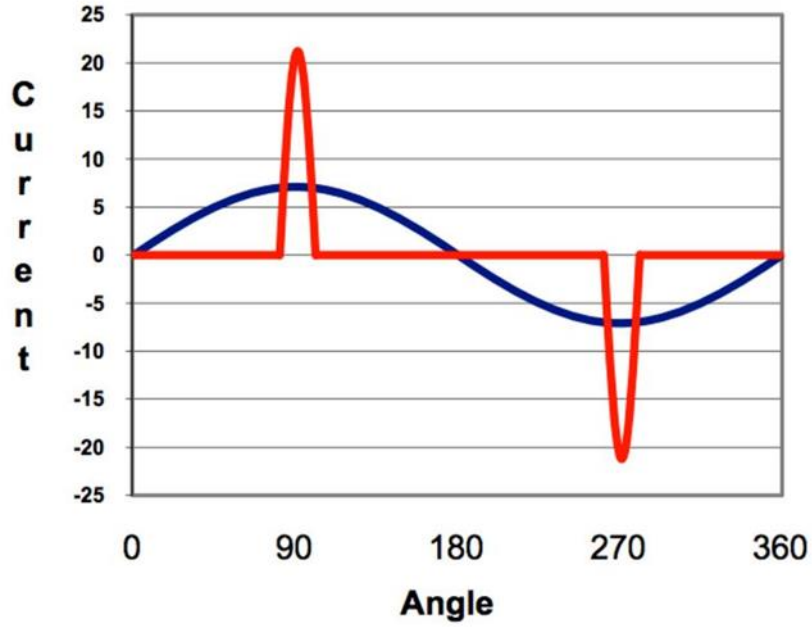

Figure 5-6: Two current waveforms with the same RMS value yet different crest factors [124]

5.6.4 Power spectral density

Power spectral density (PSD) is a powerful tool to characterize the energy of the signal at each frequency. The definition of PSD for *x(t)* is as shown in the following equation [125].

$$S_x(f) = \int_{-\infty}^{+\infty} G_x(\tau) e^{i2\pi f\tau} d\tau \qquad (5\text{-}11)$$

Where $G_x(\tau)$ is the autocorrelation function of *x(t)*.

Welch's method, named after Peter D. Welch, is now commonly employed to estimate the PSD. It has simpler computation and requires less storage space, thus making it more

easily implemented by the computers. The major steps consist of dividing the signal into different sections with overlap, taking modified periodogram for each section and calculating the average power spectral density [126].

5.6.5 Kurtosis and skewness

Kurtosis is defined as the ratio of the fourth central moment to the fourth power of standard deviation.

$$\beta_2 = \frac{m_4}{m_2^2} = \frac{\frac{1}{n}\sum_1^n (x_i - \bar{x}\,)^4}{(\frac{1}{n}\sum_1^n (x_{i-}\bar{x})^2)^2} \tag{5-12}$$

When using kurtosis, it is important to bear in mind that it reflects the combination of peakedness and tailedness. The kurtosis value for normal distribution is 3 and depending whether kurtosis is above 3 or not, the distribution can be described as either leptokurtic or platykurtic as shown in Figure 5-7Figure 5-7. The leptokurtic distribution has higher peaks and heavier tails, whereas platykurtic distribution has more flatten peaks and lighter tails, in comparison to normal distribution [127].

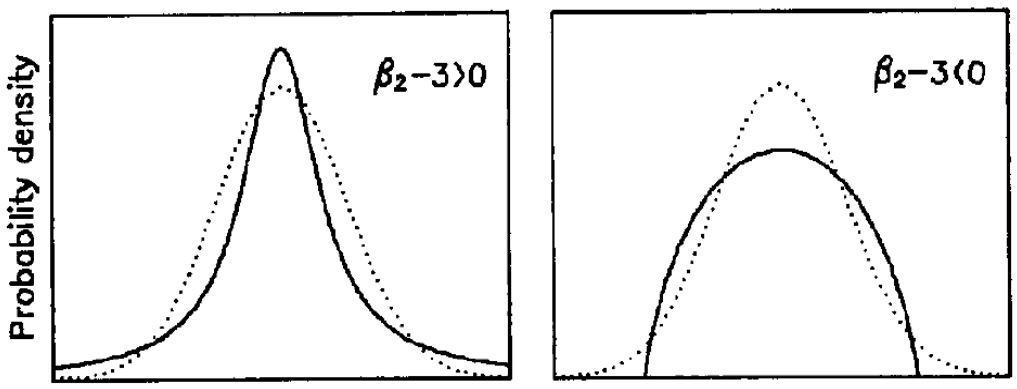

Figure 5-7: Illustration of leptokurtic and platykurtic distribution [127]

Skewness is a useful parameter to characterize the asymmetry of a set of random values relative to their mean value. The traditional formula to calculate skewness is as follows,

$$S = \frac{m_3}{m_2^{3/2}} = \frac{\frac{1}{n}\sum_1^n (x_i - \bar{x})^3}{\left[\frac{1}{n}\sum_1^n (x_i - \bar{x})^2\right]^{3/2}} \tag{5-13}$$

This is the so-called Fisher-Pearson coefficient of skewness and is used for the calculation in the following analysis here.

Skewness and kurtosis have been employed to characterise the distribution moments of RMS signal recorded during cutting and tool wearing experiments. It has been shown that both parameters could effectively detect the condition change of contact between chip and tool rake face. For catastrophic tool failure (CTF), it has been reported in previous research that RMS is not sensitive enough to detect it when it happens, whereas skewness and kurtosis can fit for the purpose. They assumed AE_{RMS} signal obeyed Beta distribution and calculated the mean and deviation of the AE_{RMS} signal. Skewness and kurtosis were then calculated based on the distribution parameters[128] [129].

In addition, it has been reported that higher order statistics including kurtosis could be used to identify the arrival time of AE signals. The even statistic moments can show a change even when the real signal is of similar intensity to background noise [129]. It should be noted that the number of samples used to reveal the distribution characteristics based on the above parameters should be guaranteed.

5.6.6 Spectral kurtosis

Spectral Kurtosis (SK) is a useful tool to characterise the transients and their location in the frequency domain. It was first introduced by Dwyer as the normalised fourth moment of real part of short time fourier transformation [130]. Later, C. Otonnello and S. Pagnan modified the original definition and they defined SK as the fourth order moment of the magnitude of STFT. Moreover, they found SK can be used to restore transient signals corrupted by external stationary noises [131, 132].

Antonio provided a formalization of SK for conditionally non-stationary (CNS) process and employed short time Fourier transform to develop an SK estimator. Equation 5-14 was proposed for calculating the SK:

$$K_Y(f) = \frac{S_{4Y}(f)}{S_{2Y}^2} - 2 \tag{5-14}$$

$$\text{And } S_{nY}(f) \triangleq < |Y_w(t,f)|^n > \tag{5-15}$$

$$Yw(t,f) \triangleq \sum_{-\infty}^{\infty} X(n) * W(n-t)e^{-j2\pi nf} \tag{5-16}$$

Where *Yw(t,f)* is estimated using STFT and *X(n)* is the selected part of the signal *X(t)* using and W(n) is the window function which is zero-valued outside the chosen interval. The principal of the algorithm is that through the calculation of the time average of spectral moments at a certain frequency, transients if any that occur at a certain frequency will contribute to a higher average of the moment. The most important parameter in designing a SK estimator is the window size. If the window size is set too big, the SK value will decrease very quickly after a certain limit is exceeded, whereas if it is set too small, some bias will be induced. He introduced the concept of Kurtogram which is a map

showing the STFT-based SK values as a function of centre frequency and window size. The centre frequency and window size corresponding to the maximum SK values are used as the optimal parameters to design a band-pass filter. The optimal band-pass filter determined by the method has two major characteristics. Firstly, the maximum SK can be determined by the centre frequency. Secondly, the window size is obtained by striking a balance between the signal-to-noise ratio and the impulse-like nature of the filtered signals [133].

Eftekharnejad et al. employed an SK-based technique to analyse the signals generated from the naturally degraded rolling bearings. They designed the band pass filter based on the centre frequency and window size (bandwidth) at which the spectral kurtosis reached the peak. They found that the Crest Factor value for the filtered signal showed an obvious increase in comparison with the original signal, suggesting that SK based filter can effectively demonstrate spikes among the noises [134, 135]. Sawalhi and Randall investigated the optimum window size for SK during their research. They found that if the window size is too small, the frequency resolution will be decreased greatly, whereas if it is too big, the SK values will be reduced compared with those obtained from a normal window size [136].

Chapter 6:

Experimental Methodology

CHAPTER 6 : EXPERIMENTAL METHODOLOGY

Experiments were carried out on R260 grade rail steel samples cut off from rails obtained with the help of Network Rail. Cast manganese steel samples were cut off using plasma cutting from a 10 mm thick plate procured from West York Steel. Some reference testing was carried out on a carbon steel sample. Various tests were carried out including metallographic evaluation, Charpy testing and fatigue testing in conjunction with the use of acoustic emission monitoring. This chapter describes the experimental configuration and parameters employed.

6.1 Metallography

Samples of Size 10*10*10 were cut off and mounted on Bakelite. The samples were ground to 1200 grit and then mirror polished to 1μm before using 2% nital to etch the surface of the samples for microscopy. Microscopy was performed using a Karl Zeiss optical microscope. Metallographic analysis of the R260 samples revealed a predominantly pearlitic microstructure as expected (Figure 6-1). Some pro-eutectoid ferrite (~1%) was observed in the pearlite colony grain boundaries. The microstructure of the cast manganese steel was found to consist of an austenitic microstructure with equiaxed grains as shown in Figure 6-1. The size of the austenite grains was found to be in the range of ~20μm. Some carbide inclusions could also be observed.

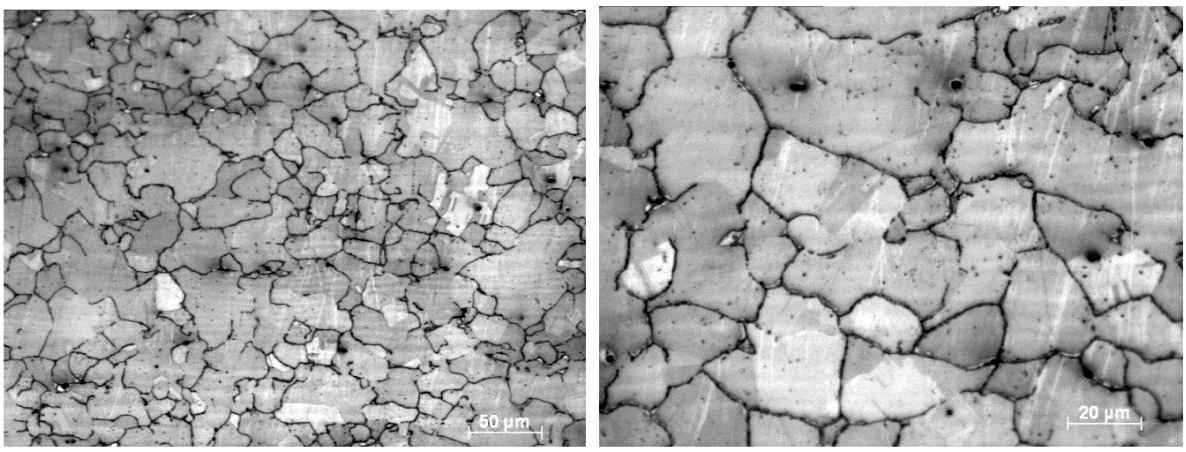

a)

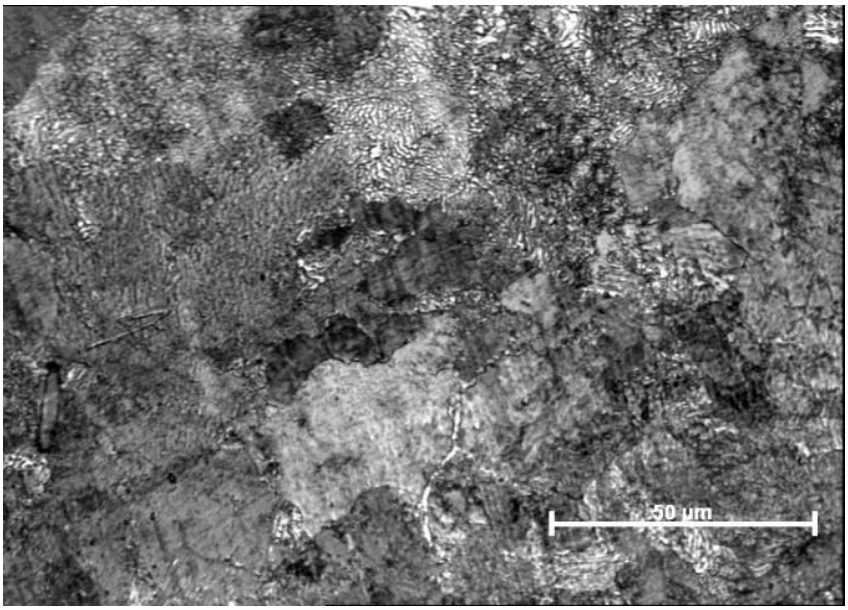

b)

Figure 6-1: the microstructure of a) Hadfield steel b) R260 steel

Five Charpy V-notch Hadfield steel specimens were prepared and tested. The specimens had standard dimensions of 10 x 10 x 55 mm (height x width x length) containing a

standard notch of depth 2.5 mm and 0.25 mm notch radius. A Charpy impact machine was used with a 298 J capability. Tests were conducted at -20°C (samples were chilled in a bath of ethanol and liquid nitrogen, the ratio is adjusted to meet the temperature requirements). The results of the tests are given in table. The Charpy test results for R260 steel specimens with the same size at the same temperature were reported in [137] and the average absorbed energy for R260 steel is 6 Joule. It can be inferred that Hadfield steel is more ductile than R260 steel even at room temperature, as austenite steel does not show fracture change behaviour with temperature.

Table 6-1: Summary of the Charpy impact tests carried out at -20℃

Temperature/℃	Impact Energy /Joule
-19	45
-19	46
-20	39
-20	42
-22	44

6.2 AE measurement

A customised AE system developed by the researchers from the University of Birmingham and Krestos Limited and the commercial AE system procured from Physical Acoustic Corporation (PAC) were employed to capture the AE signals generated during the tests.

For the commercial system, the data was captured using the PAC AEwin v2 software package. The sampling rate in all cases was set at 2MS/s. The detailed information regarding the type of sensors, filters will be introduced separately. The threshold during the data acquisition with commercial system was set as 40dB in most cases apart from the one for test on non-precracked R260 steel samples 5 which had been extracted from the used rail section. The PDT, HDT and HLT were set at 300μs, 800 μs and 800μs, respectively. For sample 5, due to the noisier testing configuration arising from the more rapid cyclic loading (10 Hz), the filtering range employed was set slightly higher at 200–1000 kHz.

The operation of the customised acoustic emission system is slightly different to that of the PAC system. The PAC acoustic emission system monitors acoustic emission activity and then deletes the complete waveform keeping only the data related to the definition of an acoustic emission hit as defined by the user, whereas the customized system can capture the original waveform during the test. The duration and frequency of the AE data acquisition were set before the measurement. The customised AE system uses Agilent 2531A 2 MSamples/s data acquisition cards with decoupling box whilst the logging and signal processing software is written in Matlab. The data acquisition card also support multi channels mode if lower sampling rate is used. It is connected to the computer via a Universal Serial Bus cable. The amplifiers and pre-amplifiers were purchased from PAC.

All the connections were done with BNC cables. The integrated analysis package and data logger developed by UoB using Matlab is as shown in figure. Due to the large amount of data generated the recording cannot be maintained indefinitely since the system will crash due to the high sampling rate (at least 1 MS/s) or the hard disk will run out of free space.

There are two types of sensors, namely single-ended sensor and differential sensor. Differential sensors have better immunity to electromagnetic interference and ground loop currents. For most applications, the single-ended sensors are preferred due to their low cost and acceptable low amplitude noise [138].

The sensitivity of AE sensor, S, which is dependent on the frequency of input sinusoidal motion, is characterized by the ratio of output voltage amplitude to input motion amplitude. The units for input motion amplitude can be displacement, velocity (m/s) or pressure (μBar).

AE sensor calibration curves are used to show how sensor sensitivity change with frequency. The X axis is the frequency of the input sinusoidal motion and Y axis is the sensitivity labelled in decibels relative to a reference value at the corresponding frequency as shown in equation below.

$$\mathrm{dB} = 20\log(S/S_f) \tag{6-1}$$

S is the sensitivity of AE sensor in V/μBar or V/ (m/s) and S_f is the corresponding reference value 1V/μBar or 1V/ (m/s). During this project, two types of AE sensors have been used, namely wideband differential sensor and R50a sensor. Wideband sensor has a good frequency response over the range of 100-900 kHz. It is ideally suitable for high

bandwidth of frequency analysis for source mechanisms identification and noise elimination. It can provide good reproduction of original source wave motion[139]. Low cost general purpose sensor can then be selected based on the frequency information obtained from wideband sensors. R50a is a narrow band resonant sensor with high sensitivity and an operating frequency range of 150-700 kHz [140].

The calibration curves for Wideband sensor and R50α sensor are shown in Figure 6-2

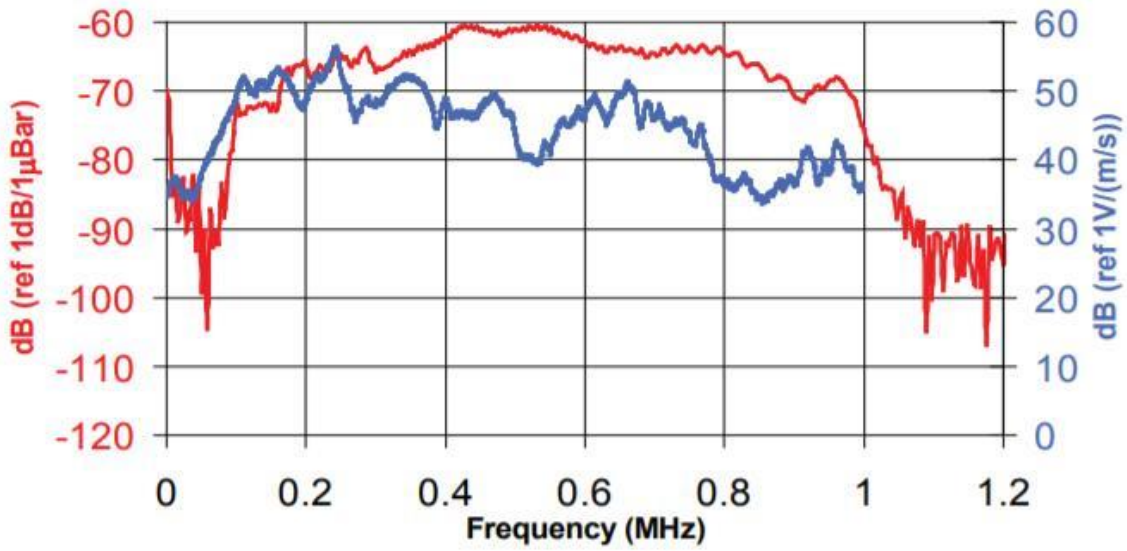

a)

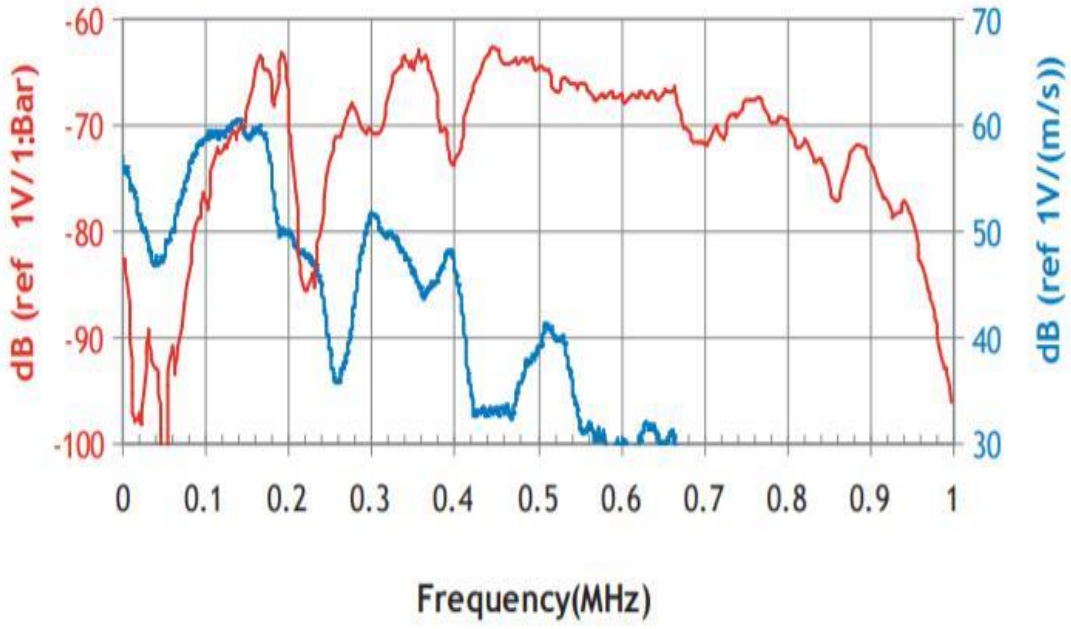

b)

Figure 6-2: AE sensor calibration curves for a) Wideband sensor b) R50α sensor [139, 140]

The good acoustic contact of AE sensors with the surface of the monitored structure is of utmost importance .The couplant should be used to remove roughness effects as well the presence of air pockets between the contact surfaces as the acoustic impedance of air is much lower than that of the sensor wear plate and steel. The couplants available include,

1) Liquid. The advantages of liquid couplants such as water are that they are straightforward to apply and can drive away the air between the sensor and material surface easily. However, due to low viscosity, they are not suitable for vertical mounting and long-period usage, as this can result in dripping and drying up of the couplant layers.

2) Gel. Gel couplants have higher viscosity and acoustic impedance than liquid counterparts, thus making them more suitable for rough surfaces. Vertical mounting is acceptable for gel couplants, as They are less likely to drip than liquid couplants.The common used gel couplants include:Vaseline, glycerine, ultrasonic gel, etc. Clamping fixtures are needed when using both gel and liquid couplants. The gel couplants around the edge of AE sensors can dry up after a few hours, making them not suitable for long-period application.
3) Grease. Grease has much higher viscosity than both liquid and gel couplants. Hence it is well suited for rough surfaces. If applied properly, it can provide better stability compared with liquid and gel couplants. However, it is difficult to clean the surface afterwards, especially for silicon based greases.
4) Adhesive. Adhesive couplants such as Araldite and superglue are preferred if AE sensors needs to be kept in place for a relatively long period of time and optimum coupling stability is needed. Two types of adhesive couplants are commonly used for AE, namely silicon rubber compound and rigid bond. In case of occurrence of surface vibration or movement, Rubber compound can offers excellent stability.For rigid bond, it can offer the best transmission of both longitudinal and shear displacement if mounted properly [141].

Apart from the above mentioned couplants, other types of couplants are also available to meet specific requirements such as when high temperature applications are involved. For the common couplants used for AE application, please refer to the table in [141]. The couplants used for this project are Vaseline and Araldite® .Before mounting the sensor, it is crucial that the material surface is as smooth and flat as possible to maximize the effect of couplant,as air trapped in the layers under the surface won't be driven away by the

couplants [142]. Sensor mounting fixtures like magnetic holders or adhesive tapes should be used for non-adhesive couplants to keep the sensors' position and applied force constant. The coupling layer between the sensor and material surface should be as thin as possible and one common practice to achieve that, which has been employed in this project, is to apply a small amount of couplant in the middle of sensor surface and push the sensor down against the material surface with a consistent force to let the couplant extend in a circle until no more couplants emerge from the edge of the sensor surface.

The preamplifier is used to increase the strength of the input signal and decrease the influence of electromagnetic noise generated along the cables during the signal transmission between the sensor and the instrument. Moreover, it can convert a high impedance signal into a low impedance signal which is suitable for long cable transmission. Preamplifiers can be either integrated with AE sensor or serve as a separated unit. The advantage of preamplifiers integrated with AE sensor is the compact design and the improved signal-to -noise ratio thanks to the minimal signal loss between the sensor and preamplifier. Sensors without integral preamplifier are lighter and smaller and preferred when the space for sensor deployment is limited. The PAC preamplifier used in this study provides a 20/40/60 dB switch selectable gain and it is powered via the output signal BNC cable. It can be connected to both single-ended and differential sensor. The PAC pre-amplifier also incorporates filters to decrease the interference of low frequency mechanical noise.

Before the test, it is very important to use a pencil lead break，also referred to as Hsu-Nielsen source, as an artificial acoustic source to check the acoustic coupling quality

between the sensor and the surface of the test-piece by pressing the pencil lead firmly against the surface of the structure until the lead breaks as shown in Figure 6-3 .

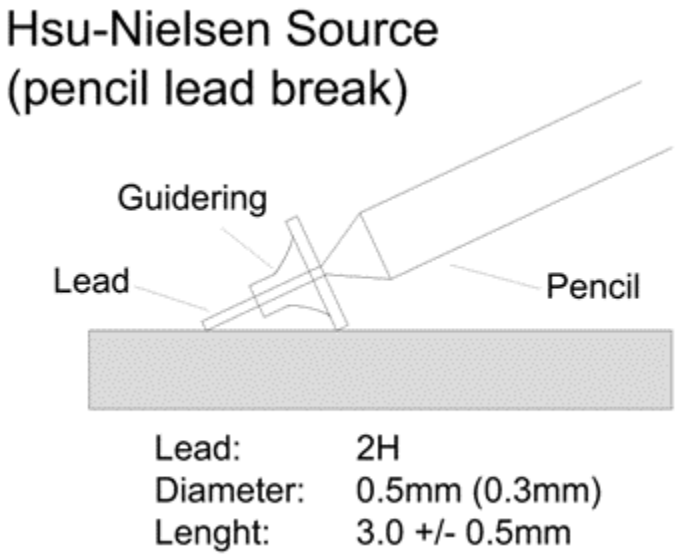

Figure 6-3: Hsu-Nielsen source [143]

6.3 Fatigue testing

Bending fatigue crack growth tests were carried out on three different specimens: R260 grade rail steel notched samples, cast manganese steel notched samples, and one carbon steel sample with no notch used as reference. The fatigue loading conditions under which tests were carried out included various loading frequencies ranging from 1Hz and up to ~100 Hz. The bending fatigue configuration employed in the tests is partially representative of the loading conditions that the rails and crossings are subjected to. The specimen used for fatigue testing can be seen in the schematic of Figure 6-4.

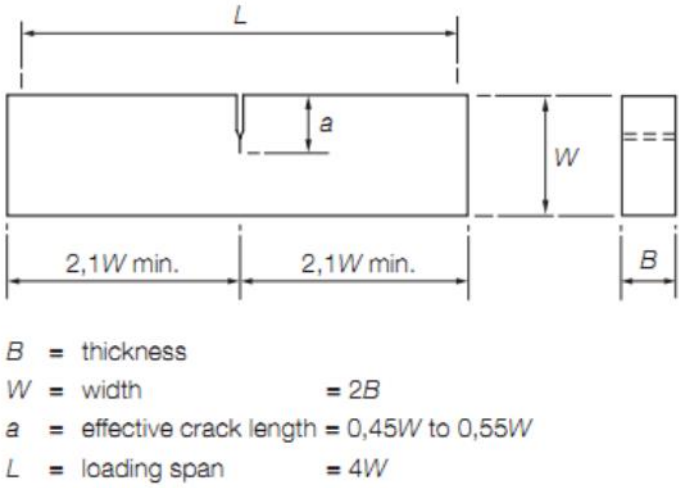

a)

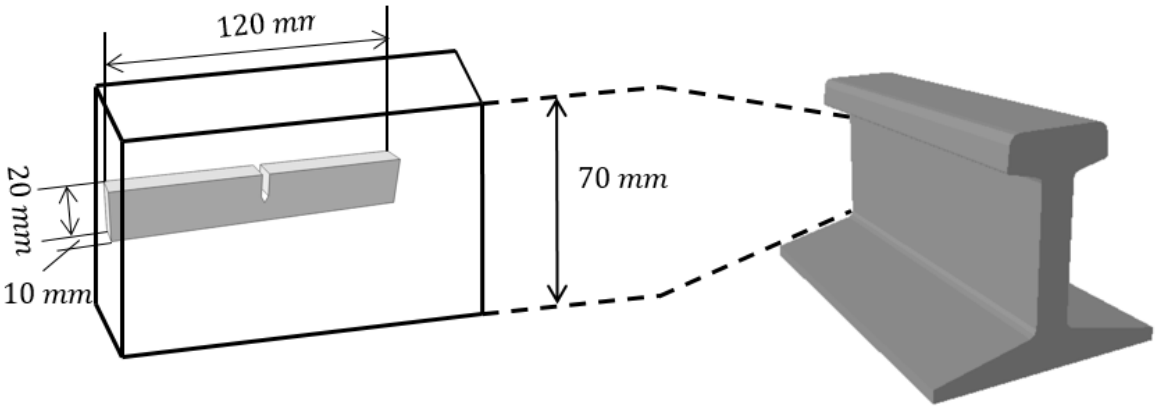

b)

Figure 6-4:a) schematic diagram to show the dimensions of the samples used for fatigue tests [144] b) example of the dimension of one R260 rail steel sample cut off the rail

Before the low frequency fatigue testing was performed, all samples except the reference carbon steel sample were pre-cracked using an Amsler 20KN Vibrophore electro-mechanical high frequency fatigue machine. The pre-cracking length was monitored by observation of the microscopy replicas of the notch tip field. If the stress at the notch tip is higher than the yield strength, a plastic zone will form ahead of the notch and upon unloading, the compressive residual stress will remain in the plastic zone. The residual stress relaxation may occur in the following crack growth test, which can be captured by AE [145-148]. A DARTEC 50kN servo-hydraulic universal test machine was used for the low frequency fatigue testing. The loading frequency was set at 1Hz and 10Hz for one rail steel sample in each case.

For the high frequency tests, Notched samples with and without pre-crack made were tested on An Amsler 20KN Vibrophore electro-mechanical high frequency fatigue machines. A carbon steel reference sample with no notch or pre-crack was also tested for comparison purpose. For samples with no pre-crack, it was expected that the AE activity during stage I, II, and III of crack growth could all be recorded. The loading ratio was set to R = 0.1 for all samples. Sinusoidal loading pattern was used during the tests.

The crack length was monitored using the Direct Current Potential Drop (DCPD) technique for all tested samples. DCPD is based on the principle that the resistance of the material will increase with decreasing size of cross section resulting from a fatigue crack growing. Base on Ohm's Law, the output voltage (V) across the cracked test piece will increase under constant input current. The crack length $\boldsymbol{\alpha}$ can be obtained by comparing the actual voltage reading with a reference voltage measured from another area of the test piece which is not affected by crack growth behaviour and using appropriate calibration

curves. The output voltage is normally in the range of 0.1 to 50 mv for common current (from 5 to 50A), sample configuration and materials.

Constant current is input through two clips into the specimen. Two voltage probes across the notch will then measure the voltage. The crack length increase can be reflected by the pen traces on the chart recorder. The crack growth rate was calculated based on the secant method as described in the British standard [144].Figure 6-5 shows the general laboratory setup employed in this study.

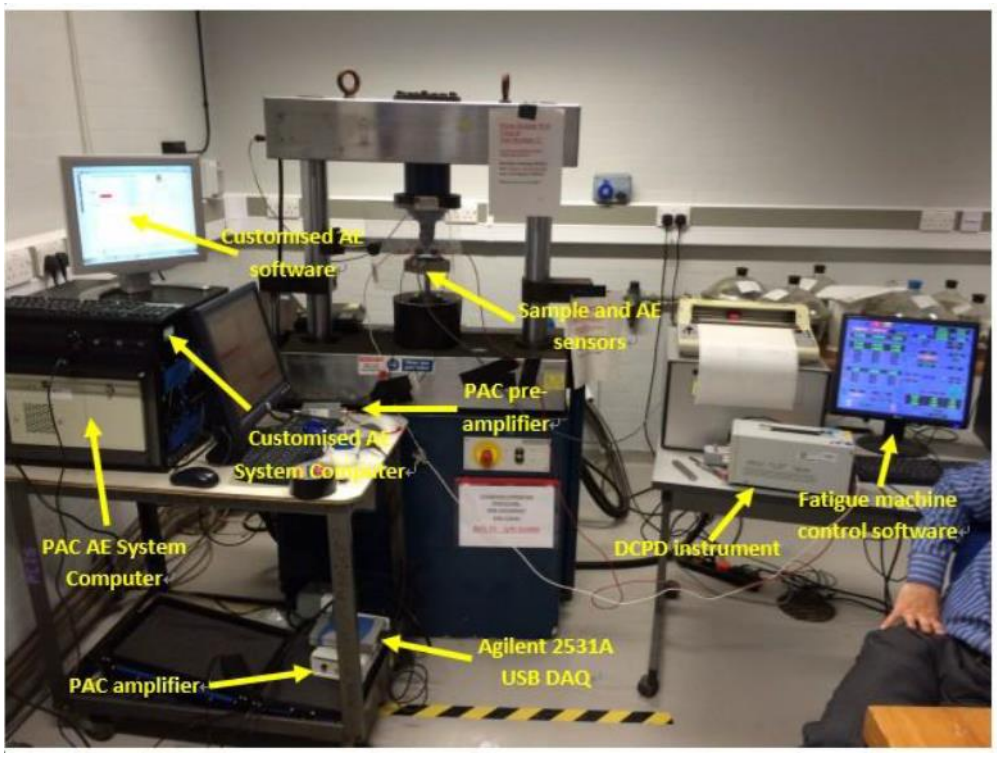

Figure 6-5: Experimental setup for the fatigue crack growth tests

6.4 Field trials

Field trials were carried out on two different crossings on the west coast mainline. The crossings are 2561A points (near Wembley Stadium - direction to Birmingham) and on Chiltern rail line (near Hatton Railway Station - direction to Birmingham), which are both

used by passenger and freight trains. The large impact load which can be induced when the rolling stock move from wing rail to crossing nose makes the crossing nose the most likely area for crack to initiate and propagate, hence AE sensors were attached to both sides of crossing nose during the field trials.

The Wembley crossing was proved to healthy using visual inspection, whereas for Hatton crossings, surface damages (cracking and lipping) are obvious. The maximum allowable train speed for both crossings is 100 MPH. The sensors was attached to the crossings using araldite, as it can provide long term adhesion as well as good electrical insulation required. Araldite is two-component epoxy adhesive which is easy to handle and can enable the installation of sensors within a few minutes. Moreover, it can enable good transmissibility of stress waves caused by growing defect due to the external loading. The analysis of field data is based on correlation analysis. The customized AE system was temporarily installed on-site to monitor the crossings with no trigger system used. The system was triggered manually once the rolling stock approached the instrumented area. The Photographs in Figure 6-6 show the measurement setup at Wembley crossing.

a)

b

c)

d)

Figure 6-6: photographs show a) AE measurement equipment b) indicative rolling stock c)instrumented crossing location d) sensor location for field trial near Wembley station.

Chapter 7:

Results and Discussion

CHAPTER 7 : RESULTS AND DISCUSSION

7.1 Low frequency fatigue tests

7.1.1 Introduction

The R260 rail steel samples numbered 1 to 4 with size 120mm*20mm*10mm and notch depth 8mm were pre-cracked to an initial length of 9.5mm,10.0mm,10.8mm and 9.5mm, respectively. The maximum load for samples 1 through 4 was set at 3.5kN. Another R260 rail steel sample, numbered as 5, was extracted from the web of a used rail section removed from the UK rail network. This sample had the same geometrical dimensions as the other four rail samples but the notch depth was kept to only 2mm with a 30° angle. It was also pre-cracked using the Vibophore fatigue machine to an initial crack length of 3 mm. The maximum load in this case was set at 9kN. All the above five samples were monitored using the PAC AE system during the bending fatigue tests. A second set of R260 rail steel samples with notch depth 8mm and angle 60° was also tested to evaluate the complete waveform using an R50a sensor connected to the customised AE system. The maximum load was also set at 3.5kN. Figure 7-1 shows a R260 rail steel sample after the final failure occurs.

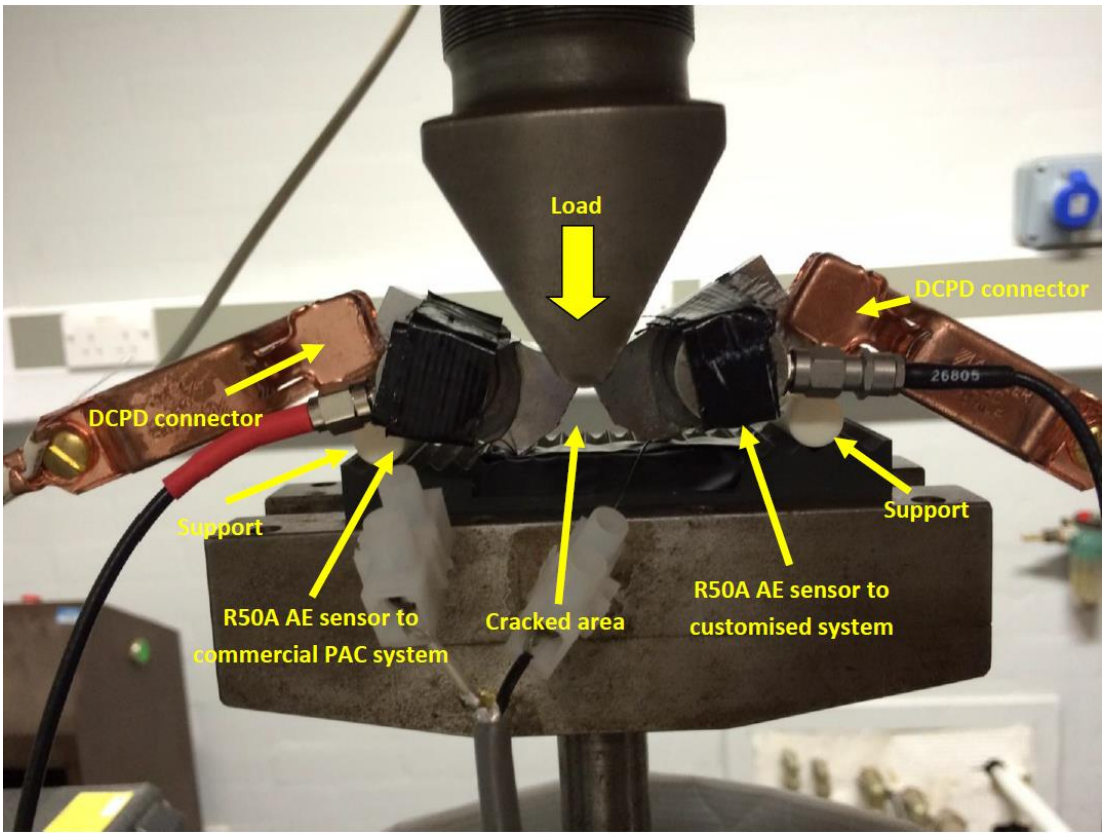

Figure 7-1 : Photograph showing a close-up of failed R260 rail steel sample

Hadfield steel samples numbered 1 to 4 with the same configuration as R260 rail steel sample 1 through 4 were pre-cracked to initial crack lengths 10.3mm,10.2mm, 10.9mm and 10.4mm.The maximum load was set at 3 kN.

Two PAC pico wideband AE piezoelectric transducers with a bandwidth range between 150 and 750 kHz were used to monitor the AE activity during fatigue testing of the R260 rail steel samples 1 through 4. The pico AE sensors were coupled to the surface of the sample using vaseline and held in place with duct tape. A band pass signal filter with a range of 100-1000 kHz was employed to reduce the effect of mechanical noise during the testing. For sample 5 and 6, R50a resonant AE sensors procured from PAC were used instead.

For the Hadfield steel samples, two PAC R50a sensors with an operating frequency range of 100-700 kHz were employed. One sensor was connected to the commercial PAC AE system and the other was connected to the customized system during testing. A 100 kHz high-pass filter was used to filter out loading-related noise in this case. The sampling rate for the customized system was set at 1 MSample/s.

The threshold during the data acquisition with commercial AE system was set as 40 dB in all cases apart from the one for test on R260 steel sample 5 which had been extracted from the used rail section. The PDT, HDT and HLT were set at 300 μs, 800 μs and 800 μs, respectively. For sample 5, due to the noisier testing configuration arising from the more rapid cyclic loading (10 Hz), the filtering range employed was set slightly higher at 200–1000 kHz. Also the amplitude threshold was set at 55 dB. The sampling rate in all cases was set at 2 MSample/s.

7.1.2 Analysis of AE signals captured from commercial system

Figure 7-11 shows the correlation of different AE parameters with crack length during low frequency bending fatigue tests on both the R260 rail steel and Hadfield steel samples. As it can be seen, both the average amplitude and duration increase with fatigue cycles, signifying the deteriorating structural integrity of the samples with increasing crack depth. It should be noted that the AE activity reduces after the initial relatively intense activity. This is attributed to the fact that the crack growth at the initial stages of the test is not stable and this is reflected in the increased AE activity recorded. The instability may be partly because of the influence of notch tip plasticity. However, as the test progresses the crack growth rate becomes more stable, resulting in reduced AE activity until the crack growth rate increases sufficiently again to give rise to higher energy AE signals. The initial instability due to the very small increments of crack growth

occurring cannot be detect by the DCPD instrument as exceeds its measuring sensitivity. It is also interesting that before the final failure of the specimens, all the four Hadfield samples show a substantial increase in AE activity, signifying the imminent failure.

The performance of each parameter in terms of their ability to describe the severity of damage is evaluated as follows.

Figure 7-2 shows the correlation of amplitude with crack length during low frequency three-point bending fatigue tests on both R260 rail steel and Hadfield steel samples. The threshold set was set at 40 dB for both types of samples. The amplitude for most of AE signals captured for ferritic, ferritopearlitic, martensitic and bainitic steel samples under the same loading condition is smaller than 70 dB as reported in [149]. For the R260 steel samples tested, the captured AE signals with amplitude above 70 dB occur even during stable crack propagation and this is attributed to brittle cleavage fracture causing high energy AE signals to be emitted [150]. The distributions of the highest amplitude AE signals captured during the tests carried out on R260 and Hadfield steel samples are different. For the Hadfield steel samples, most of the AE signals with high amplitude (>60dB) occur during the final stage of damage evolution. This is attributed to the gradual work hardening of the Hadfield samples resulting into a gradually evolving more brittle fracture as the material is work-hardened further. For the R260 steel samples the distribution of high amplitude AE events are more scattered throughout the tests. This is related to a constant pattern of brittle cleavage fracture during crack evolution as reported in [150].The highest amplitude during the tests for all Hadfield samples is smaller than that for R260 steel due to plasticity at the crack tip causing lower levels of AE energy to be emitted.

As mentioned before, the microstructure of Hadfield steel is austenitic. Hence, Hadfield steel has a FCC crystal structure. FCC crystal lattices have a large number of slip systems for dislocations to be able to move. Moreover, the Fe atoms are more closely packed in FCC structure, making the cleavage fracture less likely to happen during the crack evolution process in comparison to R260 steel. That partially explains why high amplitude or energy AE signals did not occur during the stable crack propagation process for the Hadfield steel samples but activity picked up during the latter stages due to the increasing hardness of the material due to work-hardening. At the later stage of the tests for Hadfield sample, the highest amplitude values show a close to exponential increase until final failure occurs. For the R260 steel samples, all of them exhibited a sudden jump in crack growth at a certain stage before final failure. This is attributed to larger areas in the samples fractured surface exhibiting cleavage and thus giving rise to higher AE energy to be emitted at these particular instances. This is shown in Figure 7-2(a) to Figure 7-2(d) indicating an increase in AE activity successfully being captured during sudden increases in crack growth rate as indicated by the arrows. The reason behind cleavage fracture of larger areas is likely related to inclusion present in the path of the growing crack resulting in a larger area to fracture before the crack slows down. Another possibility could be related to the presence of favourable residual stresses resulting in high stresses locally and hence a larger area to fracture.

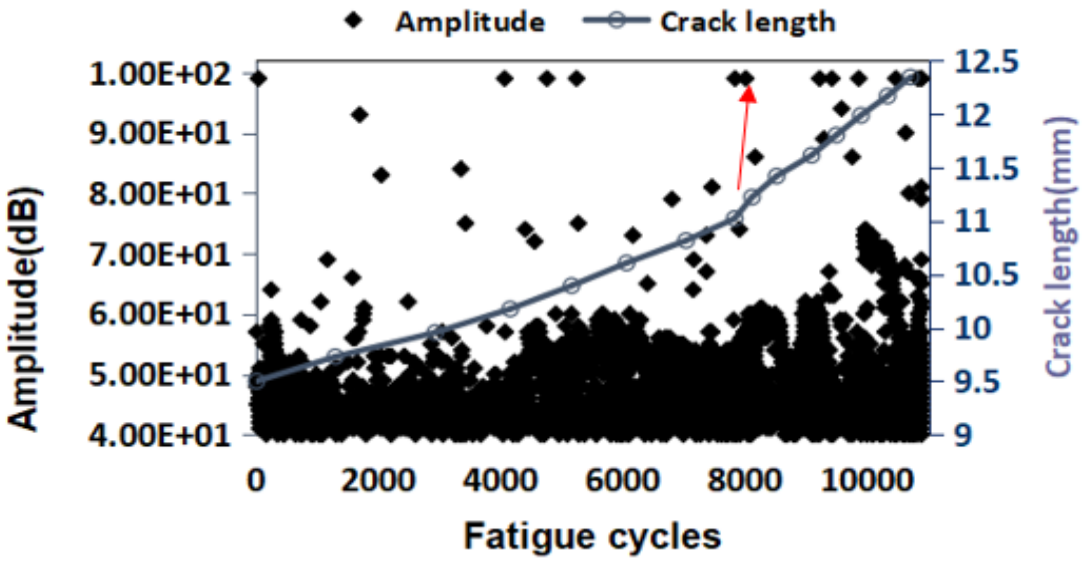
Amplitude
Crack length
1.00E+02
9.00E+01
8.00E+01
7.00E+01
6.00E+01
5.00E+01
4.00E+01
Amplitude(dB)
12.5
12
11.5
11
10.5
10
9.5
9
Crack length(mm)
0
2000
4000
6000
8000
10000
Fatigue cycles

a)

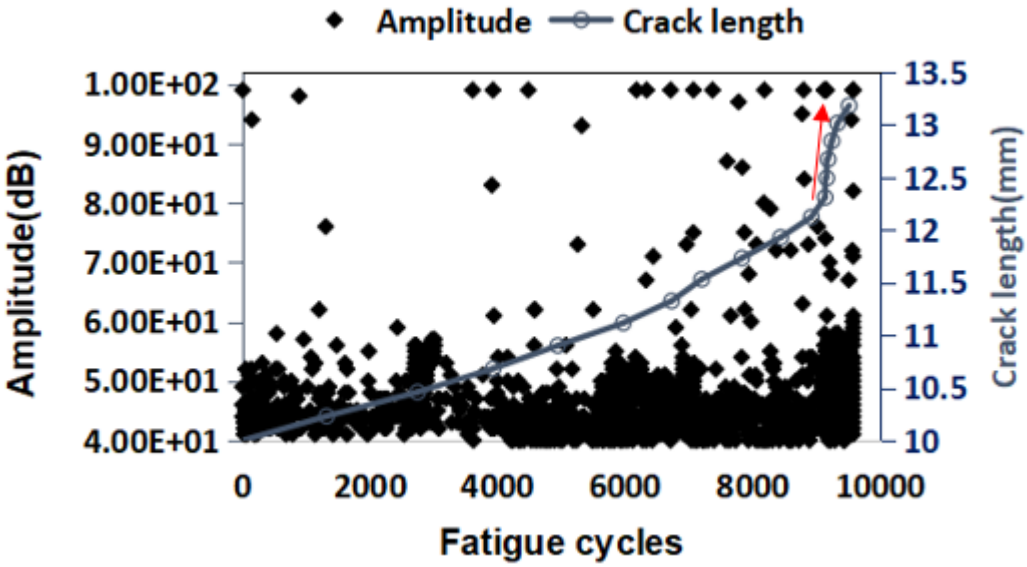
Amplitude
Crack length
1.00E+02
9.00E+01
8.00E+01
7.00E+01
6.00E+01
5.00E+01
4.00E+01
Amplitude(dB)
13.5
13
12.5
12
11.5
11
10.5
10
Crack length(mm)
0
2000
4000
6000
8000
10000
Fatigue cycles

b)

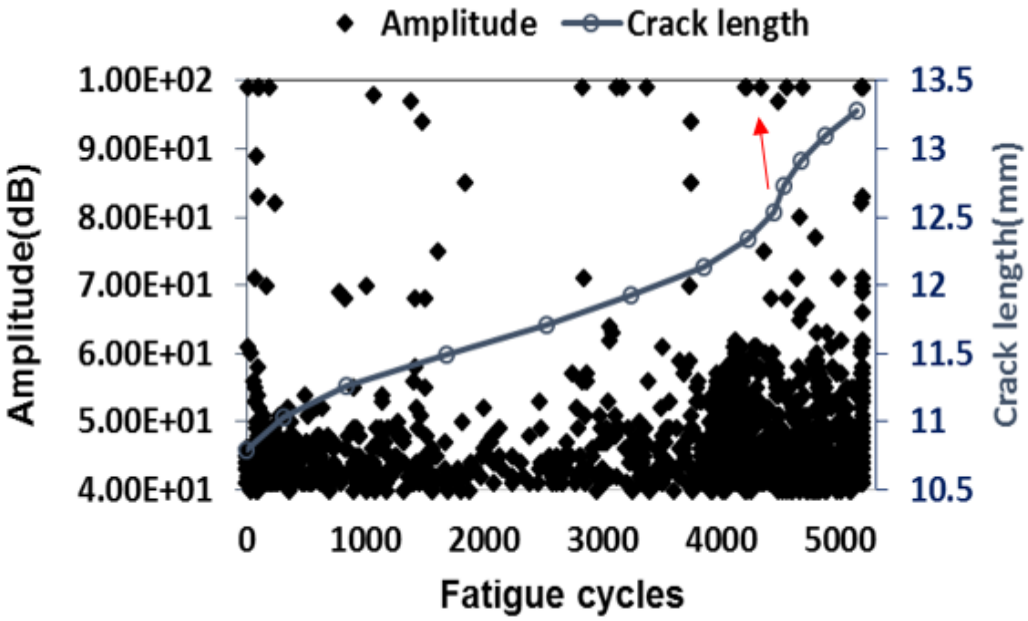
Amplitude
Crack length
1.00E+02
9.00E+01
8.00E+01
7.00E+01
6.00E+01
5.00E+01
4.00E+01
Amplitude(dB)
13.5
13
12.5
12
11.5
11
10.5
Crack length(mm)
0
1000
2000
3000
4000
5000
Fatigue cycles

c)

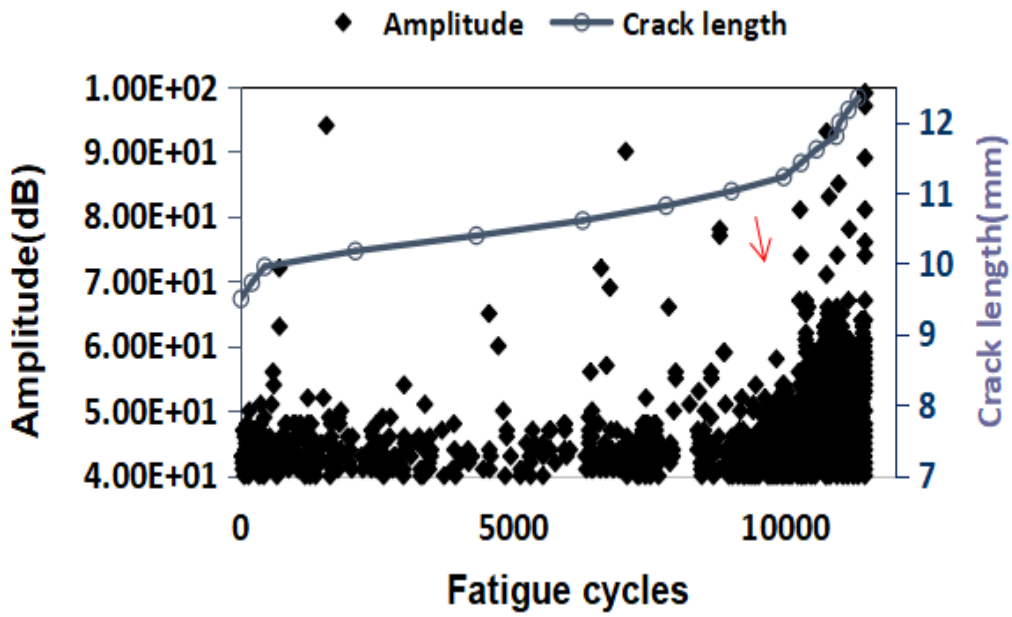
Amplitude
Crack length
1.00E+02
9.00E+01
8.00E+01
7.00E+01
6.00E+01
5.00E+01
4.00E+01
Amplitude(dB)
12
11
10
9
8
7
Crack length(mm)
0
5000
10000
Fatigue cycles

d)

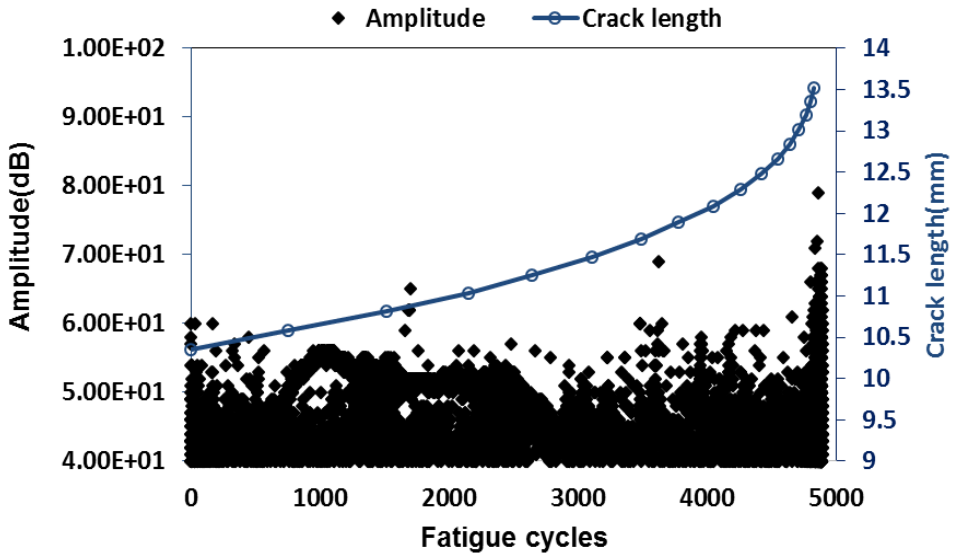
Amplitude
Crack length
1.00E+02
9.00E+01
8.00E+01
7.00E+01
6.00E+01
5.00E+01
4.00E+01
Amplitude(dB)
14
13.5
13
12.5
12
11.5
11
10.5
10
9.5
9
Crack length(mm)
0
1000
2000
3000
4000
5000
Fatigue cycles

e)

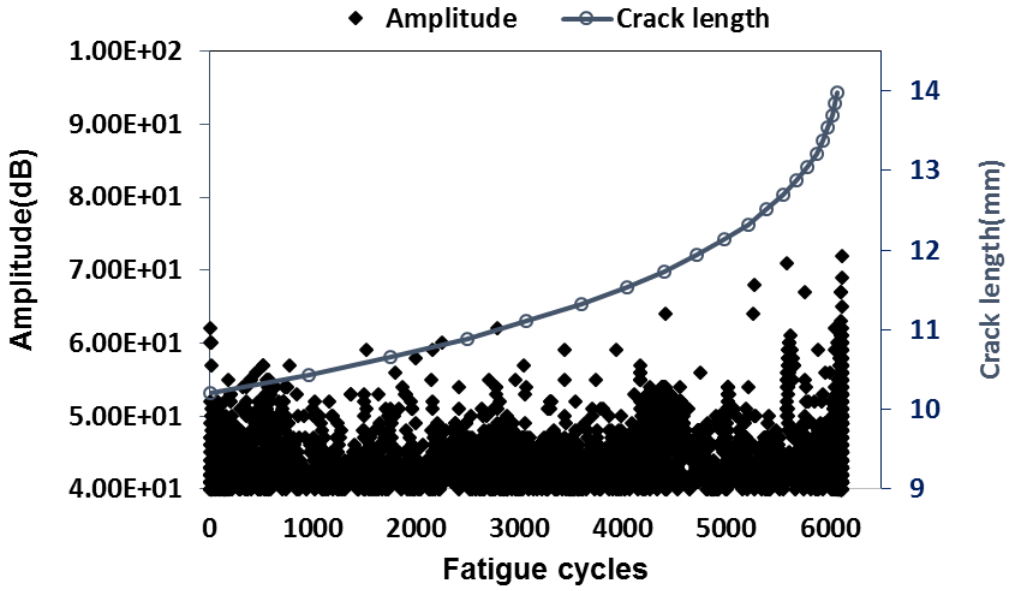
Amplitude
Crack length
1.00E+02
9.00E+01
8.00E+01
7.00E+01
6.00E+01
5.00E+01
4.00E+01
Amplitude(dB)
14
13
12
11
10
9
Crack length(mm)
0
1000
2000
3000
4000
5000
6000
Fatigue cycles

f)

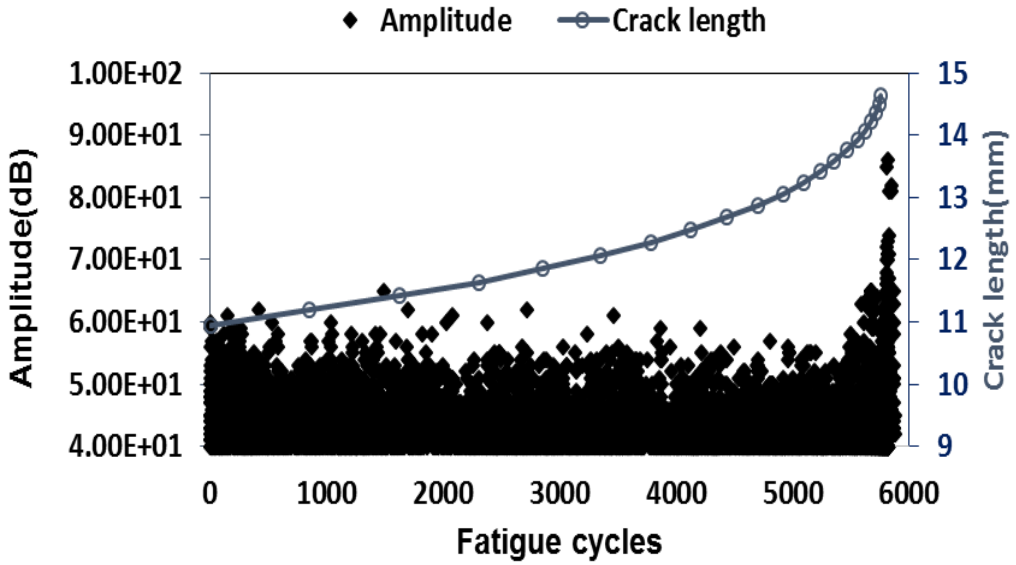

g)

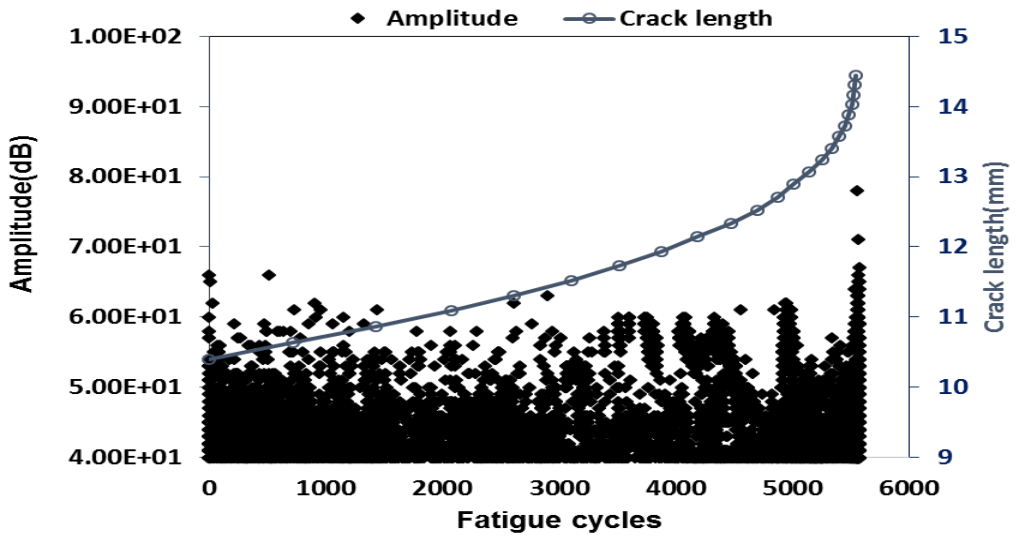

h)

Figure 7-2：AE signal amplitude in dB versus number of fatigue cycles with crack growth in mm for R260 rail steel a) sample 1, b) sample 2, c) sample 3, d) sample 4, and Hadfield steel e) sample 1, f) sample 2, g) sample 3, h) sample 4.

Figure 7-3 shows the correlation between count and crack length for all the samples. For

the R260 steel samples, the temporary increase in crack growth rate is consistent with the amplitude and the counts recorded in the AE signals captured. Moreover, the amplitude of all captured AE events with count value above 250 is higher than 70 dB. For the Hadfield samples, at the later stage of stable crack growth, indications of imminent failure can be clearly observed due to the higher AE activity recorded. Both hit number and hit counts clearly increase in comparison with the initial stages of damage evolution in the samples being tested. Some events with obviously higher count values than others and highlighted in red can also be observed. These AE events can be used as an indicator and hence alarm for the impending final failure. Some of these AE events cannot be discerned clearly just by evaluating amplitude-crack length plots. This is due to the fact that other events with similar high amplitude level can also occur at other stages of damage evolution.

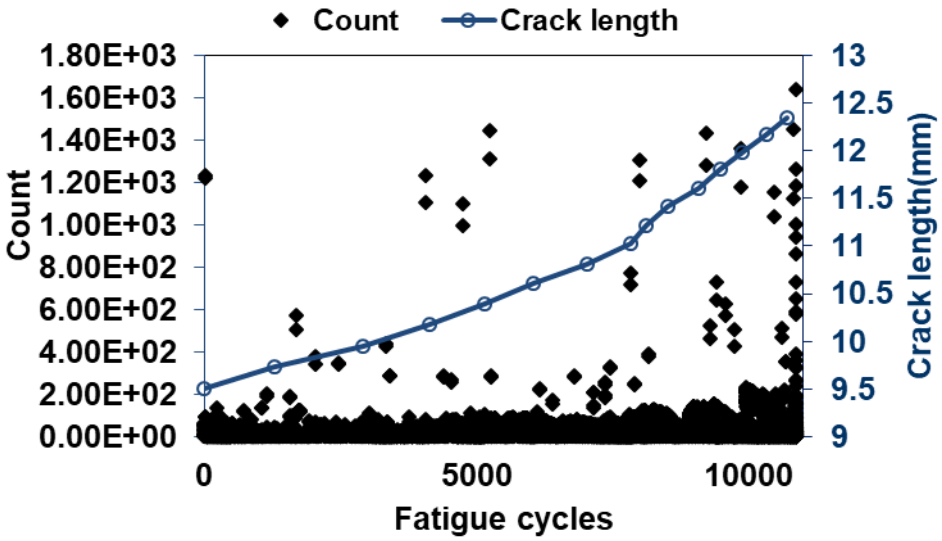
Count
Crack length
1.80E+03
1.60E+03
1.40E+03
1.20E+03
1.00E+03
8.00E+02
6.00E+02
4.00E+02
2.00E+02
0.00E+00
Count
13
12.5
12
11.5
11
10.5
10
9.5
9
Crack length(mm)
0
5000
10000
Fatigue cycles

a)

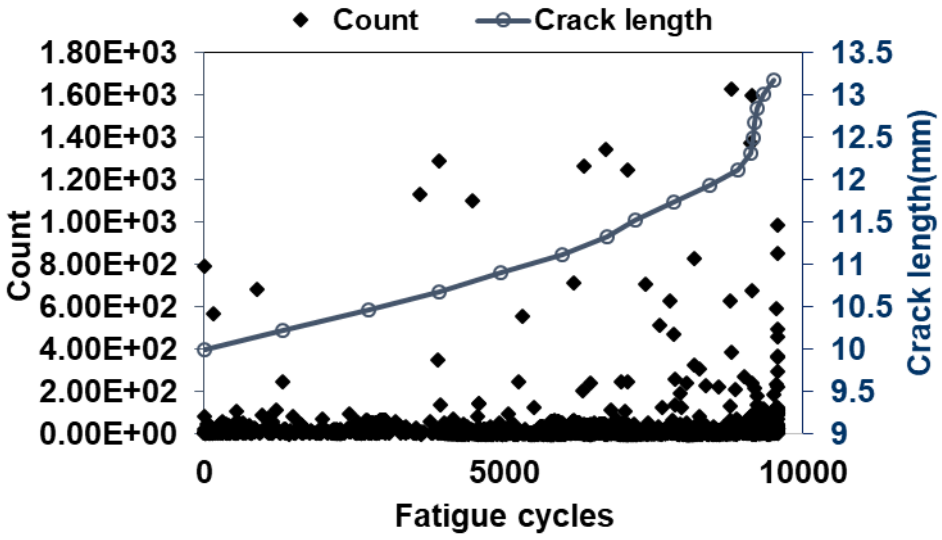
Count
Crack length
1.80E+03
1.60E+03
1.40E+03
1.20E+03
1.00E+03
8.00E+02
6.00E+02
4.00E+02
2.00E+02
0.00E+00
Count
13.5
13
12.5
12
11.5
11
10.5
10
9.5
9
Crack length(mm)
0
5000
10000
Fatigue cycles

b)

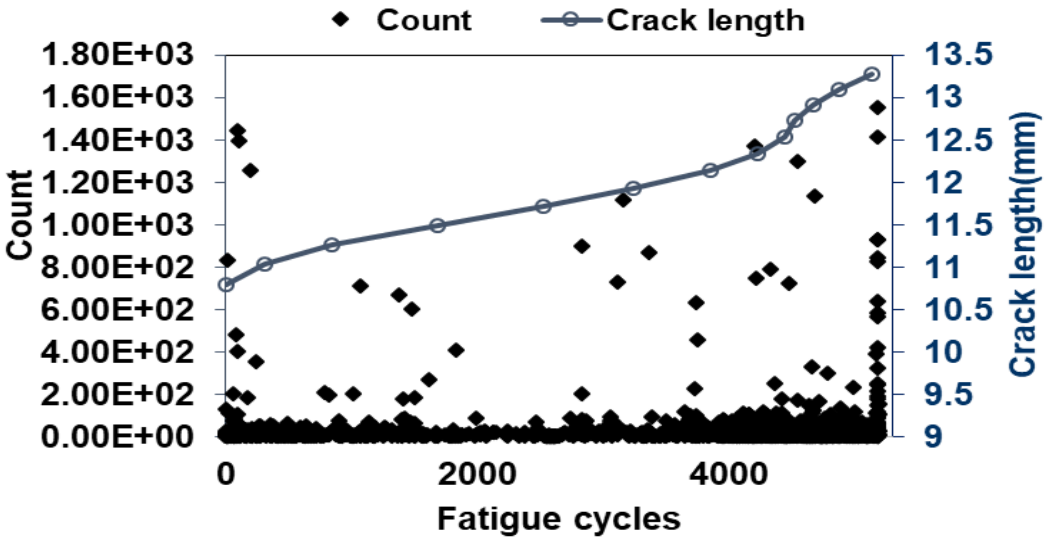
Count
Crack length
1.80E+03
1.60E+03
1.40E+03
1.20E+03
1.00E+03
8.00E+02
6.00E+02
4.00E+02
2.00E+02
0.00E+00
Count
13.5
13
12.5
12
11.5
11
10.5
10
9.5
9
Crack length(mm)
0
2000
4000
Fatigue cycles

c)

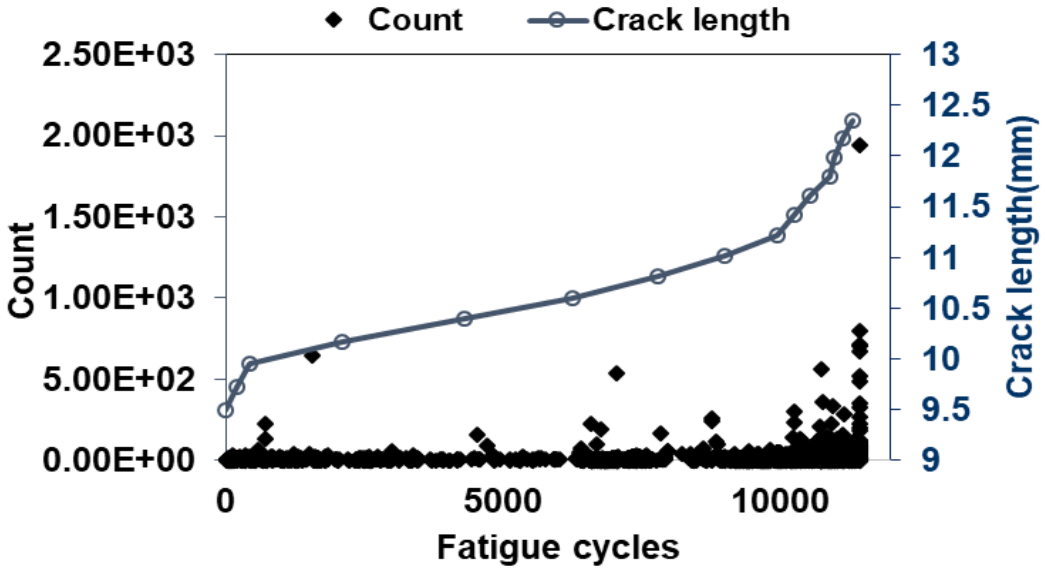
Count
Crack length
2.50E+03
2.00E+03
1.50E+03
1.00E+03
5.00E+02
0.00E+00
Count
13
12.5
12
11.5
11
10.5
10
9.5
9
Crack length(mm)
0
5000
10000
Fatigue cycles

d)

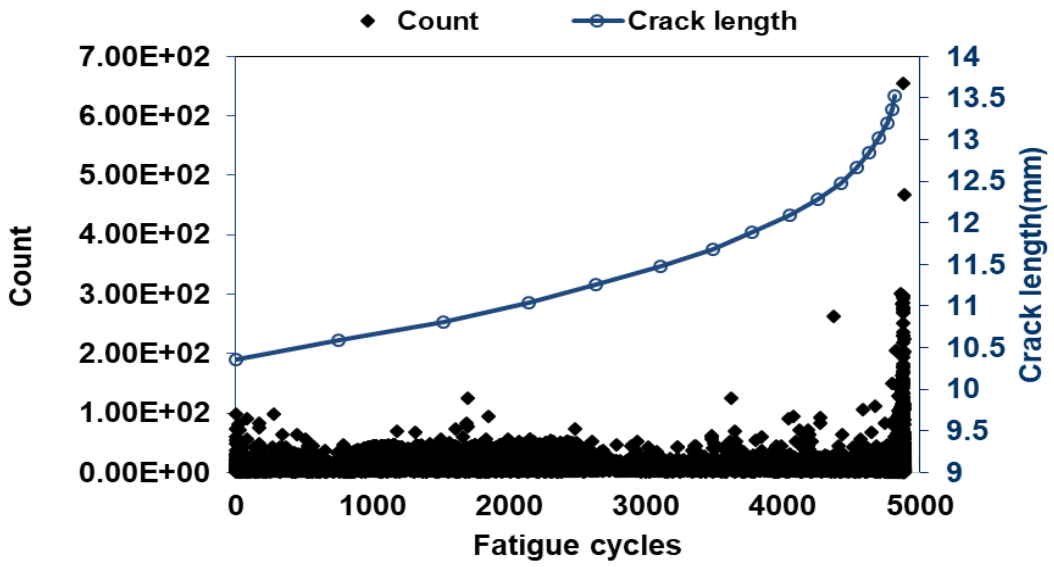
Count
Crack length
7.00E+02
6.00E+02
5.00E+02
4.00E+02
3.00E+02
2.00E+02
1.00E+02
0.00E+00
Count
0
1000
2000
3000
4000
5000
Fatigue cycles
14
13.5
13
12.5
12
11.5
11
10.5
10
9.5
9
Crack length(mm)

e)

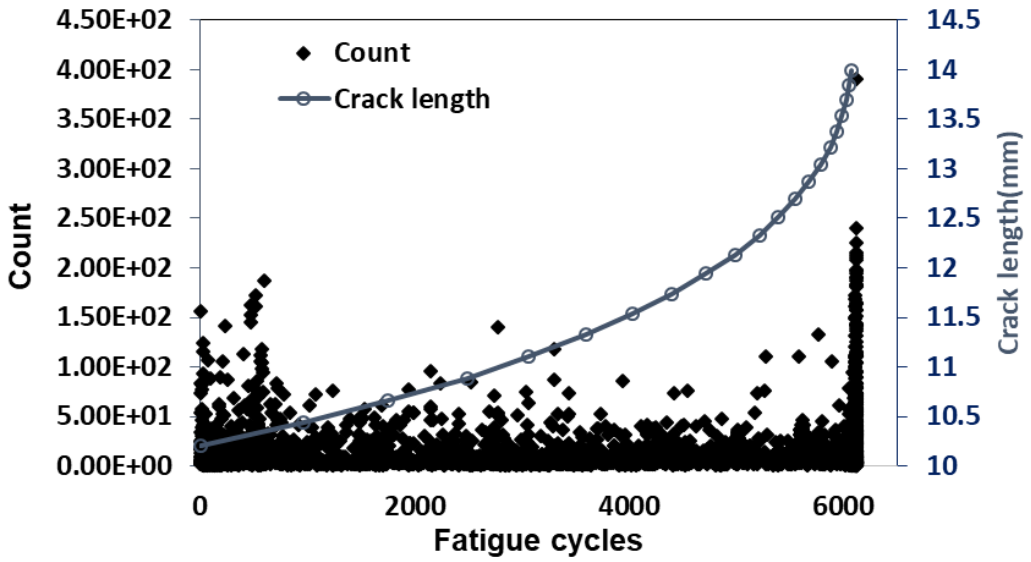
4.50E+02
4.00E+02
3.50E+02
3.00E+02
2.50E+02
2.00E+02
1.50E+02
1.00E+02
5.00E+01
0.00E+00
Count
Crack length
0
2000
4000
6000
Fatigue cycles
14.5
14
13.5
13
12.5
12
11.5
11
10.5
10
Crack length(mm)

f)

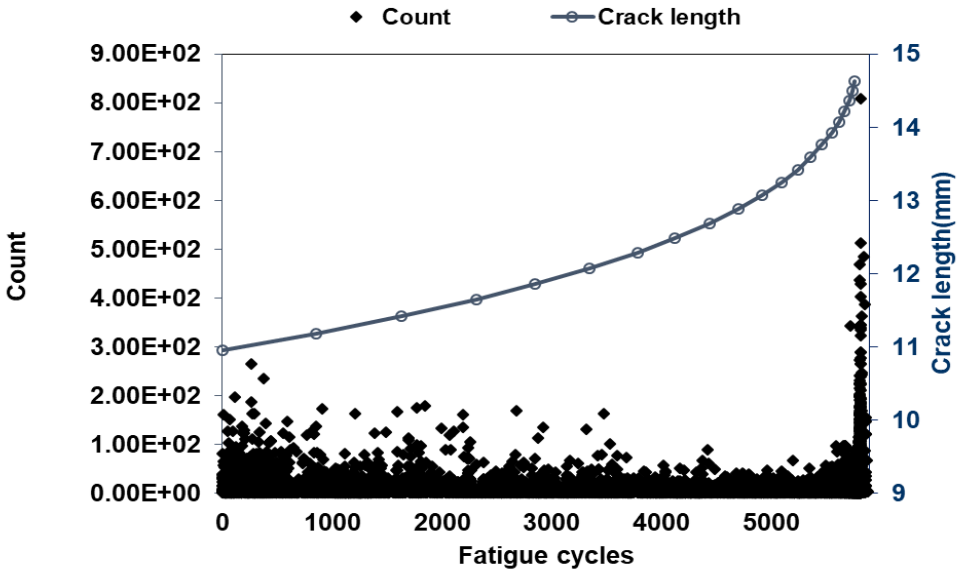

g)

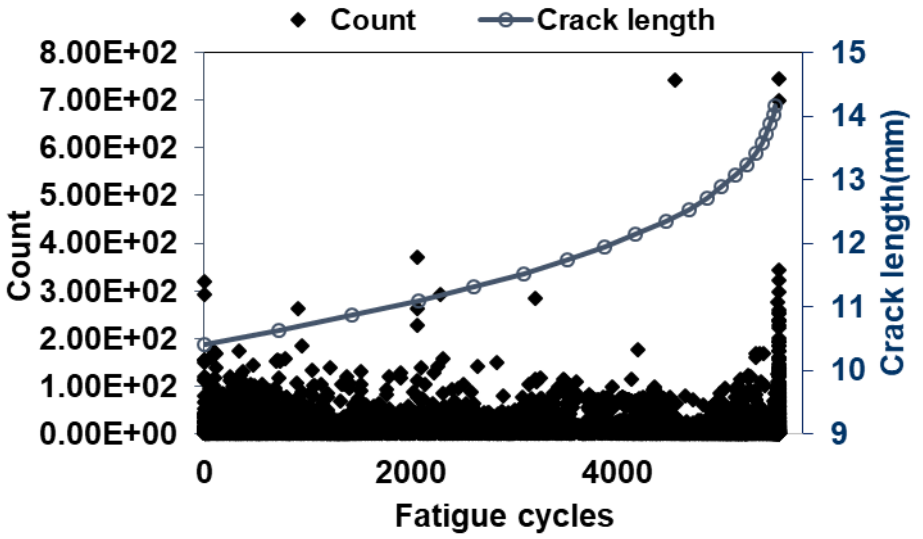

h)

Figure 7-3: AE signal count versus number of fatigue cycles with crack growth in mm for R260 rail steel a) sample 1, b) sample 2, c) sample 3, d) sample 4, and Hadfield steel e) sample 1, f) sample 2, g) sample 3, h) sample 4.

Figure 7-4 shows the correlation of the calculated AE count rate with crack growth rate and ΔK for the R260 and Hadfield steel samples in logarithmic scale. The count rate is defined as the ratio of the sum of counts of all AE hits to the time interval during which these AE hits are captured. For the R260 steel samples, the count rate shows a similar trend to the crack growth rate for every sample, although the variation between different samples is higher than that for crack growth rate. For the Hadfield steel samples, the correlation between count rate and crack growth rate is poor when ΔK is below $30MPam^{1/2}$ as indicated by the blue dashed line and the better correlation can be seen when ΔK is above $30MPam^{1/2}$ .This is very likely due to the plasticity effect at earlier stages and the evolution to cleavage fracture as the material gets harder due to work hardening during fatigue loading (bending). Obviously more AE energy will be released when the crack propagates through a more brittle area as more elastic energy will be released and subsequently captured by the AE sensors mounted on the samples. This does not occur in the R260 rail samples which behave more consistently in terms of their hardness throughout the tests with little work hardening occurring in comparison with the Hadfield samples. It should be noted that the count rate was calculated using the same method as for the crack growth rate so there is direct relationship with the Paris-Erdogan law.

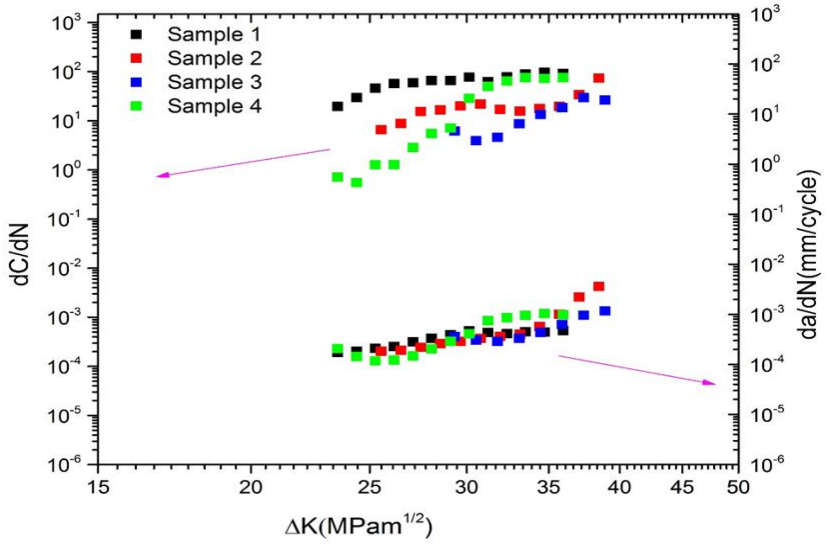

a)

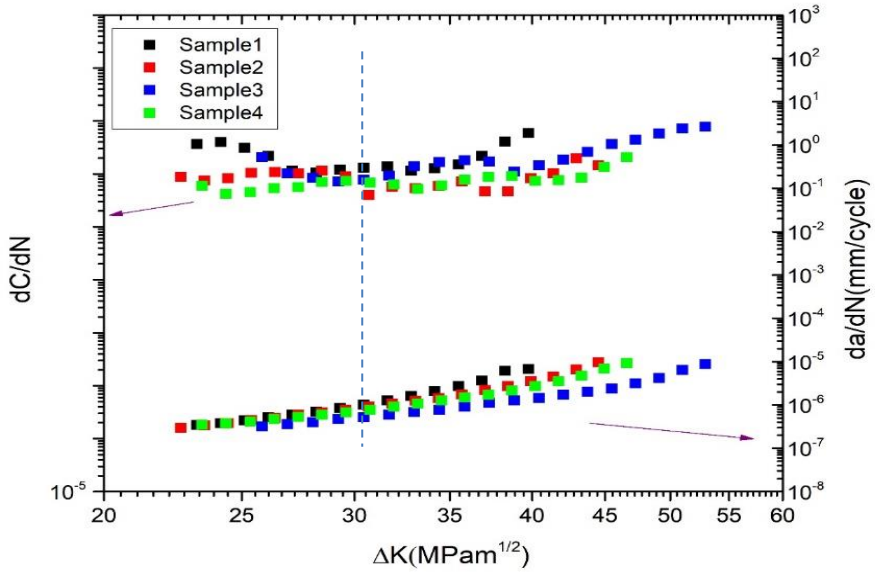

b)

Figure 7-4: Count rate and crack growth rate with ΔK for all a) rail steel and b) Hadfield steel samples in logarithmic scale.

Figure 7-5 shows the correlation between duration and crack length for all the samples. The AE events with the highest duration occur during the final stage of the fatigue crack growth tests. For Hadfield steel samples, most of AE events recorded during stable crack propagation have duration below 2000 μs, whereas for R260 steel samples, intermittent occurrence of AE events with duration above 2000 μs can be seen. For R260 steel samples, the amplitudes of all signals with duration above 2000 μs are above 60 dB during stable crack propagation as shown in Figure 7-6(a).The only few AE hits with duration above 2000 μs and amplitude smaller than 60 dB are those which occur during the final stage of crack growth and prior to final failure. The AE signal duration (above 2000 μs) exhibits a quasi-linear relationship with amplitude for R260 steel. However, for Hadfield steel samples, the distribution of amplitude versus duration is more scattered as shown in Figure 7-6(b). This is attributed to the fact that Hadfield steel is more ductile than R260 steel at the initial stages at least of the test, progressively becoming harder as work hardening effects increase. Figure 7-7 shows the correlation between the duration rate and crack growth rate with ΔK in logarithmic scale. The duration rate exhibits similar trends with the crack growth rate for all the samples.

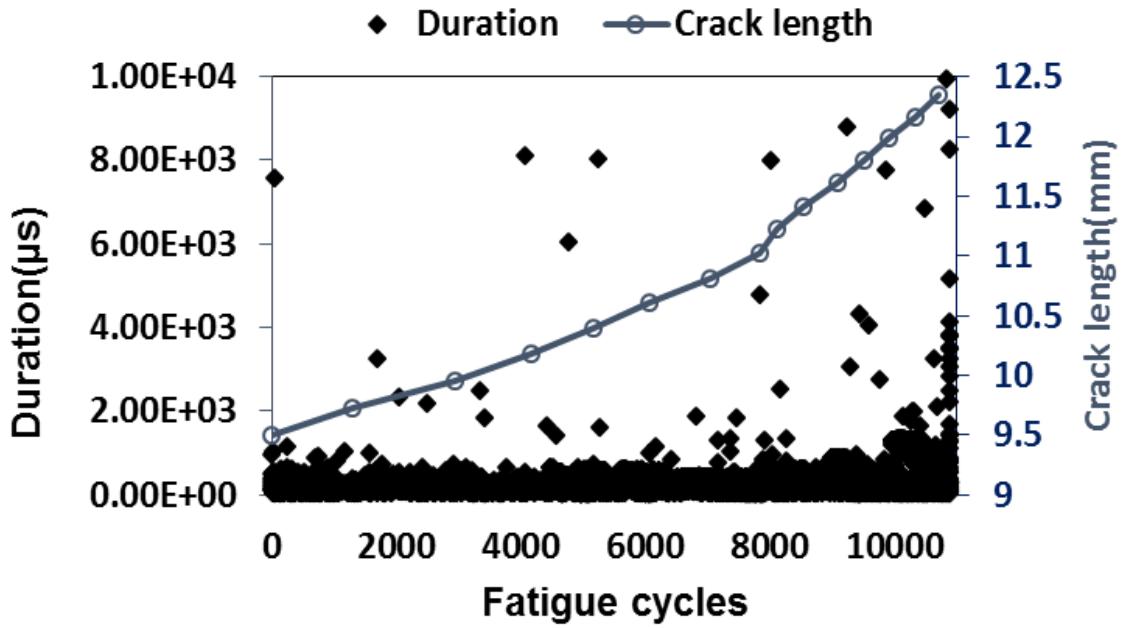
Duration
Crack length
1.00E+04
8.00E+03
6.00E+03
4.00E+03
2.00E+03
0.00E+00
Duration(µs)
12.5
12
11.5
11
10.5
10
9.5
9
Crack length(mm)
0
2000
4000
6000
8000
10000
Fatigue cycles

a)

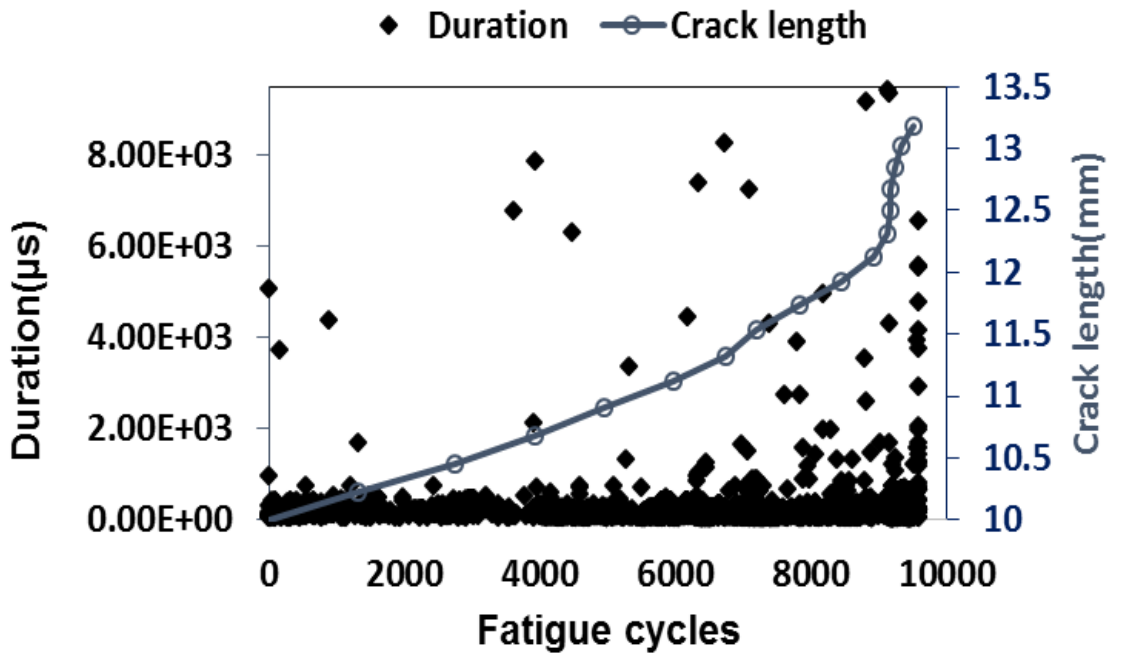
Duration
Crack length
8.00E+03
6.00E+03
4.00E+03
2.00E+03
0.00E+00
Duration(µs)
13.5
13
12.5
12
11.5
11
10.5
10
Crack length(mm)
0
2000
4000
6000
8000
10000
Fatigue cycles

b)

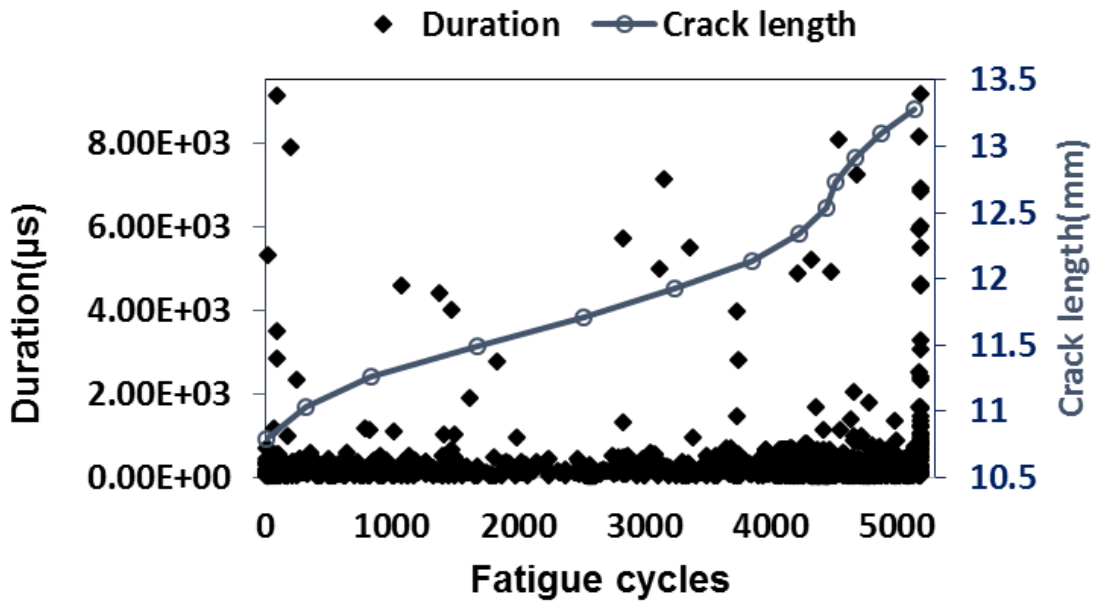
Duration
Crack length
Duration(µs)
8.00E+03
6.00E+03
4.00E+03
2.00E+03
0.00E+00
0
1000
2000
3000
4000
5000
Fatigue cycles
13.5
13
12.5
12
11.5
11
10.5
Crack length(mm)

c)

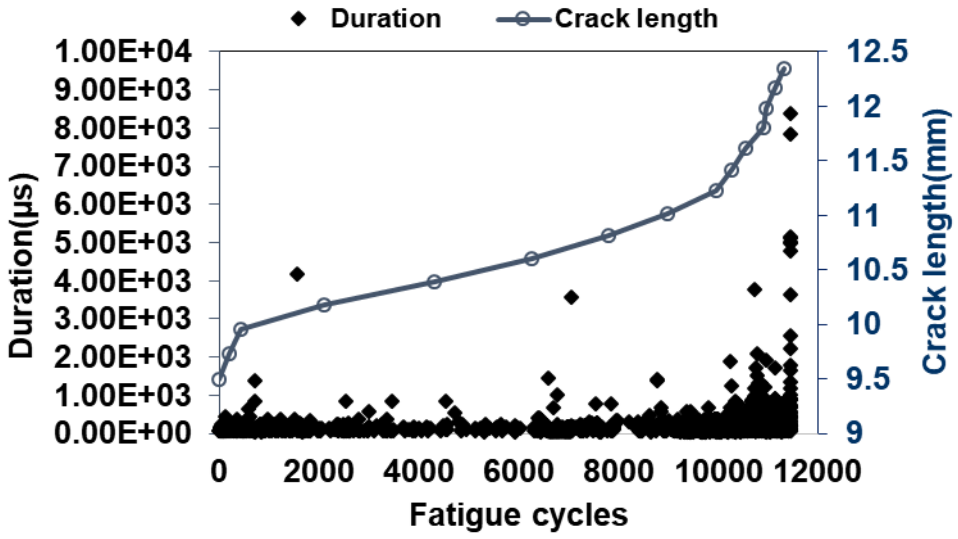
Duration
Crack length
Duration(µs)
1.00E+04
9.00E+03
8.00E+03
7.00E+03
6.00E+03
5.00E+03
4.00E+03
3.00E+03
2.00E+03
1.00E+03
0.00E+00
0
2000
4000
6000
8000
10000
12000
Fatigue cycles
12.5
12
11.5
11
10.5
10
9.5
9
Crack length(mm)

d)

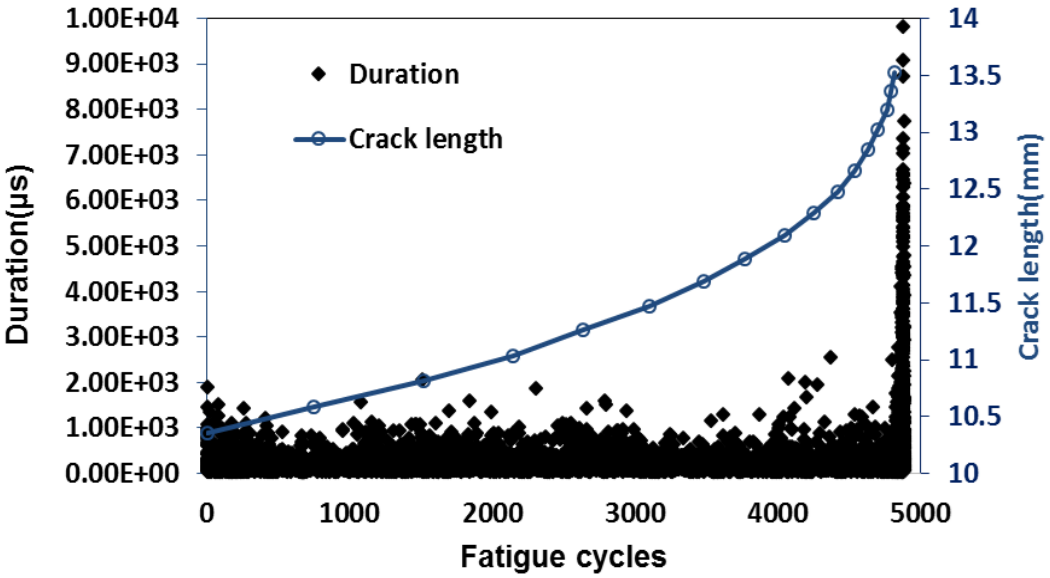
1.00E+04
9.00E+03
8.00E+03
7.00E+03
6.00E+03
5.00E+03
4.00E+03
3.00E+03
2.00E+03
1.00E+03
0.00E+00
Duration(µs)
Duration
Crack length
14
13.5
13
12.5
12
11.5
11
10.5
10
Crack length(mm)
0
1000
2000
3000
4000
5000
Fatigue cycles

e)

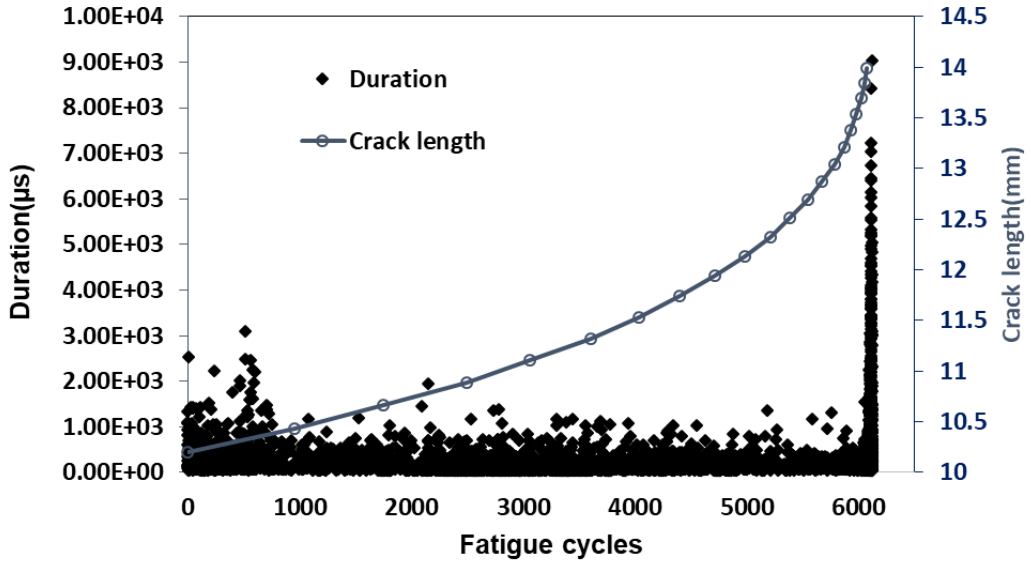
1.00E+04
9.00E+03
8.00E+03
7.00E+03
6.00E+03
5.00E+03
4.00E+03
3.00E+03
2.00E+03
1.00E+03
0.00E+00
Duration(µs)
Duration
Crack length
14.5
14
13.5
13
12.5
12
11.5
11
10.5
10
Crack length(mm)
0
1000
2000
3000
4000
5000
6000
Fatigue cycles

f)

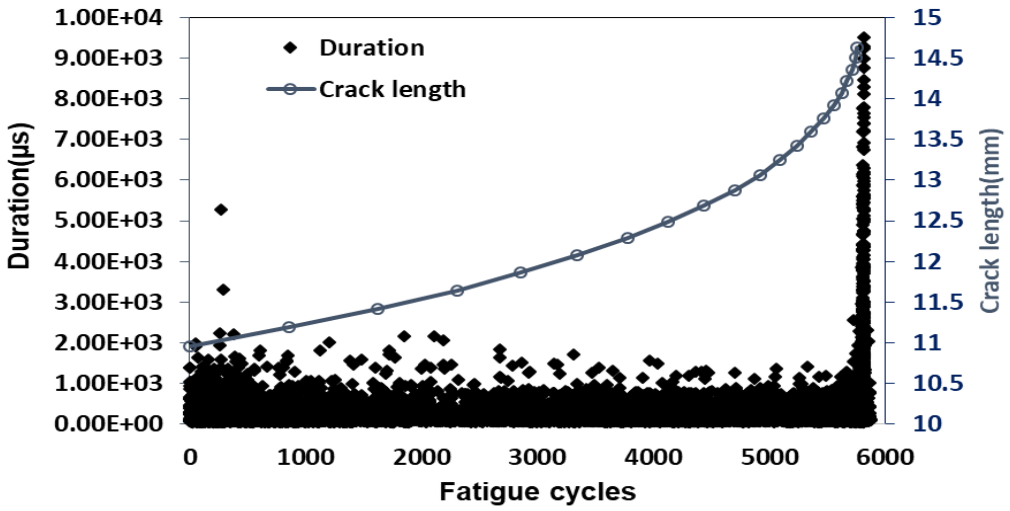

g)

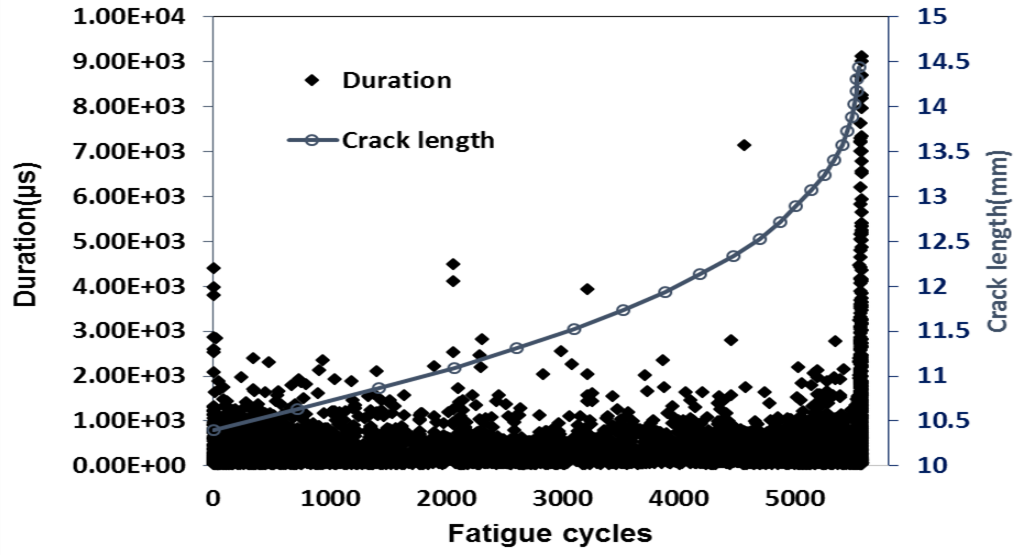

h)

Figure 7-5: AE signal duration in µs versus number of fatigue cycles with crack growth in mm for rail steel a) sample 1 b) sample 2 c) sample 3 d) sample 4 and Hadfield steel e)sample 1 f) sample 2 g) sample 3 h) sample 4

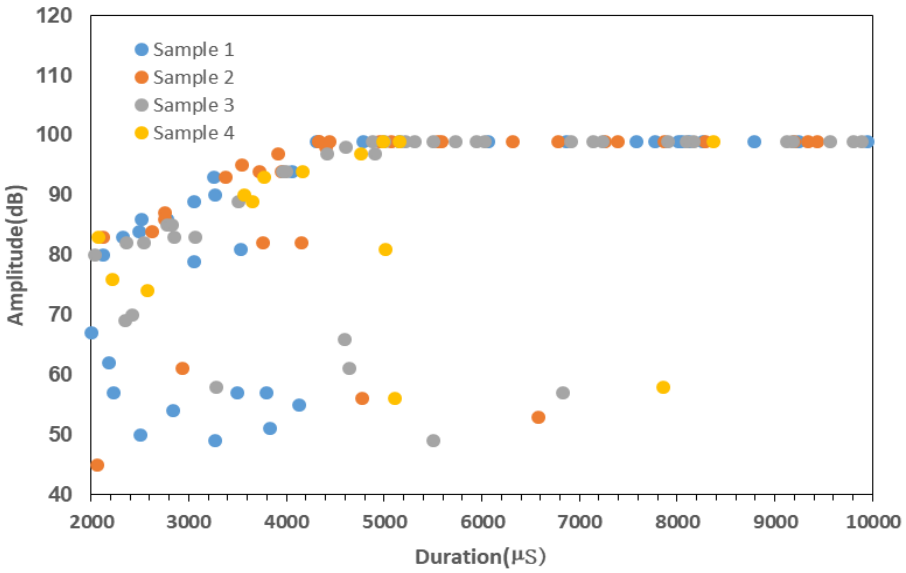

a)

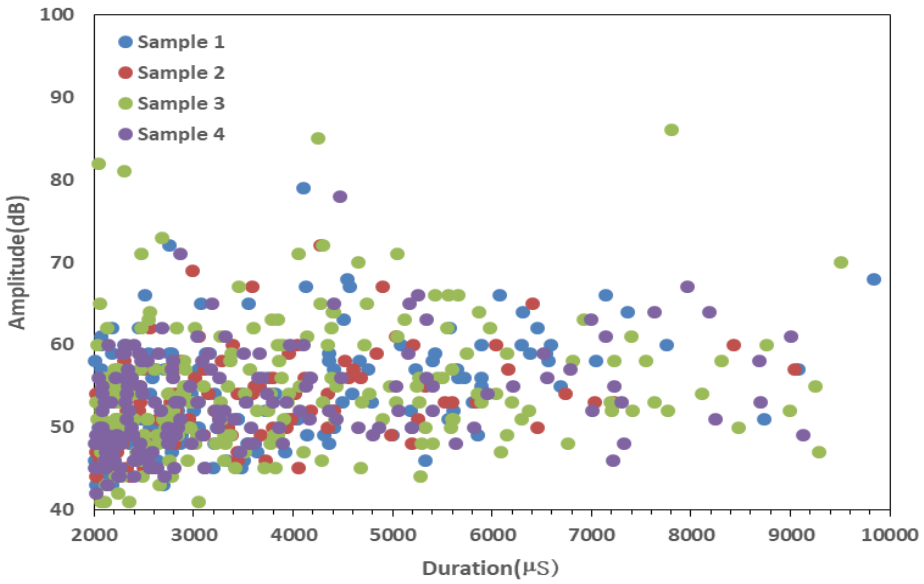

b)

Figure 7-6 : Correlation between amplitude and duration for a) R260 rail steel samples

b) Hadfield steel samples

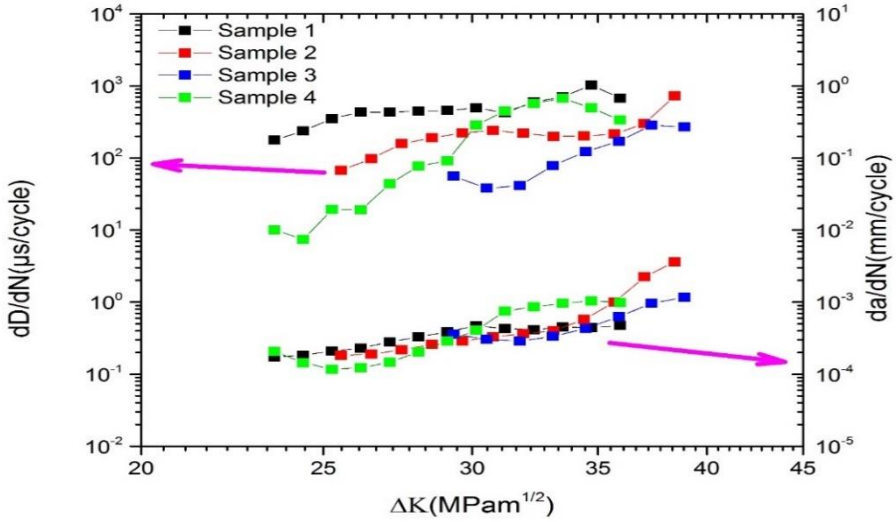

a)

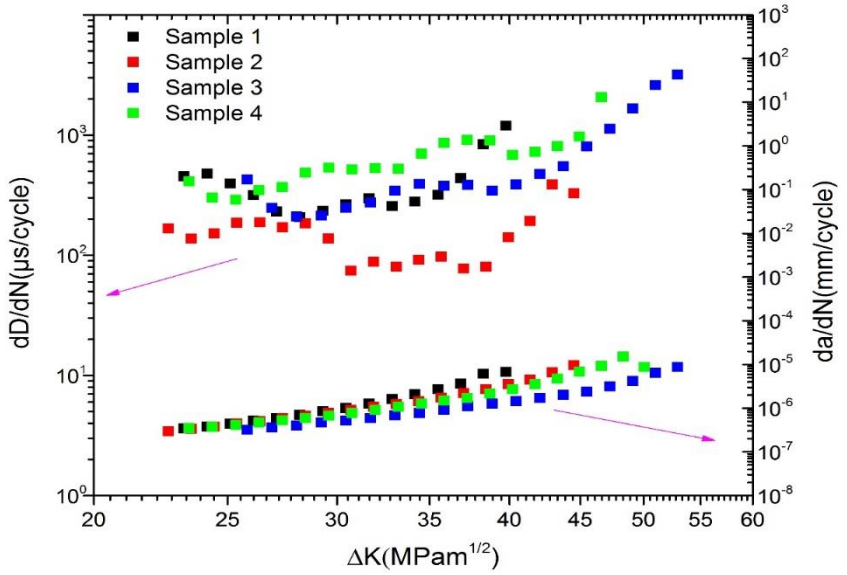

b)

Figure 7-7: Duration rate and crack growth rate with ΔK for all a) rail steel and b) Hadfield steel samples in logarithmic scale

Figure 7-8 shows the plots for energy with crack length and time for each of the samples tested. AE hits with high energy above 2000 (10μVolt-sec/count) were captured for rail steel samples during damage evolution. The high energy hits are also those exhibiting high amplitude (99 dB) which were shown previously. For the Hadfield steel samples, the energy values are shown in logarithmic scale for better resolution. The AE hits with the highest energy values occurs at the final stage. This is in line with the behaviour of this material as it gets gradually harder and hence more brittle with work hardening taking place. The number of AE hits with energy above 10 (10μVolt-sec/count) exhibits an obvious increase at a point before final failure. The AE hits with obviously higher energy can be observed in the plot indicating that the final failure is imminent. The energy rates were calculated and then the variation of the energy rate with time was compared with that of crack growth rate. The energy rate was calculated in the same way as crack growth rate. Hence, the relationship between energy rate and ΔK can be described as follows [31, 110],

$$\frac{\mathrm{dE}}{\mathrm{dN}} = \mathrm{B}\ \Delta\ \mathrm{K}^{p} \tag{7-1}$$

or

$$\log\left(\frac{\mathrm{dE}}{\mathrm{dN}}\right) = \log\mathrm{B} + p\log\Delta\ \mathrm{K} \tag{7-2}$$

The plots in Figure 7-9 show the crack growth rate with energy rate and ΔK in logarithmic scale for every sample. As it can be seen, the energy rate for Hadfield steel samples show a “trough-like” (decreasing and then increasing) trend. Generally, the energy rate for both types of materials does reflect the crack growth rate trend. However, Hadfield steel shows a more stable trend in comparison with that for R260 steel especially at the end of stage

II or the Paris-Erdogan regime. The fitting values for all the parameters are summarised in Table 7-1 and Table 7-2. For the R260 steel samples, the intermittent occurrence of cleavage fracture corresponds precisely to the high energy AE hits, which has been shown in [151].

It has been reported that Hadfield steel and other high Mn manganese steel show a ductile crack growth behaviour [17, 18]. However, as work hardening progresses, ductility will be noticeably reduced resulting in more cleavage to occur. More specifically, the Hadfield steel samples exhibit a quasi-cleavage fracture which is the dominant fracture mode during high cycle fatigue (HCF). This fracture mode is in agreement with the relatively low energy rate in comparison with that observed for pearlitic rail steel samples. The lower crack growth rate is consistent with plasticity occurring ahead of the crack tip and work hardening [17].

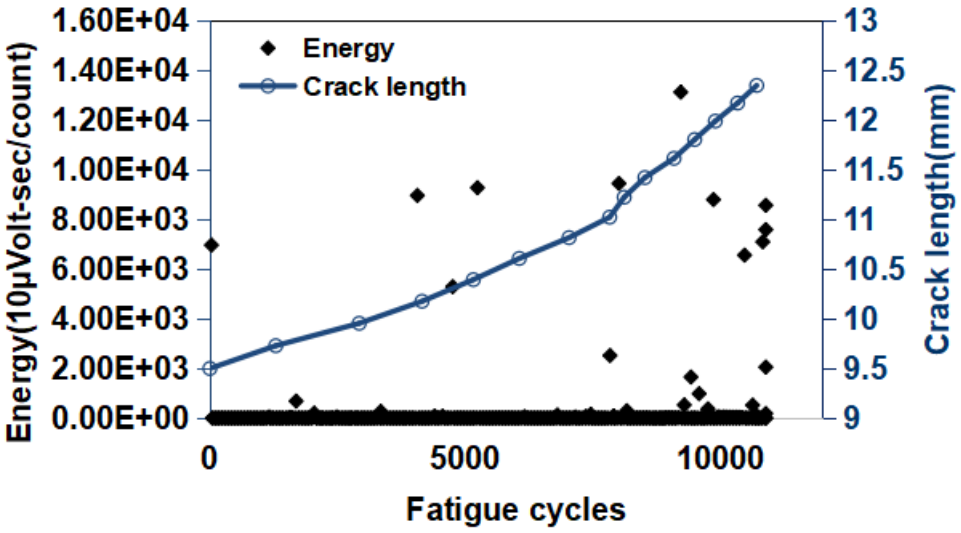
Energy
Crack length
Energy(10µVolt-sec/count)
Crack length(mm)
Fatigue cycles
1.60E+04
1.40E+04
1.20E+04
1.00E+04
8.00E+03
6.00E+03
4.00E+03
2.00E+03
0.00E+00
13
12.5
12
11.5
11
10.5
10
9.5
9
0
5000
10000

a)

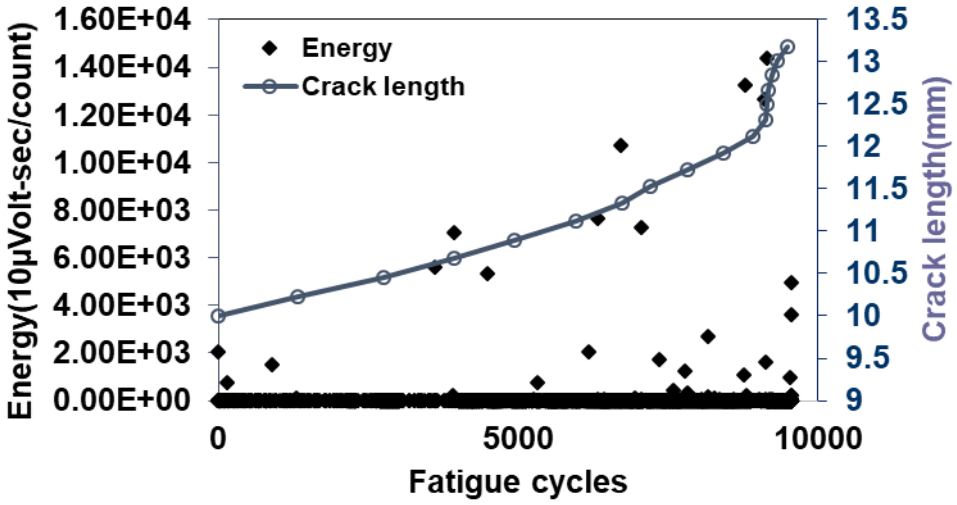
Energy
Crack length
Energy(10µVolt-sec/count)
Crack length(mm)
Fatigue cycles
1.60E+04
1.40E+04
1.20E+04
1.00E+04
8.00E+03
6.00E+03
4.00E+03
2.00E+03
0.00E+00
13.5
13
12.5
12
11.5
11
10.5
10
9.5
9
0
5000
10000

b)

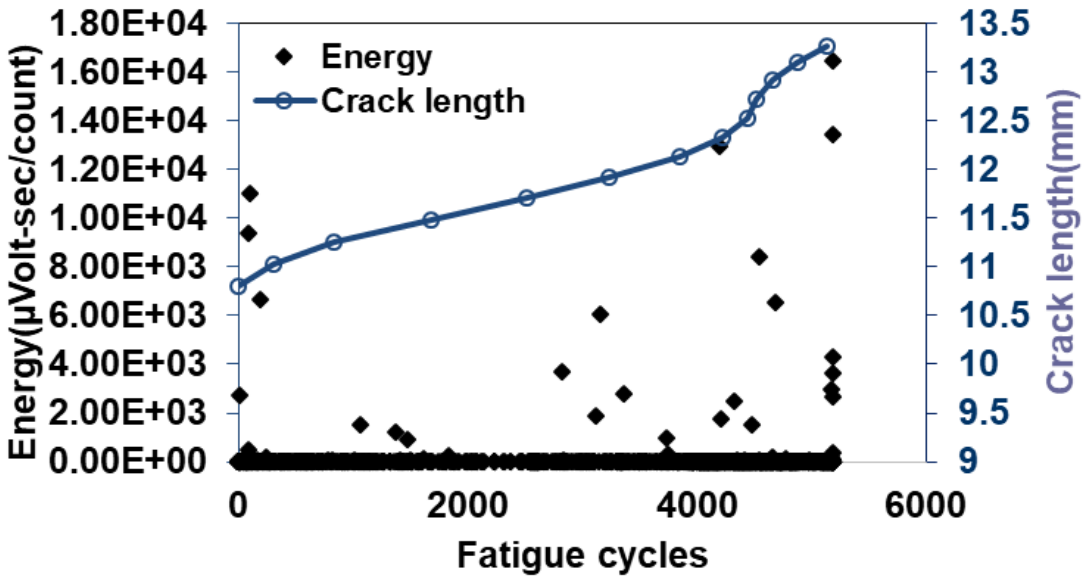
Energy
Crack length
Energy(μVolt-sec/count)
Crack length(mm)
Fatigue cycles
1.80E+04
1.60E+04
1.40E+04
1.20E+04
1.00E+04
8.00E+03
6.00E+03
4.00E+03
2.00E+03
0.00E+00
13.5
13
12.5
12
11.5
11
10.5
10
9.5
9
0
2000
4000
6000

c)

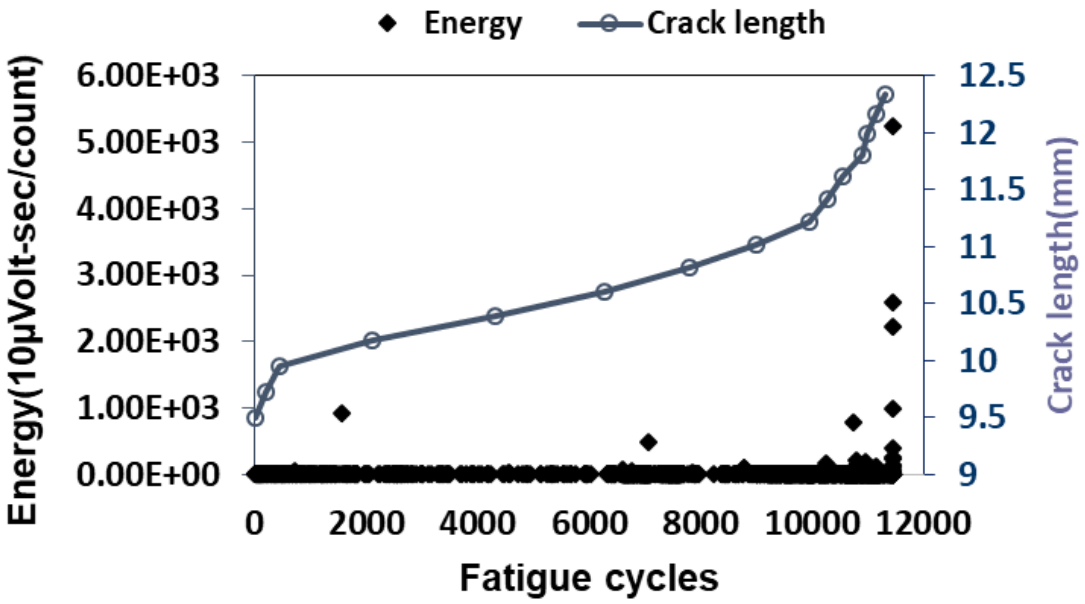
Energy
Crack length
Energy(10μVolt-sec/count)
Crack length(mm)
Fatigue cycles
6.00E+03
5.00E+03
4.00E+03
3.00E+03
2.00E+03
1.00E+03
0.00E+00
12.5
12
11.5
11
10.5
10
9.5
9
0
2000
4000
6000
8000
10000
12000

d)

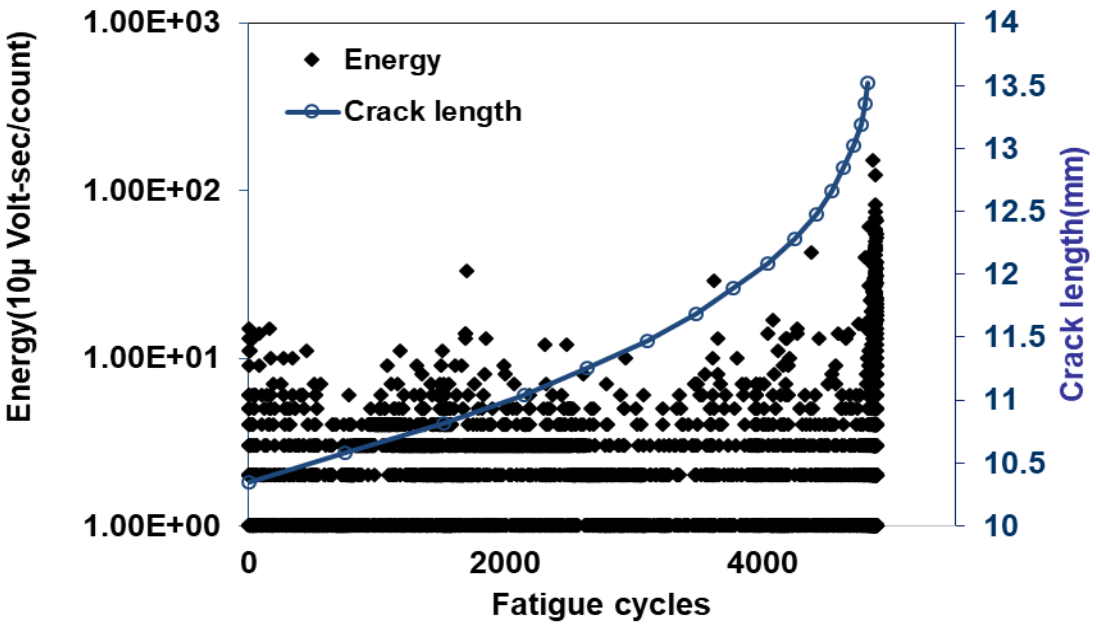
1.00E+03
1.00E+02
1.00E+01
1.00E+00
Energy(10µ Volt-sec/count)
Energy
Crack length
14
13.5
13
12.5
12
11.5
11
10.5
10
Crack length(mm)
0
2000
4000
Fatigue cycles

e)

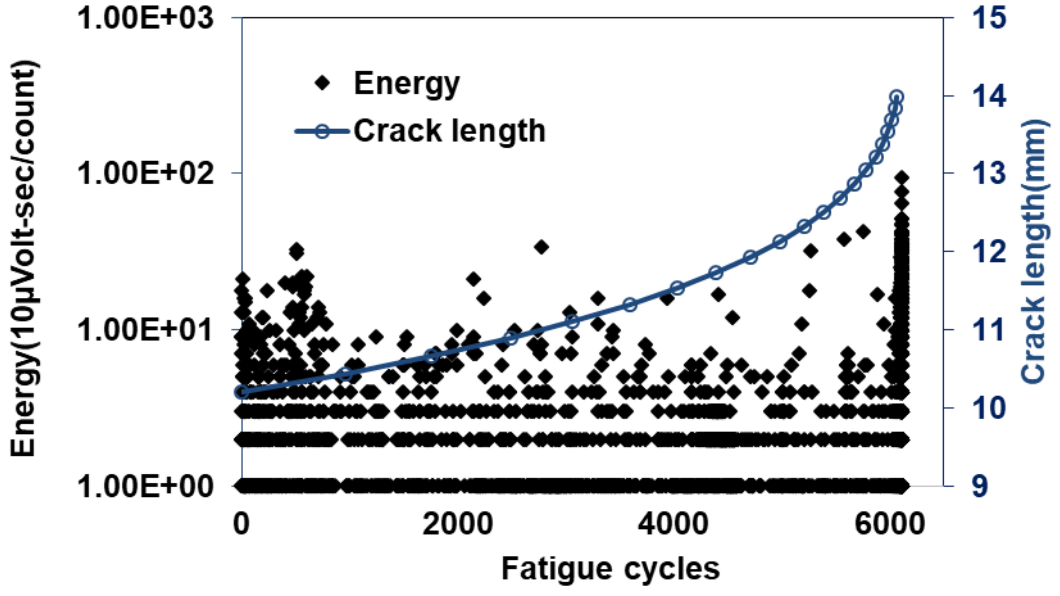
1.00E+03
1.00E+02
1.00E+01
1.00E+00
Energy(10µVolt-sec/count)
Energy
Crack length
15
14
13
12
11
10
9
Crack length(mm)
0
2000
4000
6000
Fatigue cycles

f)

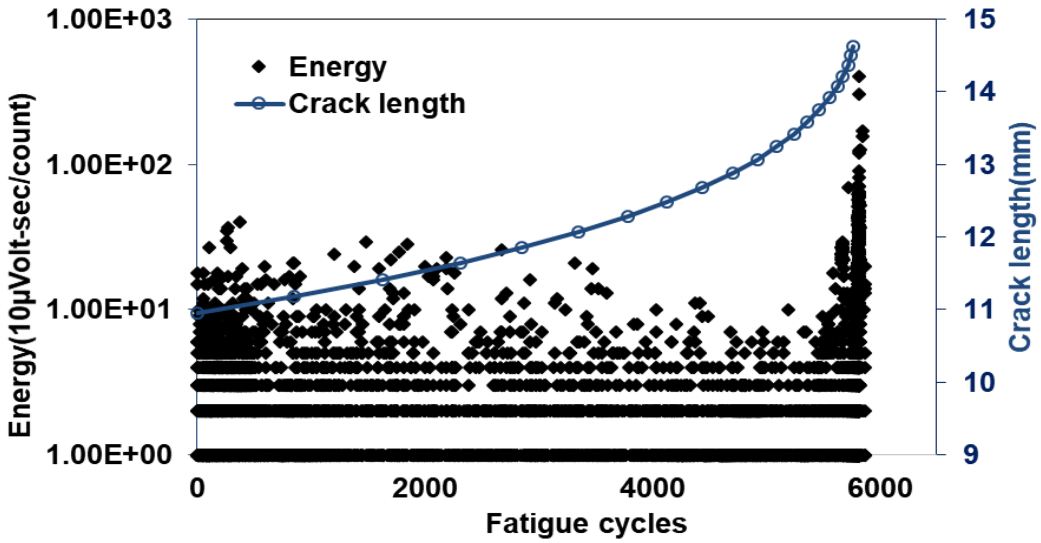

g)

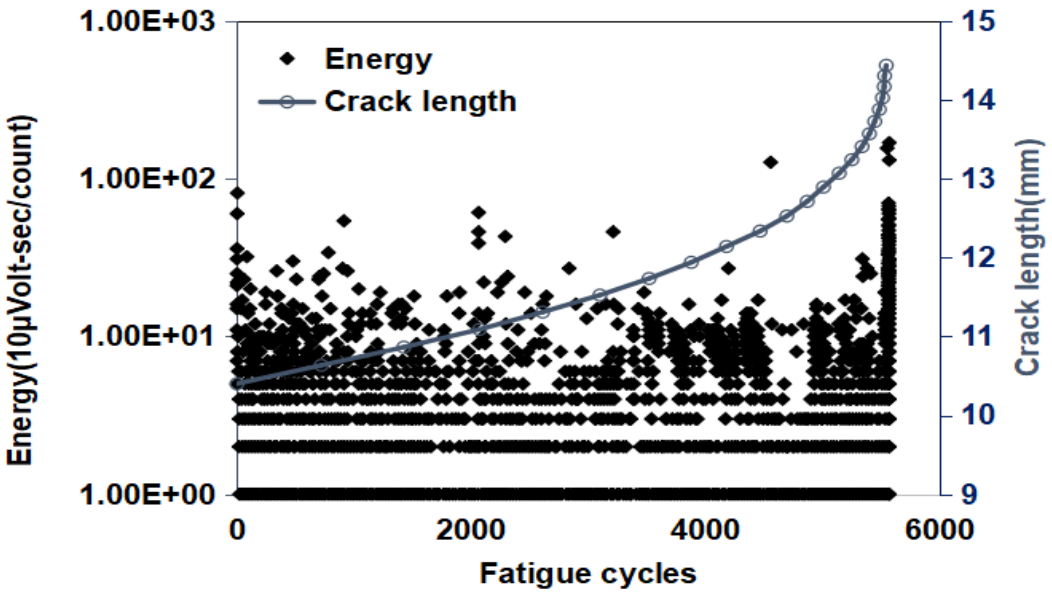

h)

Figure 7-8:AE signal energy with number of fatigue cycles with crack growth in mm for rail steel a) sample 1, b) sample ,2 c) sample 3, d) sample 4, and Hadfield steel e) sample 1, f) sample 2, g) sample 3, h) sample 4.

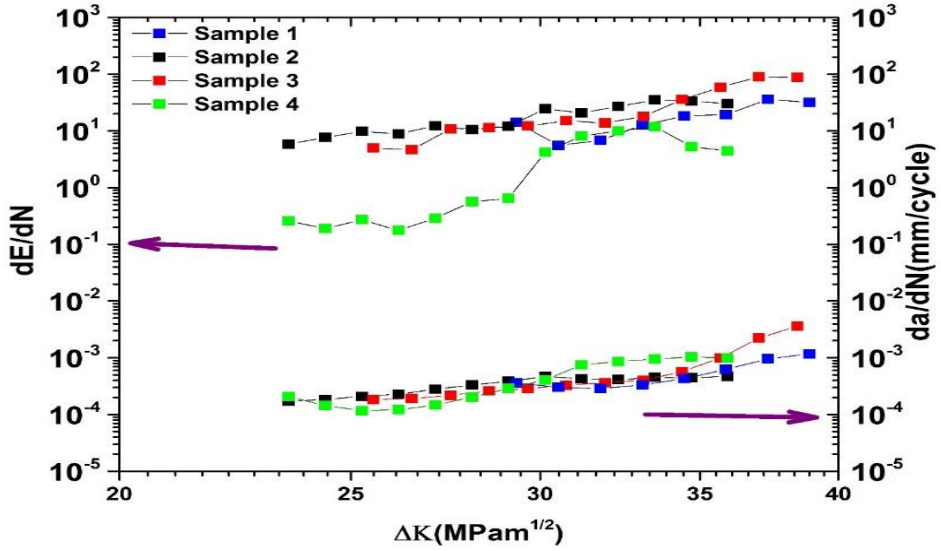

a)

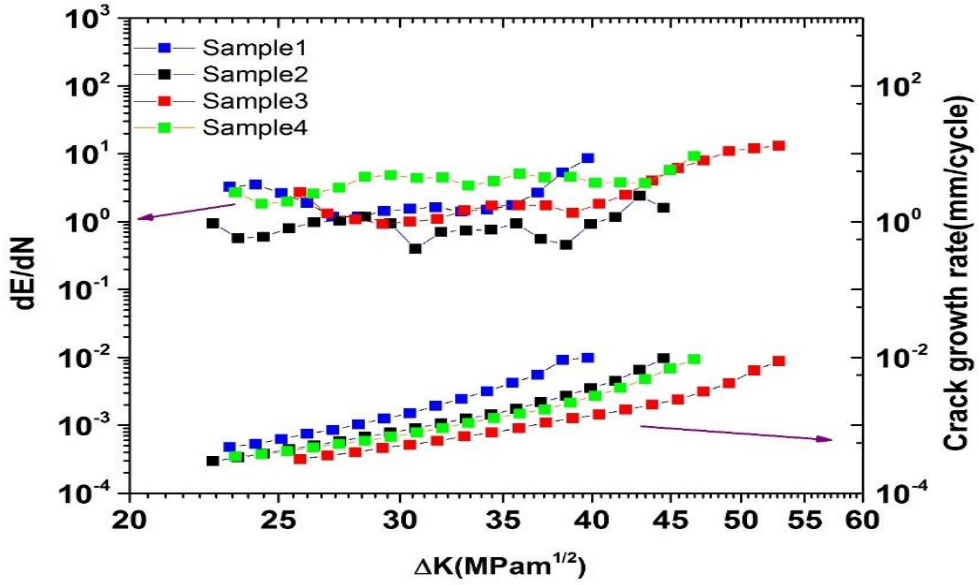

b)

Figure 7-9:Plot showing the Energy rate and crack growth rate with ΔK for all a) rail steel and b) Hadfield steel samples in logarithmic scale

Table 7-1: Fitting parameters of crack growth rate and AE constants for R260 rail steel samples

	m	C	p	B
1	4.88	2E-11	5.45	7E-8
2	2.56	6E-8	4.29	8E-6
3	6.65	5E-14	7.23	3E-10
4	5.83	1E-12	12.1	2E-18

Table 7-2: Fitting parameters of crack growth rate and AE constants for Hadfield steel samples

	M	C	p	B
1	5.79	5E-12	0.94	8E-02
2	4.80	8E-11	0.69	8E-02
3	3.67	2E-09	2.36	4E-04
4	4.58	1E-10	1.27	5E-02

Figure 7-10 shows the plots for risetime with crack length and time for each of the samples tested. For the R260 rail steel samples only a few AE events with a rise time above 1000 μs occur before the final stage prior to failure. However, nearer to final failure, a higher number of AE events with higher rise time are captured. However, most of high amplitude (>=70 dB) AE events related to brittle cleavage fracture tend to have rise time smaller than 200 μs., Therefore, it is difficult to detect brittle crack growth based on this parameter. However, the number of hits with high rise time for Hadfield steel samples is obviously higher indicating the different behaviour in crack propagation in this material

in comparison with pearlitic rail steel. This is actually in agreement with the behaviour expected due to plasticity in front of the crack tip.

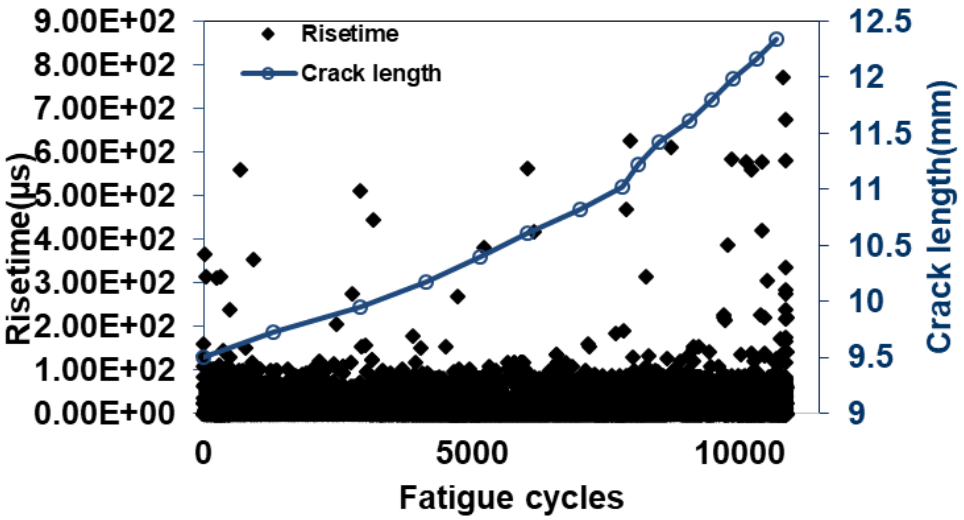

a)

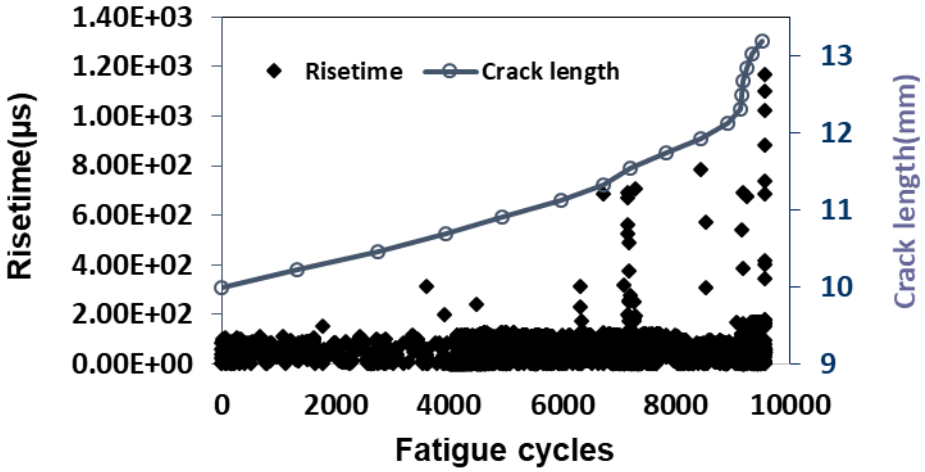

b)

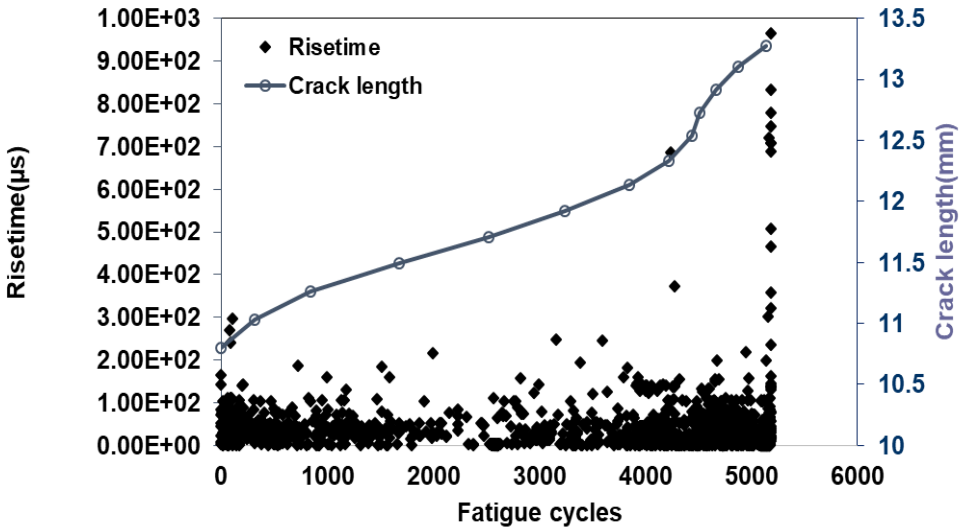
Risetime
Crack length
Risetime(µs)
Crack length(mm)
Fatigue cycles
1.00E+03
9.00E+02
8.00E+02
7.00E+02
6.00E+02
5.00E+02
4.00E+02
3.00E+02
2.00E+02
1.00E+02
0.00E+00
13.5
13
12.5
12
11.5
11
10.5
10
0
1000
2000
3000
4000
5000
6000

c)

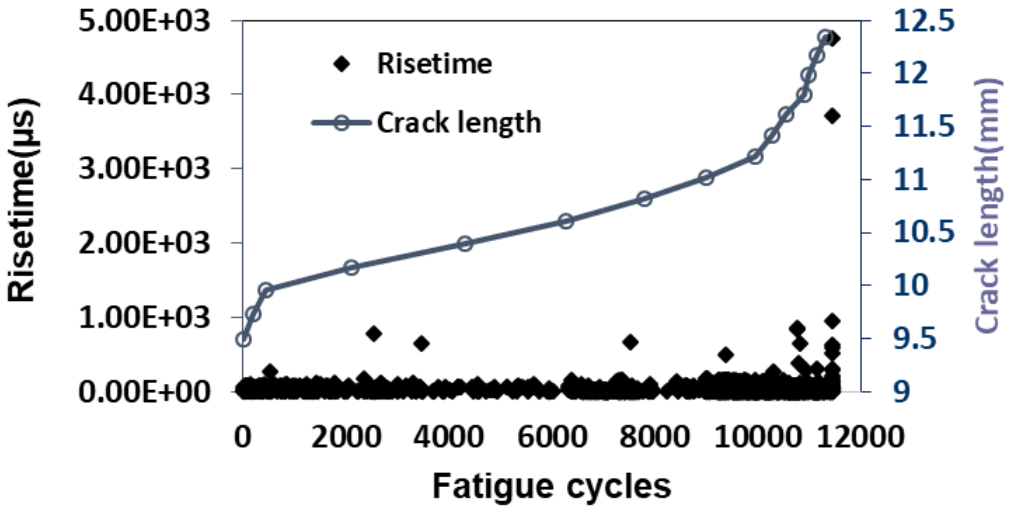
Risetime
Crack length
Risetime(µs)
Crack length(mm)
Fatigue cycles
5.00E+03
4.00E+03
3.00E+03
2.00E+03
1.00E+03
0.00E+00
12.5
12
11.5
11
10.5
10
9.5
9
0
2000
4000
6000
8000
10000
12000

d)

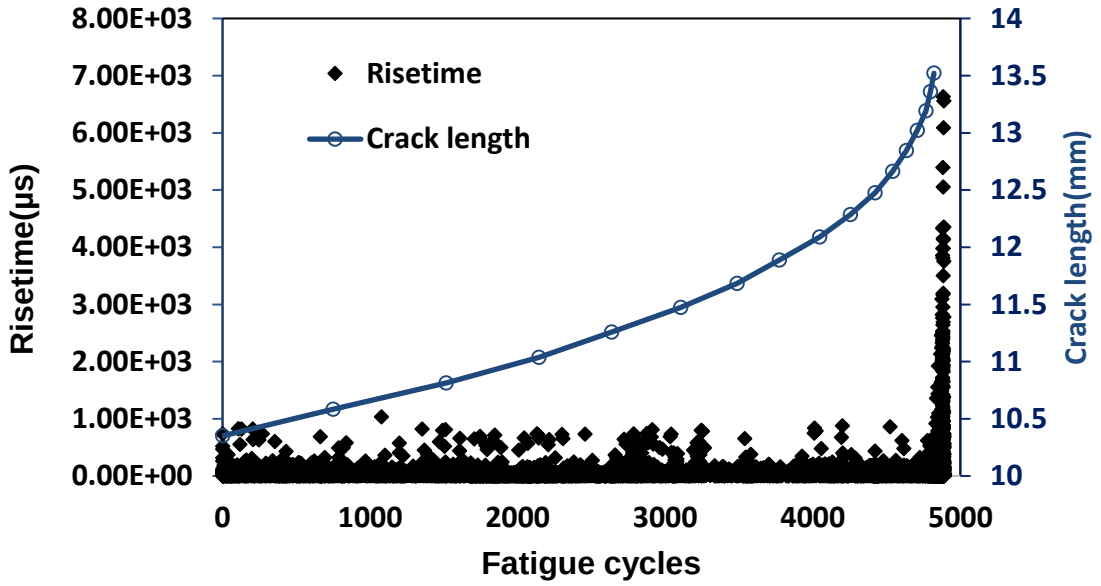
8.00E+03
7.00E+03
6.00E+03
5.00E+03
4.00E+03
3.00E+03
2.00E+03
1.00E+03
0.00E+00
Risetime(µs)
Risetime
Crack length
14
13.5
13
12.5
12
11.5
11
10.5
10
Crack length(mm)
0
1000
2000
3000
4000
5000
Fatigue cycles

e)

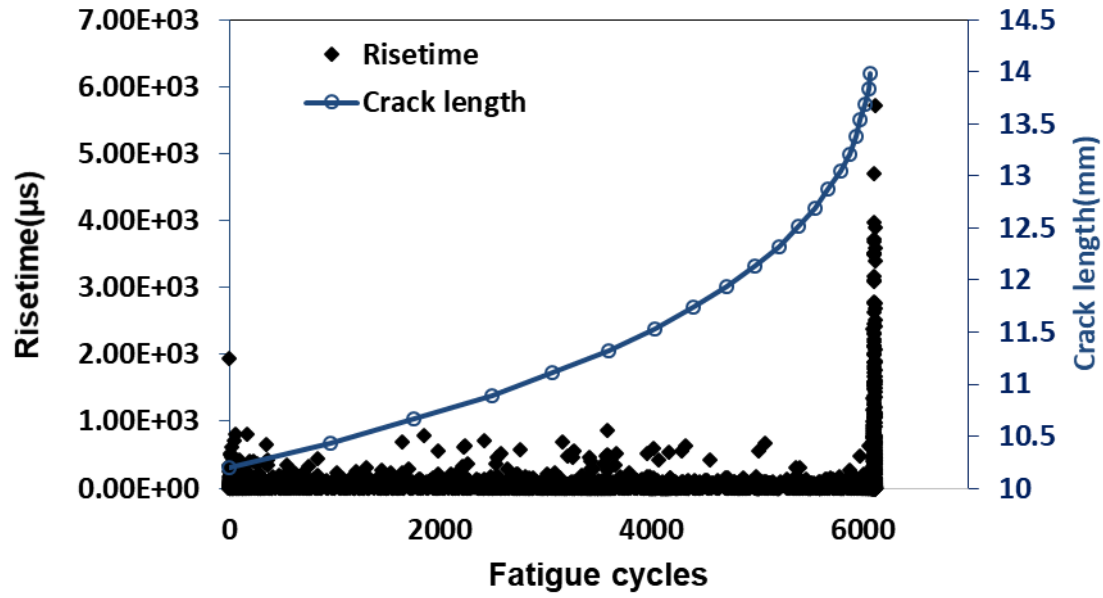
7.00E+03
6.00E+03
5.00E+03
4.00E+03
3.00E+03
2.00E+03
1.00E+03
0.00E+00
Risetime(µs)
Risetime
Crack length
14.5
14
13.5
13
12.5
12
11.5
11
10.5
10
Crack length(mm)
0
2000
4000
6000
Fatigue cycles

f)

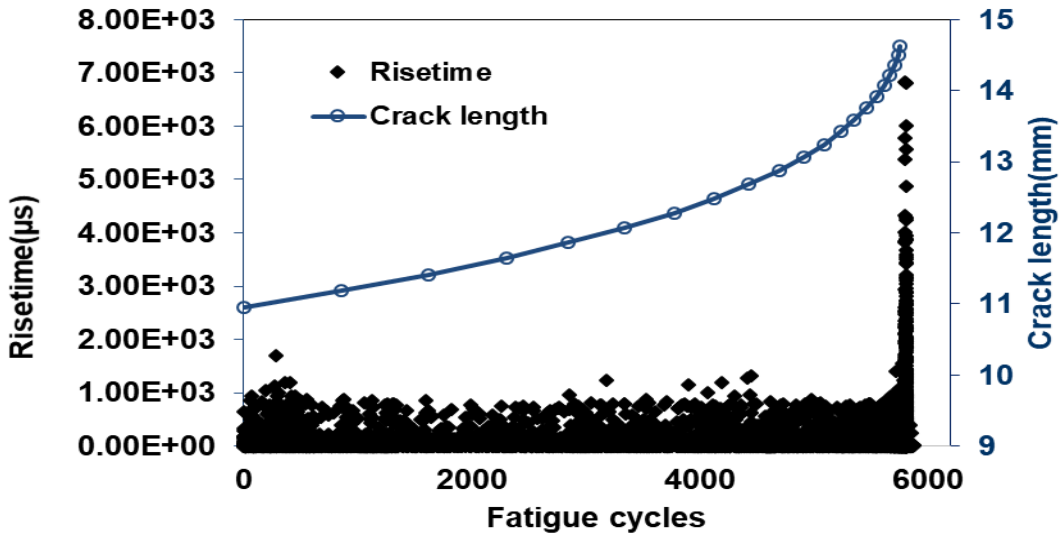

g)

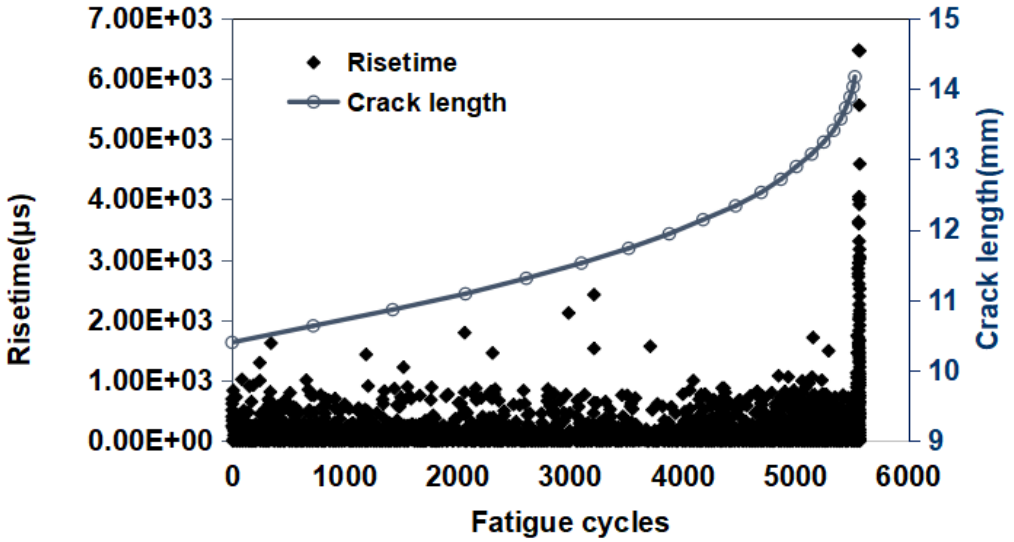

h)

Figure 7-10: AE signal risetime with number of fatigue cycles with crack growth in mm for rail steel a) sample 1, b) sample ,2 c) sample 3, d) sample 4, and Hadfield steel e) sample 1, f) sample 2, g) sample 3, h) sample 4.

Figure 7-11 shows the correlation between ASL in dB with crack length for each of the samples. For every sample, the highest ASL values are observed towards the final stage of the tests and hence prior to failure. For the Hadfield steel samples, ASL values start to show stepwise distribution. Minimum ASL values start to increase as early as around 1000 loading cycles before final failure. For the R260 rail steel samples, when final failure is impending, the minimum ASL value recorded increases accordingly. Therefore, the ASL value in this case can be used as an effective indicator of imminent failure. The last few events with low ASL is caused by the external noise when the loading machine stops suddenly at the end of the test process.

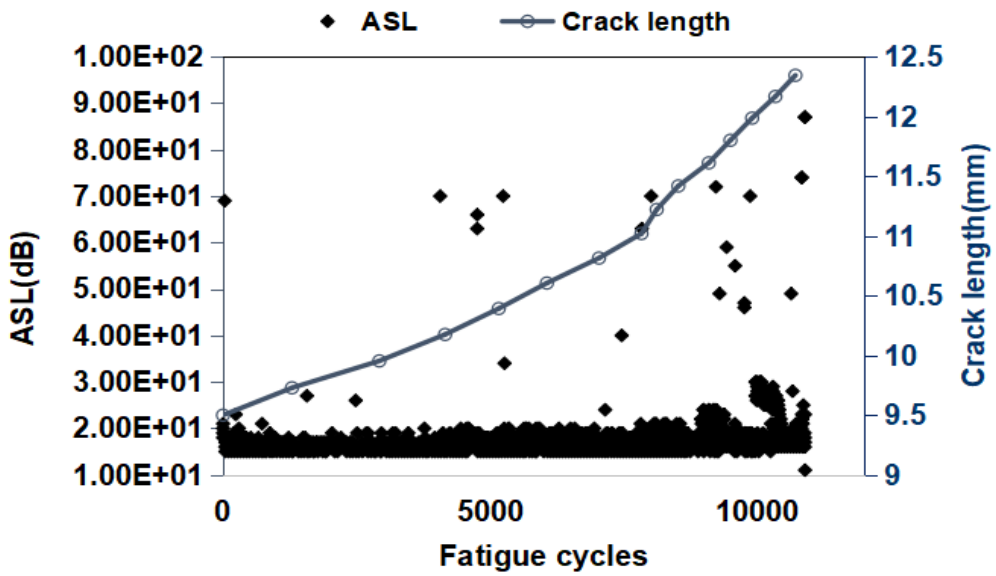

a)

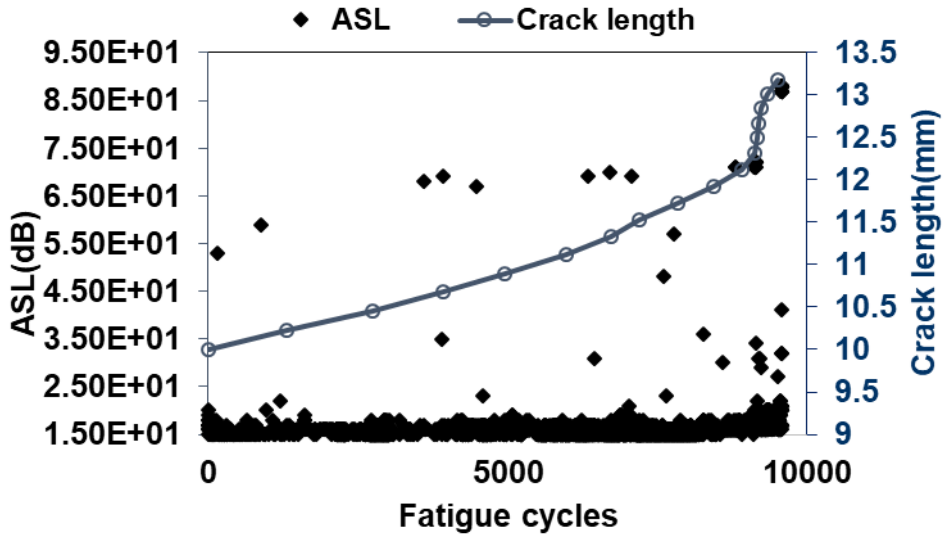
ASL
Crack length
9.50E+01
8.50E+01
7.50E+01
6.50E+01
5.50E+01
4.50E+01
3.50E+01
2.50E+01
1.50E+01
ASL(dB)
13.5
13
12.5
12
11.5
11
10.5
10
9.5
9
Crack length(mm)
0
5000
10000
Fatigue cycles

b)

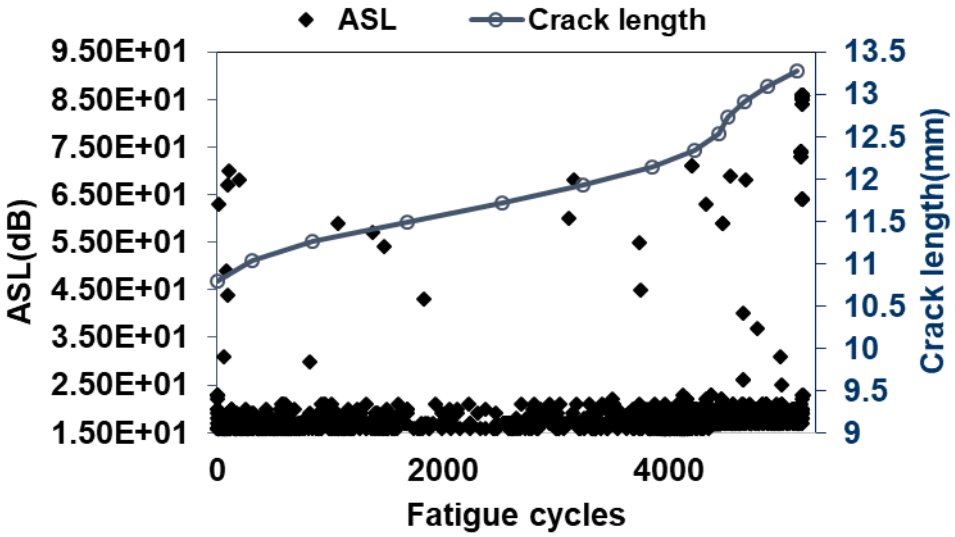
ASL
Crack length
9.50E+01
8.50E+01
7.50E+01
6.50E+01
5.50E+01
4.50E+01
3.50E+01
2.50E+01
1.50E+01
ASL(dB)
13.5
13
12.5
12
11.5
11
10.5
10
9.5
9
Crack length(mm)
0
2000
4000
Fatigue cycles

c)

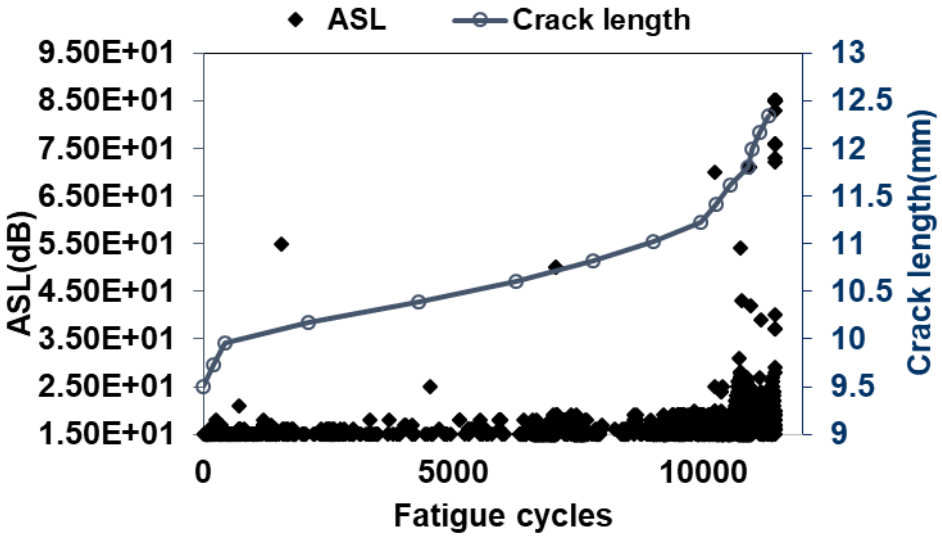
ASL
Crack length
9.50E+01
8.50E+01
7.50E+01
6.50E+01
5.50E+01
4.50E+01
3.50E+01
2.50E+01
1.50E+01
ASL(dB)
13
12.5
12
11.5
11
10.5
10
9.5
9
Crack length(mm)
0
5000
10000
Fatigue cycles

d)

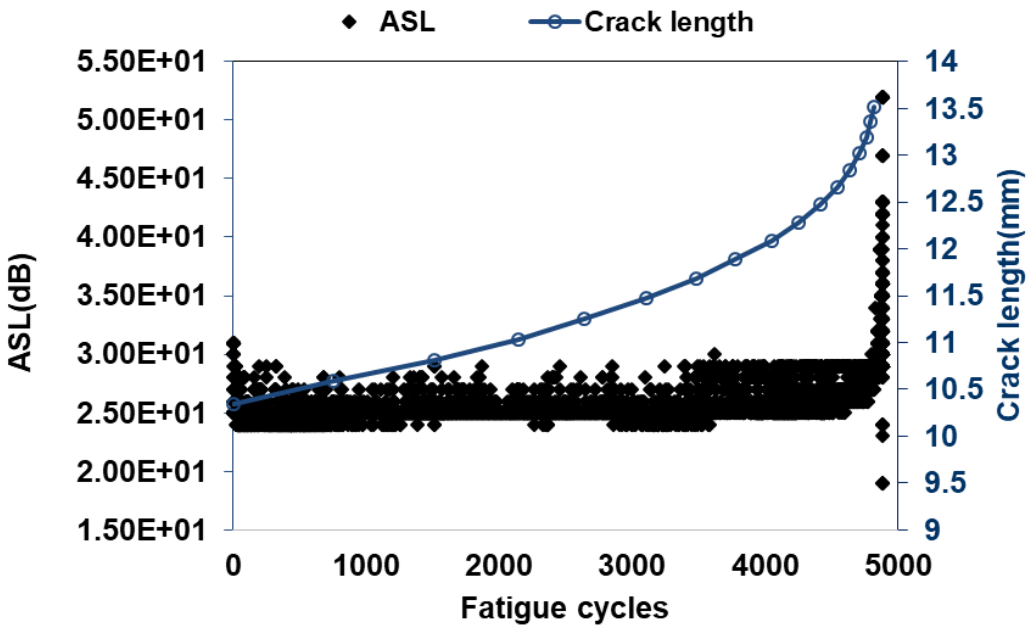
ASL
Crack length
5.50E+01
5.00E+01
4.50E+01
4.00E+01
3.50E+01
3.00E+01
2.50E+01
2.00E+01
1.50E+01
ASL(dB)
14
13.5
13
12.5
12
11.5
11
10.5
10
9.5
9
Crack length(mm)
0
1000
2000
3000
4000
5000
Fatigue cycles

e)

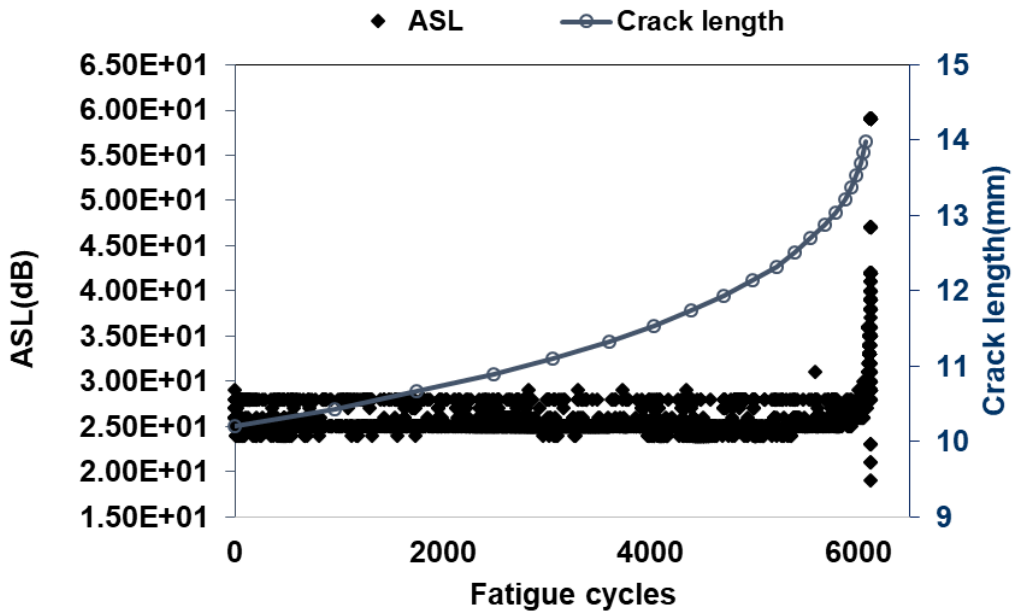
ASL
Crack length
6.50E+01
6.00E+01
5.50E+01
5.00E+01
4.50E+01
4.00E+01
3.50E+01
3.00E+01
2.50E+01
2.00E+01
1.50E+01
ASL(dB)
15
14
13
12
11
10
9
Crack length(mm)
0
2000
4000
6000
Fatigue cycles

f)

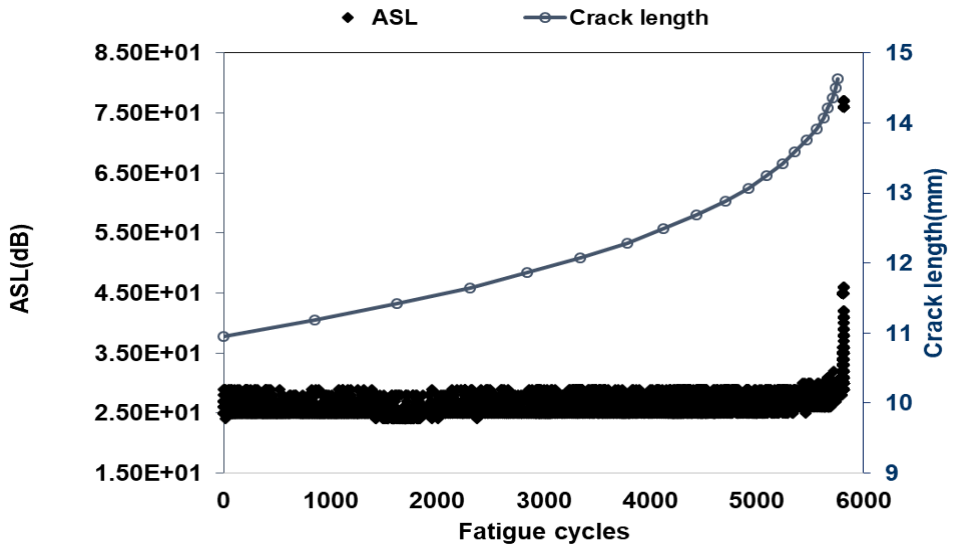
ASL
Crack length
8.50E+01
7.50E+01
6.50E+01
5.50E+01
4.50E+01
3.50E+01
2.50E+01
1.50E+01
ASL(dB)
15
14
13
12
11
10
9
Crack length(mm)
0
1000
2000
3000
4000
5000
6000
Fatigue cycles

g)

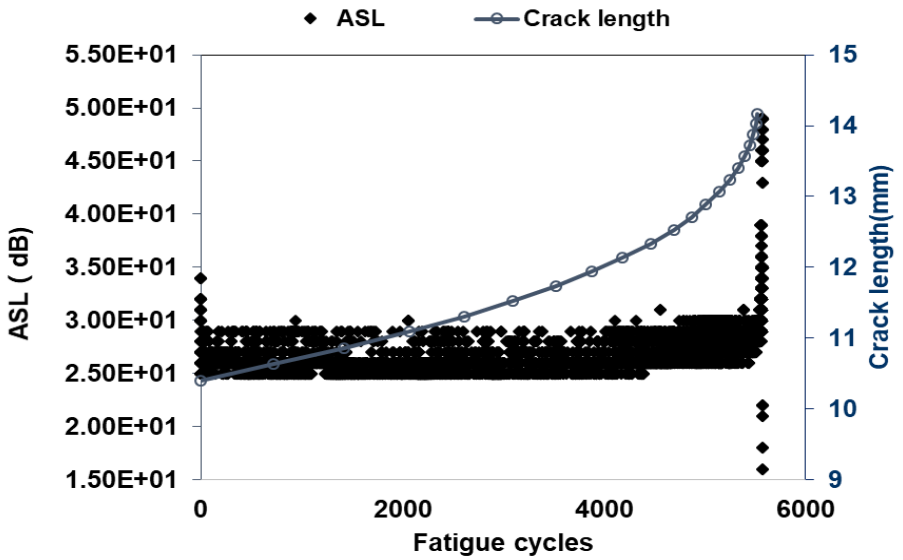

h)

Figure 7-11: AE ASL with number of fatigue cycles with crack growth in mm for rail steel a) sample 1, b) sample ,2 c) sample 3, d) sample 4, and Hadfield steel e) sample 1, f) sample 2, g) sample 3, h) sample 4.

One additional R260 steel sample cut from the used rail section was tested in three-point bending fatigue mode with an ESH servo-hydraulic universal testing machine. This sample had the same geometrical dimensions as the other four R260 rail steel samples, but the notch depth was kept to only 2mm with 30 angle. It was also pre-cracked using a Vibrophore to an initial crack length of 3 mm. The maximum load in this case was set at 9kN. The loading ratio and frequency was set at 0.1 and 10 Hz, respectively. The AE measurement threshold in this case was set to 55 dB. The sample was pre-cracked to 1 mm before the test. Figure 7-12 shows the correlation between the AE signal amplitude and measured crack length. A sudden increase in crack growth at the later stage of the test is associated with a sudden increase in the cumulative energy together with higher

amplitude AE signals. Points a, b and c in Figure 7-13 indicate the points where a sudden increase in the cumulative AE energy takes place. SEM observation of the fractured surface of the sample was subsequently carried out using a JEOL 6060. The captured SEM micrographs show evidence of cleavage fracture at the regions where sudden increment of cumulative energy occurs and are in good agreement with the AE data.

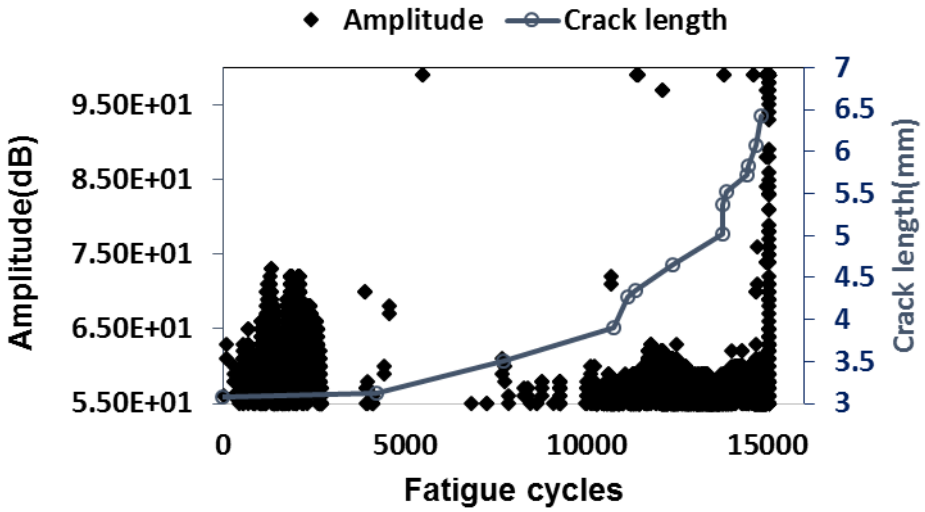

Figure 7-12: AE signal amplitude in dB versus number of fatigue cycles with crack growth in mm for the additional sample cut from used rail section.

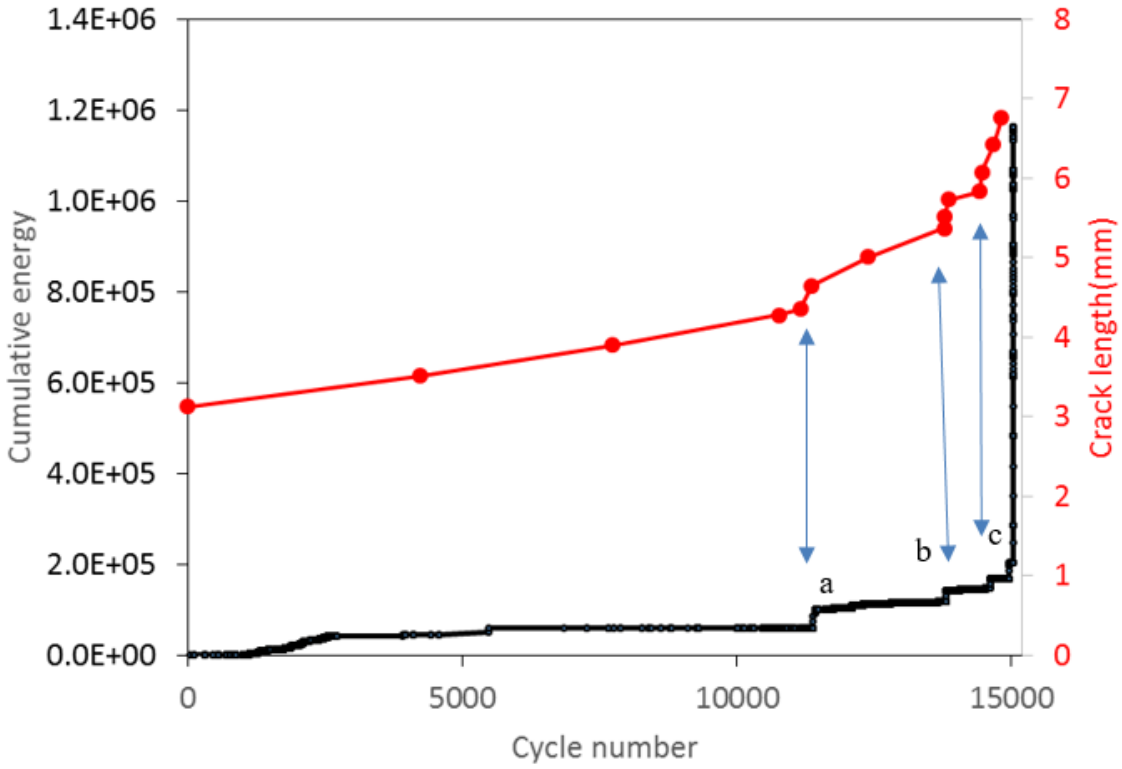

Figure 7-13: Comparison between cumulative energy and crack length with cycle number

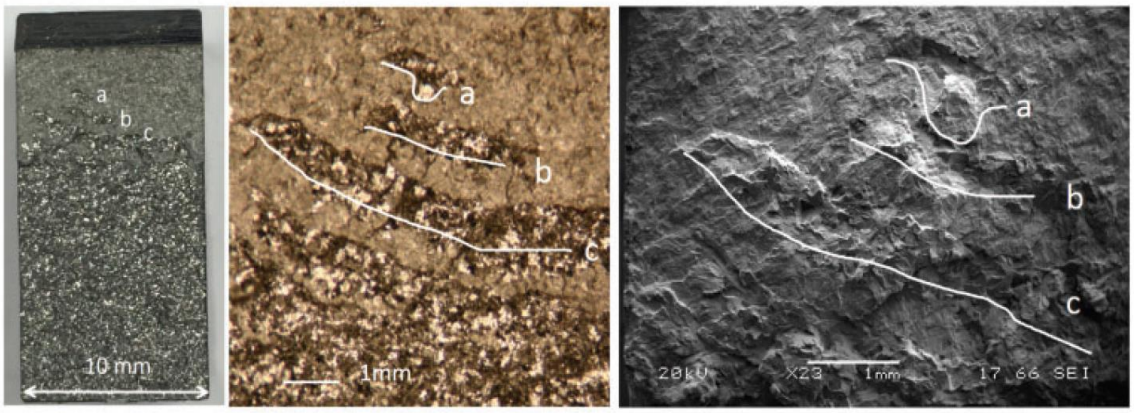

Figure 7-14: Fracture surface of R260 steel sample showing clear evidence of cleavage fracture

The ‘false’ emissions caused by hydraulic flow, friction noise, etc, can distort the genuine trend of energy rate versus time. To evaluate and impair the influence of noises generated during the test, a modified Swansong II Filters were employed to remove those ‘false ‘emission based on the characteristics of waveforms from PLB and actual tests on the reference sample. The basic principal behind the Swansong II Filters is that the generally duration of the hits generated from crack growth should increase with their amplitude. Table 7-3 shows the modified Swansong II Filters employed in the current results for the Hadfield steel sample in terms of duration and amplitude. Figure 7-15 shows the original energy rate, filtered energy rate and crack growth rate versus time for Hadfield sample 1. It can be seen that the energy rate trend after the filter being applied is quite similar to the original one and it has proved that the influence of The energy rates are generally consistent with that of crack growth rate, apart from the higher values in the initial stage. They still exist even after the filtering, suggesting that they may be caused by the extra contribution of residual stress relaxation in the plastic zone ahead of the notch tip induced in the fatigue pre-cracking process. The higher energy rates in the initial stages were also found for the other Hadfield samples.

Table 7-3: the modified Swansong II filter [152]

Duration/μs	Amplitude/dB
>1000	<53
>2000	<55
>3000	<58
>4000	<60
>5000	<63
>7000	<70
>8000	<80

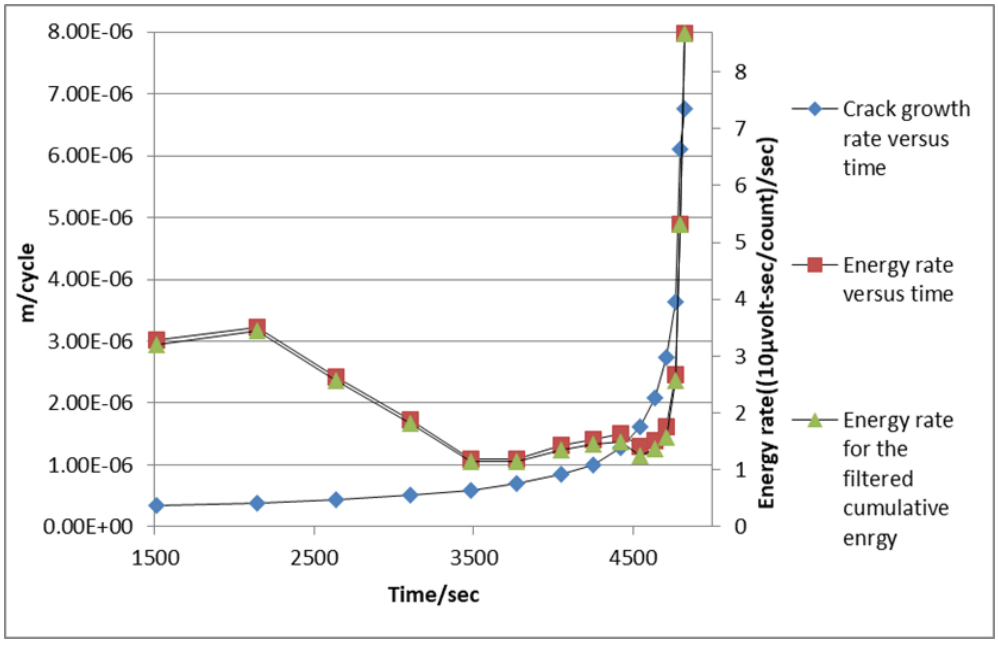

Figure 7-15: Original energy rate, filtered energy rate and crack growth rate versus time for Hadfield sample 1.

7.1.3 Analysis of AE signals captured from customized system

Figure 7-16 shows the trend of peak-peak amplitude, overall RMS, kurtosis, skewness, crest factor with measurement /time for one Hadfield steel sample during three-point bending fatigue testing under low frequency condition. A ten-second long AE measurement was taken every 5 minutes and then as the tested progressed every 1 minute at a sampling rate of 1 MSamples/s using the customised AE system. The RMS shows a clear upward trend with some fluctuations also observed especially in the early stage. However, it is not sufficient to accurately assess the severity of the damage, as it cannot reflect the other features of the captured data. Therefore, it is crucial to take into account the trend of different parameters to make AE signal evaluation effective. The trend of the other parameters has higher fluctuation in the early and middle stage with sudden increase or decrease occurring at the twentieth measurement (around 2000 cycles before final failure of the sample). The trend of peak-peak, kurtosis, crest factor in the late stage is generally consistent with that for RMS, whereas skewness exhibit decreasing trends. However, the highlighted sudden change in different parameters, which could be used as alarm for the final failure, is not reflected by the RMS results. The initial fluctuation of the parameters may be attributed to the influence of bulk (notch) plasticity on crack growth. The highest values for all the parameters are observed at the late stage of the test.

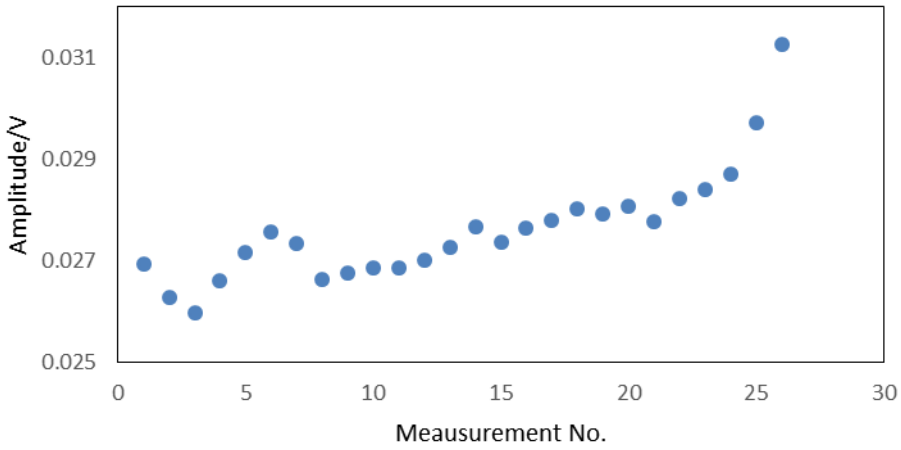
0.031
0.029
0.027
0.025
Amplitude/V
0
5
10
15
20
25
30
Meausurement No.

a)

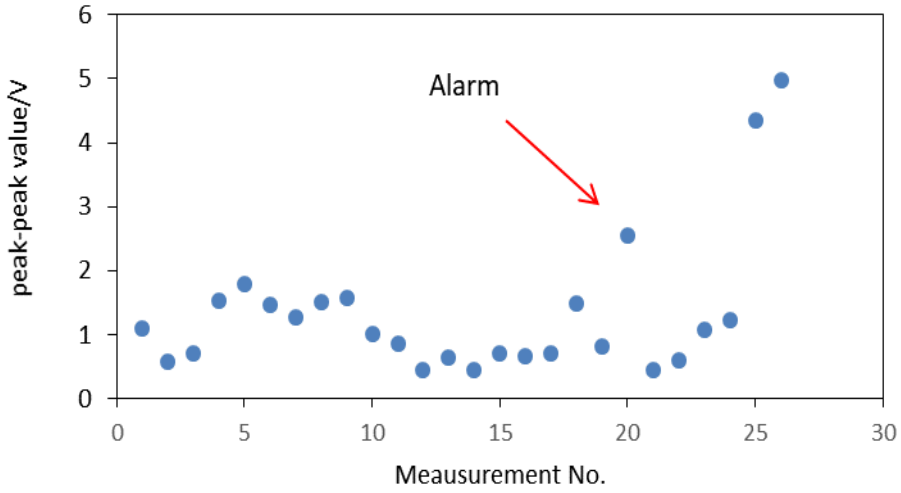
6
5
4
3
2
1
0
peak-peak value/V
Alarm
0
5
10
15
20
25
30
Meausurement No.

b)

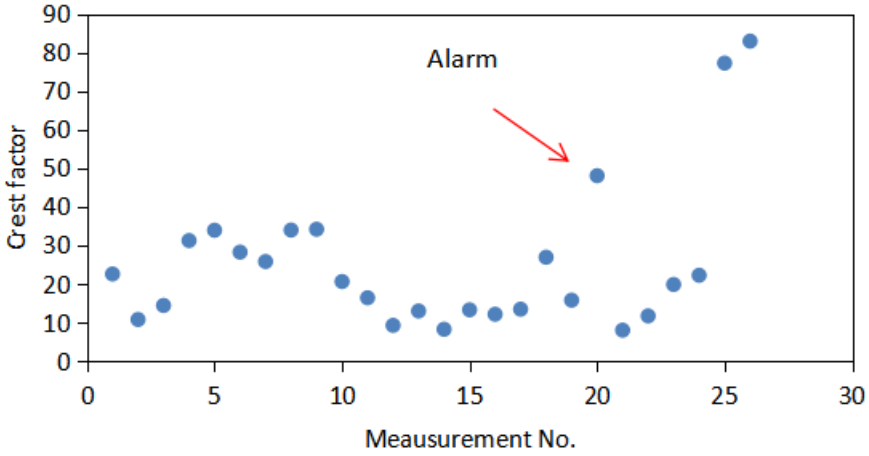
Alarm
Crest factor
Meausurement No.
0
10
20
30
40
50
60
70
80
90
0
5
10
15
20
25
30

c)

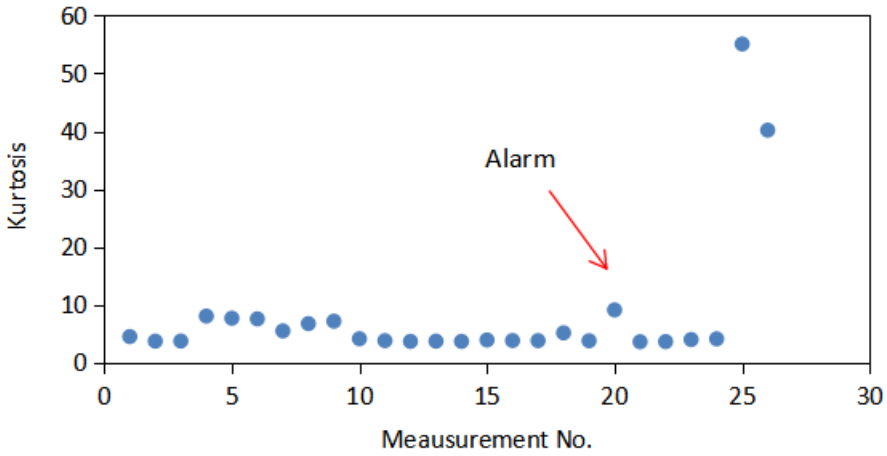
Alarm
Kurtosis
Meausurement No.
0
10
20
30
40
50
60
0
5
10
15
20
25
30

d)

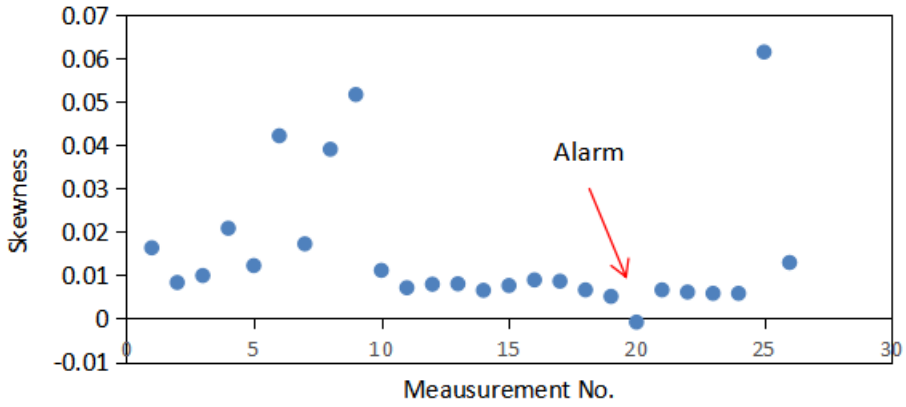

e)

Figure 7-16 : Trend of a) RMS b) peak-peak value c)crest factor d)kurtosis e) skewness during the test

Figure 7-17 shows the raw AE signal for the reference carbon steel sample captured using the customised AE system during a 10 sec period. The sinusoidal loading pattern can be obviously reflected by the waveforms. During the loading stage the signal gradually increases and drops back to background noise level during the unloading stage. This increase is associated with the bending moments and the hydraulic pump controlling the load cell. As it can be seen, there are no obvious peaks related to crack growth events. The captured signals are purely caused by the cyclic loading and can be considered as periodic deterministic signals, which are non-stationary in nature. The only few small peaks represent random noise during the acquisition. The maximum amplitude is far less than the saturation voltage of 10 V. Few peaks are related to the noise generated from the servo-hydraulic mechanism. The peak-peak value is around ±0.11V.

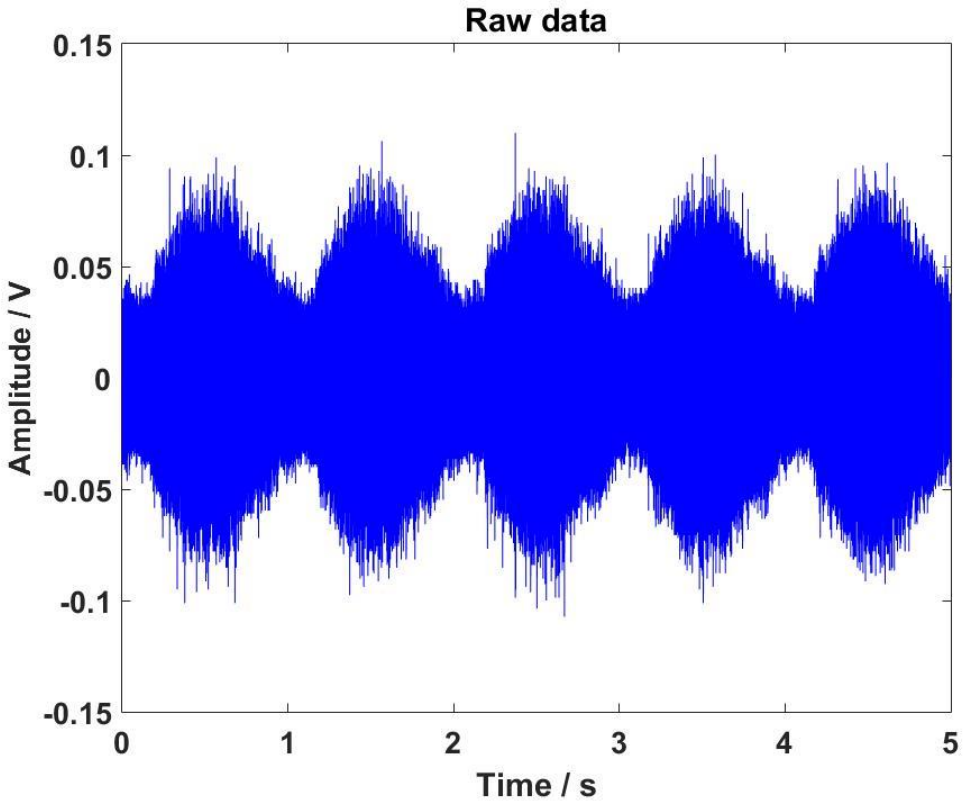

Figure 7-17: The raw AE signal for the reference sample within a 5-sec acquisition window.

Figure 7-18 shows the raw AE signal from the one of the second set of R260 rail steel samples recorded using the customised AE system at the early stage of the fatigue test. Clear peaks related to crack growth event can be seen. The maximum amplitude of these peaks related to crack growth reaches ~0.5 V.

Figure 7-19 shows the raw data for the same sample at a later stage where the crack growth rate has increased further. The amplitude of the peak related to crack growth is higher in comparison with the previous signal. However, multiple peaks attributed to crack faces closing and rubbing against each other can also be observed. The amplitude is even higher than that related to crack growth, which can be misleading. Crack closure and surfaces rubbing at later stage also cause the crack growth occur closer to peak value

of the loading cycle than the earlier stage as shown by the red arrows in zoomed-in sections.

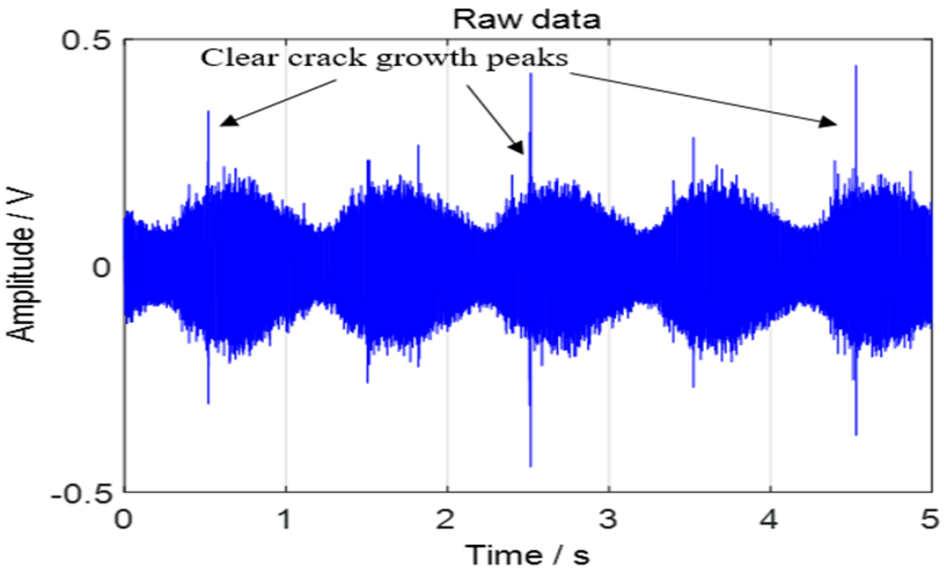

a)

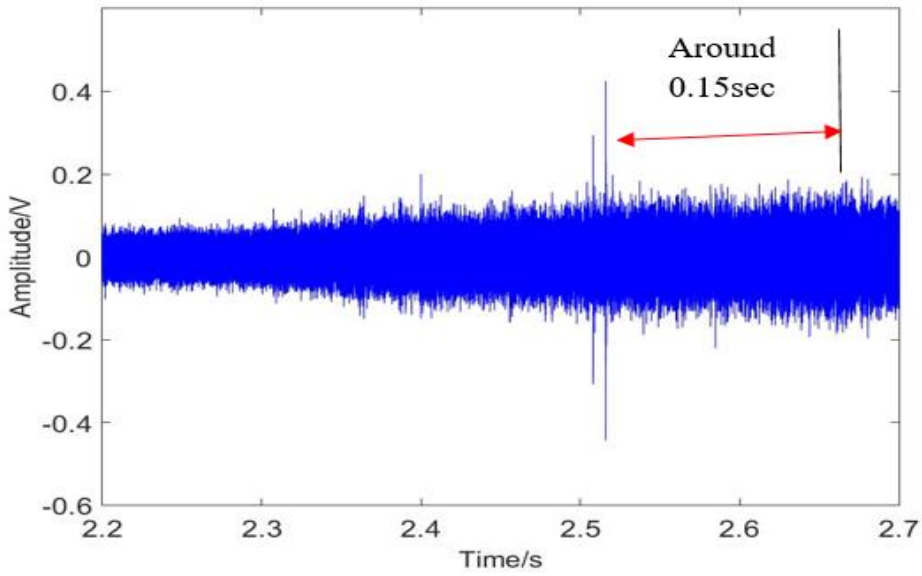

b)

Figure 7-18: a)Raw AE data and b)zoomed-in section for the R260 rail steel sample at an earlier stage during 5-sec acquisition window

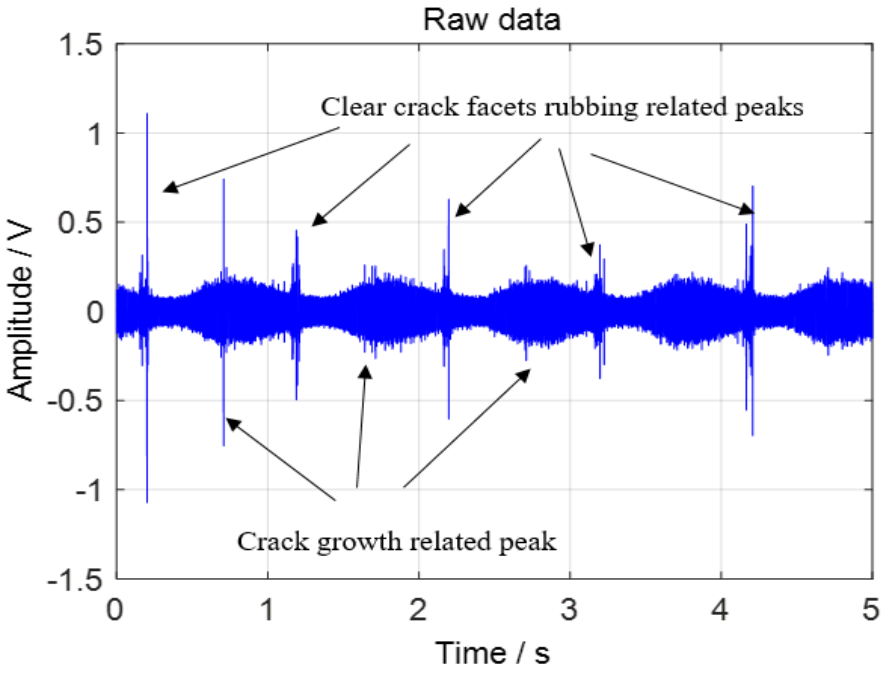

a)

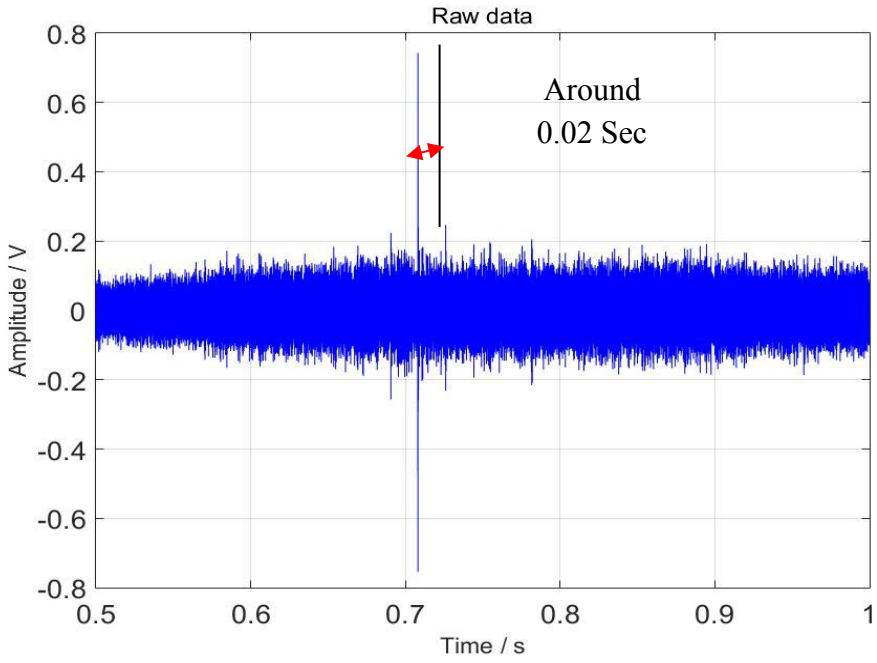

b)

Figure 7-19: a)Raw AE data and b)zoomed-in section for the 260 rail steel sample at a later stage during 5-sec acquisition window.

Figure 7-20 through Figure 7-22 show three templates selected from the waveform in Figure 7-19(a). Templates selected from the raw data which contains the crack growth related peak and crack closure related peak are both of burst type and in this case clearly it is impossible to differentiate these two types of signals just based on time domain analysis. The templates size is 5000 points.

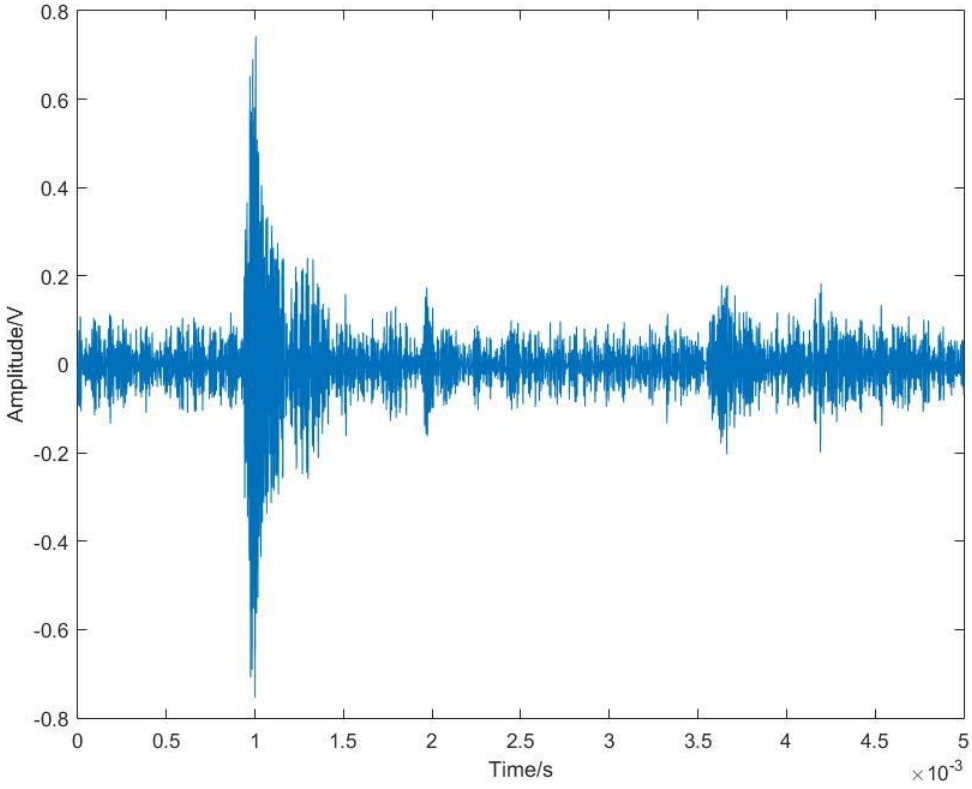

Figure 7-20: Template 1 related to crack growth

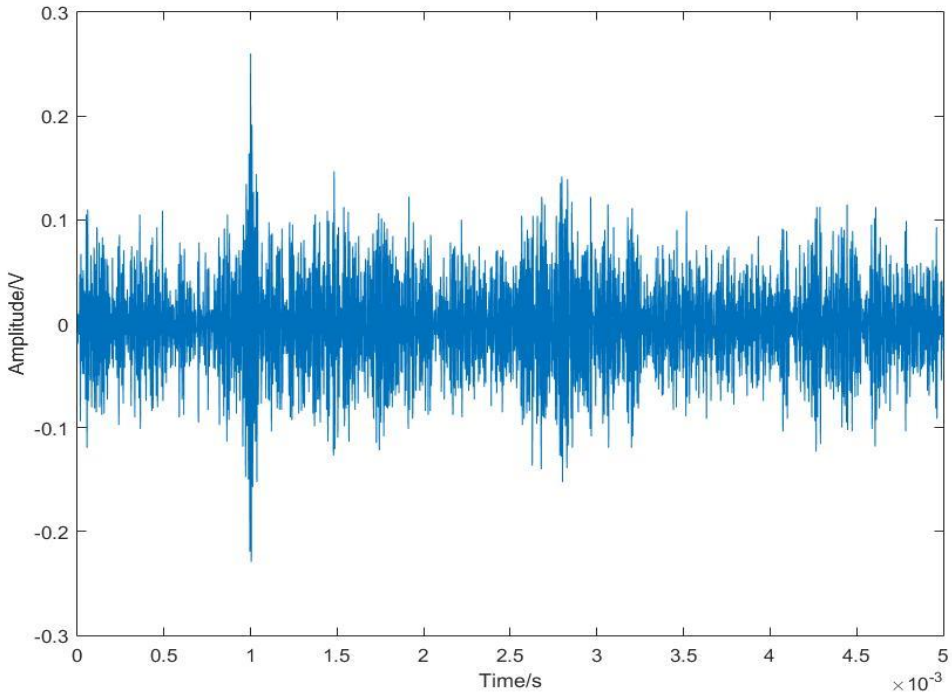

Figure 7-21: Template 2 related to crack growth

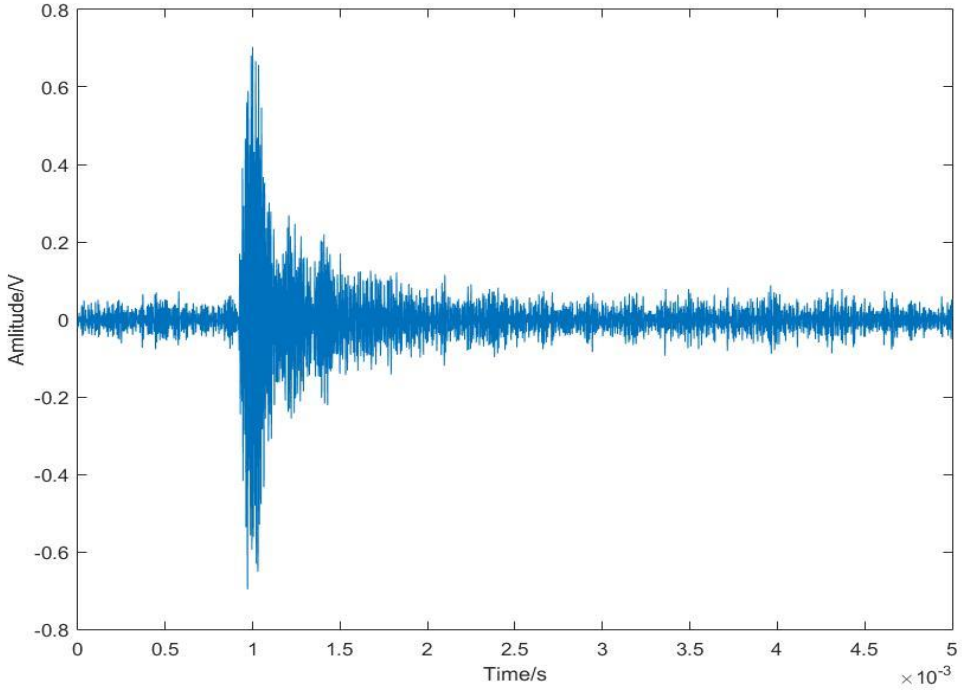

Figure 7-22: Template 3 related to crack closure

FFT analysis has been proven to be a valid tool for determining the source mechanisms of the captured AE signals. Analysis based on normalized FFT comparison between different windows containing these peaks was carried out in this case as shown in Figure 7-23. The FFT results are normalized, so the influence of signal intensity on the comparison is eliminated. As it can be seen, for crack faces closing and rubbing related peaks, the dominant frequency has a lower value as expected for mechanical noise related signals. However, the power spectrum for the two waveforms containing crack growth related peaks show similar dominant frequency at a higher value.

Figure 7-24 shows the original signal at the initial stage from one Hadfield steel sample (sample 1 in the analysis of data captured by the commercial system). Once again，the peaks signifying crack growth events can be clearly identified. Peak attributed to crack faces rubbing can also be observed, however, its intensity is smaller than that of crack growth related ones.

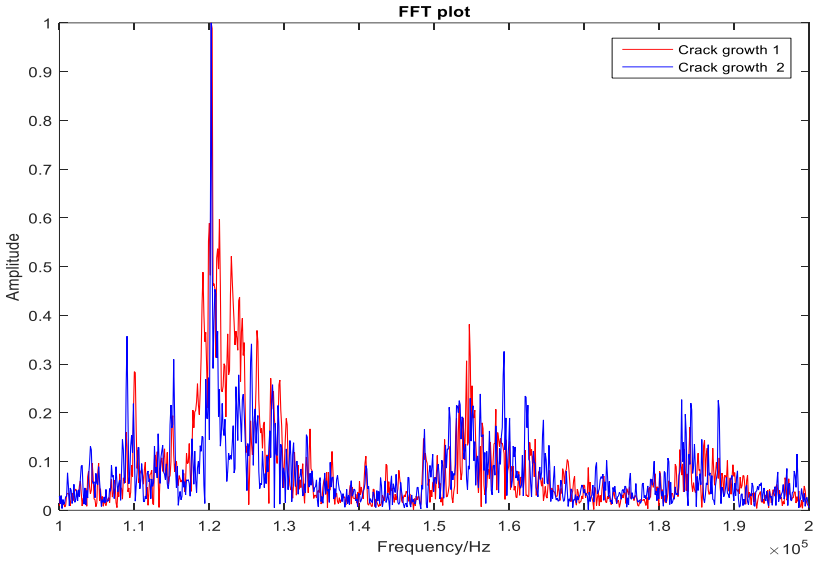

a)

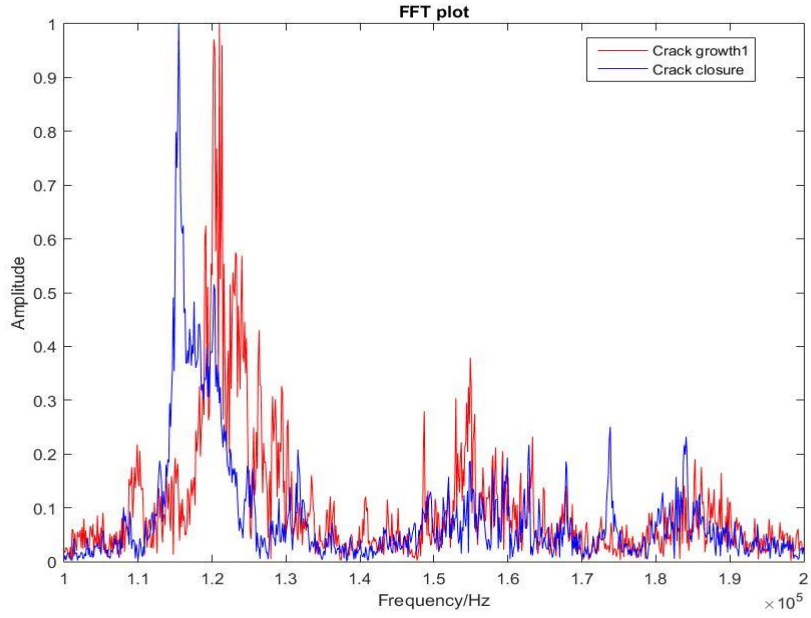

b)

Figure 7-23 :Normalized FFT comparison between a) two raw waveforms containing crack growth related peaks b) raw waveform containing crack growth related peak and raw waveform containing crack closure related peak

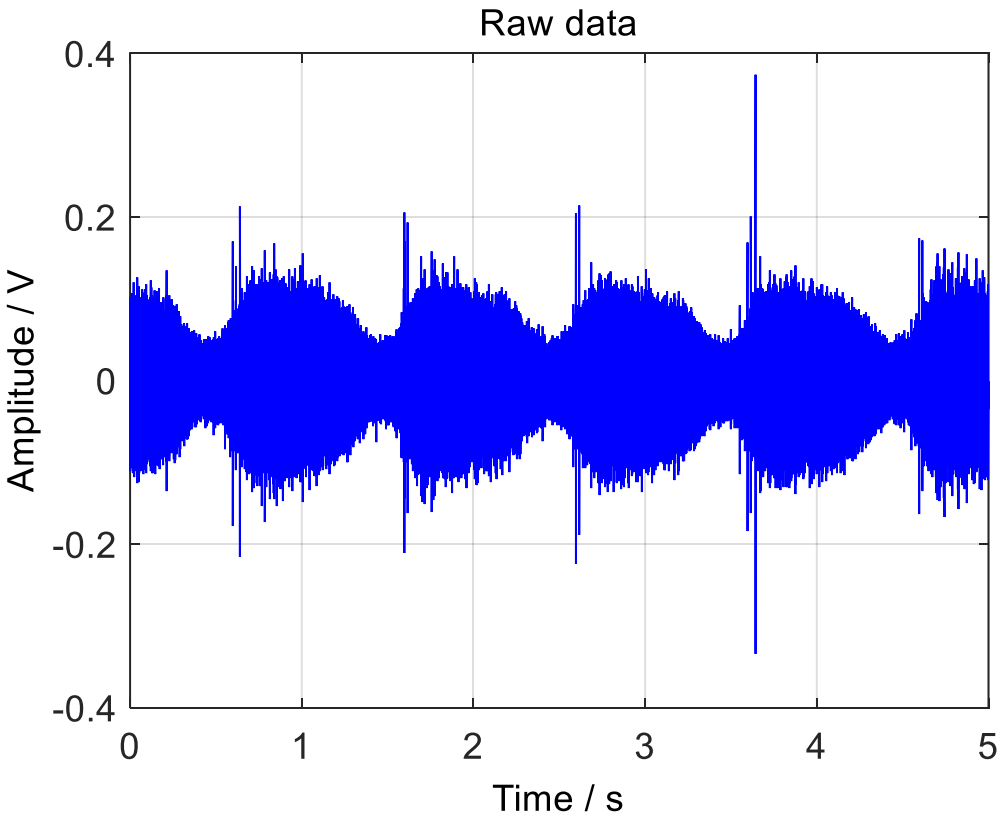

Figure 7-24: Raw AE data for the Hadfield steel sample during 5-sec acquisition at early stage.

Figure 7-25 shows the original signal from the same sample at the middle stage. Some more obvious spikes can be found and the peak amplitude is around 0.9 V, suggesting the crack grew at an accelerating rate. More peaks related to crack facets rubbing can be observed, however their intensity is still smaller than that of crack growth relate ones.

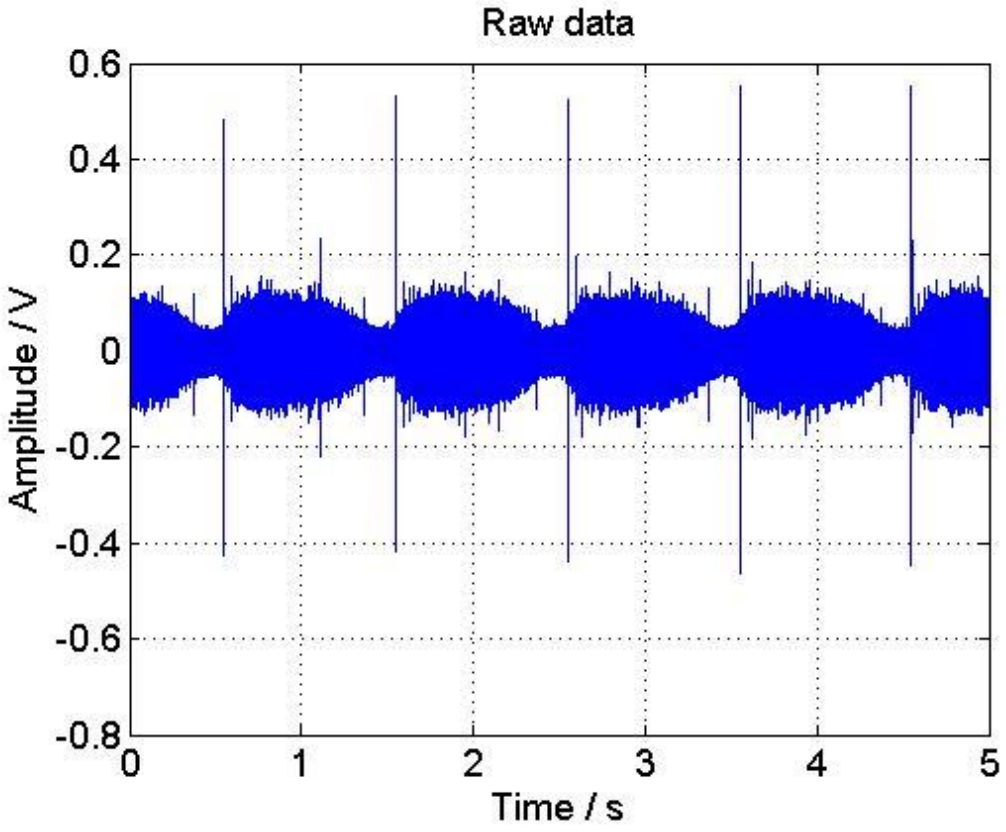

Figure 7-25: Raw AE data for the Hadfield steel sample during 5-sec acquisition at stage 2 (middle stage).

Figure 7-26 shows the signal captured at a stage which is very close to the final failure of the same sample. The peak amplitude reached the saturation value of the system (10 V) and the ratio of signal to noise is very high, suggesting that the final sample fracture is imminent. It is worth mentioning that during the final stage, the static mode is also complementary to striation growth mode and this can cause the crack to grow extremely quick, releasing high energy during a short time period.

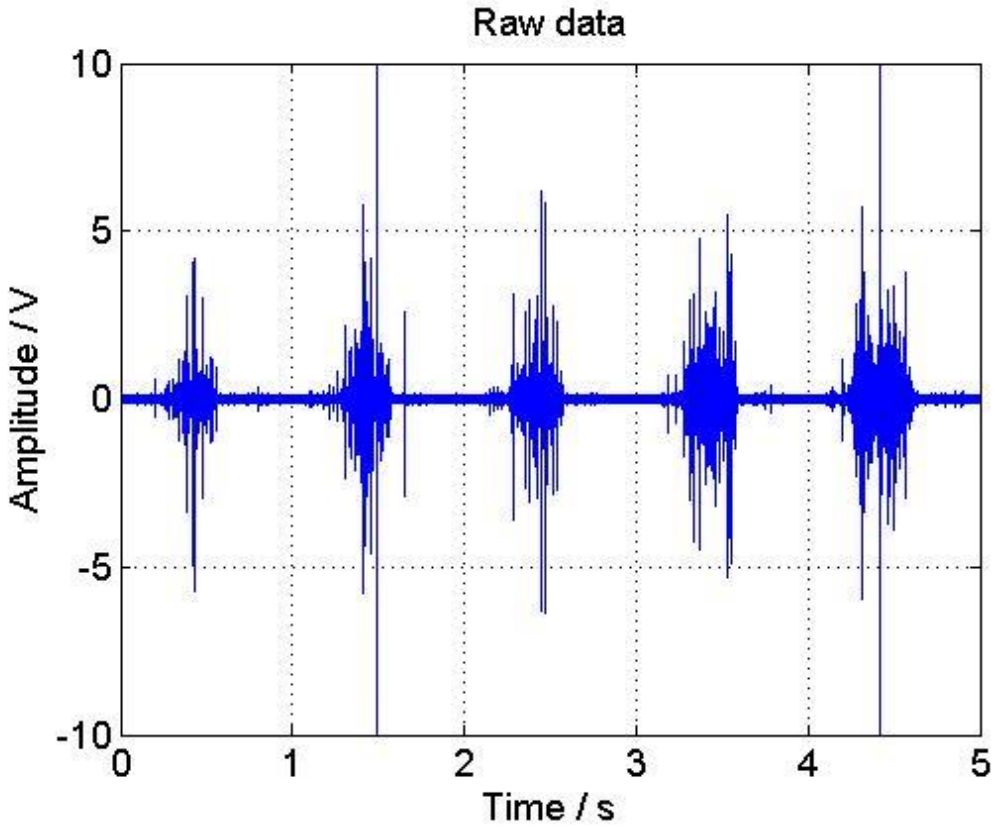

Figure 7-26: Raw AE dataset for the Hadfield steel sample at late stage (near final failure) during 5-sec window.

Figure 7-27 through Figure 7-29 show signal analysis for the reference sample and both types of steel samples for the raw data shown above in an overlapping mode during fatigue tests. The window size is 1000 with overlapping set as 500. The selection of window size is based on the characteristics of AE hits captured using the commercial system. For the reference sample, clearly no obvious peak related to crack growth can be found in the moving RMS analysis. Moving crest factor and skewness analysis is consistent with moving RMS，whereas moving kurtosis shows a big peak at around 3.2 sec, which might be caused by random noise during the loading process. For R260 rail steel sample, moving RMS analysis successfully reveals the accelerated crack growth during the test. Both moving crest factor and kurtosis analysis do not show the consistent

results. This might be caused by the smaller time difference between crack growth related peak and external loading related peak at later stage due to the effect of crack surfaces rubbing and crack closure as shown in Figure 7-18 and

Figure 7-19 , which can weaken the influence of higher crack growth related peak on the result of crest factor and kurtosis. For skewness analysis, AE data at both stages show fairly symmetric distributions (skewness between 0.5 and -0.5) [153]. For Hadfield steel samples, moving RMS at different stages can clearly reflect the integrity is deteriorating for the sample. Moving kurtosis, crest factor in this case show consistent result as RMS. More significant differences can be observed between different stages by comparing the kurtosis values. It is also noteworthy that the amplitude does not necessarily attain the maximum in the window corresponding to the maximum kurtosis value, which is reasonable given the fact that kurtosis characterizes the distribution shape. In comparison to the middle stage, the values of moving crest factor peaks at the final stage increase sharply, although the maximum value does not show the same amount of increase as that for moving kurtosis. Moderately skewed distributions (skewness between −1 and −½ or between +½ and +1) and highly skewed distributions (skewness less than −1 or greater than +1) as defined in[153] are observed for middle and late stage ,respectively.

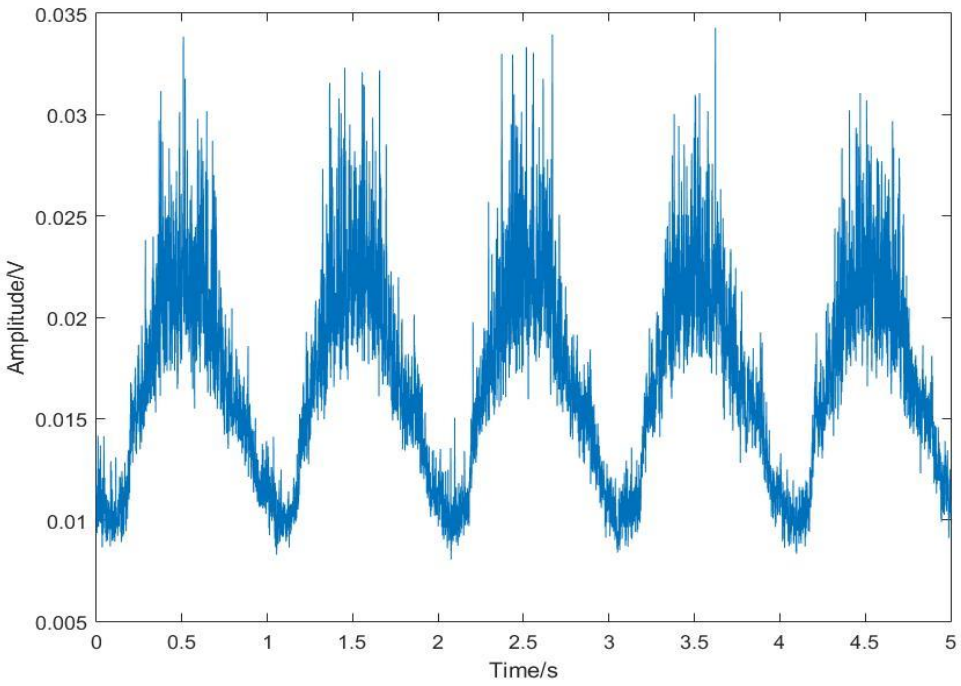
0.035
0.03
0.025
0.02
0.015
0.01
0.005
Amplitude/V
0
0.5
1
1.5
2
2.5
3
3.5
4
4.5
5
Time/s

a)

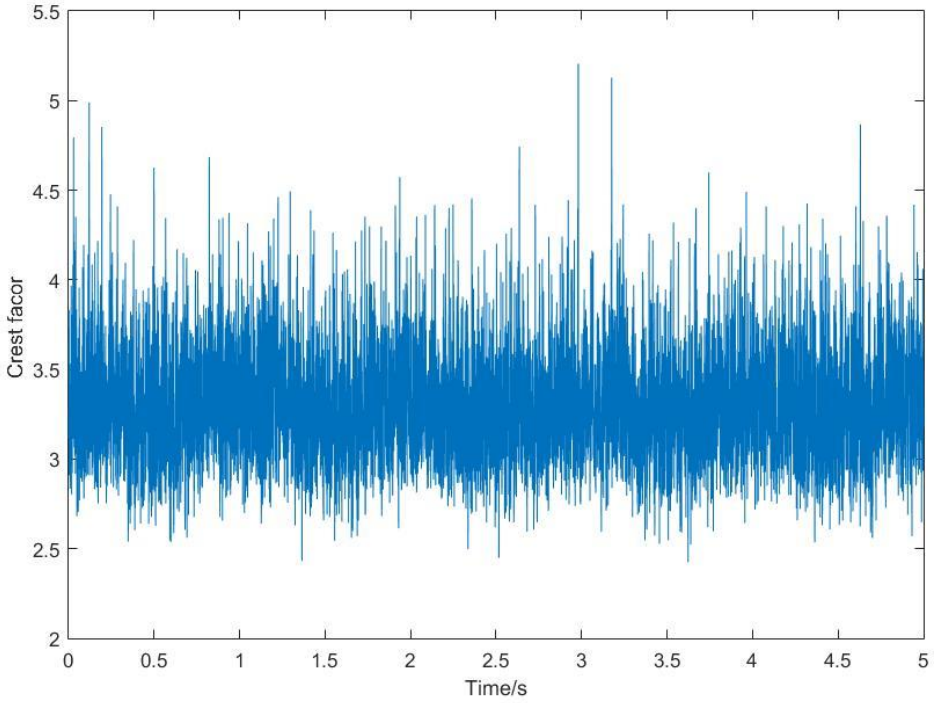
5.5
5
4.5
4
3.5
3
2.5
2
Crest facor
0
0.5
1
1.5
2
2.5
3
3.5
4
4.5
5
Time/s

b)

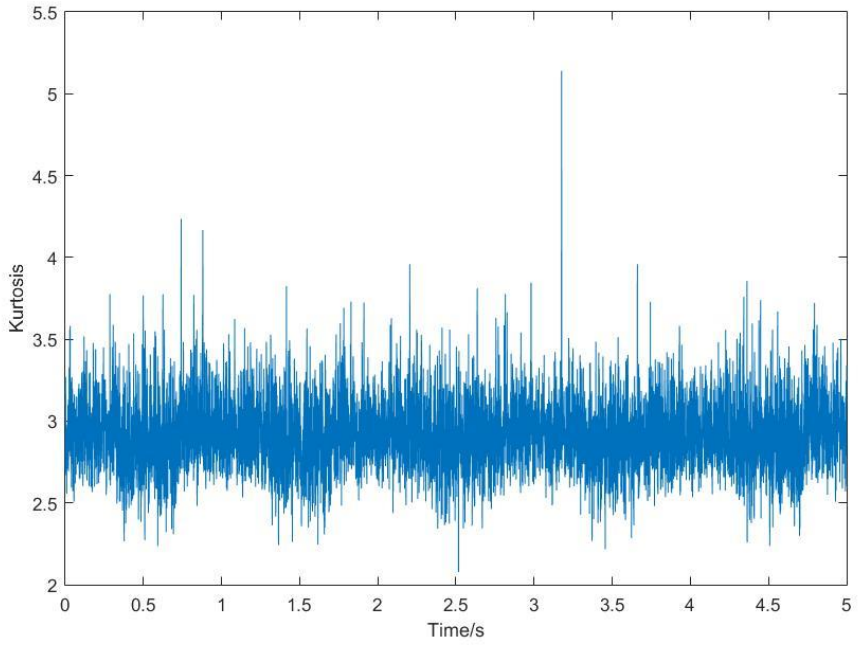

c)

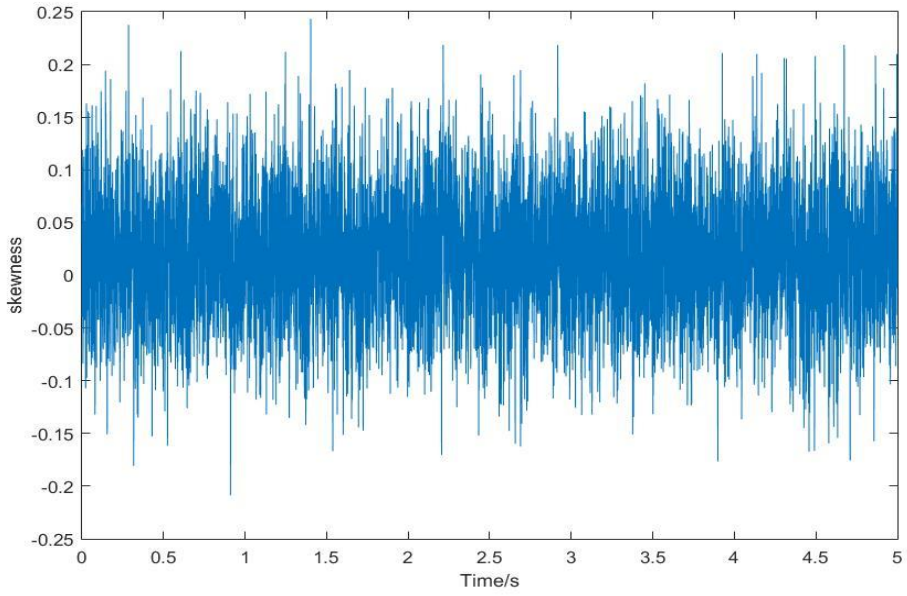

d)

Figure 7-27: AE Data for the reference sample with no crack growth happening for a) moving RMS b) moving crest factor c) moving kurtosis d) moving skewness

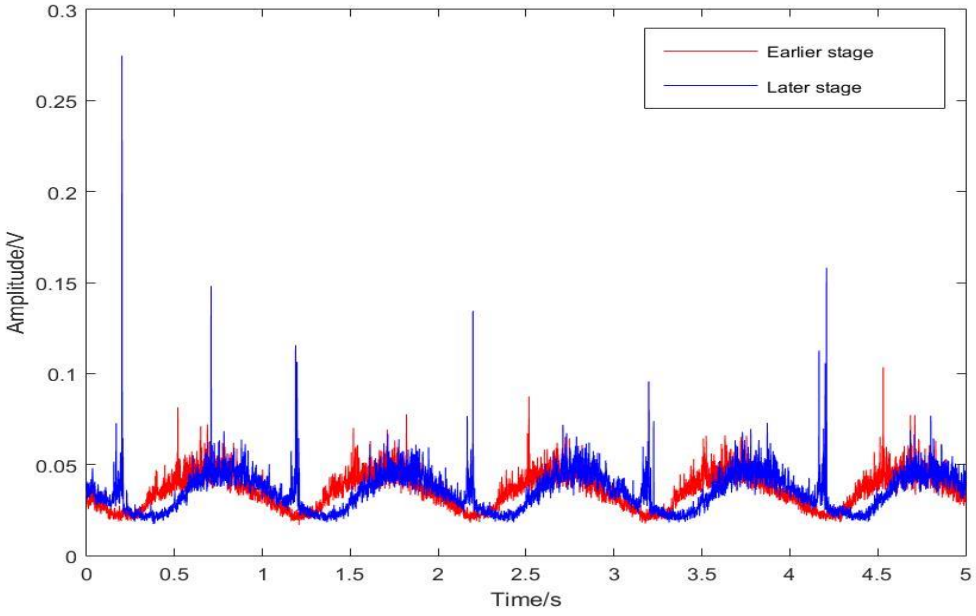
Earlier stage
Later stage
Amplitude/V
Time/s
0.3
0.25
0.2
0.15
0.1
0.05
0
0
0.5
1
1.5
2
2.5
3
3.5
4
4.5
5

a)

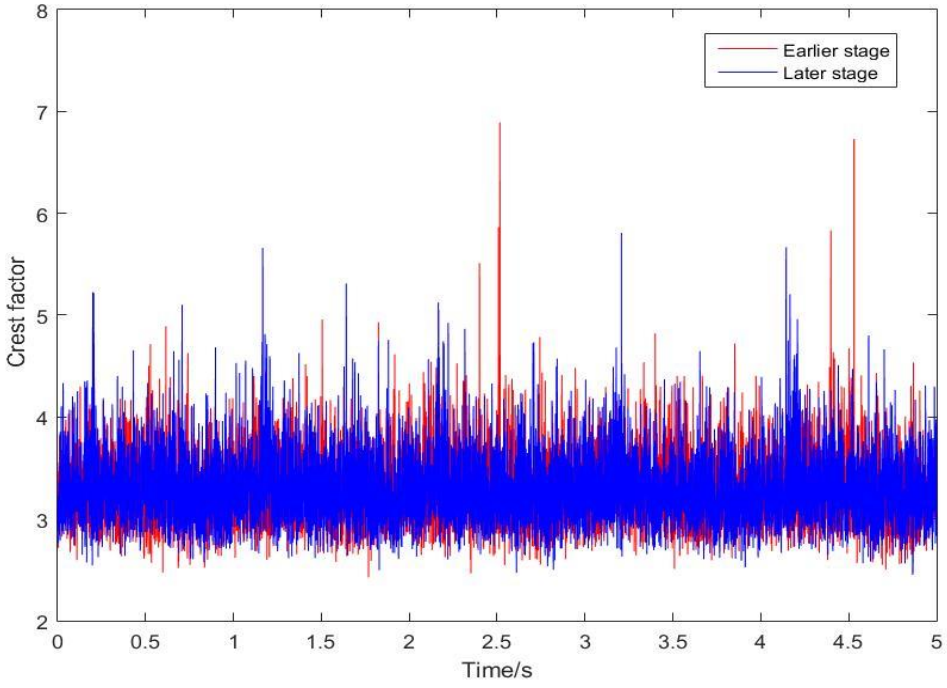
Earlier stage
Later stage
Crest factor
Time/s
8
7
6
5
4
3
2
0
0.5
1
1.5
2
2.5
3
3.5
4
4.5
5

b)

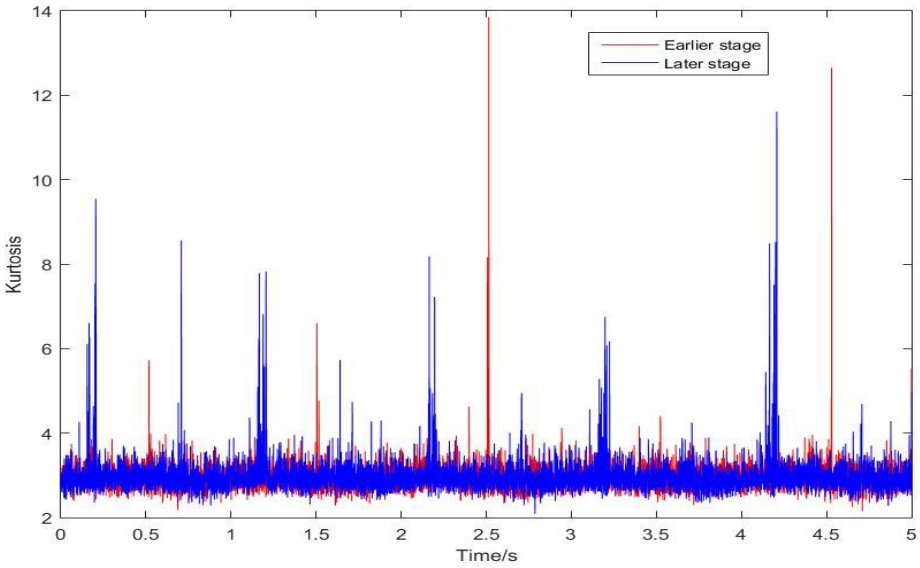

c)

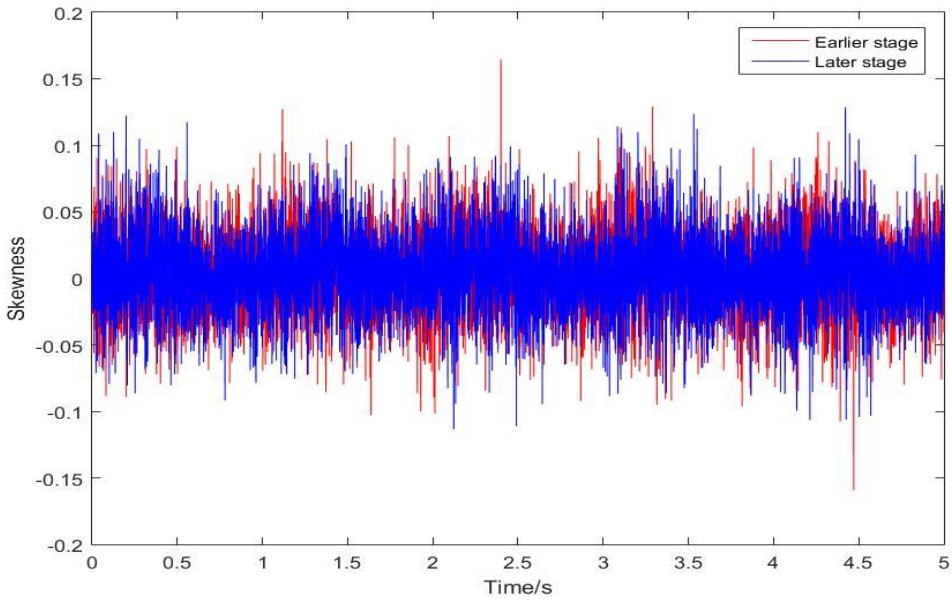

d)

Figure 7-28: Comparison between AE data for a) moving RMS b) moving crest factor c) moving kurtosis d) moving skewness at the earlier and later stage of the fatigue test for the R260 rail steel sample

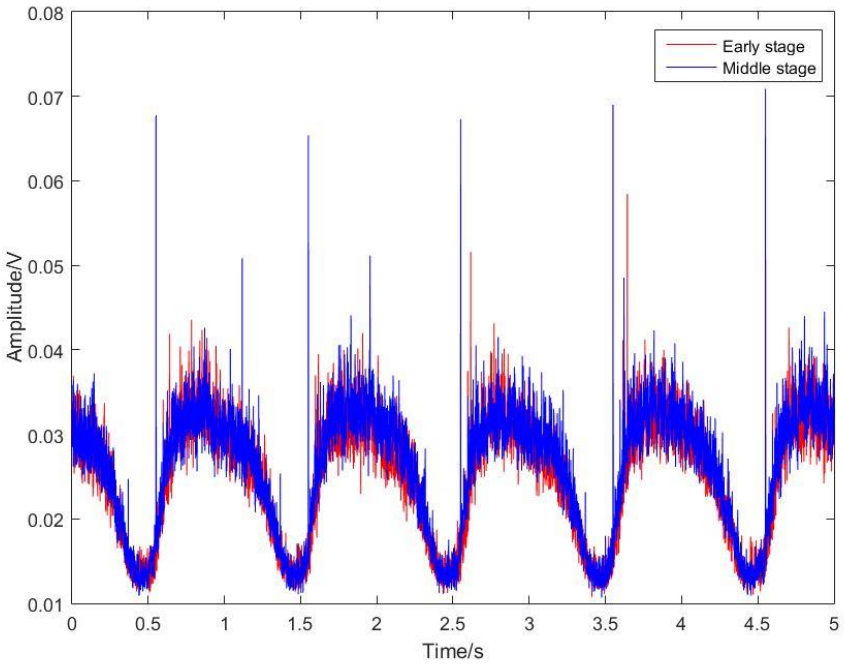
Early stage
Middle stage
Amplitude/V
Time/s
0.08
0.07
0.06
0.05
0.04
0.03
0.02
0.01
0
0.5
1
1.5
2
2.5
3
3.5
4
4.5
5

a)

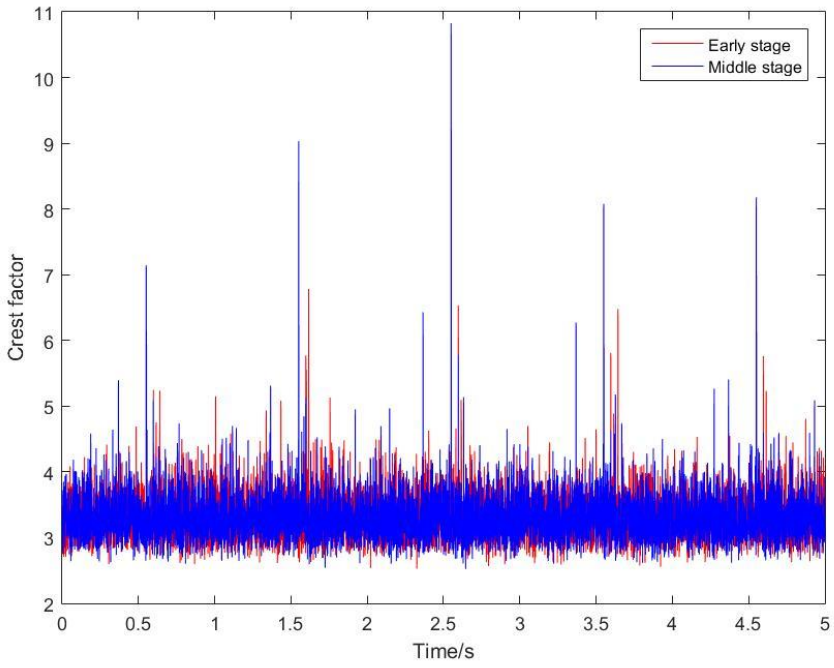
Early stage
Middle stage
Crest factor
Time/s
11
10
9
8
7
6
5
4
3
2
0
0.5
1
1.5
2
2.5
3
3.5
4
4.5
5

b)

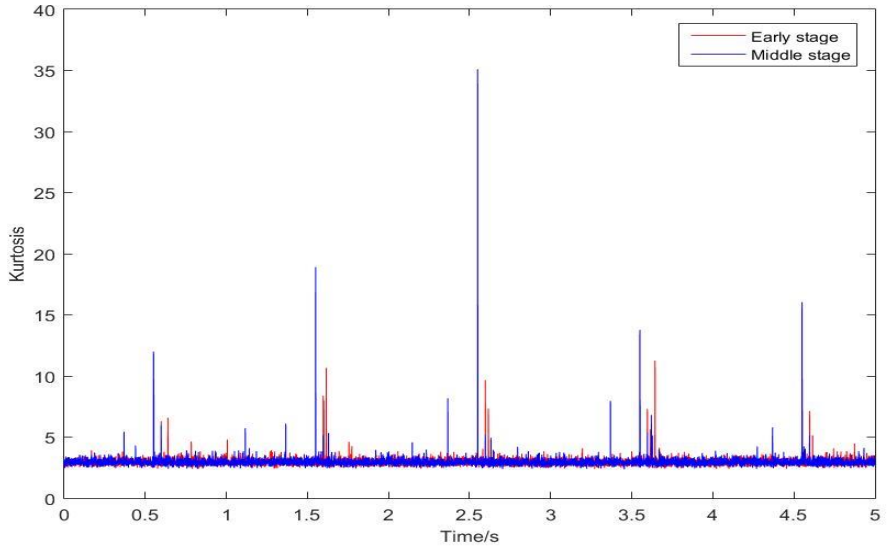

c)

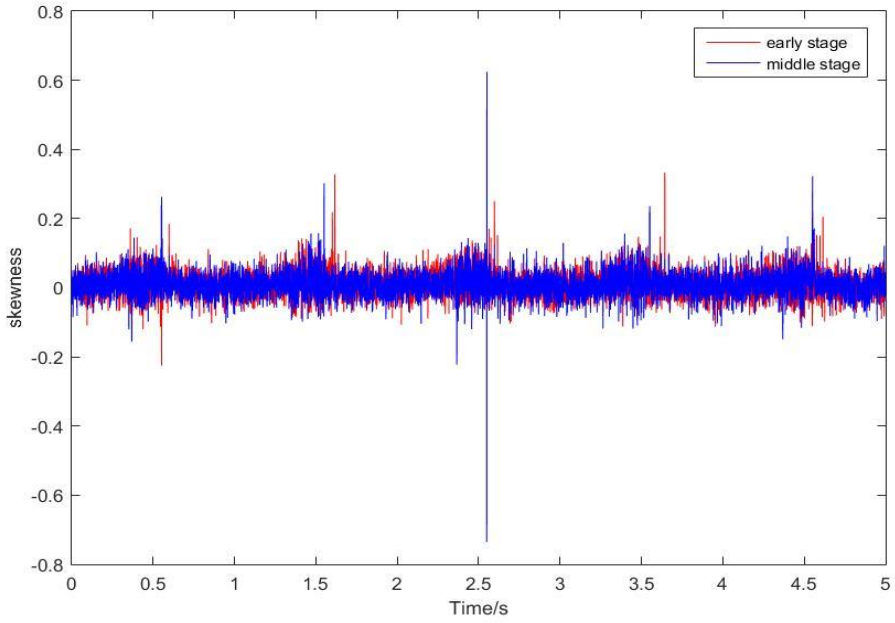

d)

Figure 7-29 : Comparison between AE data for a) moving RMS b) moving crest factor c) moving kurtosis d) moving skewness at the early and middle stage of the fatigue test for the Hadfield steel sample

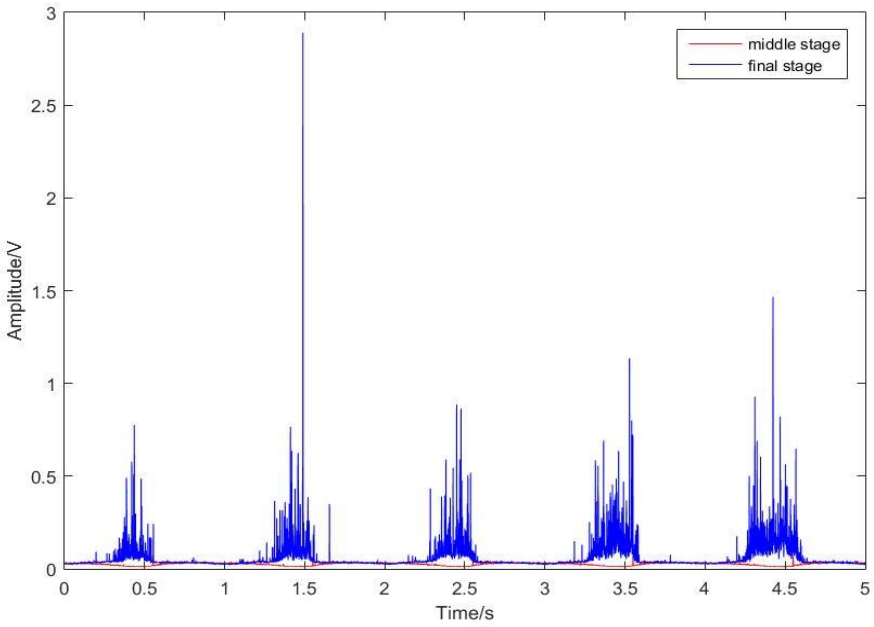
middle stage
final stage
Amplitude/V
Time/s
0
0.5
1
1.5
2
2.5
3
3.5
4
4.5
5

a)

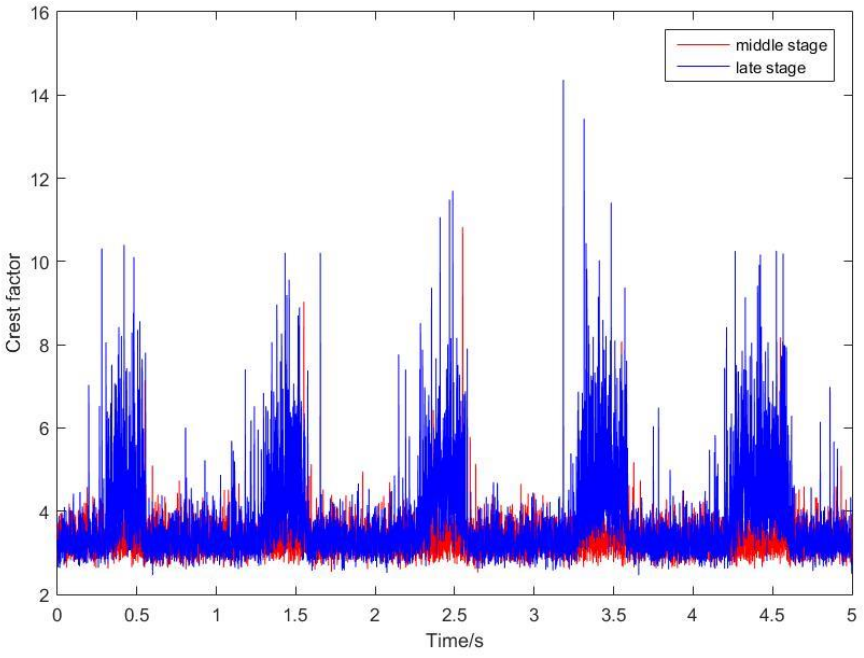
middle stage
late stage
Crest factor
Time/s
2
4
6
8
10
12
14
16
0
0.5
1
1.5
2
2.5
3
3.5
4
4.5
5

b)

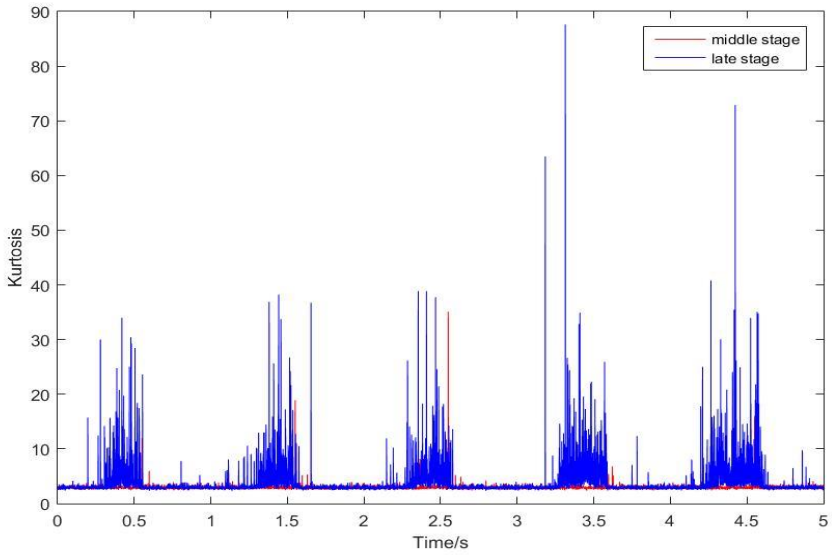

c)

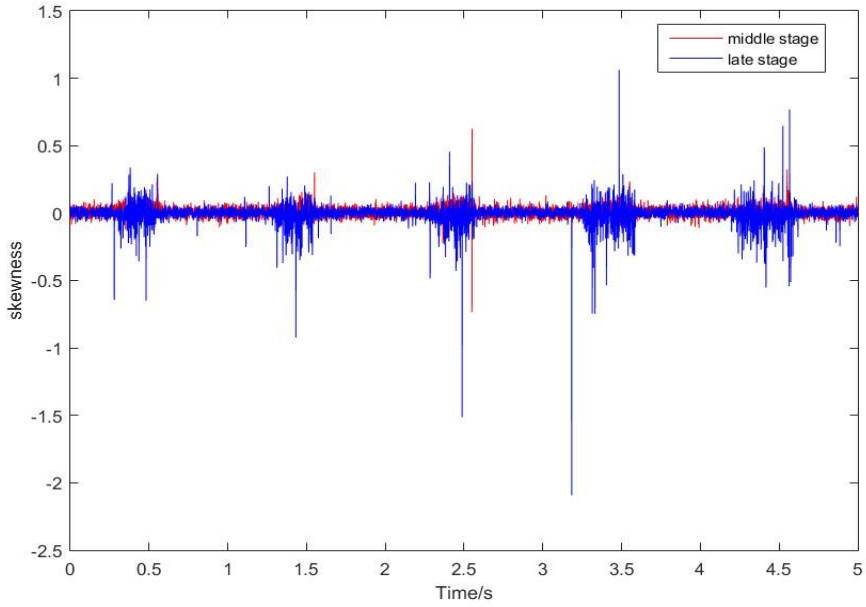

d)

Figure 7-30:Comparison between AE data for a) moving RMS b) moving crest factor c) moving kurtosis d) moving skewness at the middle and late stage of the fatigue test for Hadfield steel sample 1

In order to better characterise the signal, SK analysis was also carried out. SK is also the fundamental basis for designing an optimum band-pass filter as described later. The window span used for short time fourier transform is 100 μs. Figure 7-31 shows SK analysis for the raw data captured during the test on the reference sample. The unit frequency in this case is the sampling frequency 1MSamples/S. The SK value throughout most of the frequency range is very small (<1). Figure 7-32(a) shows the SK plots for the raw data captured at the earlier stage of fatigue test on R260 steel sample. It is clearly seen that the peaks have shifted towards higher frequencies and maximum peak value has increased considerably. For the data captured at later stage, the maximum SK value increases. However, due to the influence of crack surfaces rubbing and crack closure, the SK values vary heavily with frequencies.

It can be seen the peak value of SK increases from the early stage to the late stage for the chosen results for the cast manganese steel sample 1, suggesting the potential of using SK to monitor the damage degradation. For the R260 steel sample, the trend is similar. Further, when comparing the SK result for the R260 steel sample at later stage with that for cast manganese steel sample 1 at the middle stage, it can be seen that the peak value of the latter is much higher. This is further confirmed by the higher crack growth rate of Hadfield steel sample 1 in comparison with the R260 steel sample. However, the peak-peak value in the raw data for R260 steel sample at the later stage is higher. This has proven the better accuracy of detecting the damage evolution for SK than amplitude.

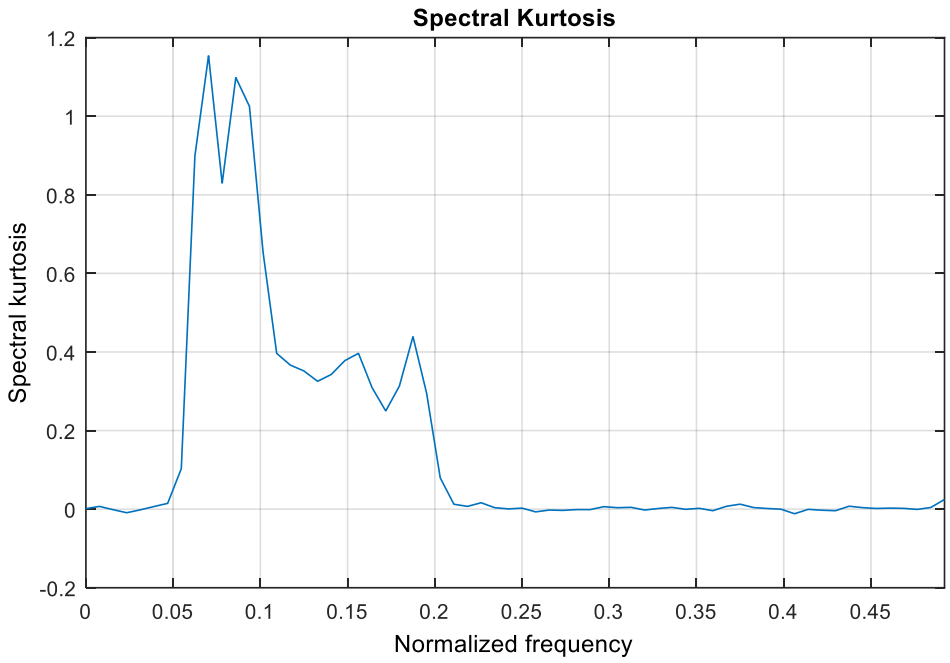

Figure 7-31 : SK versus normalized frequency for the reference sample

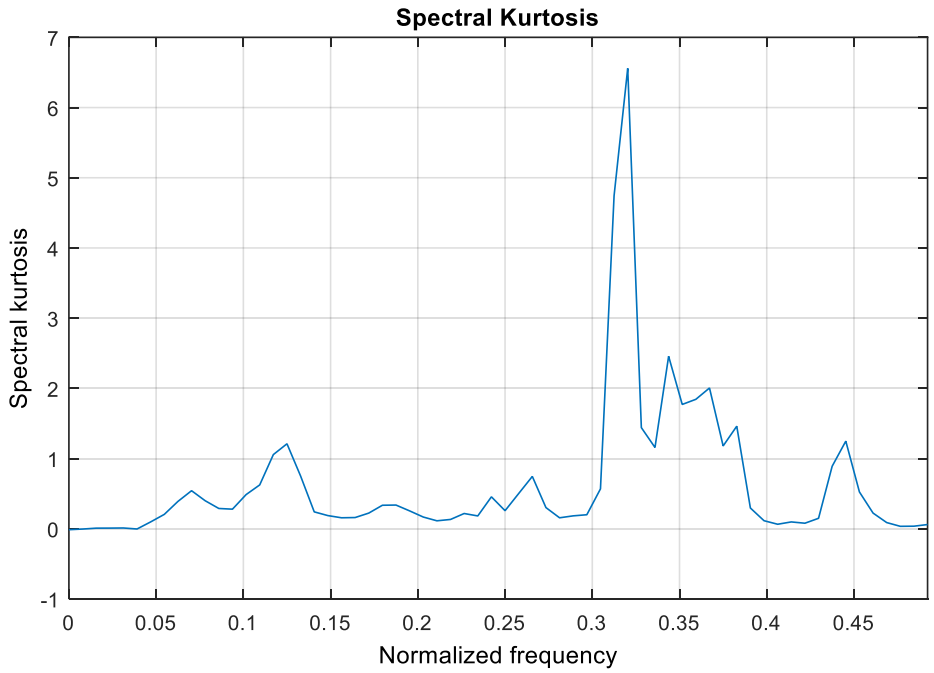

a)

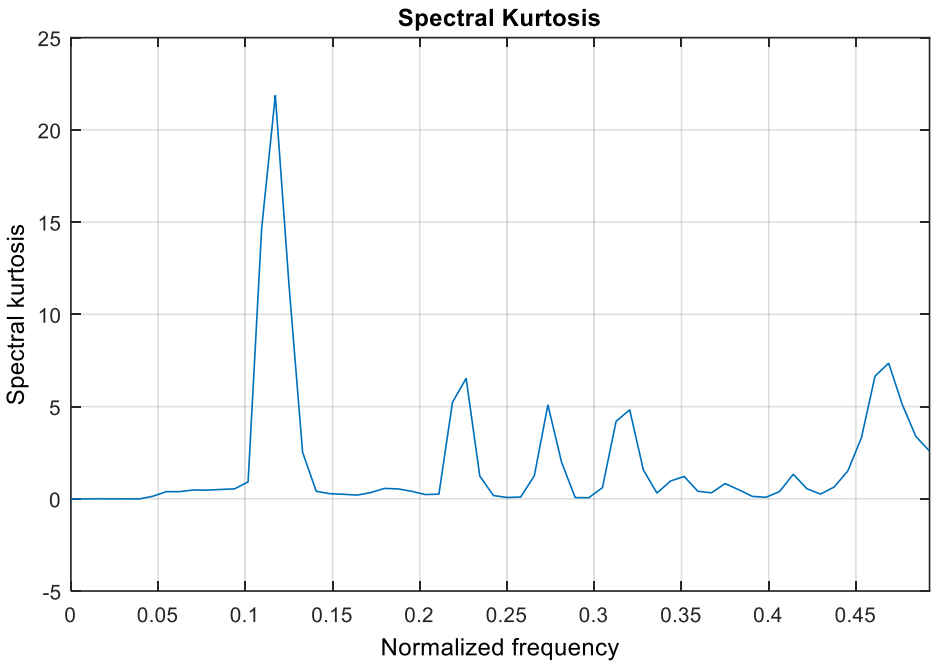

b)

Figure 7-32: SK versus normalized frequency for the R260 rail steel sample at the a) earlier stage b) later stage

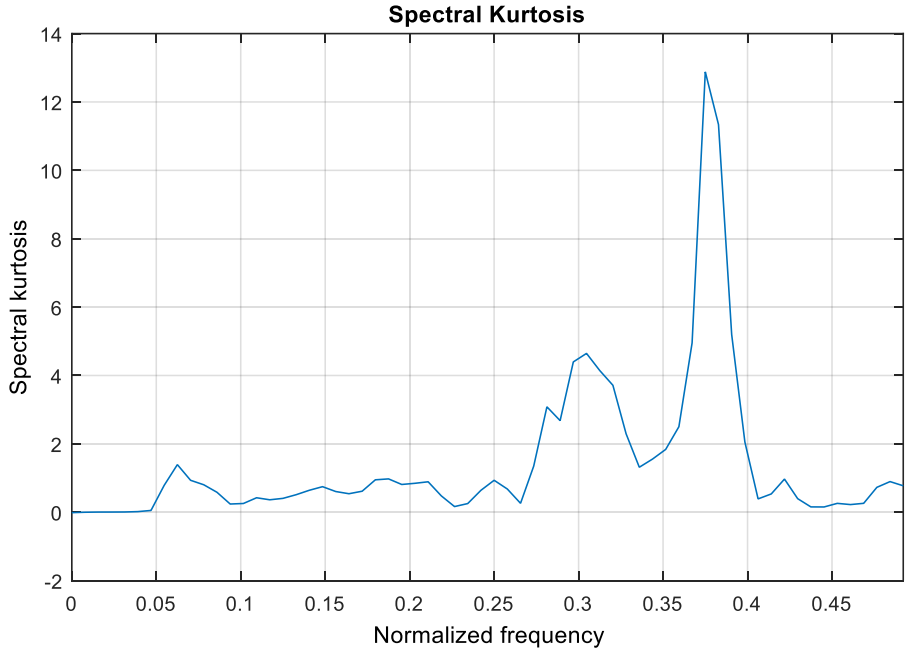

a)

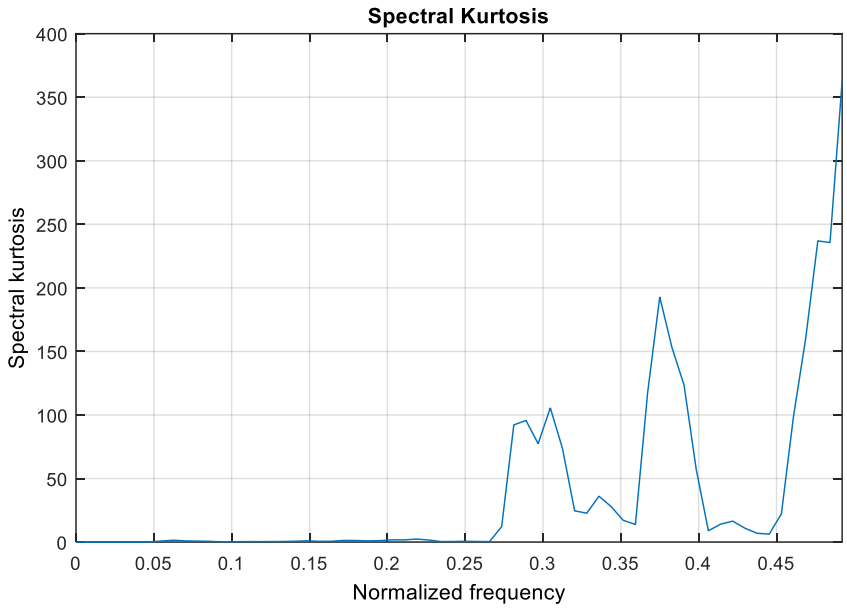

b)

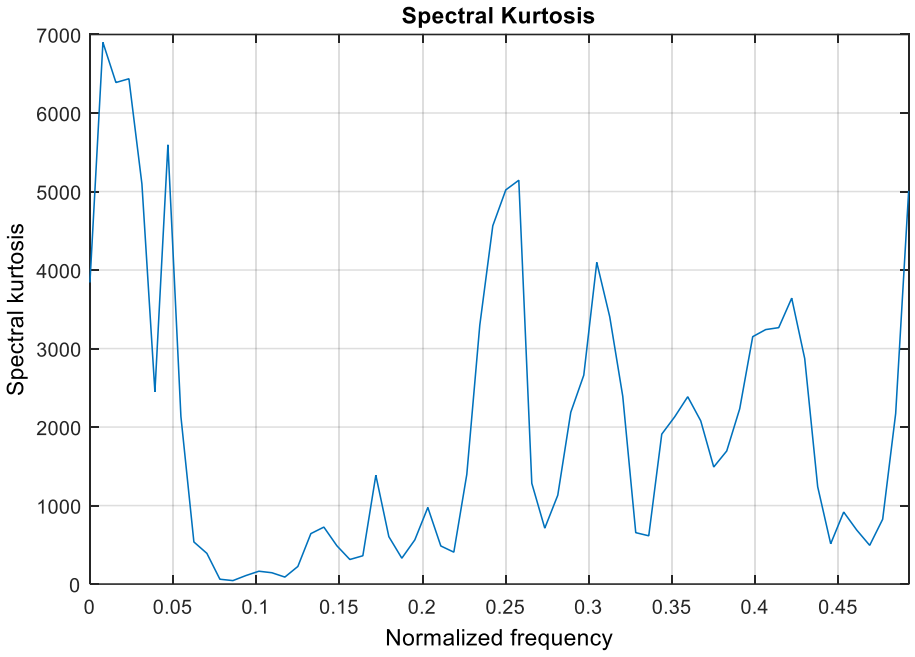

c)

Figure 7-33: Spectral kurtosis versus normalized frequency for the Hadfield steel sample at the a) early stage b)middle stage c) late stage

Once the noise reaches a higher level, especially in field condition, the defect signal can be masked. In this case certain filters can be used to remove or at least suppress the influence of the noise. Even though the noise level was not very high under the current laboratory testing condition, it is still worth to investigate the filtering effect.

Hence, the band-pass filter was designed based on the window size and centre frequency at which the SK attained the maximum. However, the window size in the above can not necessarily guarantee the SK was the maximum among all the possible choices. In this case, the Kurtogram developed by Antoni was employed to obtain the maximum SK and the corresponding window size Nw and center frequency [154]. The Kurtogram for the original dataset at the early stage for Hadfield steel sample 1 is as shown in Figure 7-34.

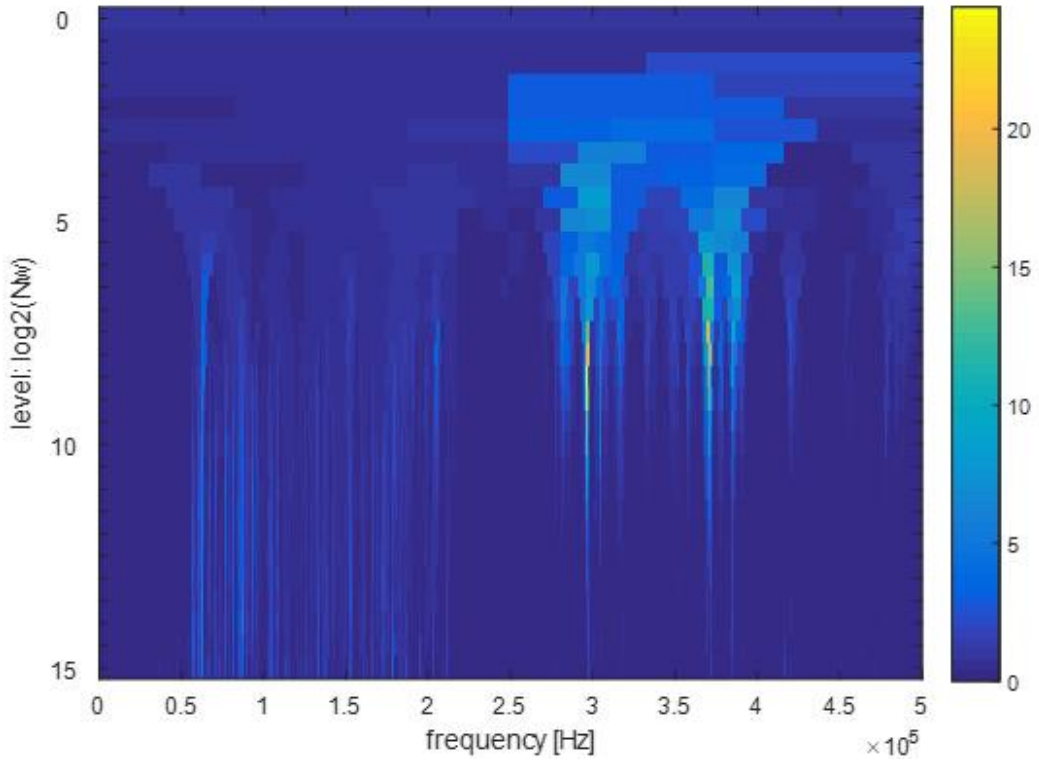

Figure 7-34: Kurtogram for the previous AE signal.

The Centre frequency and window size at which the maximum kurtosis can be obtained at all the stages for Hadfield steel sample 1 are shown in Table 7-4.

Table 7-4: Optimum Bandwidth and centre frequency for AE signal from manganese sample at different stages.

	Centre Frequency /Hz	$Log_2(Nw)$	Maximum kurtosis
Early stage	297526	8.5	24.4
Middle stage	476562	5	394.2
Late stage	10416	4.5	20049

Bandpass filter was designed based on the centre frequency and the window size Nw as shown in the above table and the filtered waveforms for the Hadfield samples at the three stages are shown in Figure 7-35.

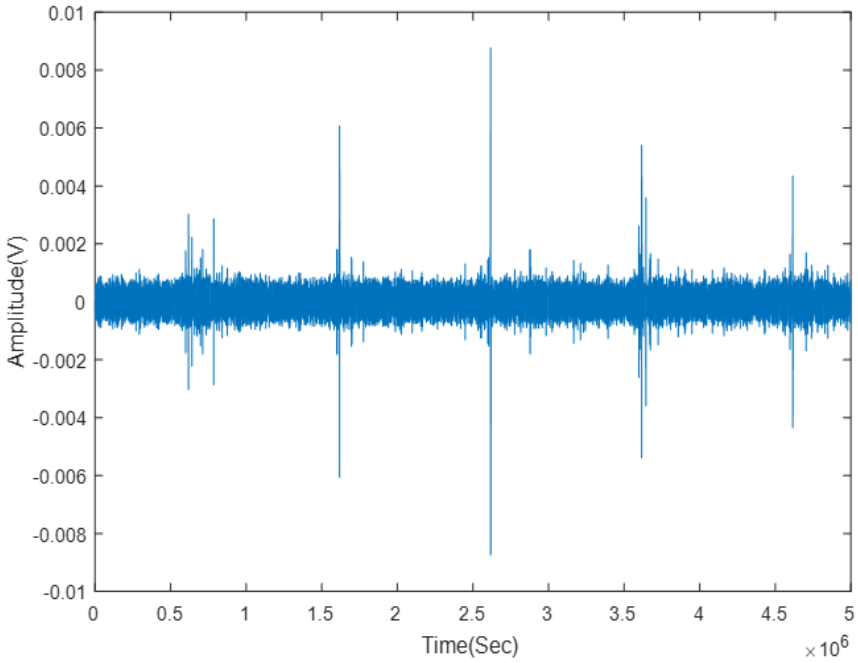
0.01
0.008
0.006
0.004
0.002
0
-0.002
-0.004
-0.006
-0.008
-0.01
Amplitude(V)
0
0.5
1
1.5
2
2.5
3
3.5
4
4.5
5
Time(Sec)
×10^6

a)

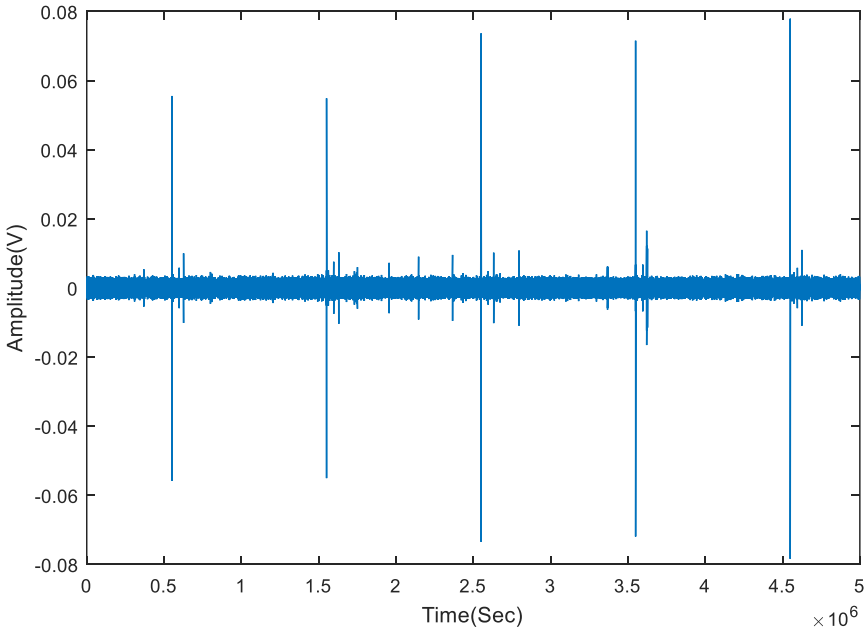
0.08
0.06
0.04
0.02
0
-0.02
-0.04
-0.06
-0.08
Amplitude(V)
0
0.5
1
1.5
2
2.5
3
3.5
4
4.5
5
Time(Sec)
×10^6

b)

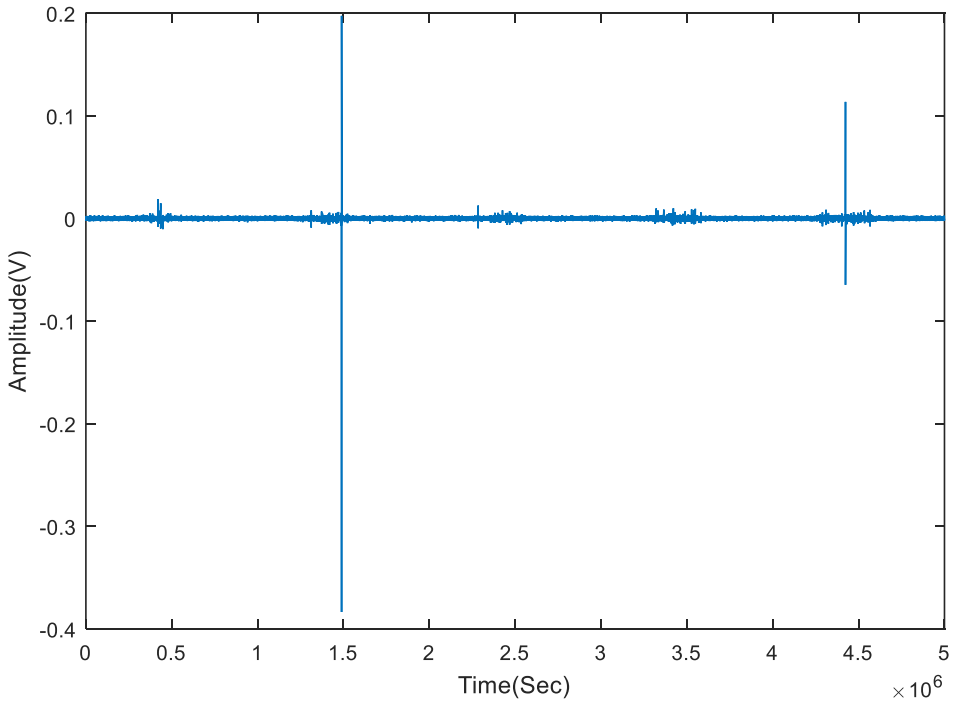

c)

Figure 7-35: Filtered waveform for the Hadfield sample at the a) early stage b) middle stage c) late stage

As it can be seen the signal to noise ratio shows an obvious increase for every filtered waveform compared with their corresponding original waveform. It cannot be ignored that the original signal to noise ratio is still acceptable under this laboratory testing condition. However, in the actual field condition, the noise level can increase dramatically, and SK-based filter may contribute to the identification of spikes related to defect evolution in the rails based on the current result.

7.2 High frequency fatigue tests

7.2.1 Introduction

Three and four point bending fatigue tests are carried out on four pre-cracked Hadfield steel samples numbered 1 through 4. They were also pre-cracked using the Vibrophore fatigue machine to an initial crack length of 9- 11 mm. Sample 1 and 2 were tested under 3 point bending condition, whereas sample 3 and 4 were tested under 4 point bending condition . The maximum load in this case was set at 3.75kN.Both R50a sensors were connected to the commercial PAC system. The thresholds for all the four samples were set to 40dB

To further investigate the capability of AE to detect crack initiation and propagation , three point bending fatigue crack growth tests have been carried out on Hadfield steel centre-notched samples of rectangular cross-section with dimension 120mm (L)×20mm(W)×10mm(H) and notch depth 9mm. The samples have not been pre-cracked in this case. Reference test have also been performed on a dummy sample with no notch or pre-cracking. Same as low frequency tests mentioned previously, one R50a sensor was connected to the commercial PAC AE system and the other one was connected to the customized system during testing.

Two 260 rail steel samples numbered 1 and 2 were tested with the frequency set at around 88Hz. The notch depth in this case was 2mm for both samples and no pre-cracking was made, so the signal features for all fatigue crack propagation process could be analysed. The peak loads used during the tests were set at 9kN, 9.2kN respectively. The analog filter 200 KHz-1MHz in the PAC system was applied for both samples before further processing. The thresholds for sample 1 and 2 were set to 71dB and 74 dB, respectively.

The reasons why thresholds were set at the above values are twofold. The first one is to reduce the influence of loading-related noise on post-processing and the second one is to reduce the amount of data that needs to be stored in the computer for ease of operation and post-processing.

7.2.2 Analysis of AE signals captured from commercial system

Figure 7-36 shows the change of crack growth rate with time and Figure 7-37 through Figure 7-40 show the correlation of amplitude, count, duration, energy with crack length for the samples in three and four point-bending fatigue test respectively. Zoomed-in sections of the correlation plots have also been shown in Figure 7-37 through Figure 7-40 as indicated by the blue arrows. Time (second) instead of cycles was plotted on the abscissa as the machine could not keep loading frequency constant at the later stage of the tests. For three point bending sample, the crack growth starts to pick up speed from around 100s (indicated by the red arrow) and at the same period AE activities starts to show steady increase until final failure. At around 60s, a cluster of relatively high amplitude AE hits which are similar to those captured during final stage in terms of intensity. However, their count, energy and duration values are clearly smaller than those captured during the final stage. For four point bending sample, the crack growth starts to pick up speed at around 200s (indicated by the red arrow), at which point significant amount of AE hits with amplitude above 60dB occurs which might be related to a mixed intergranular and transgranular failure mode as shown from the micrographs in Figure 7-41 and for all the parameters, a region with nearly no AE hits can be observed. After that, the crack growth rate keep increasing and the values of different parameters (count, duration and energy) except for amplitude show a clear upward trend. The crack growth rate reaches a plateau before final failure at around 310s (circled in red), at which point

all the parameters show a sudden drop. However, the high amplitude (equal or above 70dB) AE hits captured at the same time also indicates impending collapse of the sample.

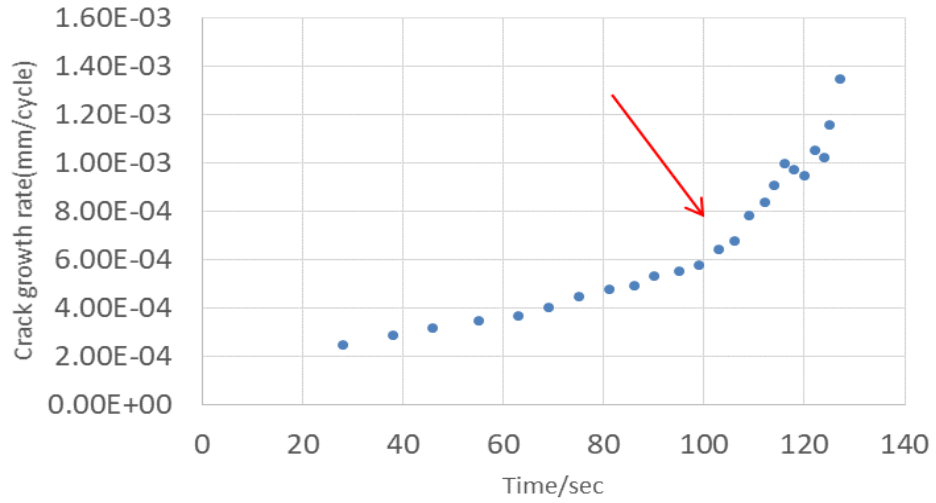

a)

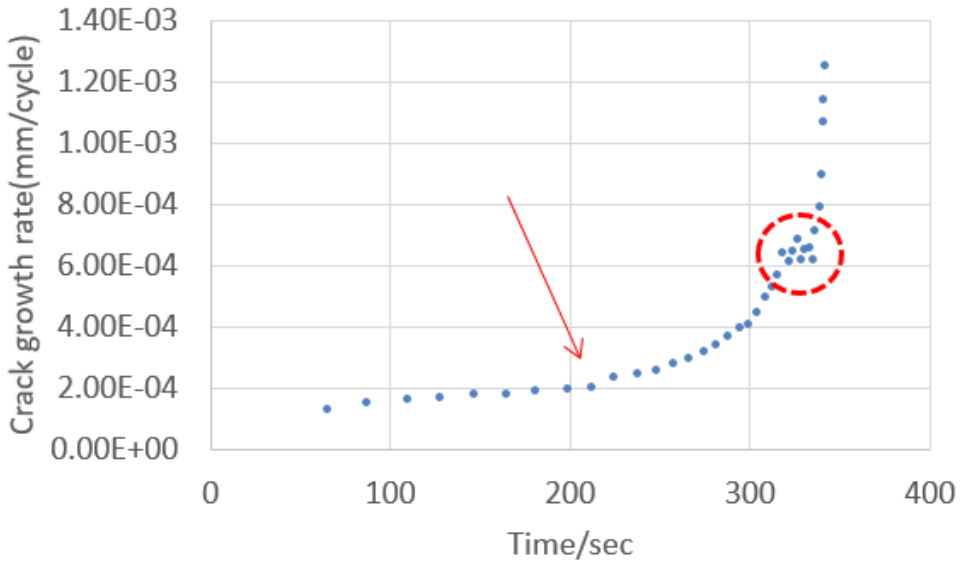

b)

Figure 7-36: Crack growth rate with time Hadfield steel sample in a) three point and b) four point bending fatigue test.

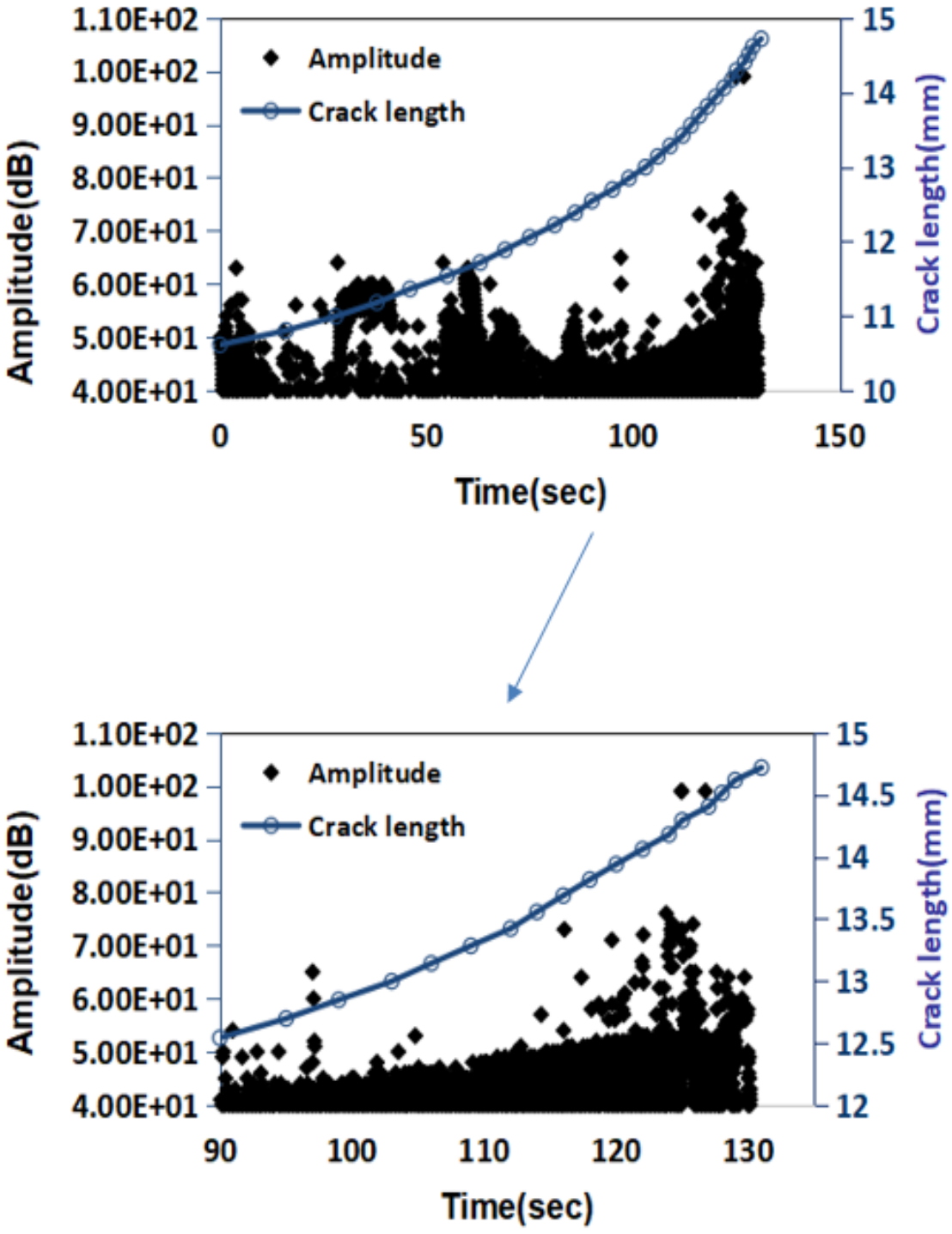
1.10E+02
1.00E+02
9.00E+01
8.00E+01
7.00E+01
6.00E+01
5.00E+01
4.00E+01
Amplitude(dB)
Amplitude
Crack length
15
14
13
12
11
10
Crack length(mm)
0
50
100
150
Time(sec)
1.10E+02
1.00E+02
9.00E+01
8.00E+01
7.00E+01
6.00E+01
5.00E+01
4.00E+01
Amplitude(dB)
Amplitude
Crack length
15
14.5
14
13.5
13
12.5
12
Crack length(mm)
90
100
110
120
130
Time(sec)

a)

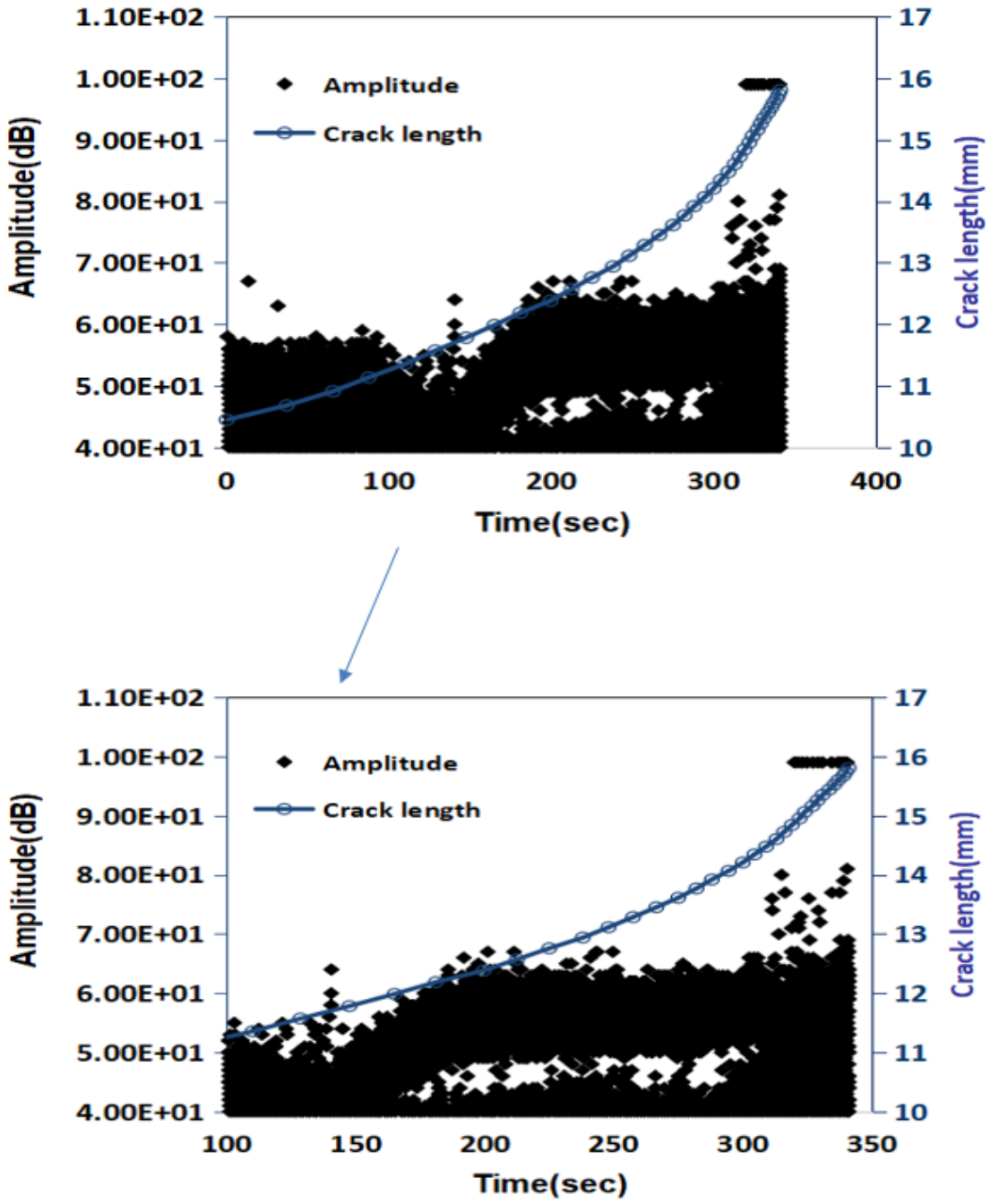

b)

Figure 7-37: AE signal amplitude in dB versus time with crack growth in mm for Hadfield steel sample in a) three point and b) four point bending fatigue tests.

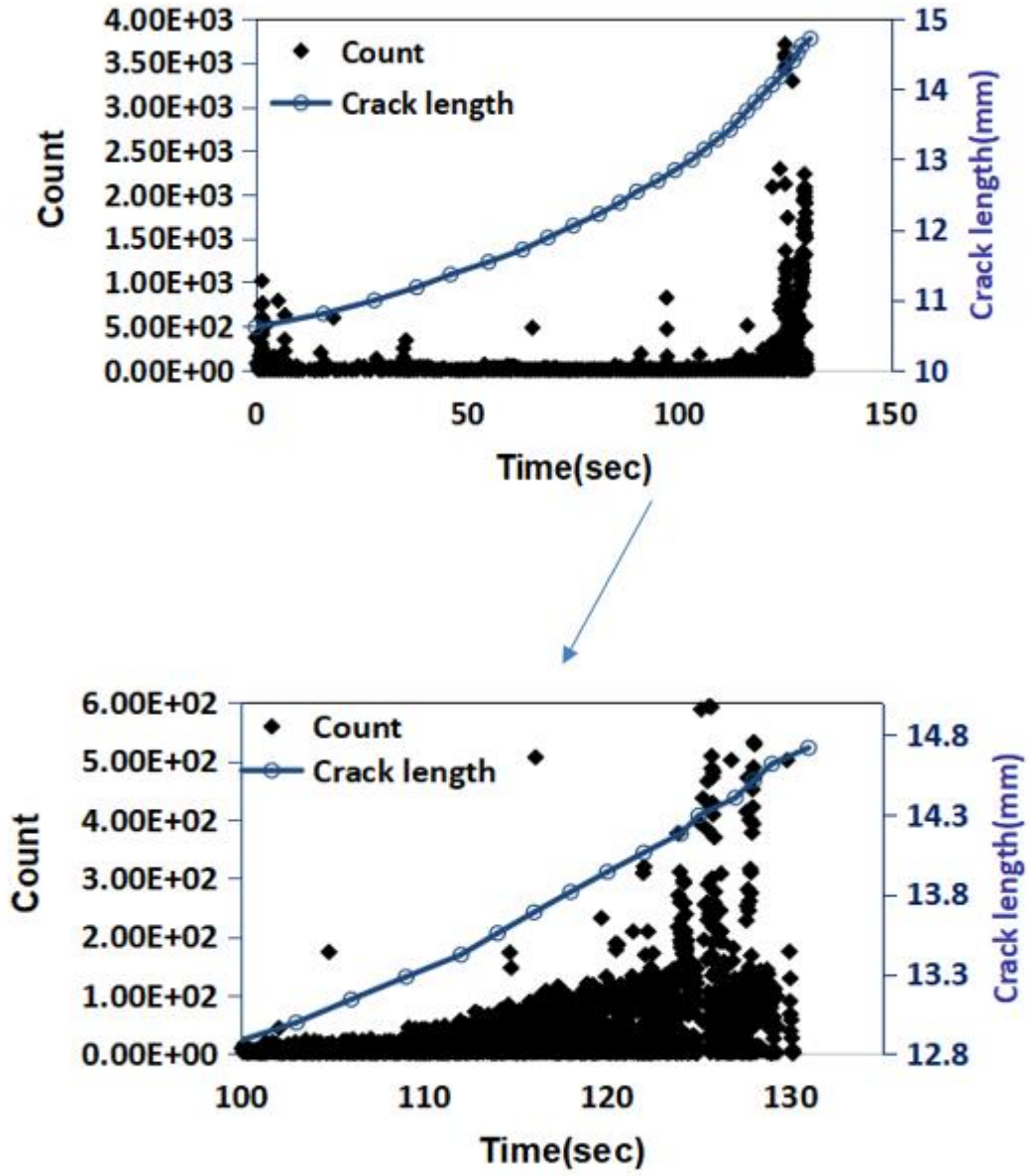
Count
Crack length
Count
Crack length(mm)
Time(sec)
4.00E+03
3.50E+03
3.00E+03
2.50E+03
2.00E+03
1.50E+03
1.00E+03
5.00E+02
0.00E+00
15
14
13
12
11
10
0
50
100
150
6.00E+02
5.00E+02
4.00E+02
3.00E+02
2.00E+02
1.00E+02
0.00E+00
14.8
14.3
13.8
13.3
12.8
100
110
120
130

a)

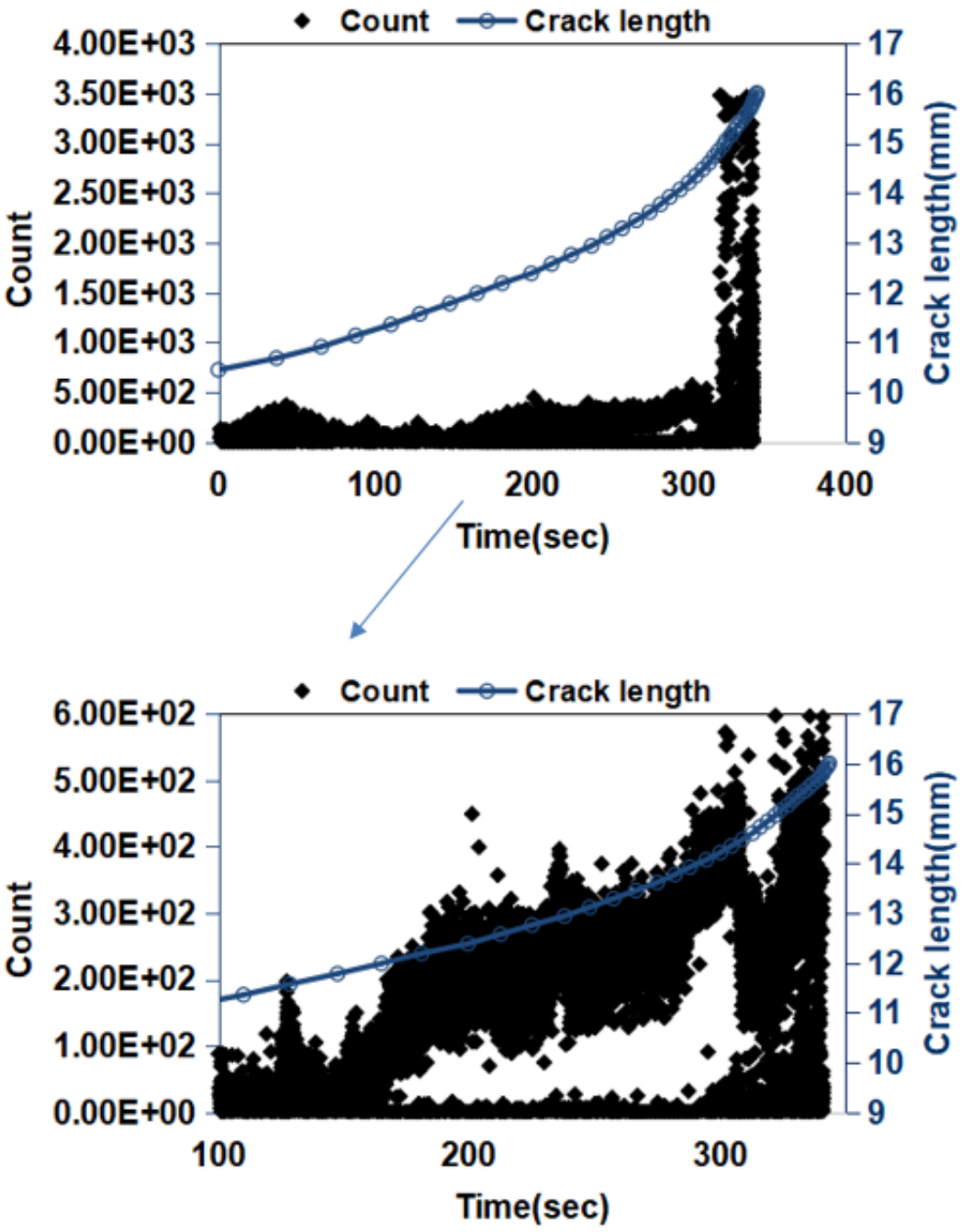

b)

Figure 7-38: AE signal count versus time with crack growth in mm for Hadfield steel sample in a) three point and b) four point bending fatigue tests.

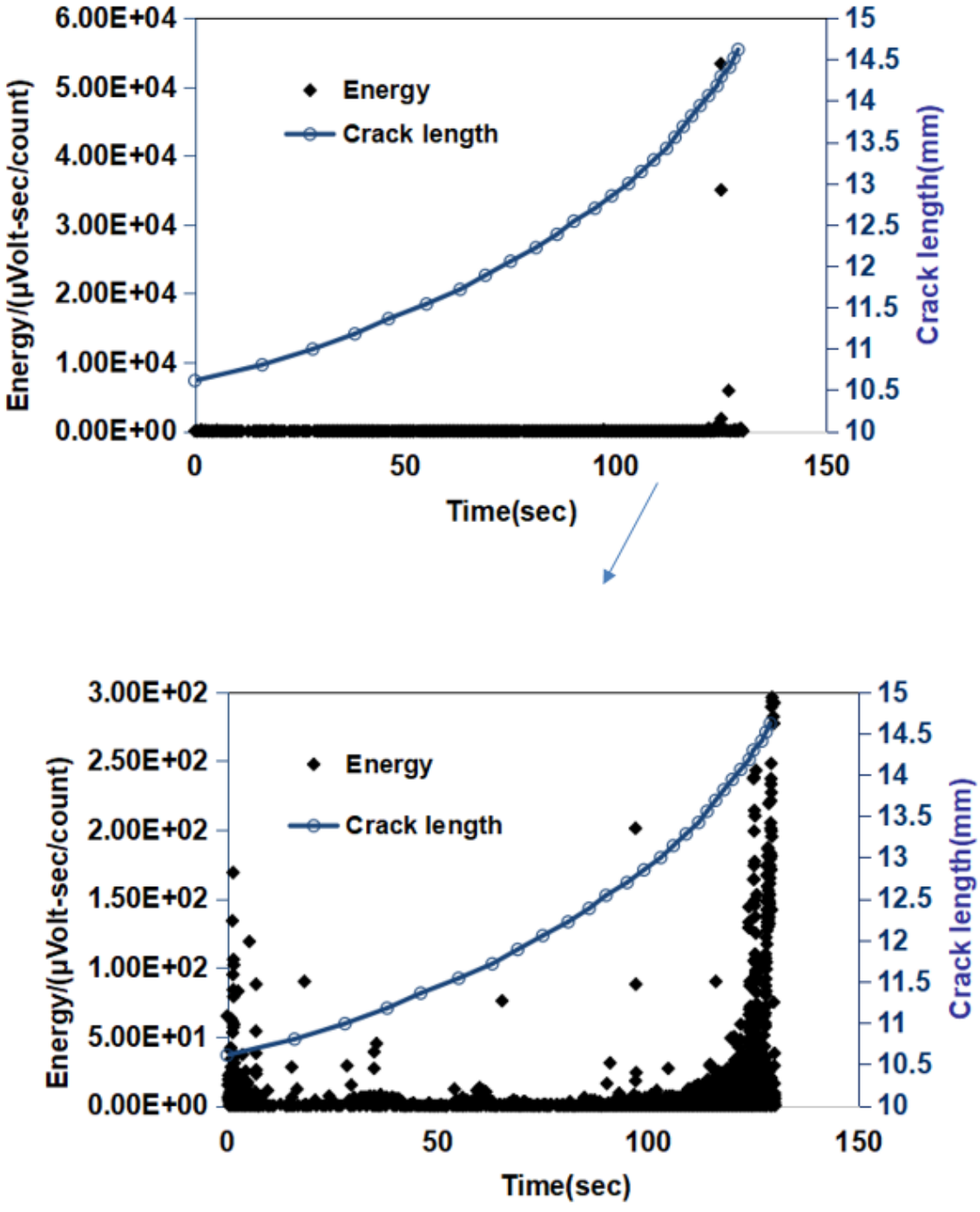
6.00E+04
5.00E+04
4.00E+04
3.00E+04
2.00E+04
1.00E+04
0.00E+00
Energy/(µVolt-sec/count)
Energy
Crack length
15
14.5
14
13.5
13
12.5
12
11.5
11
10.5
10
Crack length(mm)
0
50
100
150
Time(sec)
3.00E+02
2.50E+02
2.00E+02
1.50E+02
1.00E+02
5.00E+01
0.00E+00
Energy/(µVolt-sec/count)
Energy
Crack length
15
14.5
14
13.5
13
12.5
12
11.5
11
10.5
10
Crack length(mm)
0
50
100
150
Time(sec)

a)

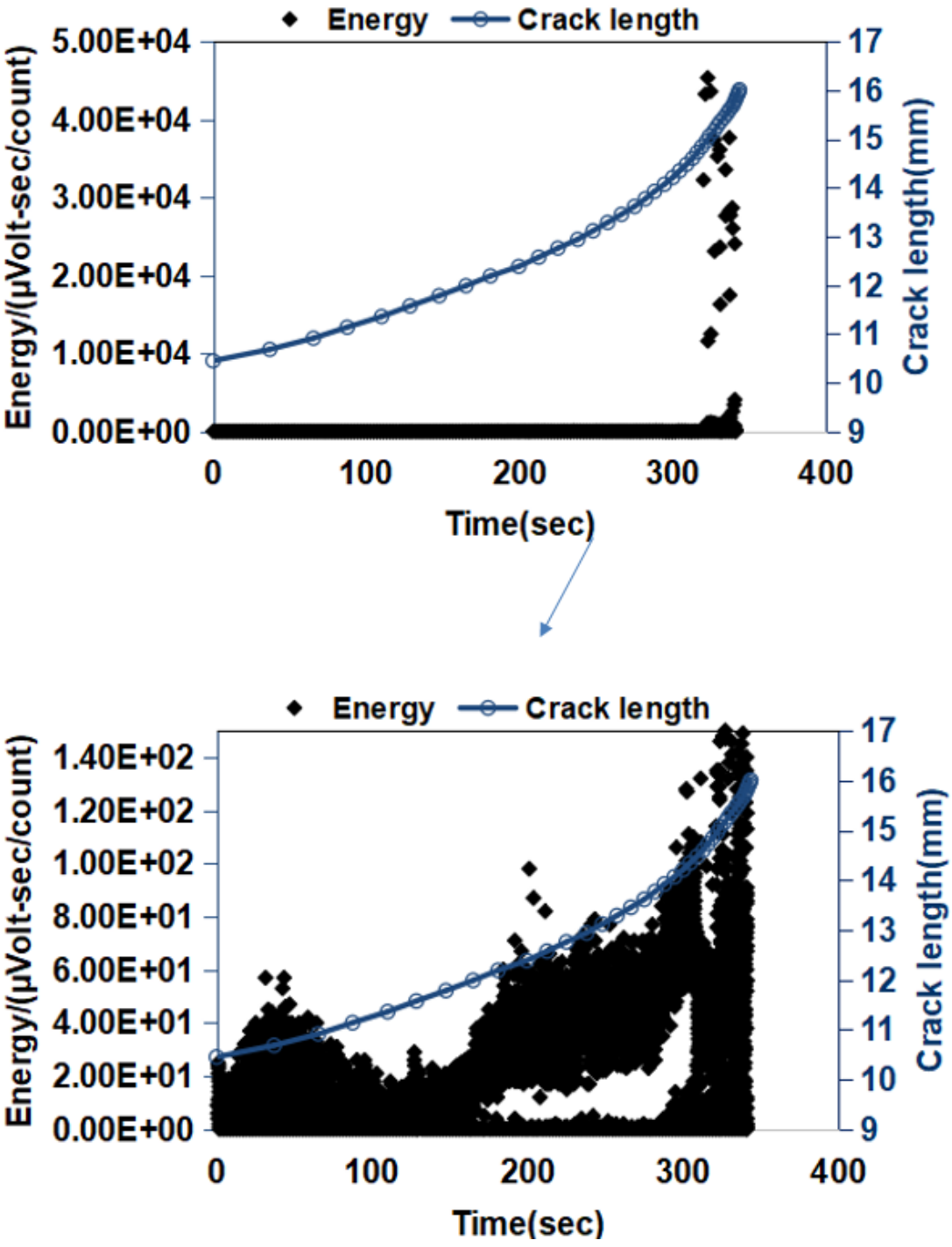

b)

Figure 7-39: AE signal energy versus number of fatigue cycles with crack growth in mm for Hadfield steel sample in a) three point and b) four point bending fatigue tests.

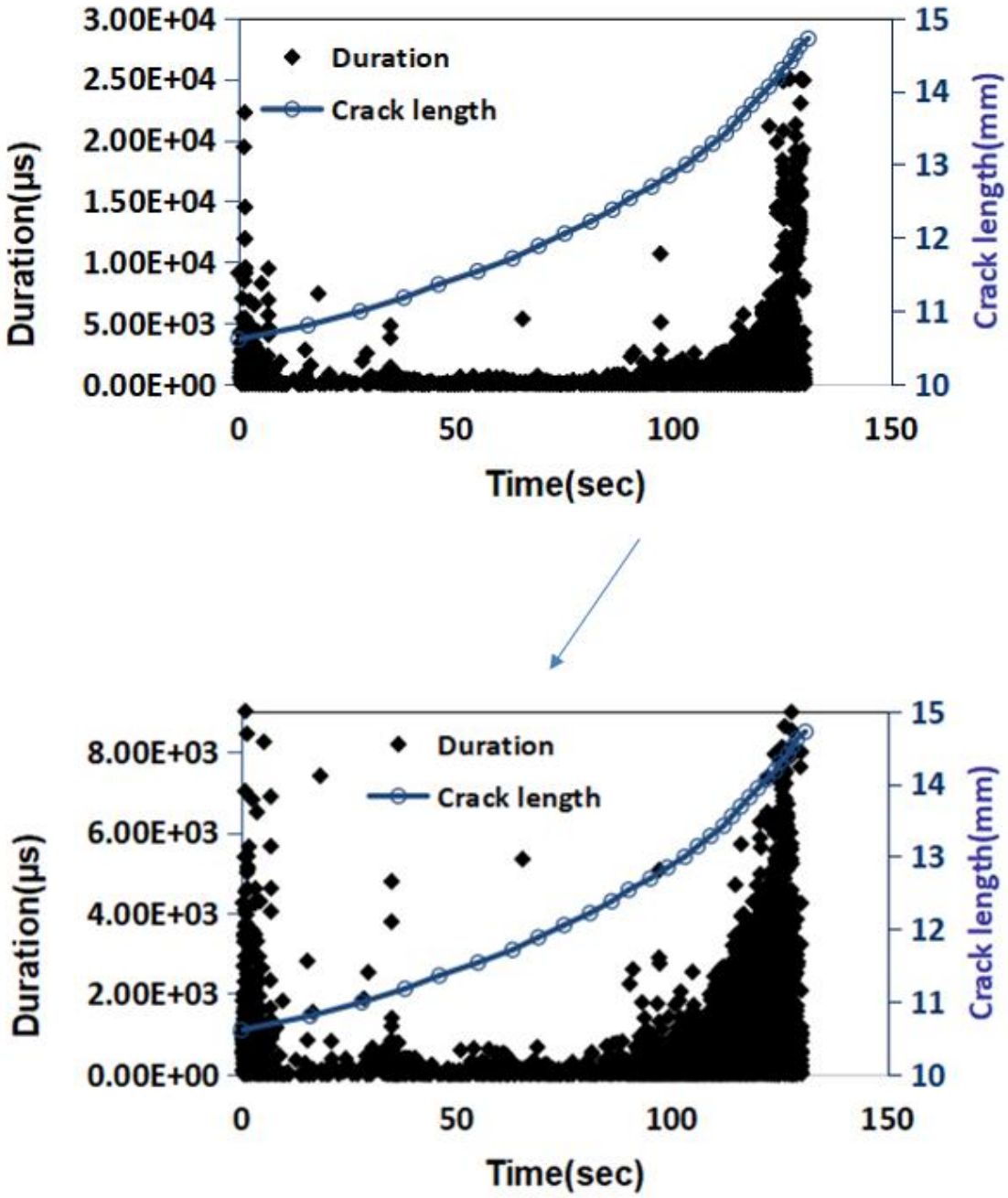
Duration
Crack length
Duration(μs)
Crack length(mm)
Time(sec)
3.00E+04
2.50E+04
2.00E+04
1.50E+04
1.00E+04
5.00E+03
0.00E+00
8.00E+03
6.00E+03
4.00E+03
2.00E+03
0.00E+00
0
50
100
150
15
14
13
12
11
10

a)

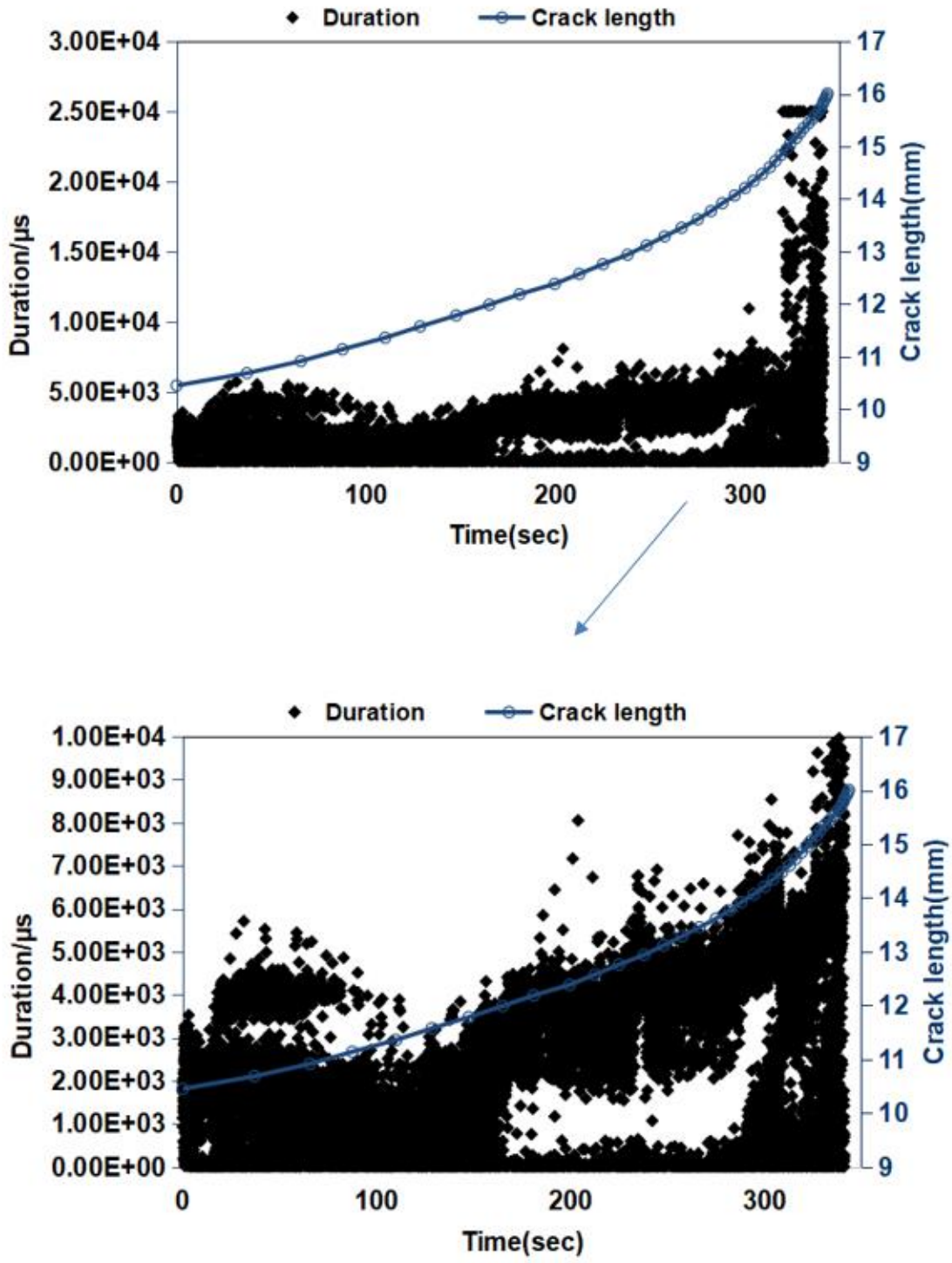

b)

Figure 7-40: AE signal energy versus number of fatigue cycles with crack growth in mm for Hadfield steel sample in a) three point and b) four point bending fatigue tests.

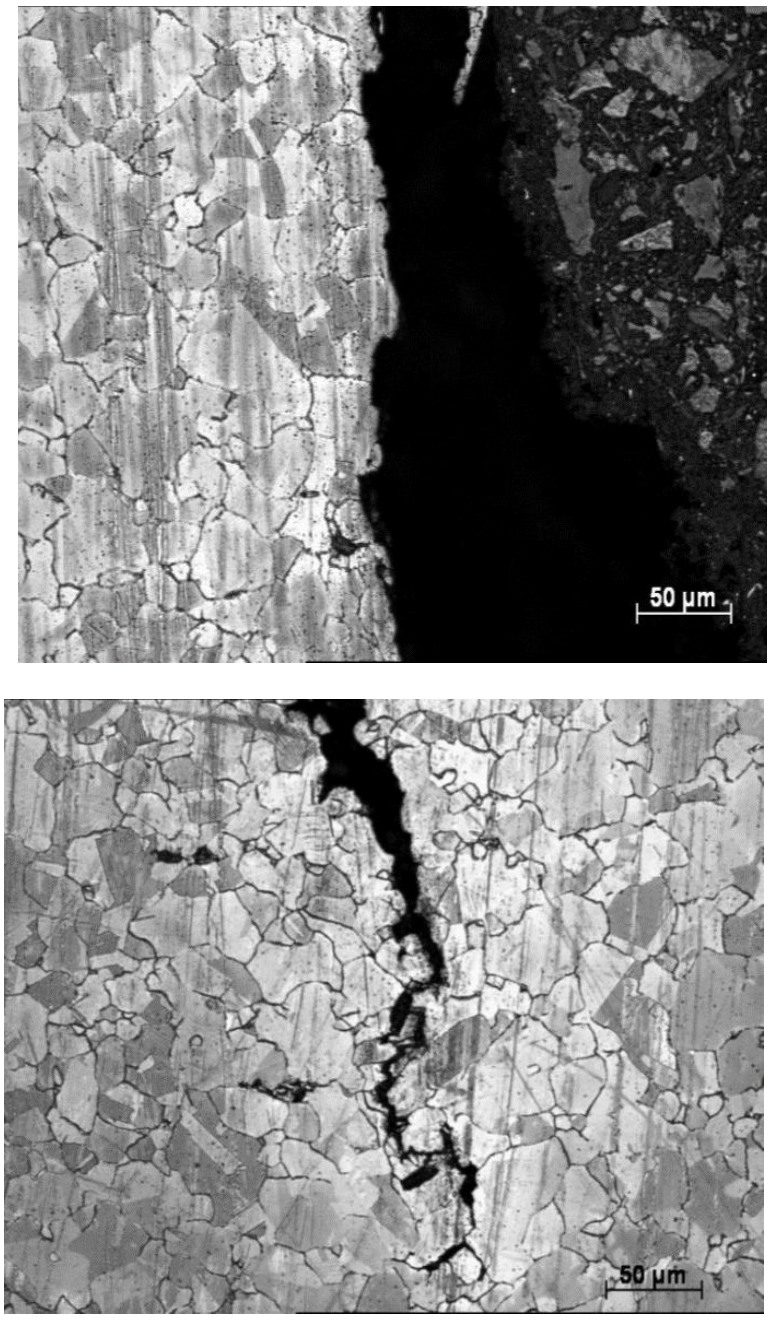

Figure 7-41: Micrographs showing the crack path after a fatigue crack test (from sample 4) showing a mixture of both transgranular and intergranular cracking

Figure 7-42 shows the correlation between dC/dN, dD/dN,dE/dN and da/dN for all the four samples . Sample 1 and 2 were subjected to three point bending load, whereas Sample 3 and 4 were subjected to four point bending load. For the three point bending fatigue tests, it has been shown that both count rate and energy rate start to show upward trend beyond a certain value of ΔK. The initial drop was attributed to the influence of the residual stress generated in the pre-cracking process and it proves that AE is very sensitive to the loading history of the structure. It can be found that the crack growth rates under three-point bending are higher than those under four point bending for the same ΔK. Generally, count rate, energy rate and duration rate show similar trend for all the samples. For the samples under three point bending tests, however, energy rate exhibits a higher increase close to the end of stable crack growth indicating final failure is imminent, which is not reflected by neither count rate nor duration rate. Therefore, the energy rate is better indicator for later stage of stable crack propagation than count rate and duration rate for three point bending fatigue tests. Although energy rates for four point bending test are higher than those for three point bending tests for most of the ΔK range, the slopes of linear regression fit equations are lower than those for three point bending tests. It proves the energy rates values may be more sensitive to the loading configuration, whereas the slope of energy rate is more closely related to the magnitude of crack growth rate.

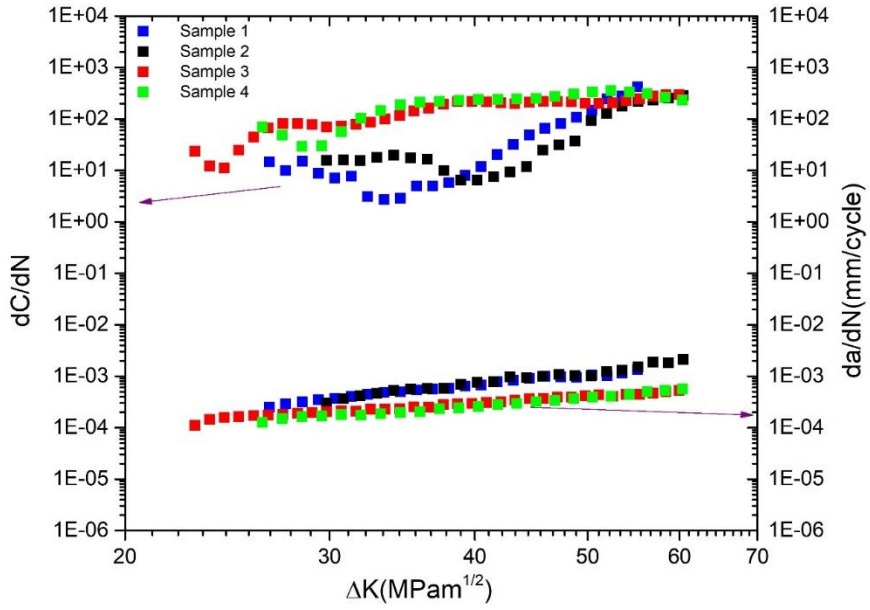
Sample 1
Sample 2
Sample 3
Sample 4
dC/dN
da/dN(mm/cycle)
ΔK(MPam^1/2)
1E+04
1E+03
1E+02
1E+01
1E+00
1E-01
1E-02
1E-03
1E-04
1E-05
1E-06
20
30
40
50
60
70

a)

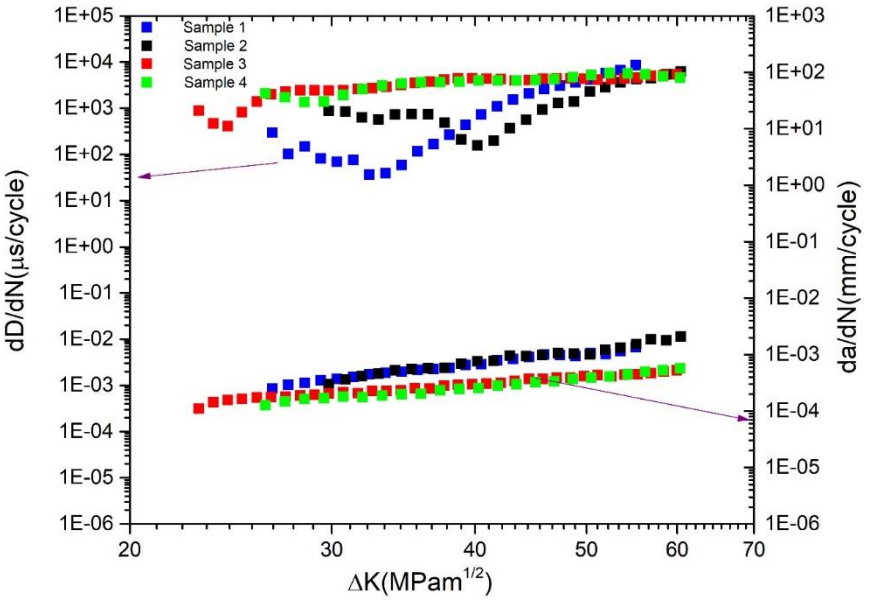
Sample 1
Sample 2
Sample 3
Sample 4
dD/dN(μs/cycle)
da/dN(mm/cycle)
ΔK(MPam^1/2)
1E+05
1E+04
1E+03
1E+02
1E+01
1E+00
1E-01
1E-02
1E-03
1E-04
1E-05
1E-06
20
30
40
50
60
70

b)

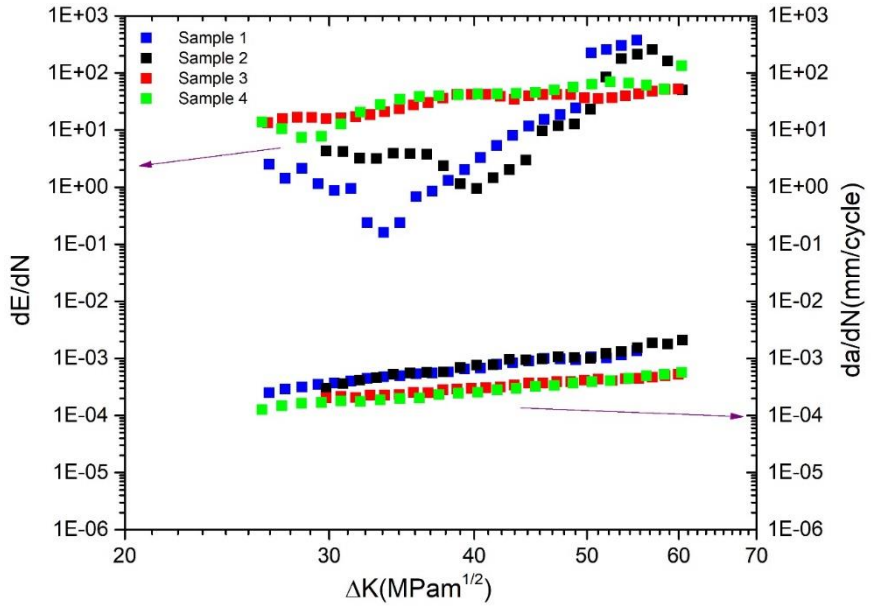

c)

Figure 7-42: Comparison between crack growth rate and a) count rate b) duration rate c) energy rate for two pre-cracked Hadfield sample during high frequency bending fatigue test.

Figure 7-43 through Figure 7-50 show the results for Hadfield steel centre-notched samples and the dummy sample with no notch or pre-cracking. Figure 7-43 shows the energy frequency distribution for AE events recorded during the test on the dummy sample. As no crack initiation and growth activity is expected, all the events can thus be attributed to external noises generated by friction, impact, machine running, etc. It is obvious that energy values of the noises are mainly distributed in the range 0-2(μVolt-sec/count). Hence AE events with energy in the range 0-2(μVolt-sec/count) could be removed for Hadfield steel samples during the post-processing.

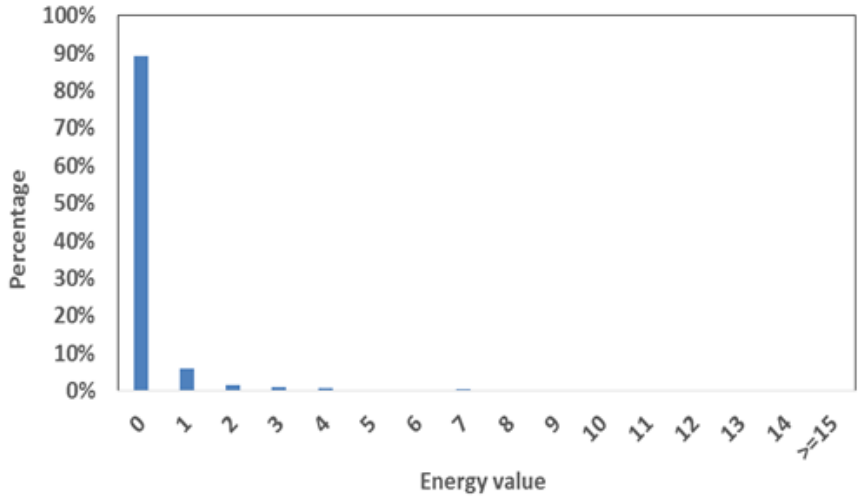

Figure 7-43: Energy frequency distribution for AE events AE events recorded during the test on the dummy sample.

Another parameter that can be used for signal filtering is risetime. Under current experiment condition, AE events with rise time above 1ms are most likely caused by external noise.AE events with energy in the range (0-2) (μVolt-sec/count) or risetime above 1ms are removed during the analysis.

Figure 7-44 shows the evolution of crack length with time for two Hadfield samples numbered 1 and 2, respectively. The peak load for sample 1 was initially set as 3kN and after around 0.5h.The value was increased to 3.3kN to reduce the amount of time for crack initiation and the AE results shown here are captured after the load increase. For sample 2, throughout the test, the peak load was set as 3.3kN with the loading frequency of around 70Hz.For both samples, the macro cracks initiate at around 960s and 800s respectively.

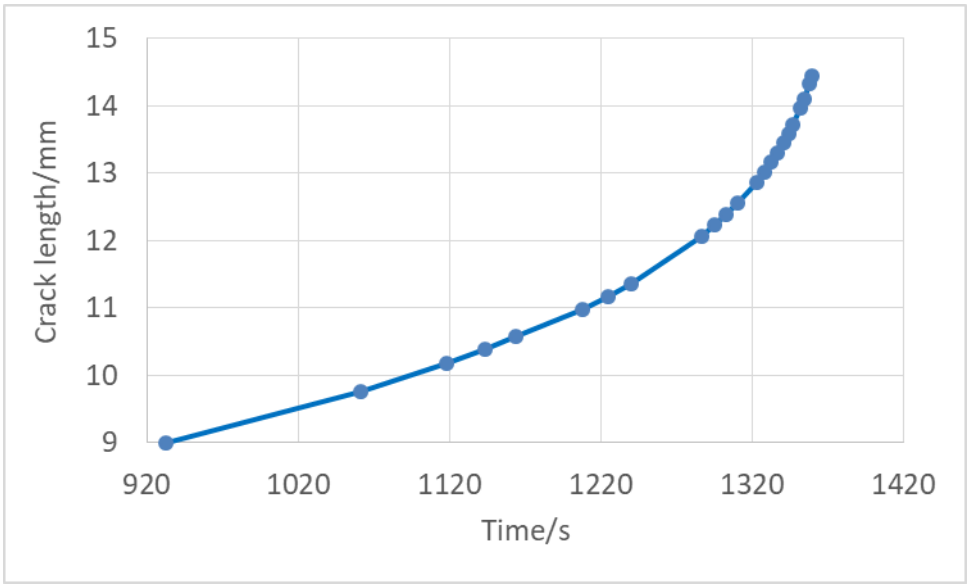

a)

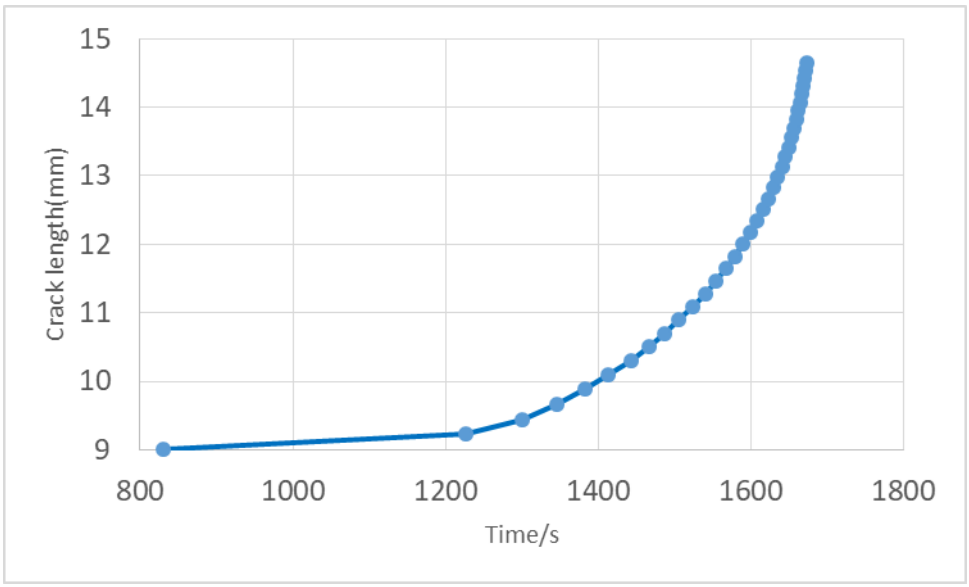

b)

Figure 7-44: Crack length with time for a) Sample 1 b) Sample 2

Figure 7-45 through Figure 7-48 show the AE activity captured during the tests. Zoomed in views of AE activities around the time of crack initiation have also been shown in each figure as indicated by the blue arrows. It can be seen that the intensity of AE activity drop as indicated by the red arrows after crack initiation and this may be attributed to the decreasing crack growth rate typical of microstructurally small crack[29]. When crack length grows 1mm from the notch, it is assumed that the crack growth enter into stage II. As it can be seen, the intensity of AE activity increases with increasing crack length during the second stage of the fatigue test. However, it is noteworthy that even at stage I, which covers a large percentage of the fatigue life time, high intensity AE signals have also been generated. This can be partly attributed to the movement of slip bands and micro-crack formation.

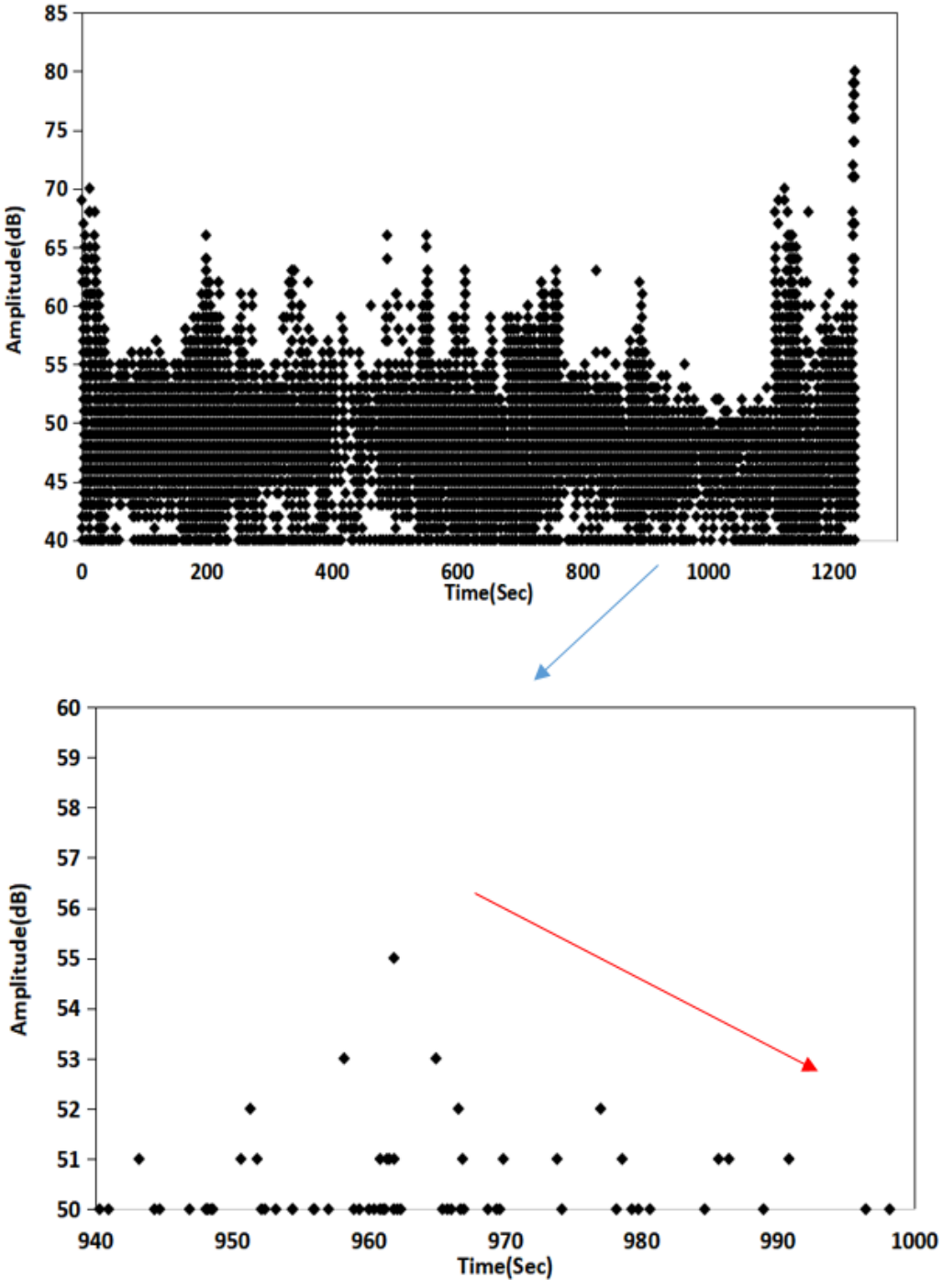
Amplitude(dB)
85
80
75
70
65
60
55
50
45
40
0
200
400
600
800
1000
1200
Time(Sec)
Amplitude(dB)
60
59
58
57
56
55
54
53
52
51
50
940
950
960
970
980
990
1000
Time(Sec)

a)

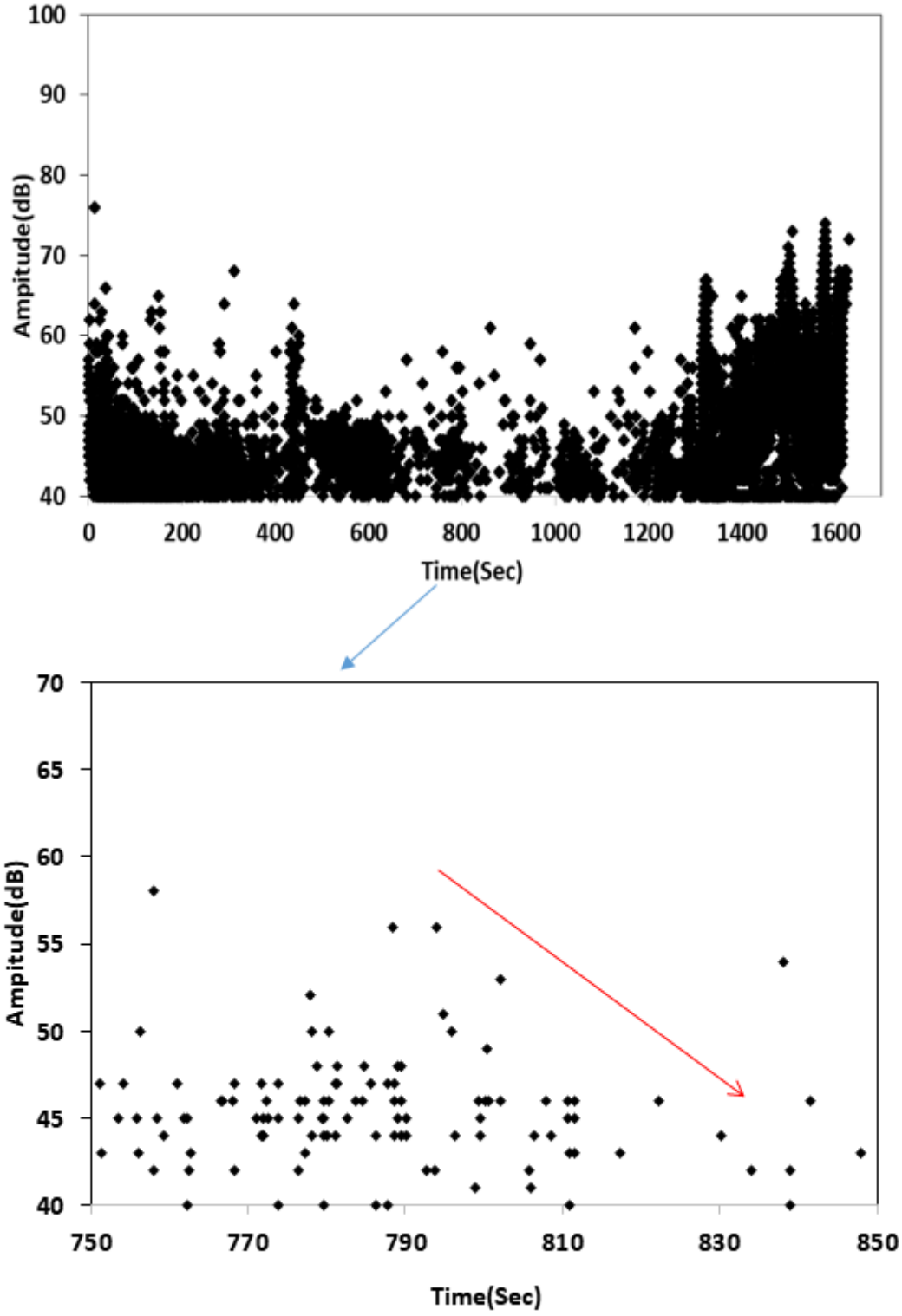

b)

Figure 7-45: Correlation between amplitude and crack length for a) sample 1 b) sample 2

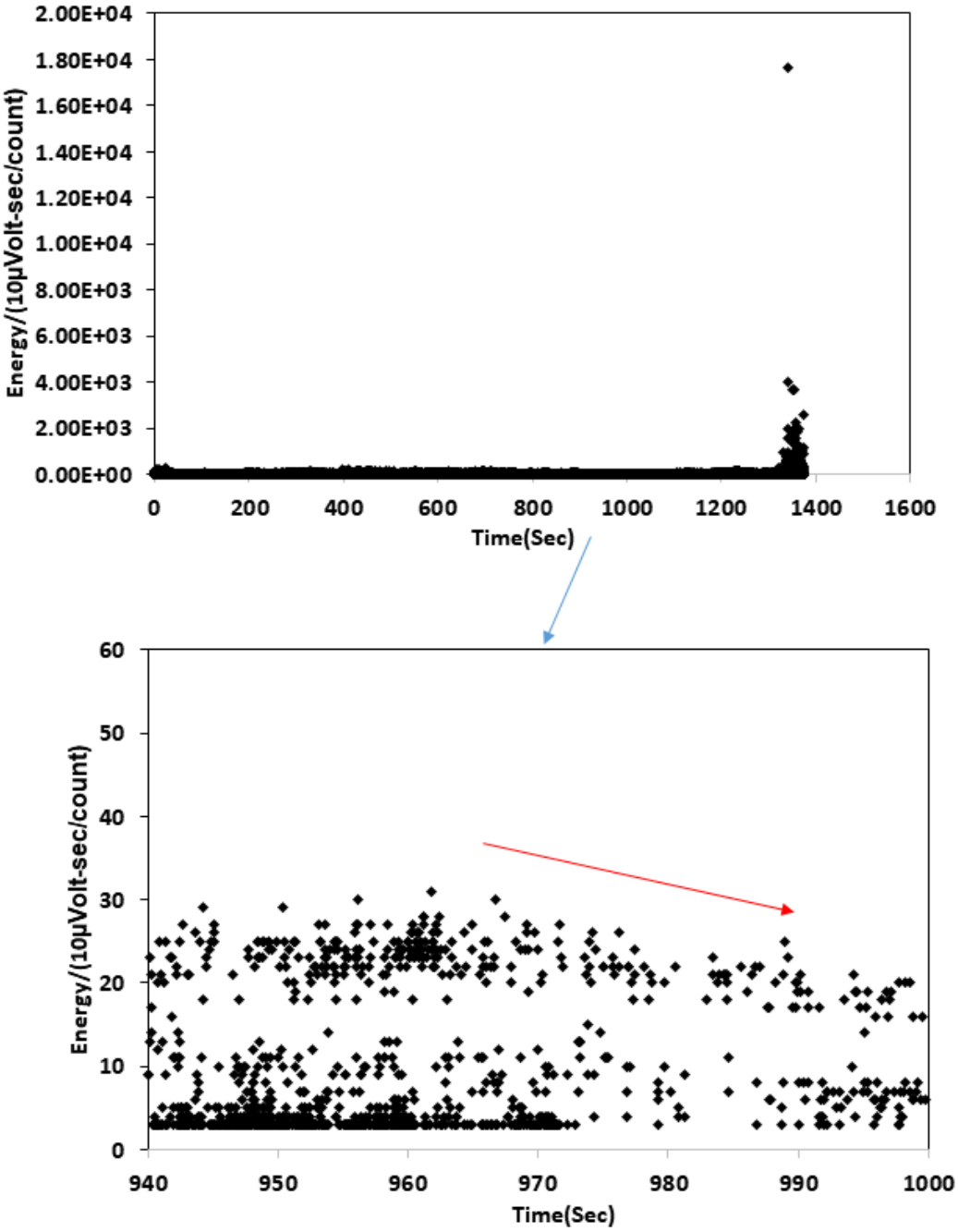
2.00E+04
1.80E+04
1.60E+04
1.40E+04
1.20E+04
1.00E+04
8.00E+03
6.00E+03
4.00E+03
2.00E+03
0.00E+00
Energy/(10µVolt-sec/count)
0
200
400
600
800
1000
1200
1400
1600
Time(Sec)
60
50
40
30
20
10
0
Energy/(10µVolt-sec/count)
940
950
960
970
980
990
1000
Time(Sec)

a)

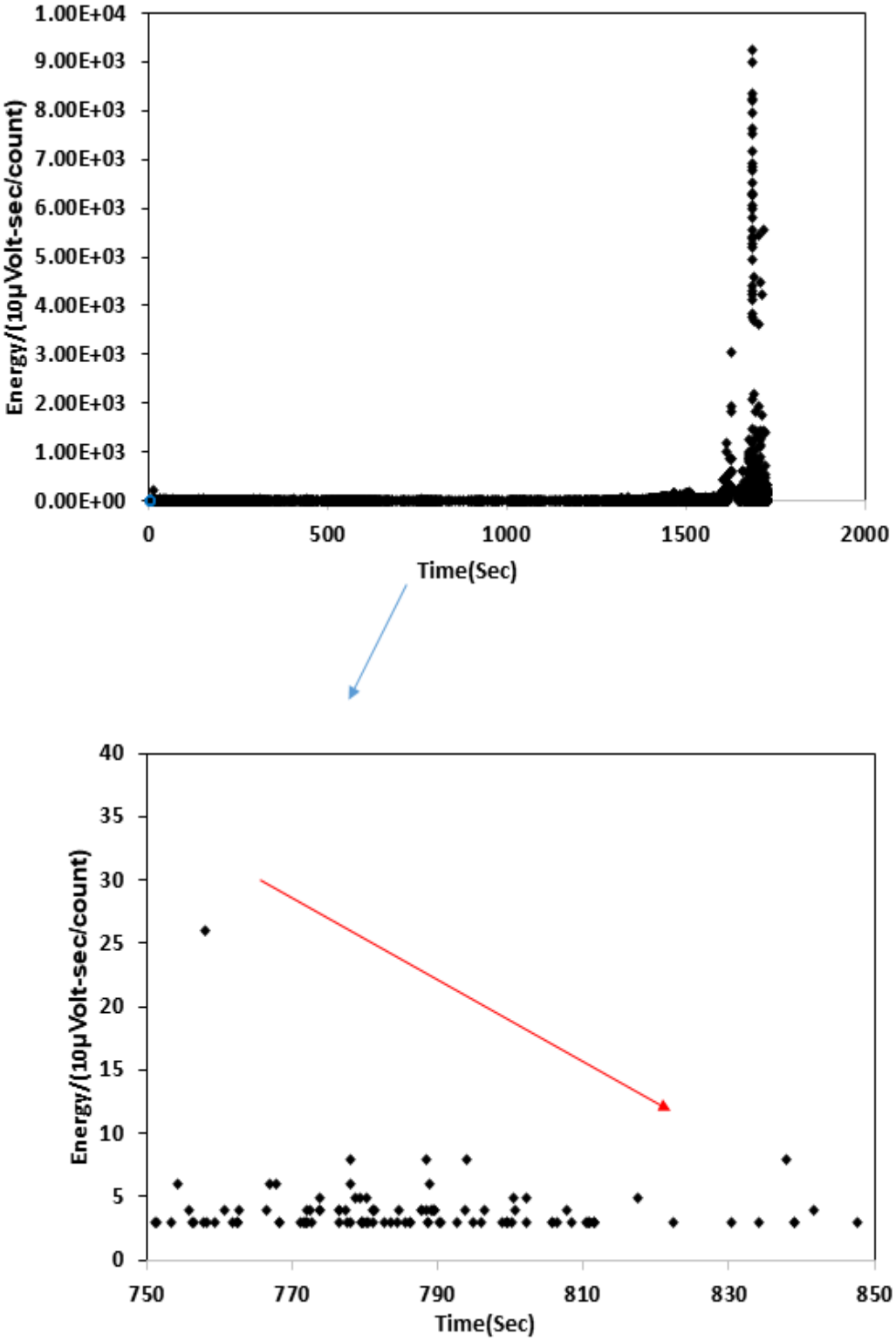

b)

Figure 7-46: Energy versus time for a) sample 1 b) sample 2

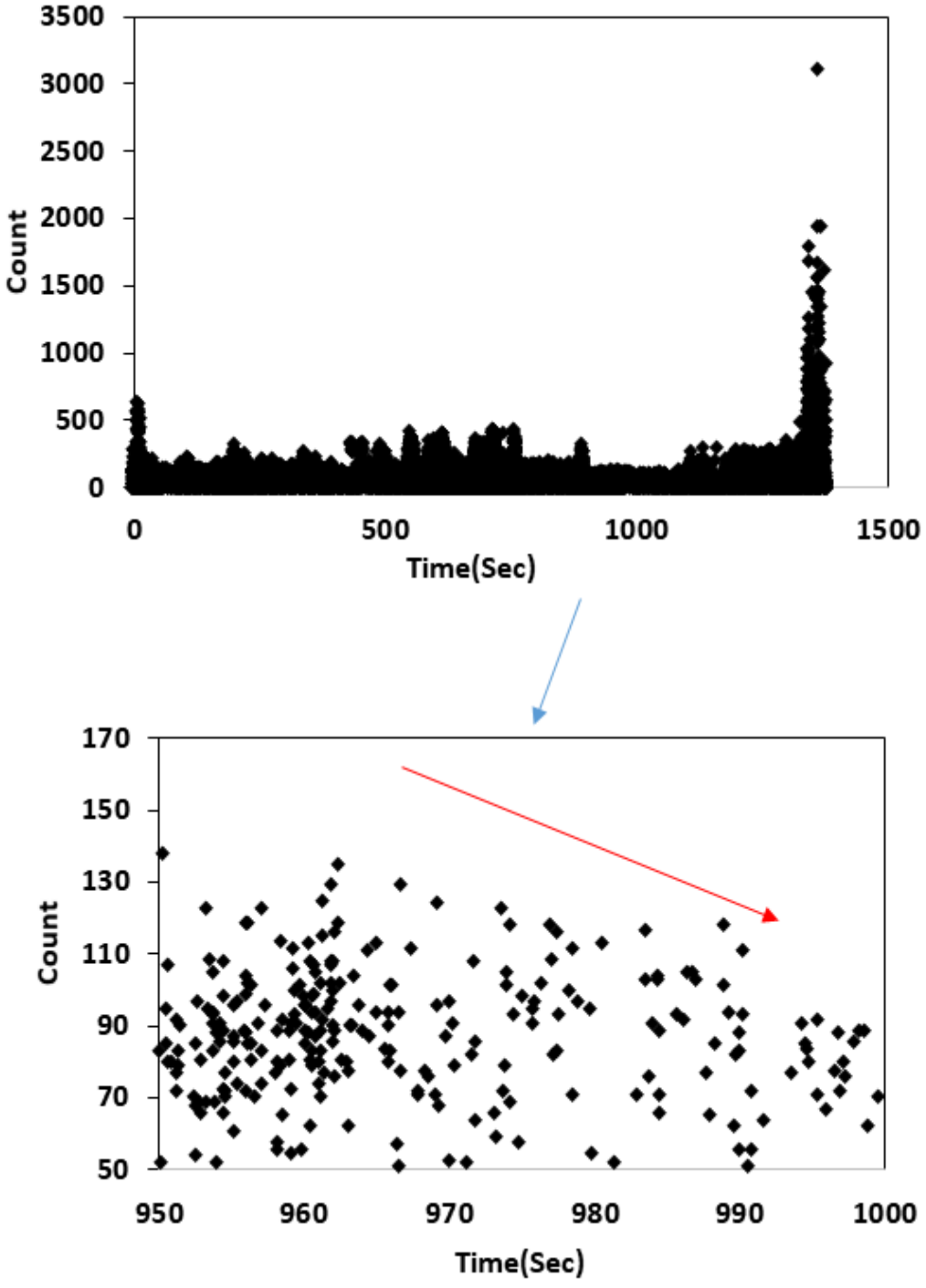
3500
3000
2500
2000
1500
1000
500
0
Count
0
500
1000
1500
Time(Sec)
170
150
130
110
90
70
50
Count
950
960
970
980
990
1000
Time(Sec)

a)

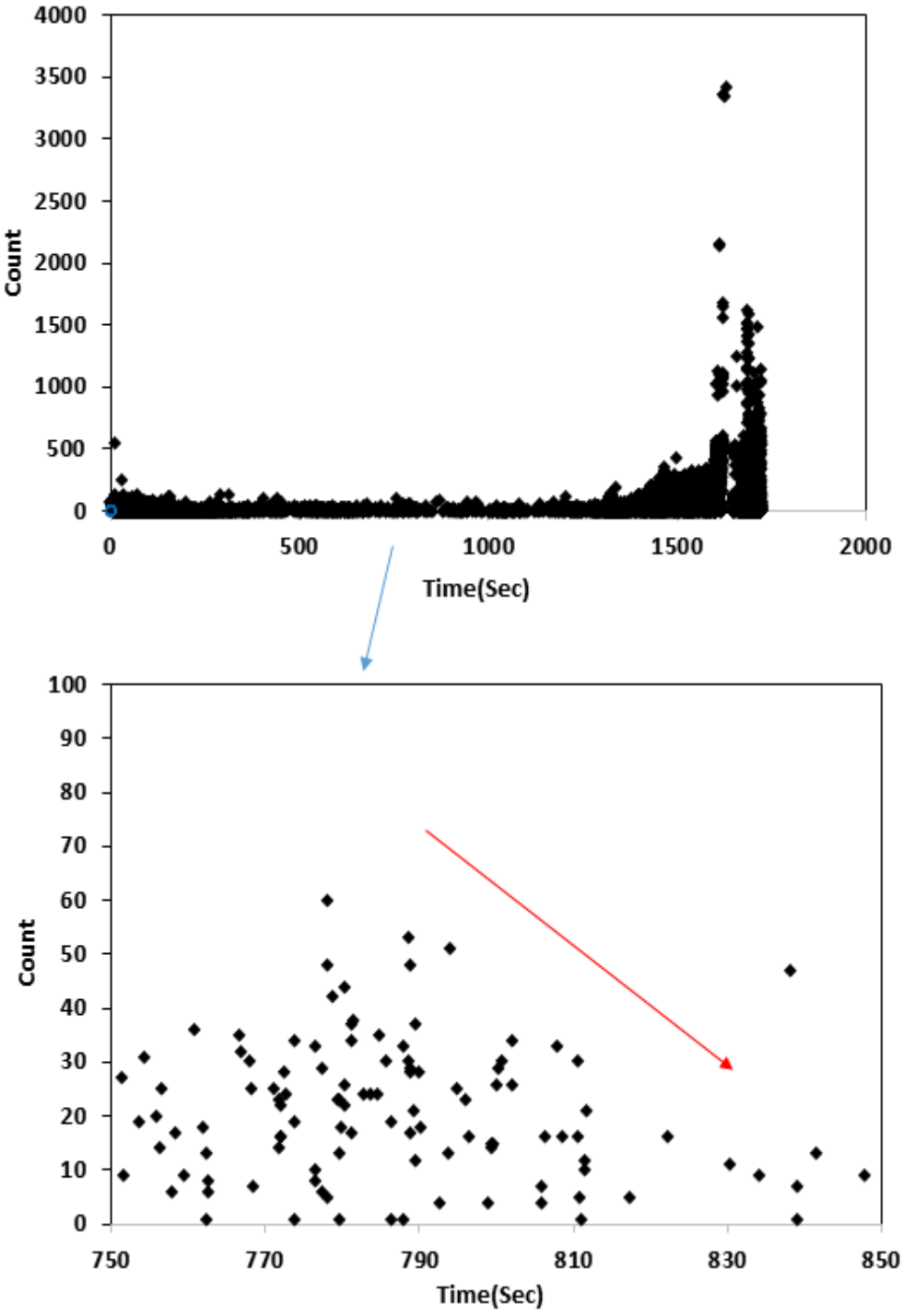

b)

Figure 7-47: count versus time for 1) sample 1 2) sample 2

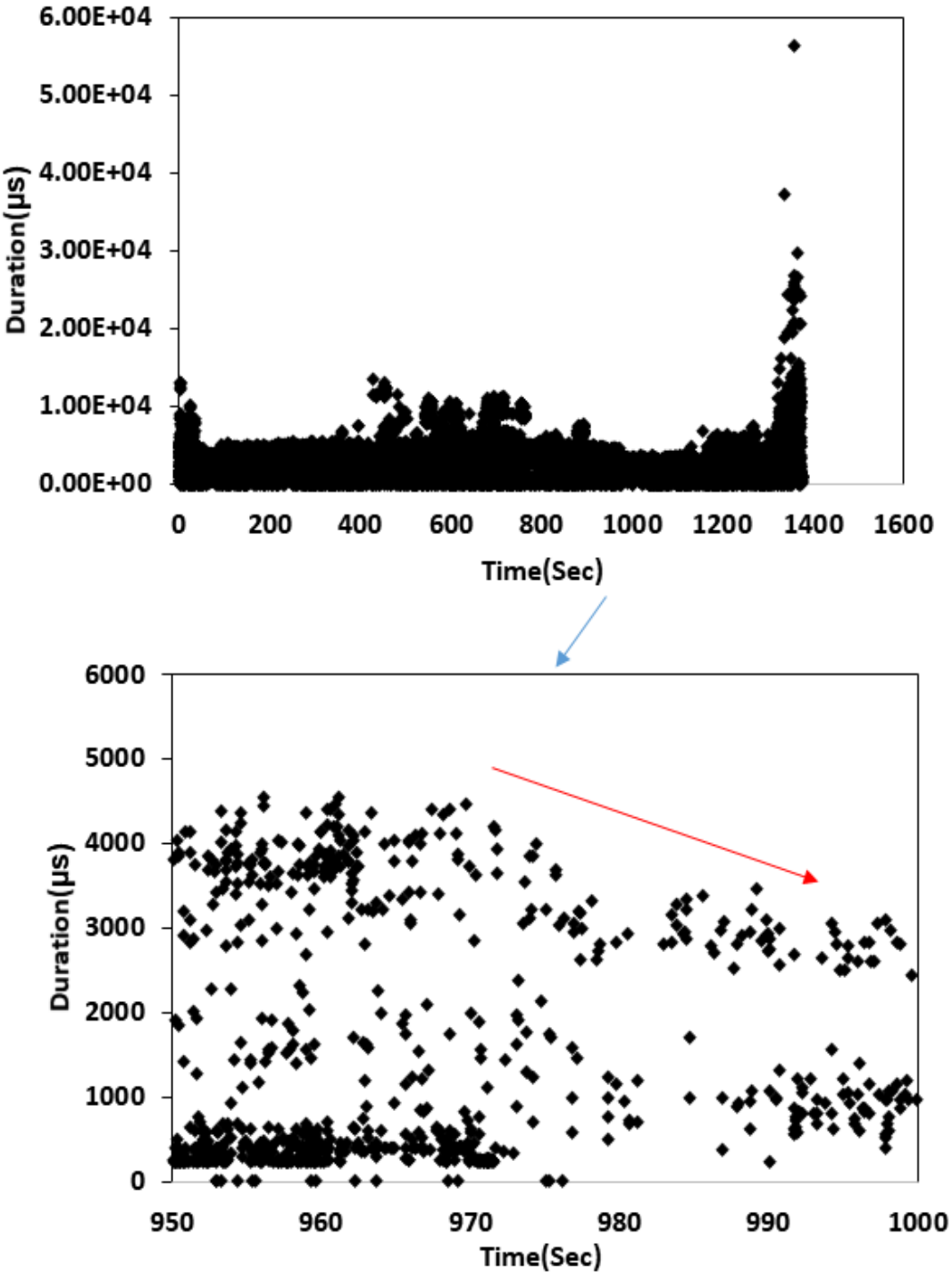
6.00E+04
5.00E+04
4.00E+04
3.00E+04
2.00E+04
1.00E+04
0.00E+00
Duration(µs)
0
200
400
600
800
1000
1200
1400
1600
Time(Sec)
6000
5000
4000
3000
2000
1000
0
Duration(µs)
950
960
970
980
990
1000
Time(Sec)

a)

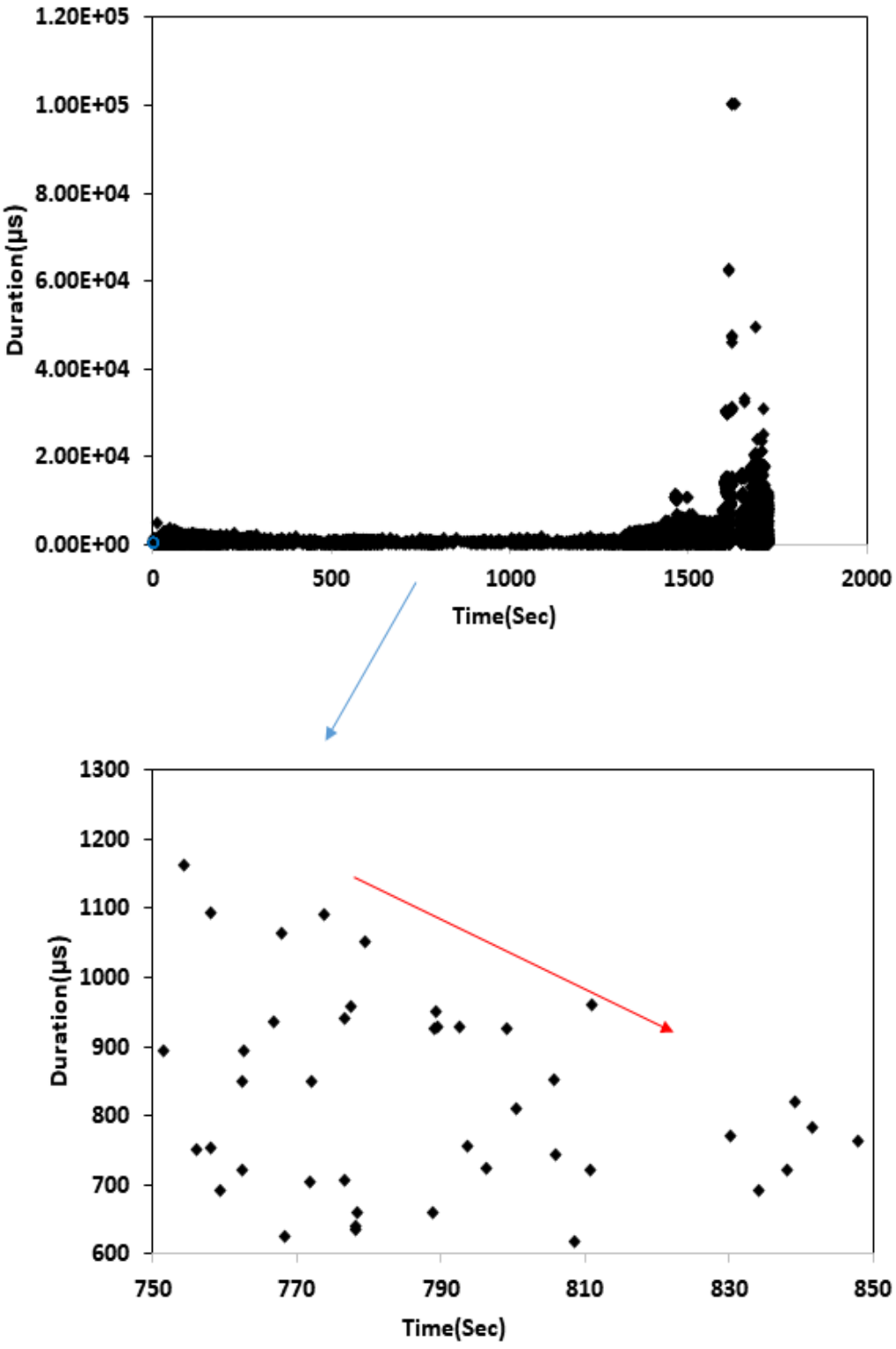

b)

Figure 7-48: Duration with time for a) sample 1 b) sample 2

Figure 7-49 shows the plots of cumulative energy and crack growth rate versus time for sample 2. It is obvious that most of the test time is spent on stage 1,which is consistent with the classification of fatigue life regime in [24].The slope of cumulative energy versus time curve is relatively small, compared with that for stage II. However, at the end of stage I, the slope starts to increase gradually. Once the crack growth enters into stage II, the cumulative energy shows an exponential increase. However, it shows a slow-down in the slope at the transition between stage II and III.

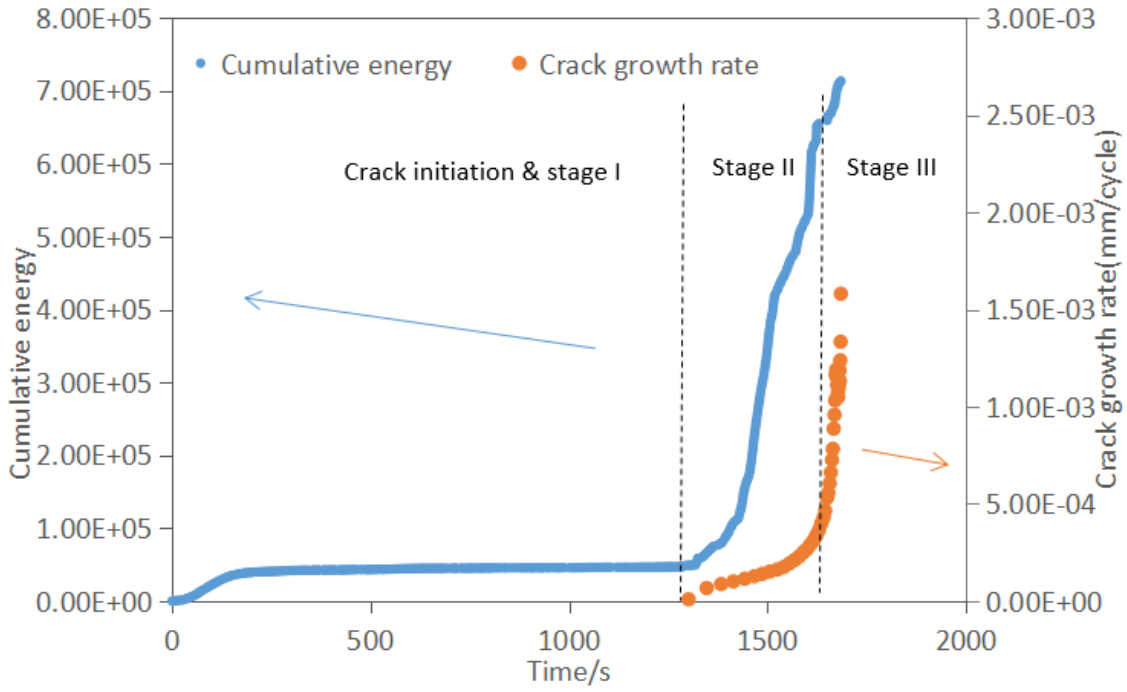

Figure 7-49: Comparison between cumulative energy and crack growth rate for sample 2

Figure 7-50 shows the correlation of count rate, energy rate with crack growth rate for both samples. Both samples show a “trough-like” trend (‘decrease-increase alternation) and the initial drop of count rate and energy rate for sample 1 may be caused by the release of residual stress induced during the previous loading with a smaller peak load. It is noteworthy that for sample 2, count rate and energy rate show different trend in the

ΔK range of around 25-30MPam$^{1/2}$ .Count rate show consistent increase whereas energy rate show a decrease trend.

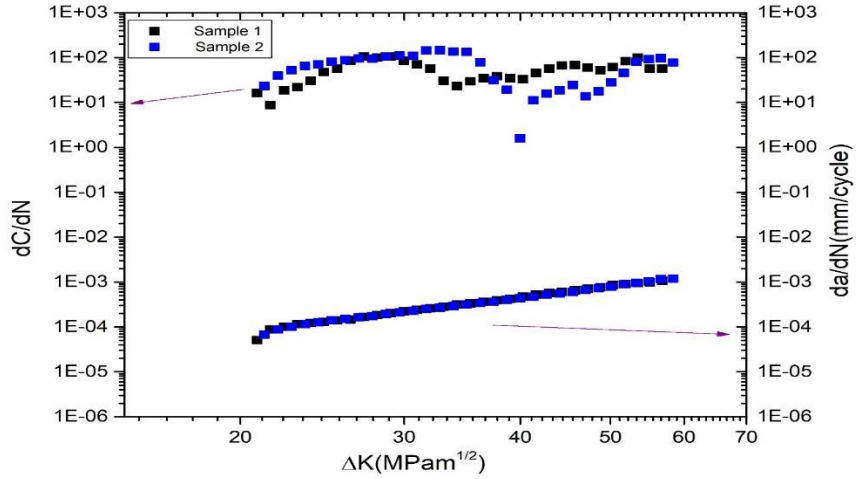

a)

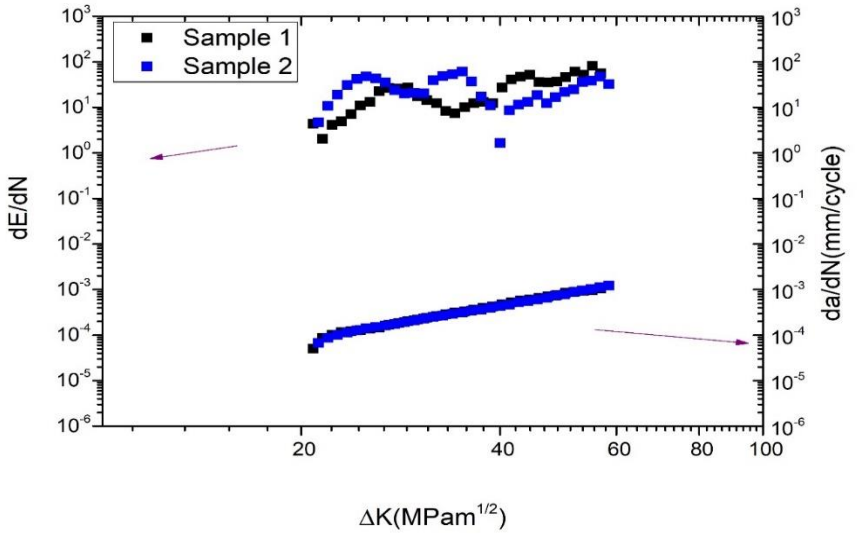

b)

Figure 7-50: Comparison between crack growth rates and a) count rates b) energy rates for sample 1 and 2 during the bending fatigue tests

Figure 7-51 and Figure 7-52 show AE activity captured during the tests on 260 rail steel sample 1 and sample 2, respectively. For sample 1, according to DCPD measurement, the macrocrack initiate at around 68000s and strong AE activity can be observed. The AE intensity increases when the peak load increases from 9 to 9.2kN. After macrocrack initiation, the AE activity decreases and this is more obvious for sample 2. Higher loading force (9.2kN) contributed to more obvious drop of AE activity and this is because the stress intensity factors increase as the loading forces go up, strengthen the AE sources of cyclic plasticity and crack extension. Therefore, higher loading forces make the AE indications visually easier. When the crack initiate, both amplitude and count of the captured events tend to be of similar magnitude, whereas they are more scattered in terms of the distribution of the magnitude at the final stage. Both cumulative energy and count plots can show the occurrence of crack initiation and final failure. The crack nucleation generates high intensity AE signals resulting in the sharp increase of the slope of cumulative plots. Cumulative count in this case proves to be a better indicator for crack initiation than cumulative energy .The large increase of cumulative energy and count before the final failure is attributed to cleavage fracture as shown in Figure. At the top part of crack, the roughness morphology indicates the cyclic fatigue propagation which has low AE output. The cleavage fracture at the bottom part of crack indicates the brittle fracture which is very high AE releasing.

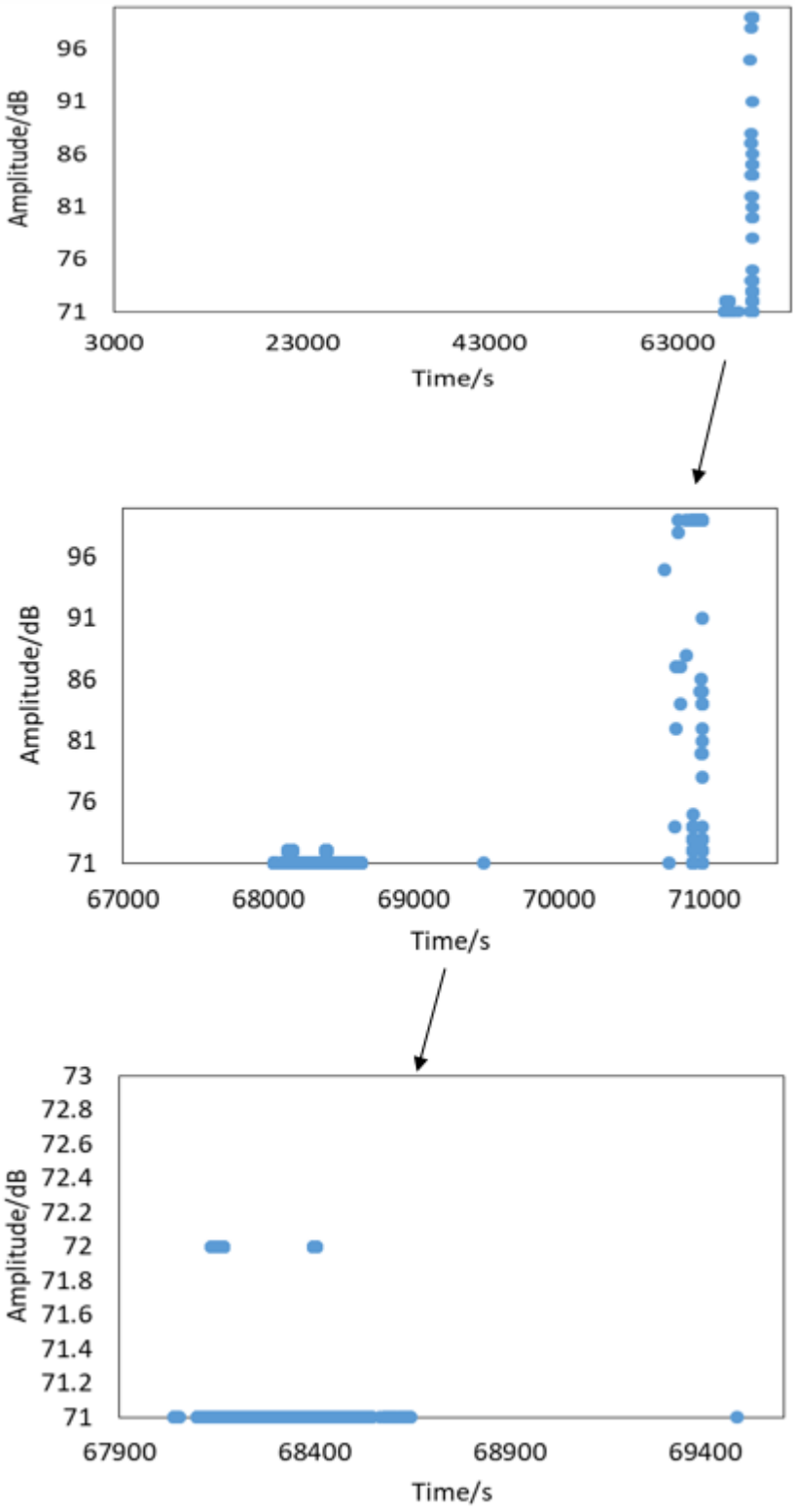
96
91
86
81
76
71
Amplitude/dB
3000
23000
43000
63000
Time/s
96
91
86
81
76
71
Amplitude/dB
67000
68000
69000
70000
71000
Time/s
73
72.8
72.6
72.4
72.2
72
71.8
71.6
71.4
71.2
71
Amplitude/dB
67900
68400
68900
69400
Time/s

a)

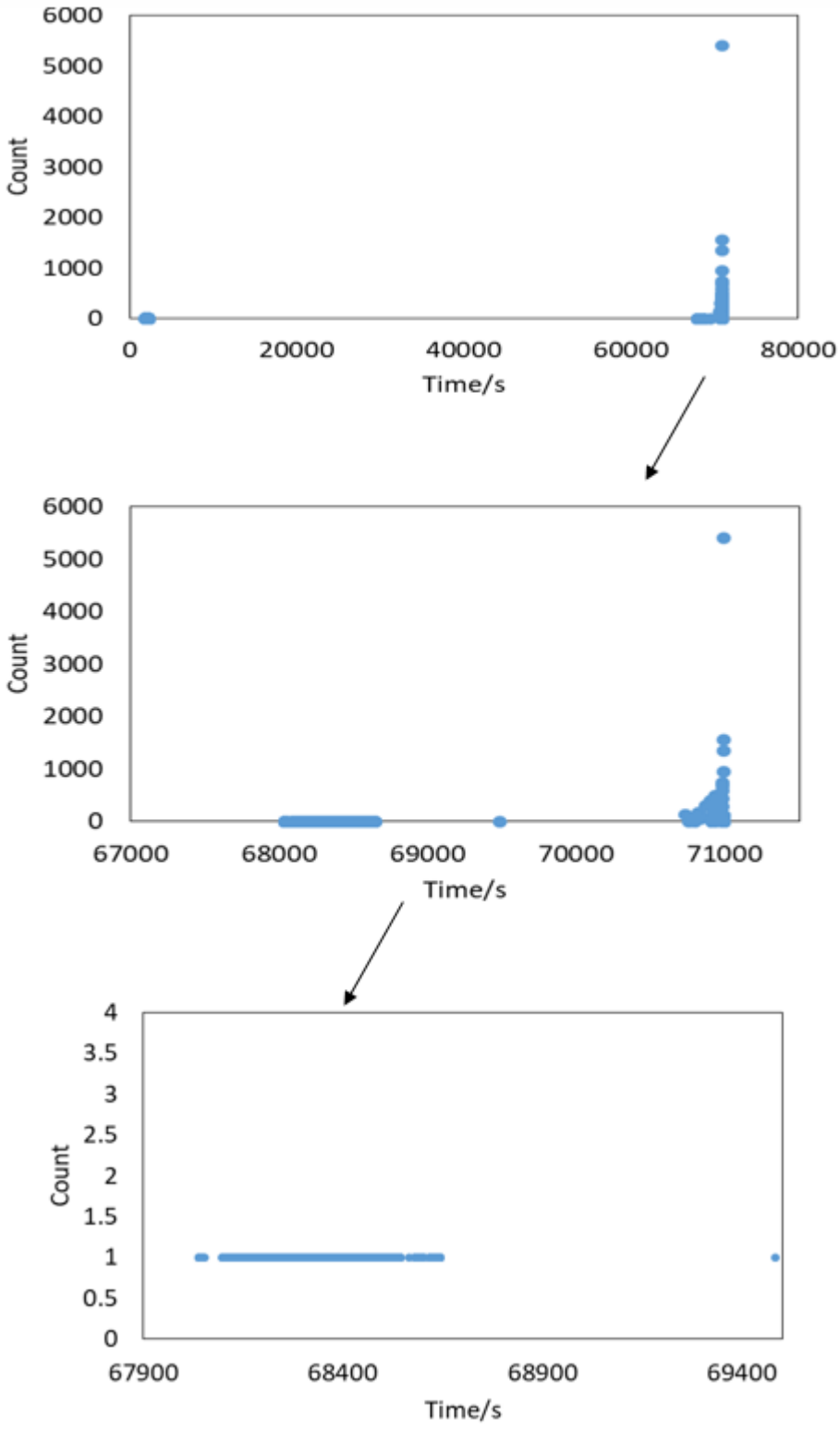
6000
5000
4000
3000
2000
1000
0
Count
0
20000
40000
60000
80000
Time/s
6000
5000
4000
3000
2000
1000
0
Count
67000
68000
69000
70000
71000
Time/s
4
3.5
3
2.5
2
1.5
1
0.5
0
Count
67900
68400
68900
69400
Time/s

b)

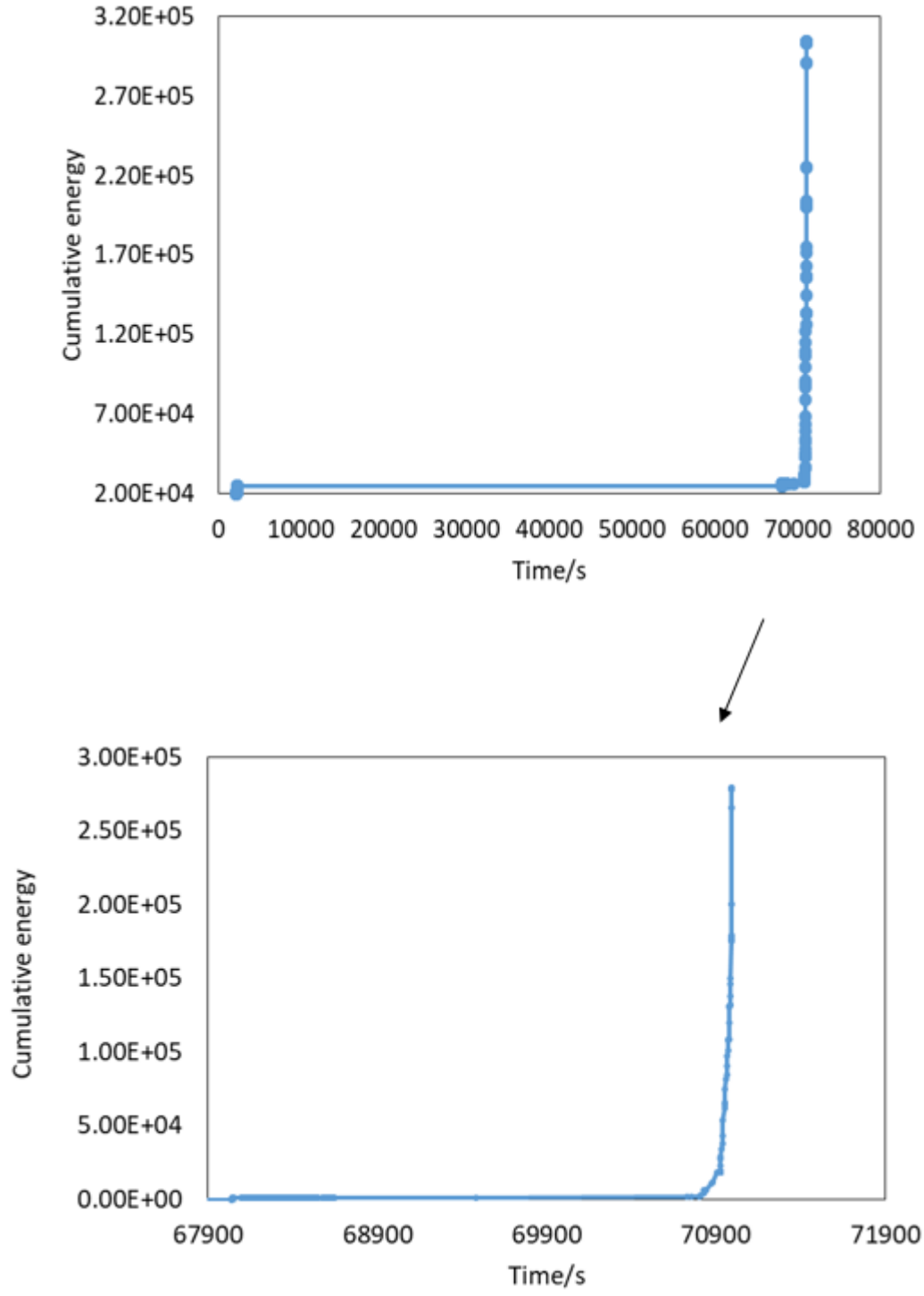
3.20E+05
2.70E+05
2.20E+05
1.70E+05
1.20E+05
7.00E+04
2.00E+04
Cumulative energy
0
10000
20000
30000
40000
50000
60000
70000
80000
Time/s
3.00E+05
2.50E+05
2.00E+05
1.50E+05
1.00E+05
5.00E+04
0.00E+00
Cumulative energy
67900
68900
69900
70900
71900
Time/s

c)

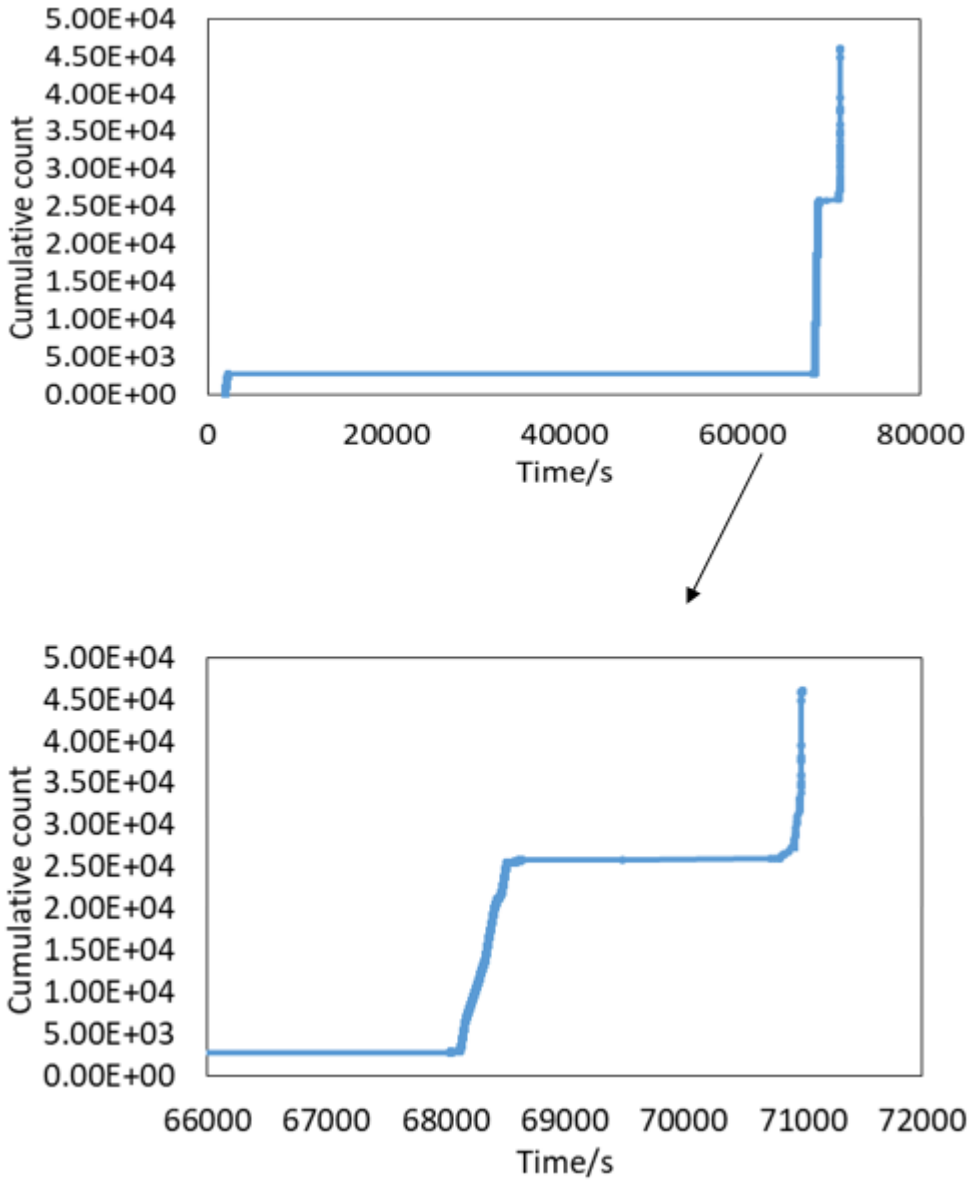

d)

Figure 7-51: a)amplitude b) count c)cumulative energy d)cumulative count versus time for 260 rail steel sample 1

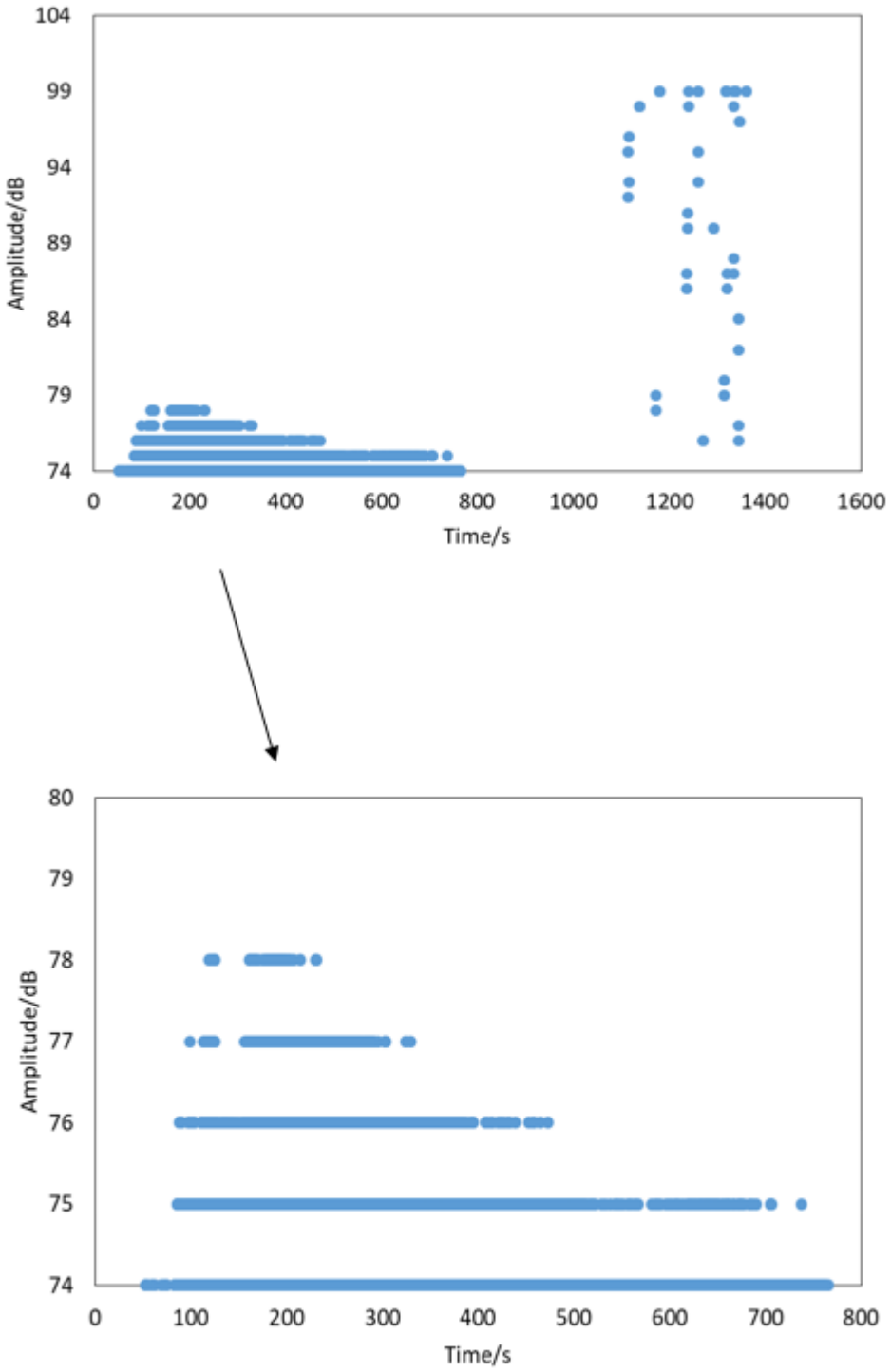
104
99
94
89
84
79
74
Amplitude/dB
0
200
400
600
800
1000
1200
1400
1600
Time/s
80
79
78
77
76
75
74
Amplitude/dB
0
100
200
300
400
500
600
700
800
Time/s

a)

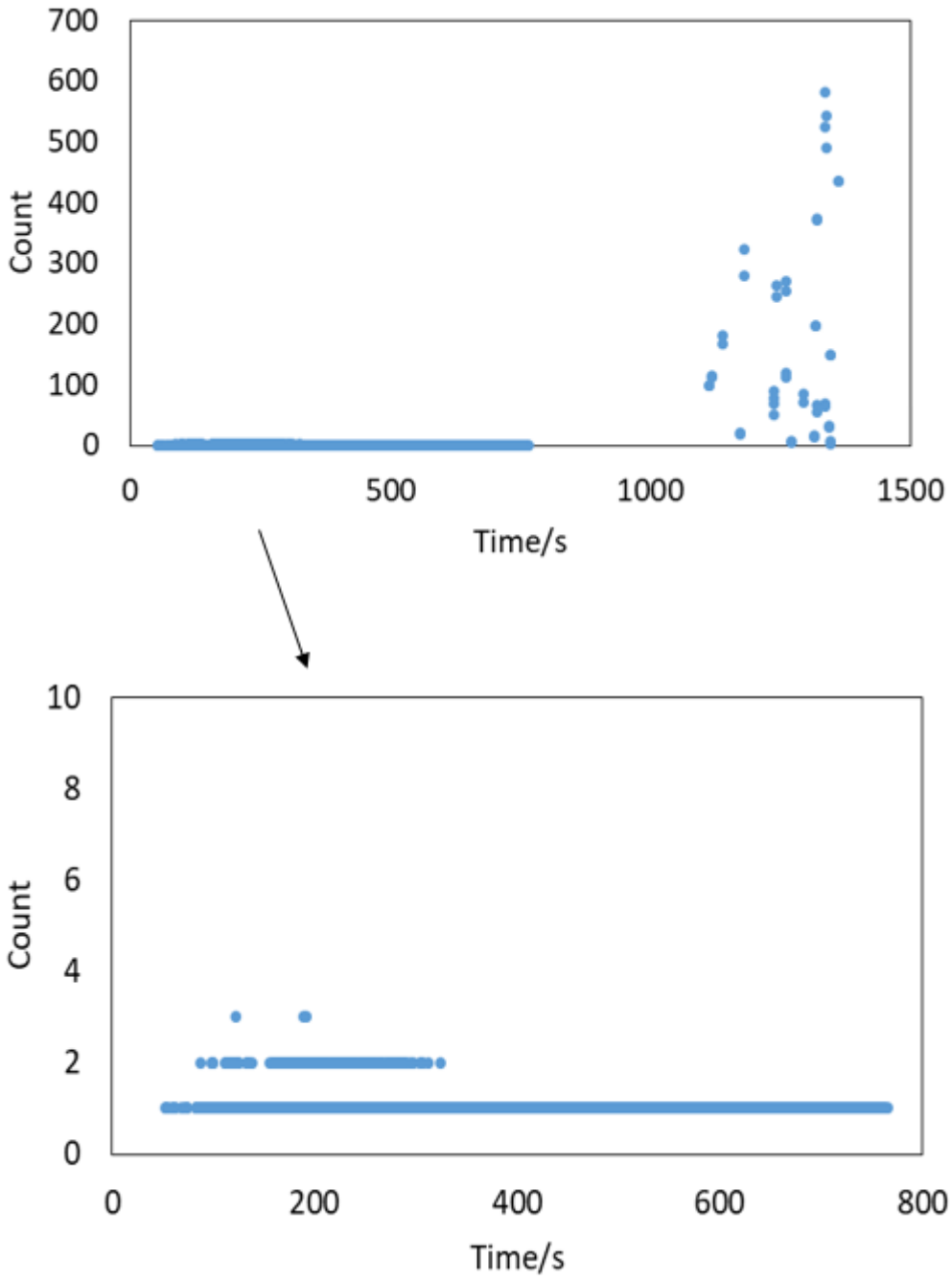
700
600
500
400
300
200
100
0
Count
0
500
1000
1500
Time/s
10
8
6
4
2
0
Count
0
200
400
600
800
Time/s

b)

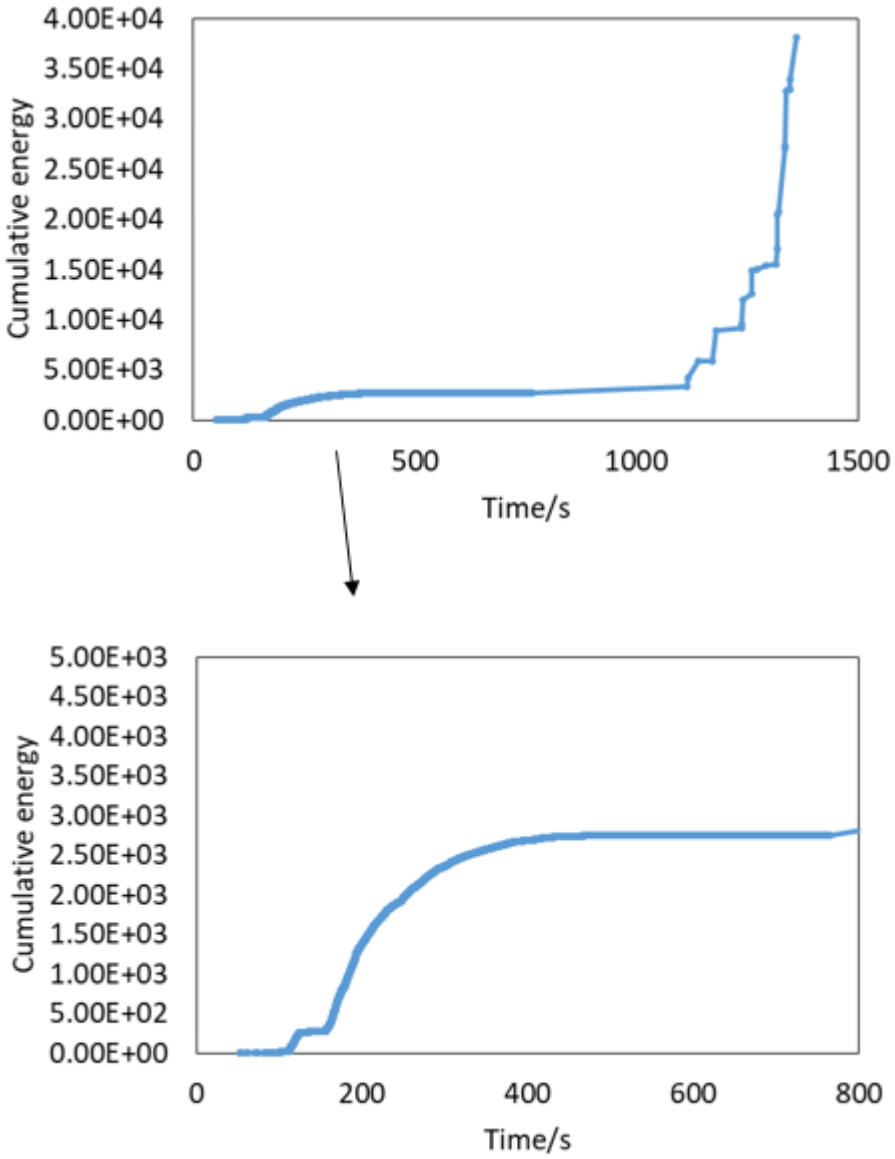
4.00E+04
3.50E+04
3.00E+04
2.50E+04
2.00E+04
1.50E+04
1.00E+04
5.00E+03
0.00E+00
Cumulative energy
0
500
1000
1500
Time/s
5.00E+03
4.50E+03
4.00E+03
3.50E+03
3.00E+03
2.50E+03
2.00E+03
1.50E+03
1.00E+03
5.00E+02
0.00E+00
Cumulative energy
0
200
400
600
800
Time/s

c)

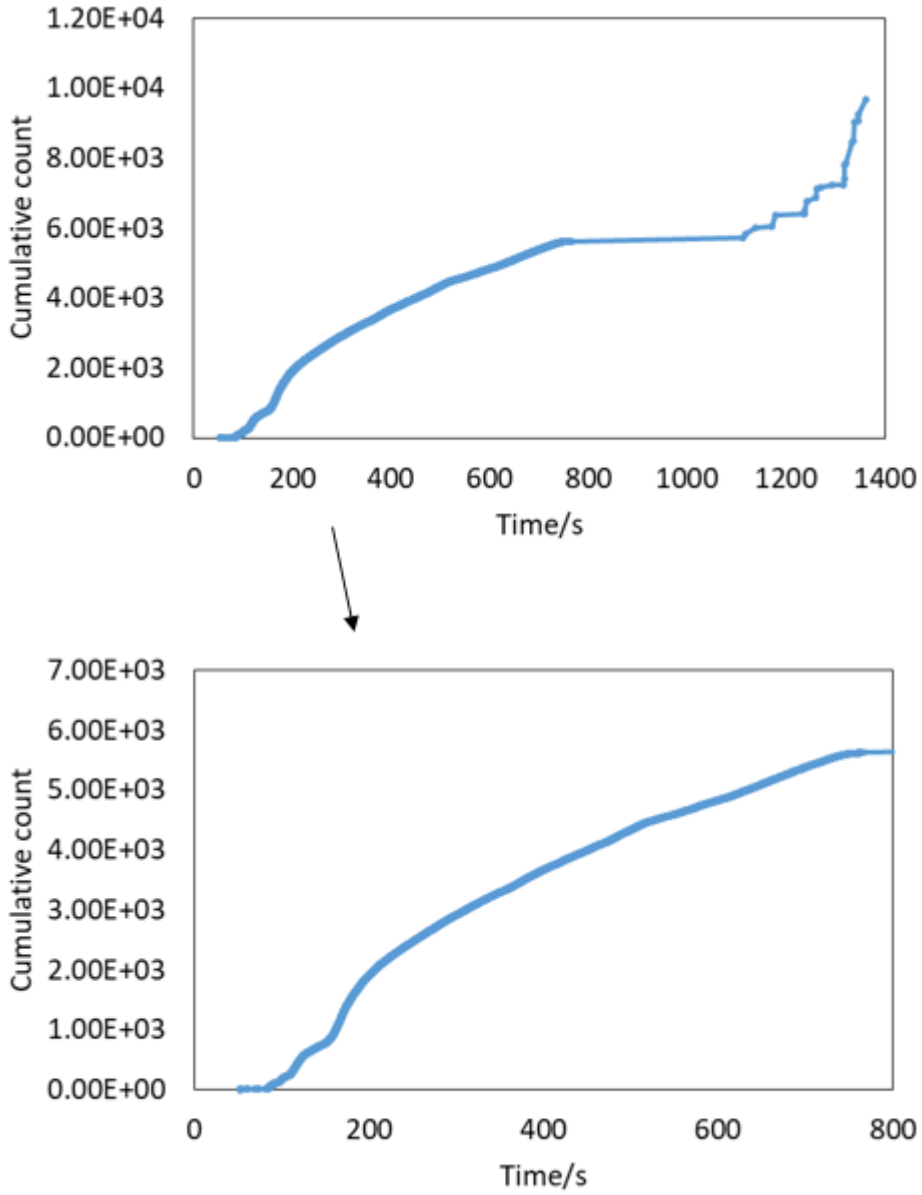

Figure 7-52: a) amplitude b) energy c) cumulative energy d) cumulative count versus time for 260 rail steel sample 2

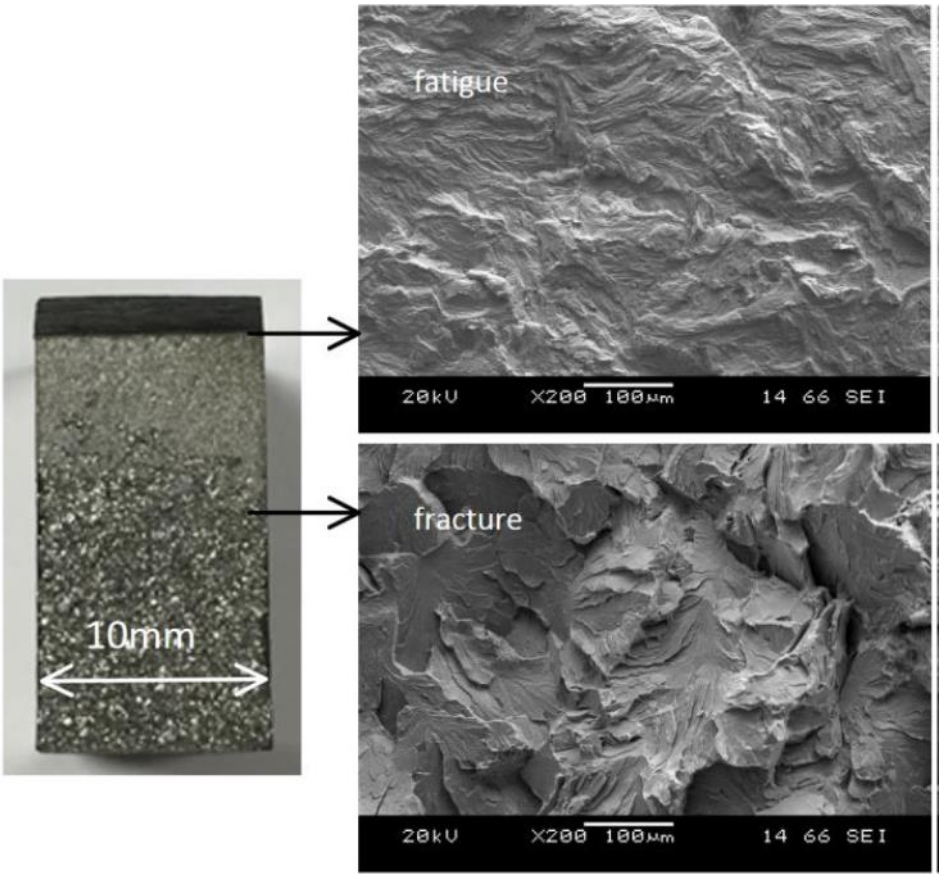

Figure 7-53: Fracture surface of three point bending sample

7.2.3 Analysis of AE signals captured with the customized system

Figure 7-54 shows the variation of different parameters with measurement time for one non-precracked Hadfield sample during the high frequency test. The RMS values successfully show the degradation process of the tested sample .The RMS shows obvious increase trend after initial decrease following the crack initiation captured by the DCPD technique, although some fluctuation in the results can also be observed. Peak-peak values at two different levels can be found before and after crack initiation, respectively. The peak-peak values do not show increase trend as that shown by RMS. It is obvious that crest factor and kurtosis values before and after crack initiation in this case do not

show big difference, however they can also capture the big value jump(indicated by the red arrows) that has been reflected by RMS and peak-peak analysis. Skewness shows a downward trend after crack initiation, however the big deviations can still be observed.

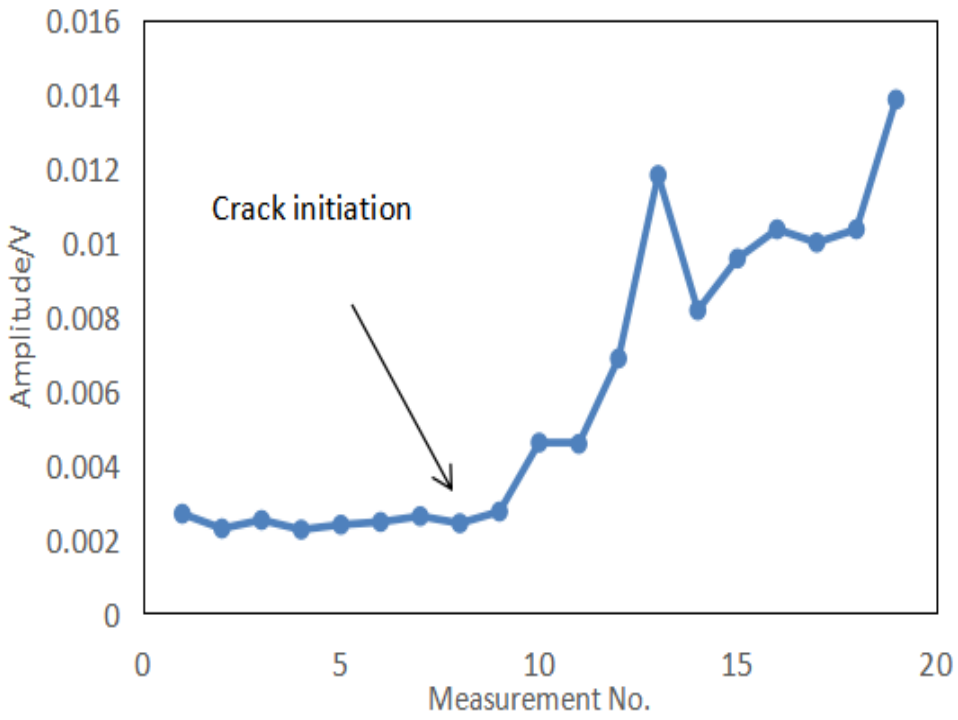

a)

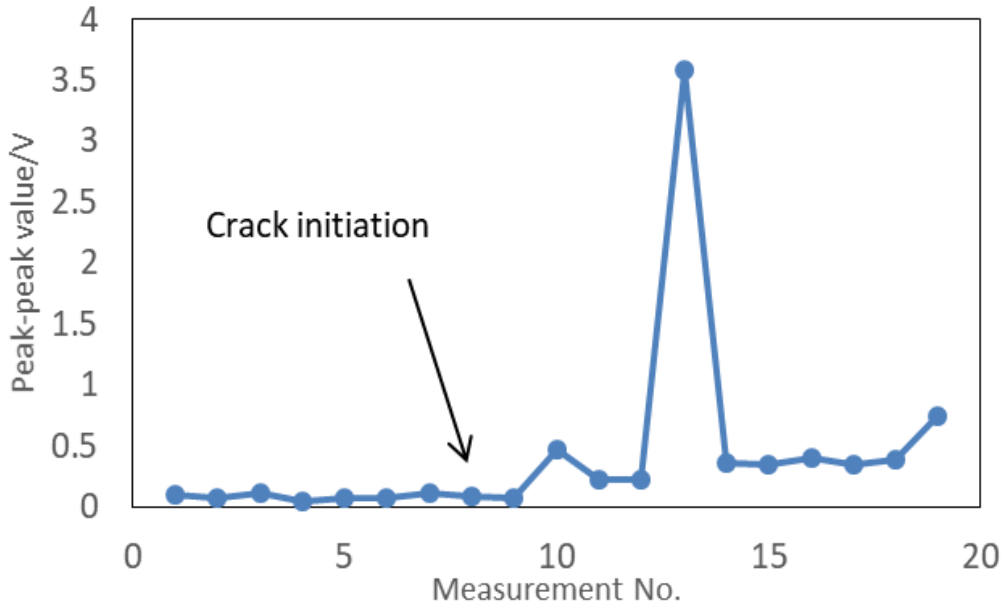
Peak-peak value/V
4
3.5
3
2.5
2
1.5
1
0.5
0
Crack initiation
0
5
10
15
20
Measurement No.

b)

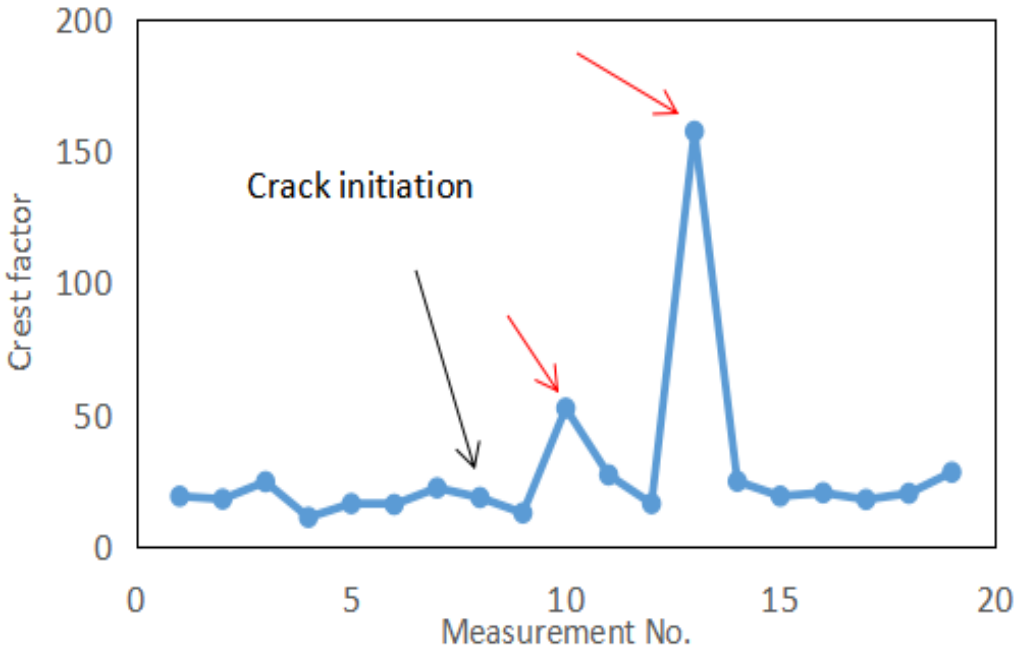
Crest factor
200
150
100
50
0
Crack initiation
0
5
10
15
20
Measurement No.

c)

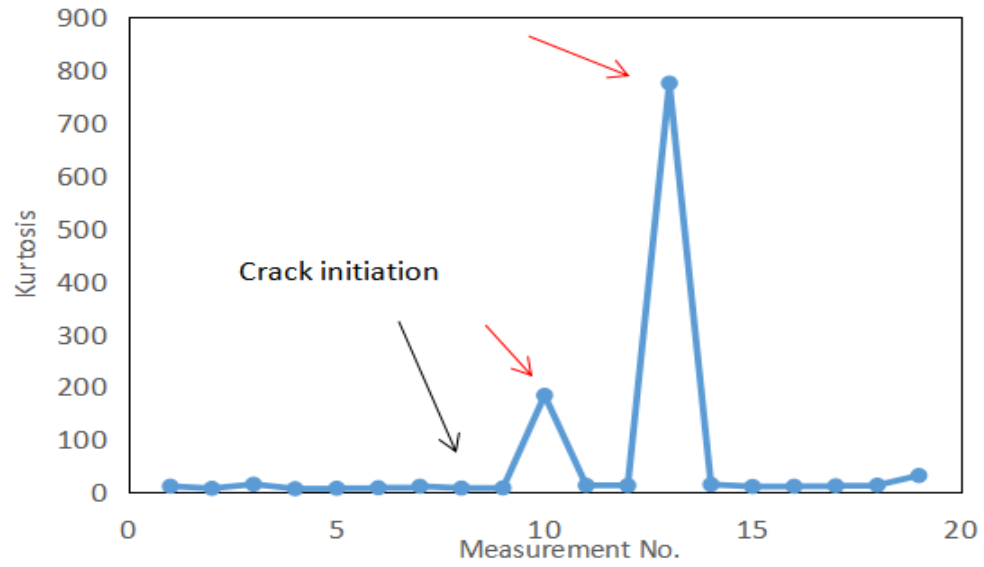

d)

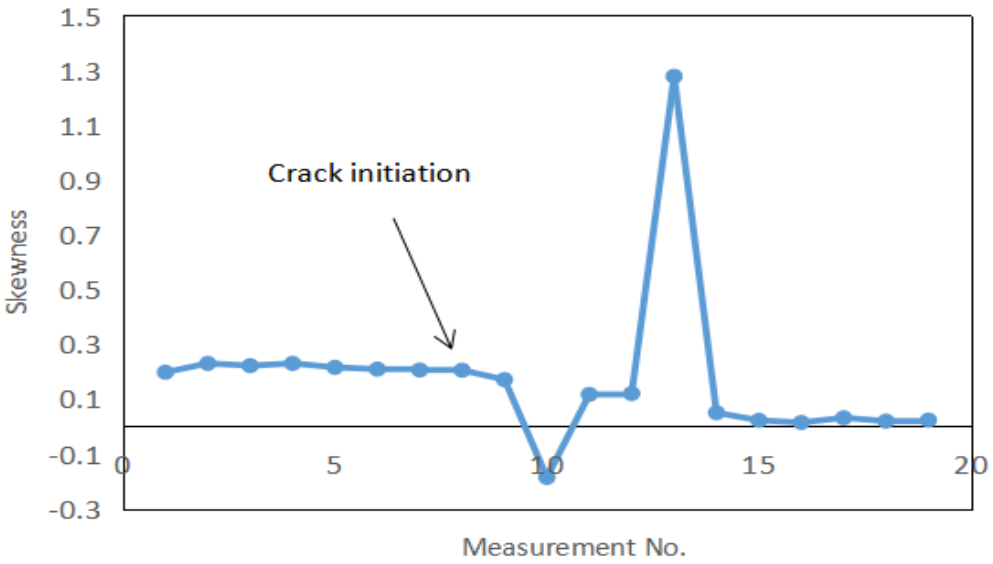

e)

Figure 7-54: Variation of overall a)RMS b)peak-peak value c)crest factor d)kurtosis e)skewness with measurement No.

Figure 7-55 shows the signal differences between early stage and later stage of the Hadfield sample during the high frequency test. The moving RMS, crest factor and kurtosis values of the signal at the late stage show obvious increase compared with those of the signal at the early stage, whereas most moving skewness values show a decrease the signal at the late stage.

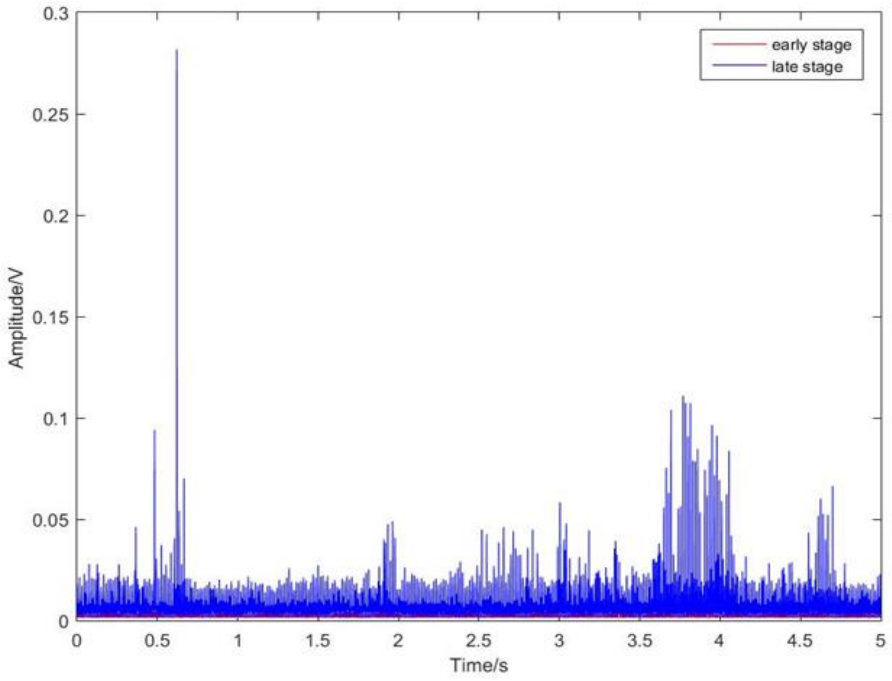

a)

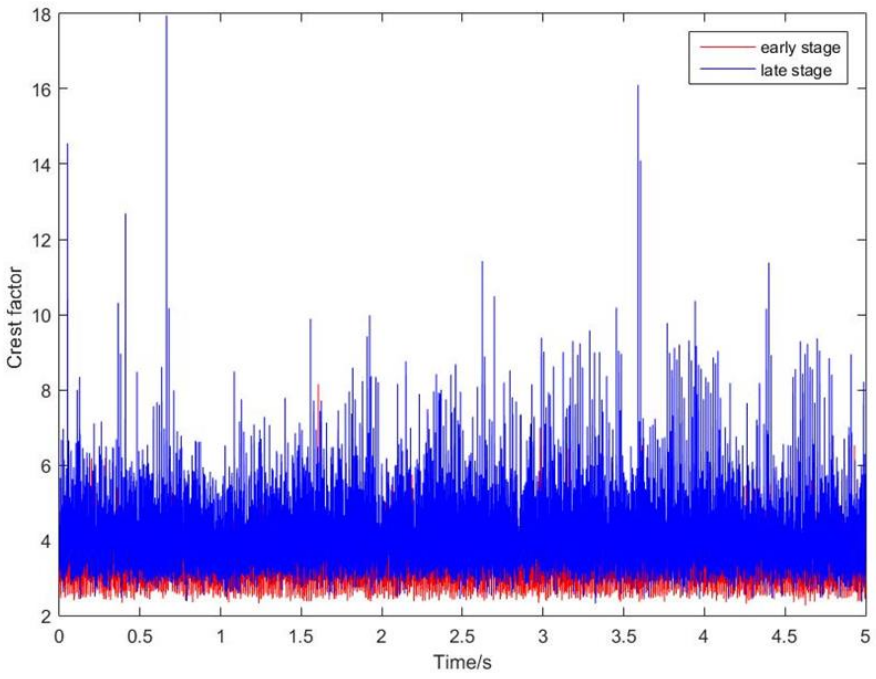
early stage
late stage
Crest factor
Time/s
18
16
14
12
10
8
6
4
2
0
0.5
1
1.5
2
2.5
3
3.5
4
4.5
5

b)

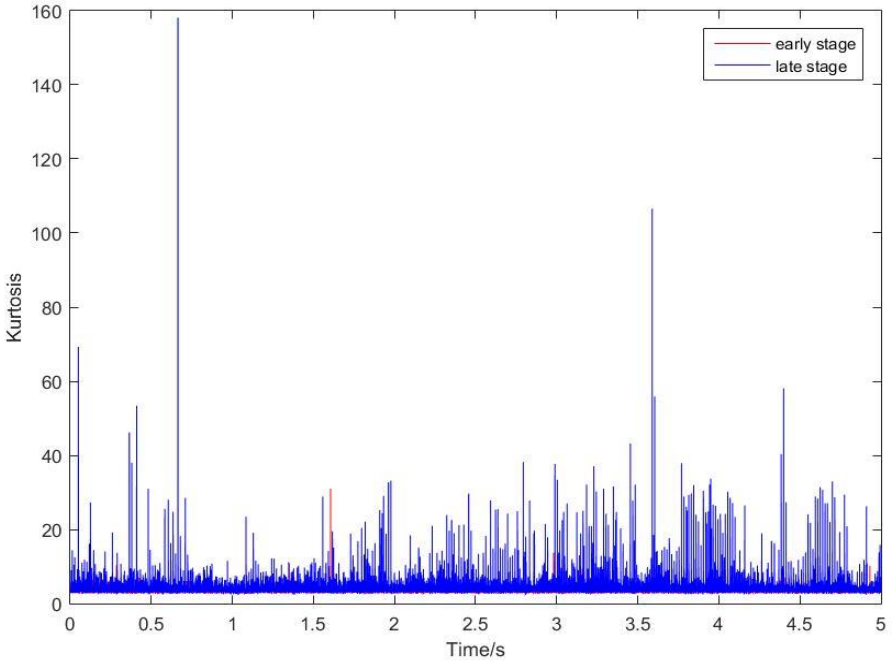
early stage
late stage
Kurtosis
Time/s
160
140
120
100
80
60
40
20
0
0
0.5
1
1.5
2
2.5
3
3.5
4
4.5
5

c)

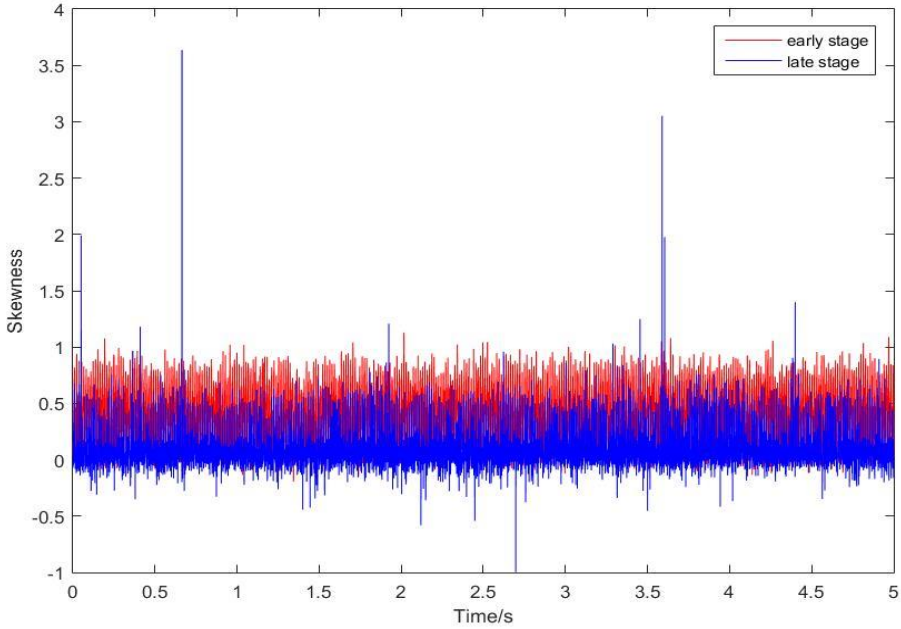

d)

Figure 7-55: Comparison between data captured at early and late stage for a)moving RMS b)moving crest factor c)moving kurtosis d)moving skewness

The application of AE to monitor the integrity of rails and crossings in the field can be complicated by two main factors. Firstly, the external noise level in the field can be much higher than that during the laboratory trials. Secondly, some types of crack grow under mixed mode loading condition. However, as the bending fatigue configuration employed during the laboratory trials is partially representative of the loading conditions that the rails and crossings are subjected to, the feasibility of applying AE to monitor the integrity of rails and crossings has been justified.

7.3 Field tests

Frequency and power distribution analysis can be effective on AE signals. Such conclusion is also suitable for wayside crossing monitoring mainly because crack growth

and plastic deformation would generate unique spectral information and are not correlated with other AE sources.

Therefore, the power spectrum estimation (PSE) is used as the feature to perform correlation processing. By calculating the similarity between the PSE of both template and the acquired AE data, we are able to determine whether such a signal is generated by crack growth or plastic deformation.

The signals attributed to crack evolution from the laboratory tests have been used as templates for correlation analysis, as the loading conditions during the laboratory tests are partially representative of the loading conditions of crossings in the field. The principle is that if signals captured from the instrumented crossing have similar features to the templates, it is highly possible that damage evolution occurs in the crossings. Frequency and power distribution can be used as the feature for correlation processing.

The severity of damage in the crossings have been evaluated based on the correlation between the signals and the templates. Low frequency components of the signals have been filtered out before correlation analysis to weaken the influence of false AE sources.

One template related to crack growth has been selected from the raw data captured from laboratory tests on Hadfield steel samples as shown in Figure 7-56.

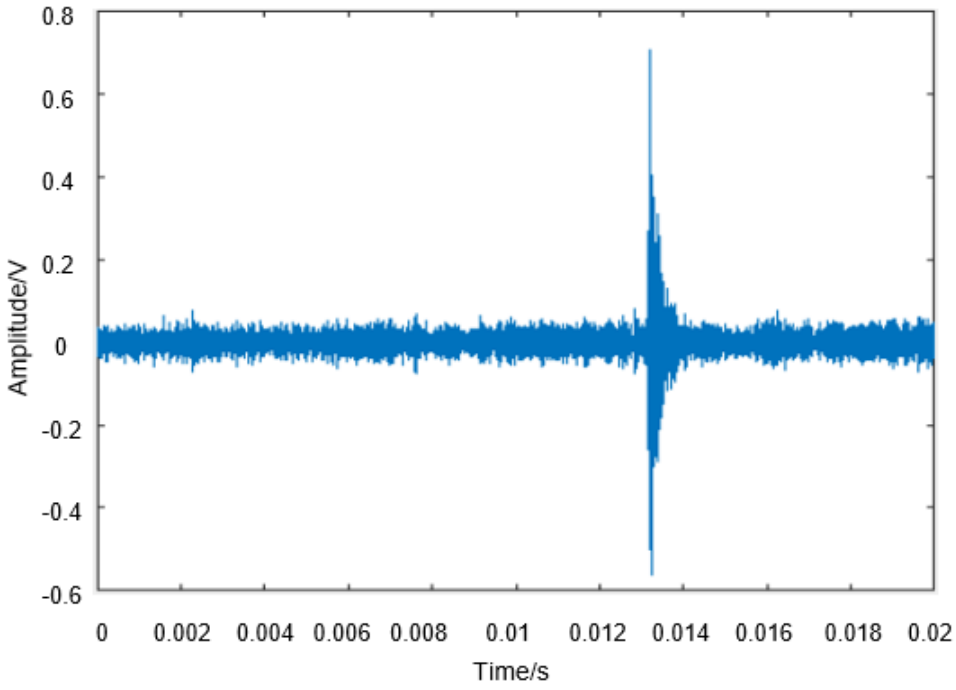

Figure 7-56: Template related to crack growth at the early stage

As mentioned earlier, the Wembley crossing was confirmed to be healthy using visual inspection, so no indication of damage evolution is anticipated from the correlation analysis. Figure 7-57 shows the raw AE signal captured from one of the AE sensors while a passenger train passed over the crossing. The only few high peaks might be caused by the sliding of the wheels.

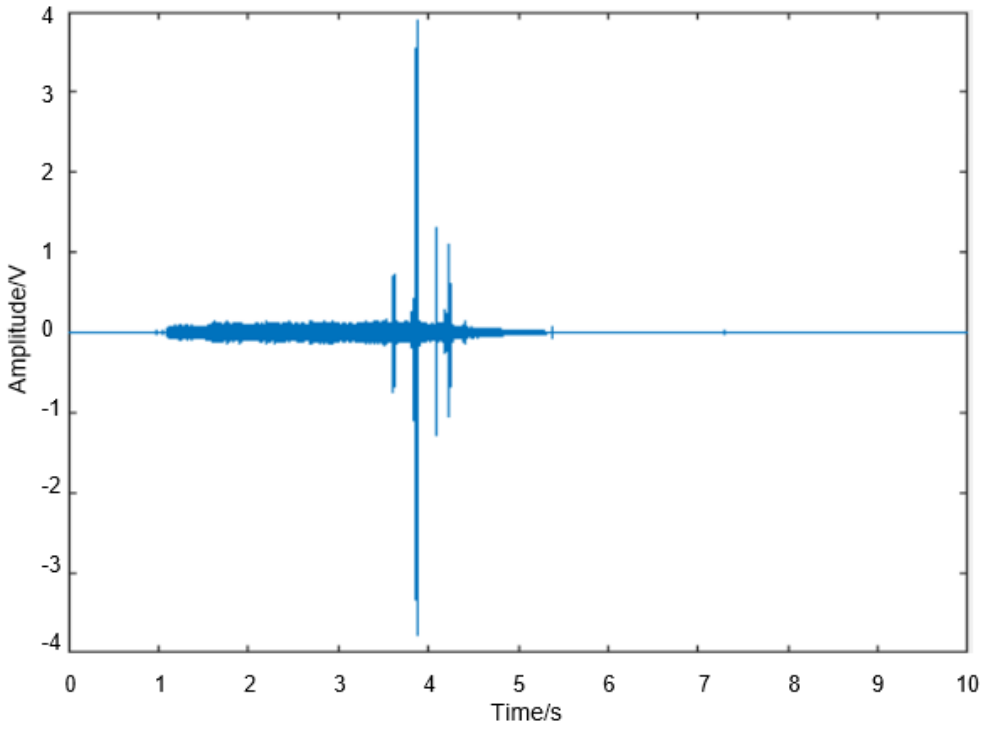

Figure 7-57: Raw AE signal from passenger train passing over the Wembley crossing.

Figure 7-58 shows the cross-correlation result using the template related to crack growth at the early stage. No obvious indication of damage evolution can be observed in the result. The correlation between the raw signal and the template related to crack growth at the middle stage further confirms that there is no damage evolution happening in Wembley crossing.

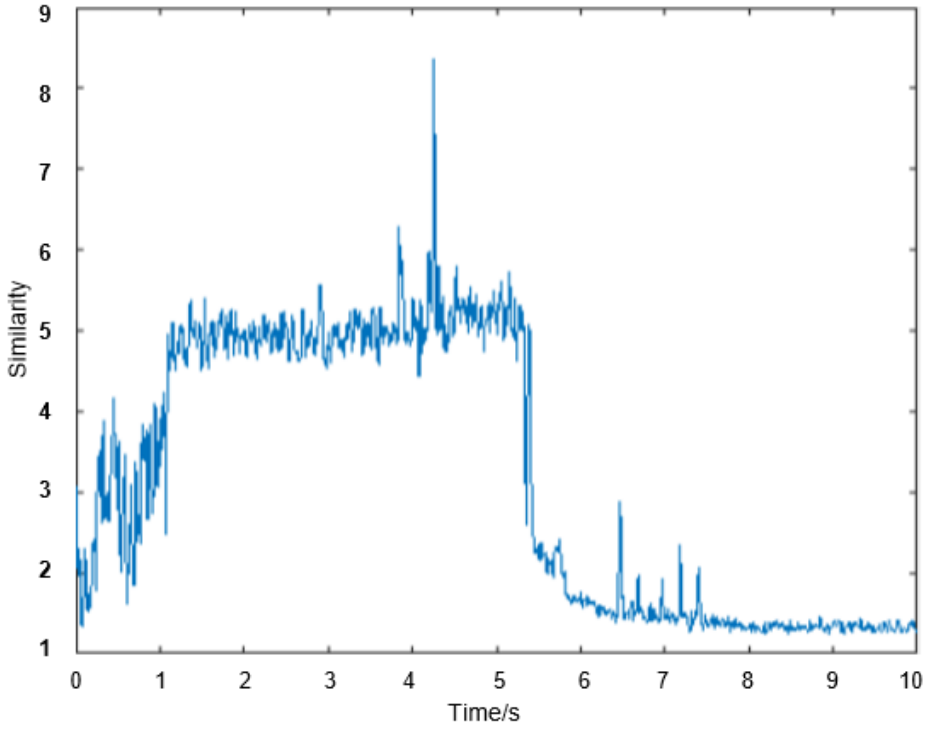

Figure 7-58: Cross-correlation result using the early stage crack growth template.

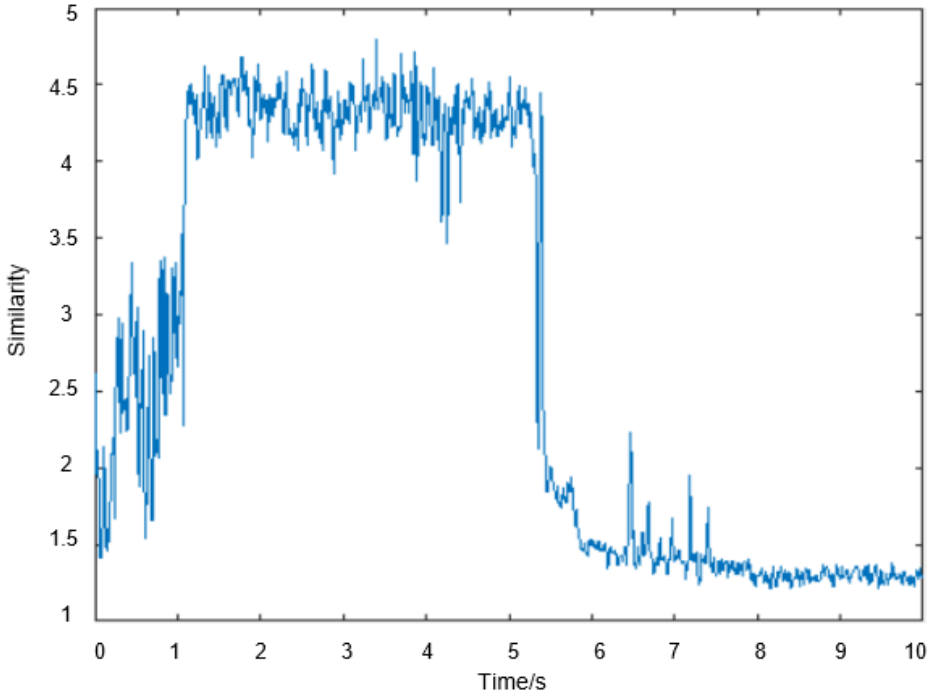

Figure 7-59: Cross-correlation result using the middle stage crack growth template

Figure 7-60 shows signals captured during the passing of a freight train. The high peaks in the signal are mainly generated by engine noise causing sliding of locomotive wheels. Apart from the engine noise induced peaks, no other visible peaks can be observed during the passing of the rest of train, which indicates no crack growth occurs in the crossing.

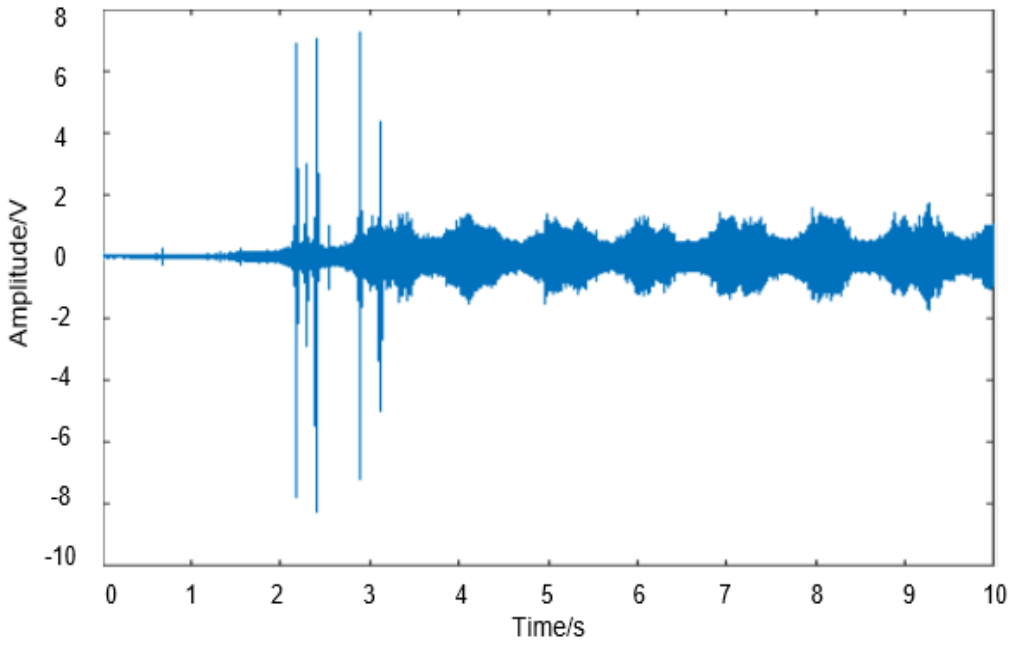

Figure 7-60: Raw AE signal captured during the passing of a freight train.

Figure 7-61 shows the correlation result using the early stage damage template. No obvious peaks indicative of crack growth can be found in the plot.

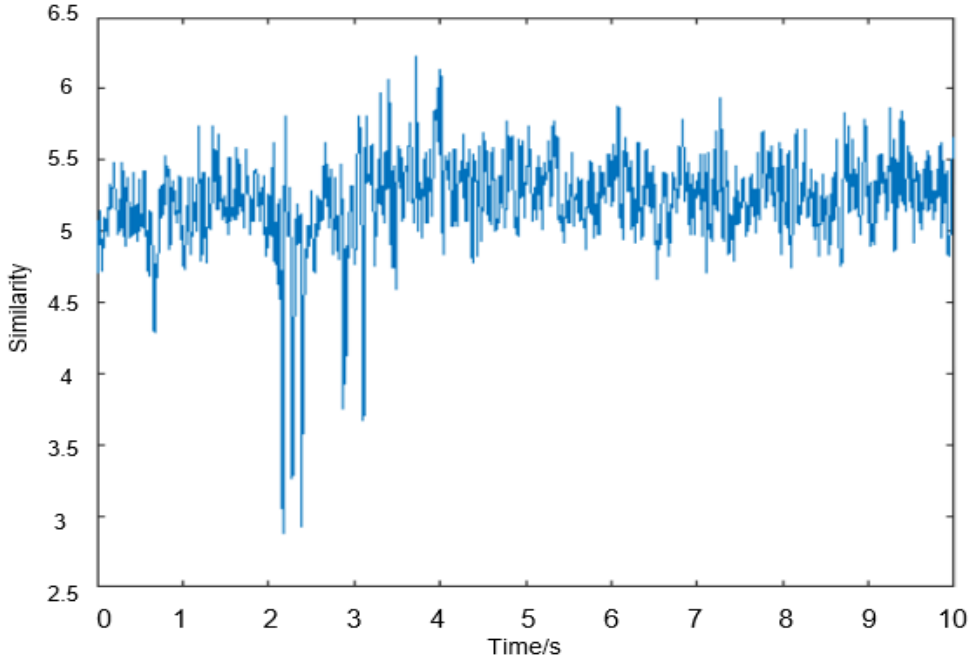

Figure 7-61: Correlation result using the early stage crack growth template.

Figure 7-62 shows cross-correlation result based on the moderate stage damage template. Similarly, no obvious peaks indicative of crack growth can be found in the plot.

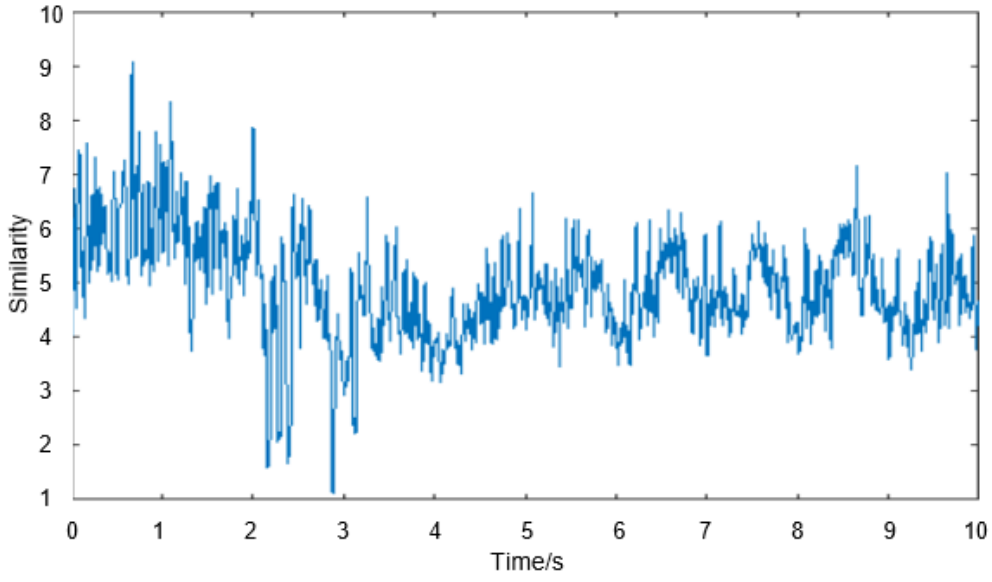

Figure 7-62: Cross-correlation result using the middle stage crack growth template.

AE raw data have been acquired during the passing of both passenger and freight train at Hatton crossing. Figure 7-63 shows the raw AE data captured during the passing of one of the Chiltern passenger trains at the instrumented crossing. As can be seen, several high amplitude peaks can be observed in the waveform, although the Chiltern passenger train is similar to the one passing by at the Wembley crossing in terms of size and weight. In addition, the gain value used at the Hatton crossing has been decreased from 40dB to 29dB to further undermine the influence of background noise.

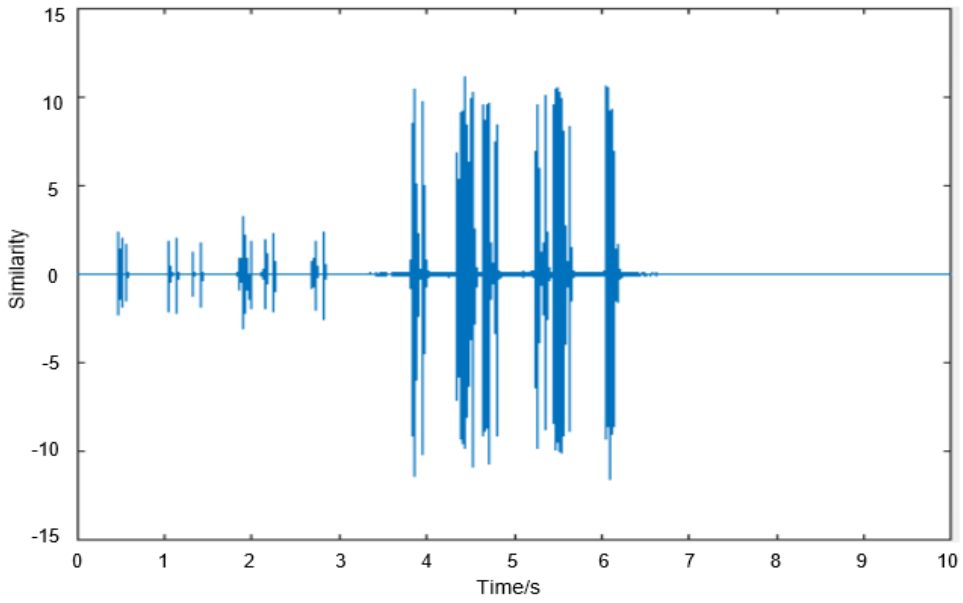

Figure 7-63: AE data captured during the passing of one of the Chiltern passenger trains

Figure 7-64 shows the cross-correlation result using the early stage crack growth template. Several clearly visible peaks signifying crack growth can be found in the result. It is noteworthy that the lower values of the peaks than those at the Wembley crossing is caused by the lower amplification level used at the Hatton crossing. Hence it is important to check the background signal level when comparing the peaks for different tests.

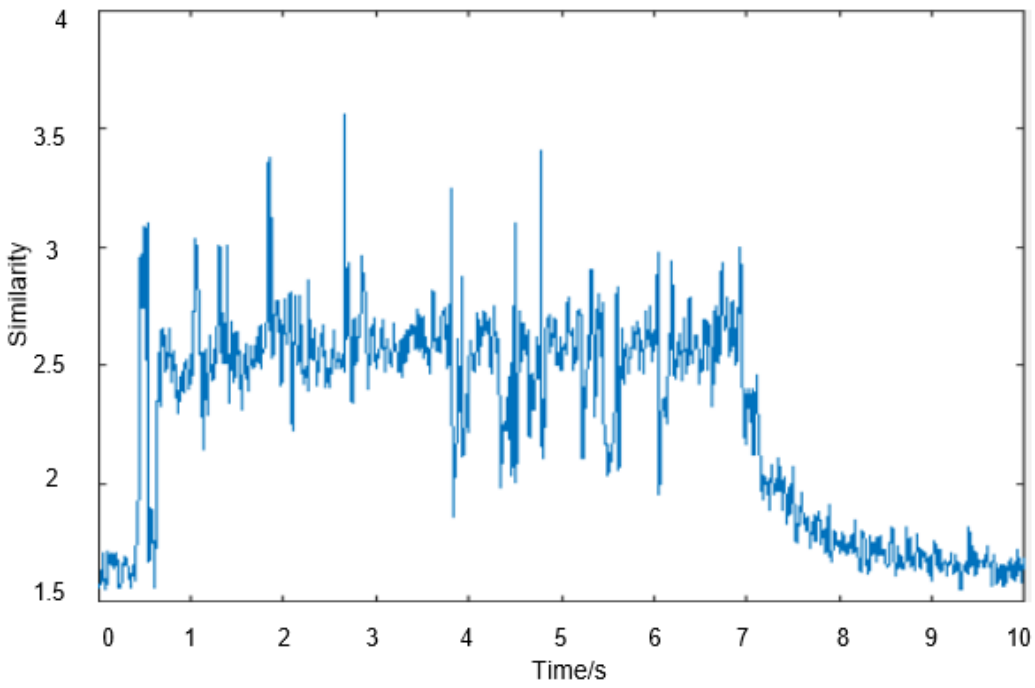

Figure 7-64: Cross-correlation result using the early stage crack growth template.

Figure 7-65 shows the cross-correlation result using the early stage crack growth template. Several peaks signifying damage progression during the loading sequence can be found in the waveform.

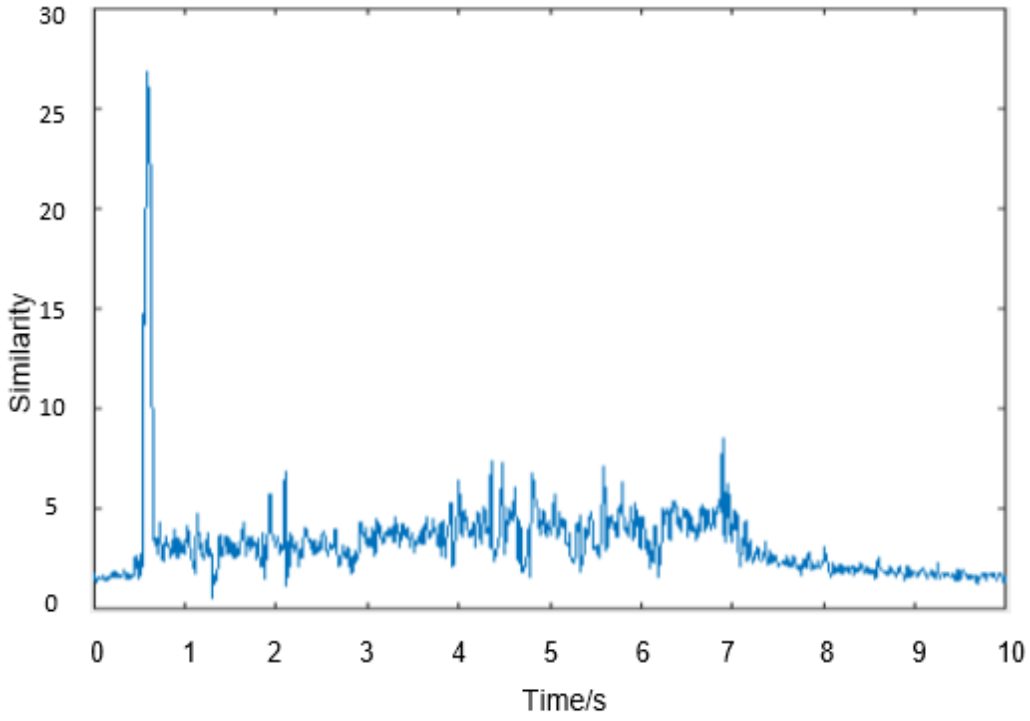

Figure 7-65: Cross-correlation result based on the middle stage crack growth template

Figure 7-66 shows the raw AE data captured during the passing of a heavy freight train at the instrumented crossing. The small peaks in the waveform are caused by periodical loading of the wheels on the crossing and the few high peaks might be due to heavier weight of one of the wagons

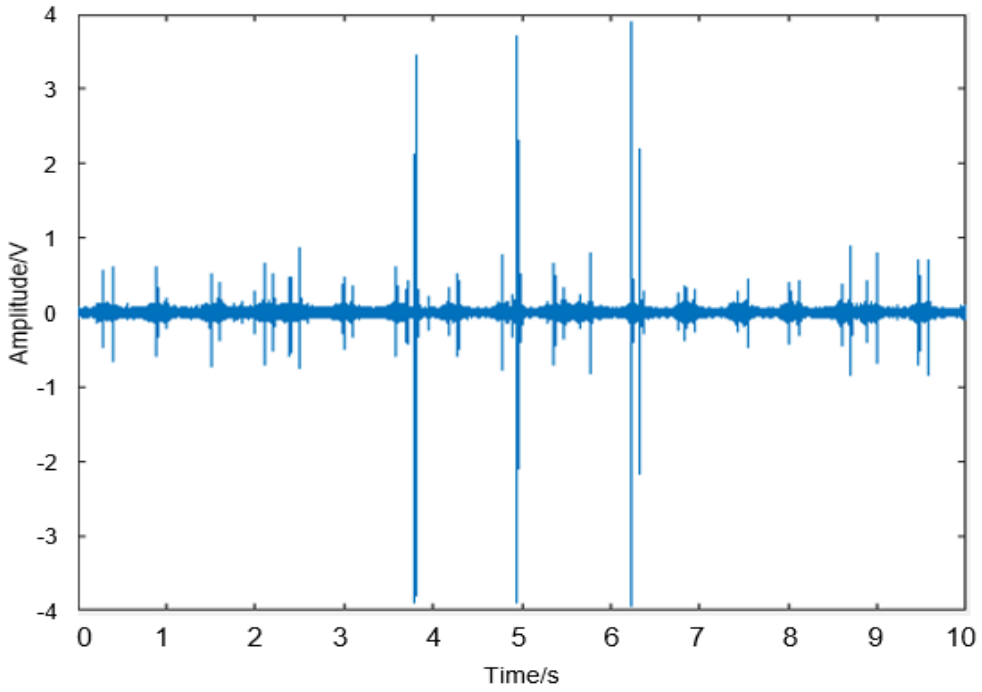

Figure 7-66: AE data captured during the passing of a heavy freight train

Figure 7-67 shows the cross-correlation result using the early stage crack growth template. Peaks indicative of crack growth nearly appear in every loading cycle.

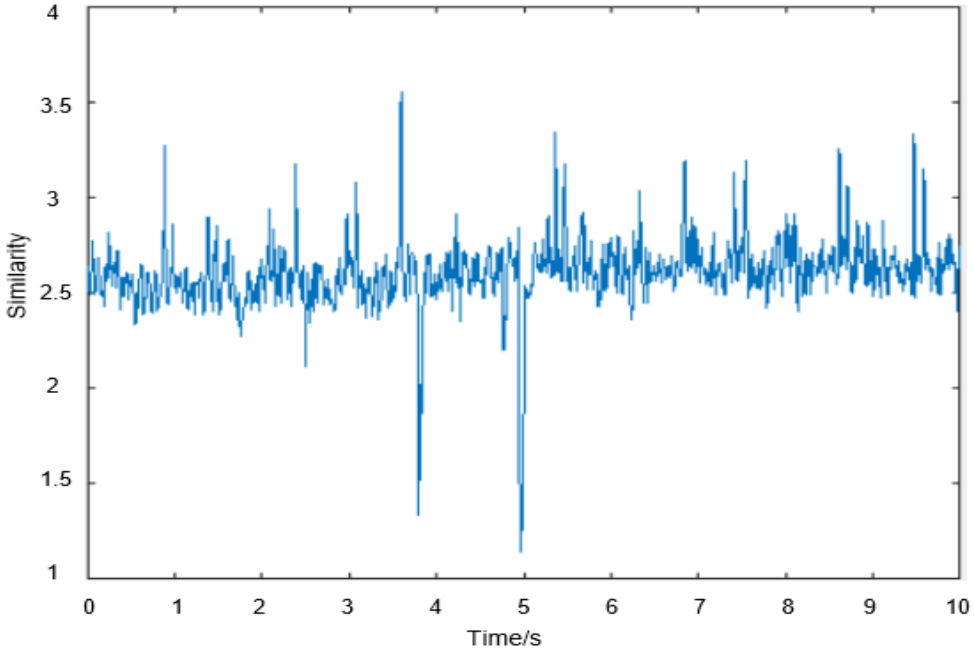

Figure 7-67: Cross-correlation result using the early stage crack growth template.

Figure 7-68 shows the cross-correlation result using the middle stage crack growth template. It is noteworthy that at the 5 sec a very high peak is clearly evident indicating the crack grows more rapidly at that point.

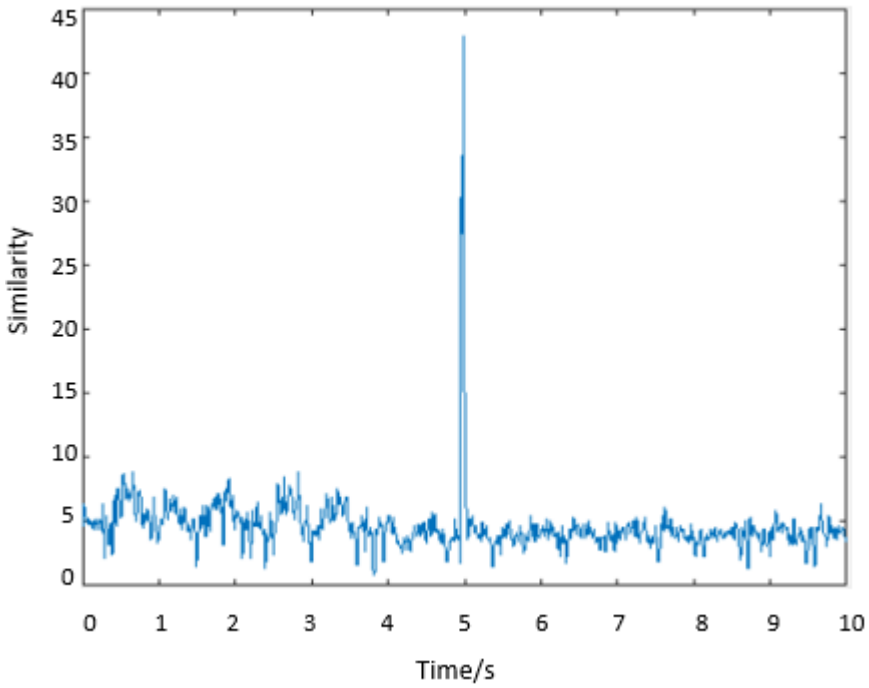

Figure 7-68: Cross-correlation result using the middle stage crack growth template.

Chapter 8:

Conclusions and Future Work

CHAPTER 8 : CONCLUSIONS AND FUTURE WORK

8.1 Conclusions

This research has investigated the possibility of using acoustic emission technique to monitor the structural integrity of rails and crossings in real time. Low and high frequency bending fatigue crack growth tests have been carried out on the three different types of specimens: R260 grade rail steel samples(precracked and non-precracked), Hadfield steel samples(precracked and non-precracked), and carbon steel sample with AE being used to monitor the damage evolution process. The configuration of the bending tests is partially representative of the actual loading experienced by the rails and crossings.

For laboratory tests, both a customised system developed by University of Birmingham and a commercial AE system procured from Physical Acoustics Corporation were used to monitor the bending fatigue tests. For the commercial system, parameters including amplitude, energy, risetime, duration, count and ASL were used to correlate crack length with AE hits. For R260 steel, high amplitude (>70dB) AE hits occur even during stable crack propagation and this is attributed to brittle cleavage fracture. Sudden increase of crack length at certain stage before final failure can be successfully detected by AE. The fractograph and AE energy results show brittle cleavage fracture occur certain crack length for all R260 steel specimens. The AE cumulative energy was clearly correlated to microstructural features related to brittle cleavage fracture. Hence it has confirmed that brittle fracture can be quantitatively described using AE.For Hadfield steel, nearly all high amplitude(>70dB) hits occur at the final stage of crack growth and the stair-like amplitude distribution can be observed before final failure. The correlation between AE parameter rate (count, duration, energy) and crack growth rate, is performed for the whole load range. The parameter rate generally shows similar trend to crack growth rate for both

types of steel. However, the previous loading history like precracking can influence the correlation.

The waveform based analysis has been carried out on the data captured with the customized system developed by University of Birmingham. Crack growth related peaks can be clearly observed in the raw AE waveforms captured by the customized system during the low frequency bending fatigue tests on both R260 and Hadfield steel samples. The intensity of crack growth related peaks increases from early stage to final stage. Peaks due to crack surface rubbing can also be found in some of the waveforms. Fourier transform has been proved to be capable of differentiate crack growth related peaks from those due to crack surfaces rubbing. The trend of various parameters with time for the AE waveforms captured during the bending fatigue test on Hadfield steel sample was obtained. The RMS shows a clear upward trend with some fluctuations also observed especially in the early stage. The trend of peak-peak, kurtosis, crest factor in the late stage is generally consistent with that for RMS, whereas skewness shows decreasing trend for low frequency fatigue tests.

The possibility of using algorithms like moving RMS, crest factor, kurtosis and skewness to characterize the severity of damage have also been investigated. All the algorithms show the capability to reflect the severity of damage accurately. However, the results obtained by various algorithms should be interpreted based on the principal of each algorithm. In addition, SK has been employed to analyse the signals. Although SK values can reveal the damage progression, the frequency ranges at which SK attain the peak values vary considerably at different stages. This is due to the influence of noise caused by crack faces rubbing during crack opening and closing. In addition, the feasibility of applying various filters to weaken the influence of noise has been explored. The influence

of applying Swansong II filters in this case is very limited. The bandpass filter designed based on bandwidth and centre frequency derived from Kurtogram analysis has proved to be effective in undermining the influence of external noise.

Finally, initial field trials have been carried out on two different crossings on the west coast mainline. Template-based cross correlation analysis, which is capable of differentiating the AE source mechanisms, like crack growth, impact etc., has been employed to analyse the data captured from the instrumented crossing. It has shown that cross correlation analysis is effective in evaluating the health state of the monitored crossings. Overall, this research has shown that AE can be used as a tool to effectively evaluate the structural integrity of rails and Hadfield steel crossings online.

8.2 Future work

Further work could be done from the following aspects to improve the accuracy of evaluation of the damage of rails and crossings with AE.

The fatigue crack growth tests carried out in the current research are of mode I, however in actual railway line, some types of crack grow under mixed mode loading condition. Hence it would be beneficial that AE monitoring of fatigue crack growth tests on both types of steel samples under Mix-mode (mode I and mode II) loading could be performed to obtain the signal features. The relationship between different AE parameters including amplitude, energy, risetime, count ,duration etc. during the fatigue tests could be investigated in more depth to see its change with damage progression. More signal processing techniques should be investigated in terms of their capability to reveal the severity of damage accurately.

The possibility of using the average duration of AE events captured using the commercial system to determine optimal window size for time series analysis should also be investigated.

REFERENCES

1. Network Rail's Strategic Business Plan-Maintenance activity and expenditure, *Document ref. SBPT222, Version 0.14*. 01/2013.
2. Turner, C., et al., *A review of key planning and scheduling in the rail industry in Europe and UK.* Proceedings of the Institution of Mechanical Engineers, Part F: Journal of Rail and Rapid Transit, 2015: p. 0954409714565654.
3. Yılmazer, P., A. Amini, and M. Papaelias, *The structural health condition monitoring of rail steel using acoustic emission techniques.* 2012.
4. Dadashi, N., et al. *A framework of data processing for decision making in railway intelligent infrastructure*. in *Cognitive Methods in Situation Awareness and Decision Support (CogSIMA), 2011 IEEE First International Multi-Disciplinary Conference on*. 2011. IEEE.
5. Office of Rail and Road, *UK Rail Industry Financial Information 2015-16*. 02/2017.
6. Garnham, J.E. and C.L. Davis, *5 - Rail materials*, in *Wheel–Rail Interface Handbook*, R. Lewis and U. Olofsson, Editors. 2009, Woodhead Publishing. p. 125-171.
7. Herring, D.H. *Principles of Gas Nitriding: The Nitriding Process (Part 1)*. [online] 2011; Available from: http://www.industrialheating.com/articles/89998-principles-of-gas-nitriding-the-nitriding-process-part-1?v=preview.
8. Maya-Johnson, S., A. Ramirez, and A. Toro, *Fatigue crack growth rate of two pearlitic rail steels.* Engineering Fracture Mechanics, 2015. **138**: p. 63-72.
9. Wu, K. and H. Bhadeshia, *Extremely fine pearlite by continuous cooling*

transformation. Scripta Materialia, 2012. **67**(1): p. 53-56.

10. Aglan, H., et al., *Mechanical and fracture behavior of bainitic rail steel.* Journal of materials processing technology, 2004. **151**(1): p. 268-274.
11. Rae, *BS EN 13674-1:2011 - Railway applications. Track. Rail. Vignole railway rails 46 kg/m and above*. Bahnanwendungen. Oberbau. Schienen. Vignolschienen ab 46 kg/m.
12. EN, T., *13674-1): Railway applications–track–rail–part 1: Vignole railway rails 46 kg/m and above*. 2011, Brussels.
13. El-Shabasy, A.B. and J.J. Lewandowski, *Effects of load ratio, R, and test temperature on fatigue crack growth of fully pearlitic eutectoid steel (fatigue crack growth of pearlitic steel).* International journal of fatigue, 2004. **26**(3): p. 305-309.
14. Srivastava, A.K. and K. Das, *Microstructural characterization of Hadfield austenitic manganese steel.* Journal of Materials Science, 2008. **43**(16): p. 5654-5658.
15. Ham, Y.-S., et al., *Critical cooling rate on carbide precipitation during quenching of austenitic manganese steel.* China Foundry, 2010. **2**: p. 016.
16. Zhang, F., et al., *Explosion hardening of Hadfield steel crossing.* Materials Science and Technology, 2010. **26**(2): p. 223-229.
17. Kang, J., et al., *Cyclic deformation and fatigue behaviors of Hadfield manganese steel.* Materials Science and Engineering: A, 2014. **591**: p. 59-68.
18. Niendorf, T., et al., *Fatigue crack growth—microstructure relationships in a high-manganese austenitic TWIP steel.* Materials Science and Engineering: A, 2010. **527**(9): p. 2412-2417.

19. Hamada, A., L. Karjalainen, and J. Puustinen, *Fatigue behavior of high-Mn TWIP steels.* Materials Science and Engineering: A, 2009. **517**(1): p. 68-77.

20. Harzallah, R., et al., *Rolling contact fatigue of Hadfield steel X120Mn12.* Wear, 2010. **269**(9): p. 647-654.

21. Mahlami, C. and X. Pan, *An Overview on high manganese steel casting.* 2014.

22. Pook, L., *Why Metal Fatigue Matters*. 2007: Springer.

23. Callister, W.D. and D.G. Rethwisch, *Materials science and engineering: an introduction*. Vol. 7. 2007: Wiley New York.

24. Milella, P.P., *Fatigue and corrosion in metals*. 2012: Springer Science & Business Media.

25. Frost, N.E., K.J. Marsh, and L.P. Pook, *Metal fatigue*. 1974: Courier Corporation.

26. eFunda. *Stress Intensity Factor and Crack Tip Stresses*. [online] 2018 [cited 2018 04/01]; Available from: http://www.efunda.com/formulae/solid_mechanics/fracture_mechanics/fm_lefm_K.cfm.

27. Noels, L. *Fracture Mechanics Online Class*. unknown; Available from: http://www.ltas-cm3.ulg.ac.be/FractureMechanics/print.php?p=overview_P5.

28. ASM International. *Fatigue in Elements of Metallurgy and Engineering Alloys*. [online] 2008; Available from: http://www.asminternational.org/documents/10192/1849770/05224G_Chapter14.pdf.

29. Suresh, S. and R. Ritchie, *Propagation of short fatigue cracks.* International Metals Reviews, 1984. **29**(1): p. 445-475.

30. Milne, I., R.O. Ritchie, and B.L. Karihaloo, *Comprehensive structural integrity:*

cyclic loading and fatigue. Vol. 4. 2003: Elsevier.

31. Suresh, S., *Fatigue of materials*. 1998, Cambridge university press.
32. Pineau, A. and R. Pelloux, *Influence of strain-induced martensitic transformations on fatigue crack growth rates in stainless steels.* Metallurgical Transactions, 1974. **5**(5): p. 1103-1112.
33. Hornbogen, E., *Martensitic transformation at a propagating crack.* Acta Metallurgica, 1978. **26**(1): p. 147-152.
34. Kim, J.-K. and C.-S. Kim, *Fatigue crack growth behavior of rail steel under mode I and mixed mode loadings.* Materials Science and Engineering: A, 2002. **338**(1): p. 191-201.
35. Ritchie, R.O., *Mechanisms of fatigue-crack propagation in ductile and brittle solids.* International Journal of Fracture, 1999. **100**(1): p. 55-83.
36. totalmateria. *Linear Elastic Fracture Mechanics : Part One*. [Online] 2010; Available from: http://www.totalmateria.com/page.aspx?ID=CheckArticle&site=kts&NM=295.
37. Huang, M., et al., *Using acoustic emission in fatigue and fracture materials research.* JOM, 1998. **50**(11): p. 1-14.
38. Ringsberg, J.W. and A. Bergkvist, *On propagation of short rolling contact fatigue cracks.* Fatigue & Fracture of Engineering Materials & Structures, 2003. **26**(10): p. 969-983.
39. Ringsberg, J.W., *Life prediction of rolling contact fatigue crack initiation.* International Journal of fatigue, 2001. **23**(7): p. 575-586.
40. Sinclair, G. and R. Pieri, *On obtaining fatigue crack growth parameters from the literature.* International journal of fatigue, 1990. **12**(1): p. 57-62.

41. Hearn, E., *Mechanics of Materials, Vol. 2-The Mechanics of Elastic and Plastic Deformation of Solids and Structural Materials*. 1997, Butterworth-Heinemann.

42. Onal, O., et al., *Investigation of rolling contact crack initiation in bainitic and pearlitic rail steels.* Fatigue & Fracture of Engineering Materials & Structures, 2012. **35**(11): p. 985-997.

43. UMIST. *Failure of Materials* [online] Unknown [cited 2014 05/07]; Available from: http://pwatlas.mt.umist.ac.uk/internetmicroscope/micrographs/failure.html.

44. Care, R., et al., *Why rails crack: Gauge corner cracking on the British network-Analysis.* Arup Journal, 2006. **41**(1): p. 16.

45. ARTC. *Rail Defects Handbook*

Some Rail Defects, their Characteristics,

Causes and Control. [Online] 2006; Available from: http://extranet.artc.com.au/docs/eng/track-civil/guidelines/rail/RC2400.pdf.

46. Ayasse, J.-B. and H. Chollet, *Wheel-rail contact.* Handbook of railway vehicle dynamics, 2006: p. 86-120.

47. Remennikov, A.M. and S. Kaewunruen, *A review of loading conditions for railway track structures due to train and track vertical interaction.* Structural control and Health monitoring, 2008. **15**(2): p. 207-234.

48. Cannon, D., et al., *Rail defects: an overview.* Fatigue & Fracture of Engineering Materials & Structures, 2003. **26**(10): p. 865-886.

49. Zerbst, U., et al., *Introduction to the damage tolerance behaviour of railway rails–a review.* Engineering fracture mechanics, 2009. **76**(17): p. 2563-2601.

50. Yan, W. and F. Fischer, *Applicability of the Hertz contact theory to rail-wheel contact problems.* Archive of Applied Mechanics, 2000. **70**(4): p. 255-268.

51. Zerbst, U., K. Mädler, and H. Hintze, *Fracture mechanics in railway applications—an overview.* Engineering Fracture Mechanics, 2005. **72**(2): p. 163-194.

52. Schleinzer, G. and F. Fischer, *Residual stress formation during the roller straightening of railway rails.* International Journal of Mechanical Sciences, 2001. **43**(10): p. 2281-2295.

53. SMITH, R., *Fatigue and the railways: an overview.* Fatigue in Railway Infrastructure, 2009: p. 1.

54. Zwanenburg, W.-J., *Modelling degradation processes of switches & crossings for maintenance & renewal planning on the Swiss railway network.* 2009.

55. Cornish, A., *Life-time monitoring of in service switches and crossings through field experimentation.* 2014.

56. Andersson, C. and T. Dahlberg, *Wheel/rail impacts at a railway turnout crossing.* Proceedings of the Institution of Mechanical Engineers, Part F: Journal of Rail and Rapid Transit, 1998. **212**(2): p. 123-134.

57. Pålsson, B.A. and J.C. Nielsen, *Wheel–rail interaction and damage in switches and crossings.* Vehicle System Dynamics, 2012. **50**(1): p. 43-58.

58. Board, H.I., *Train Derailment at Hatfield: A Final Report by the Independent Investigation Board,July 2006*. 2006: London.

59. Ringsberg, J., *Rolling contact fatigue of railway rails with emphasis on crack initiation*. 2000: Chalmers University of Technology.

60. Grassie, S. and J. Kalousek, *Rail corrugation: characteristics, causes and treatments.* Proceedings of the Institution of Mechanical Engineers, Part F: Journal of Rail and Rapid Transit, 1993. **207**(1): p. 57-68.

61. Grassie, S., *Rail corrugation: characteristics, causes, and treatments.* Proceedings of the Institution of Mechanical Engineers, Part F: Journal of Rail and Rapid Transit, 2009. **223**(6): p. 581-596.

62. Popović Z, P.L., Lazarević L, *Rail defects due to rolling contact fatigue.* Rail defects due to rolling contact fatigue, 2011. **54**(2): p. 17-29.

63. Vidaud, M. and W.-J. Zwanenburg. *Current situation on rolling contact fatigue–a rail wear phenomenon*. in *9th Swiss Transport Research Conference*. 2009.

64. Grassie, S.L., *Rolling contact fatigue on the British railway system: treatment.* Wear, 2005. **258**(7): p. 1310-1318.

65. Fletcher, D., F. Franklin, and A. Kapoor, *Rail surface fatigue and wear.* Wheel-Rail Interface Handbook, 2009: p. 280.

66. Popović, Z., et al., *Rail defects head checking on the Serbian Railways.* Tehnički vjesnik, 2014. **21**(1): p. 147-153.

67. Plu, J., et al., *Application of fracture mechanics methods to rail design and maintenance.* Engineering Fracture Mechanics, 2009. **76**(17): p. 2602-2611.

68. Ringsberg, J.W., *Shear mode growth of short surface-breaking RCF cracks.* Wear, 2005. **258**(7): p. 955-963.

69. Marich, S., *Marich Consulting Services - Module 1: Wheel rail dynamics* in *Wheel Rail Interface Forum*. 2014: Brisbane.

70. Grassie, S., *Squats and squat-type defects in rails: the understanding to date.* Proceedings of the Institution of Mechanical Engineers, Part F: Journal of Rail and Rapid Transit, 2012. **226**(3): p. 235-242.

71. Lewis, R. and U. OLOfssOn, *Basic tribology of the wheel–rail contact.* Wheel-Rail Interface Handbook, 2009: p. 34.

72. Kaewunruen, S., *Monitoring structural deterioration of railway turnout systems via dynamic wheel/rail interaction.* Case Studies in Nondestructive Testing and Evaluation, 2014. **1**: p. 19-24.

73. Lovejoy, M., *Magnetic particle inspection: a practical guide*. 2012: Springer Science & Business Media.

74. Falkenach, G.J., D. Kooger, and R. Meister, *Improvement in Magnetic Techniques for Rail Inspection*. 1981.

75. Clark, R., *Rail flaw detection: overview and needs for future developments.* NDT & E International, 2004. **37**(2): p. 111-118.

76. University of Birmingham, *D4.4.1- Rail Inspection Technologies*. 2007: Birmingham.

77. Krull, R., et al. *Eddy-current Detection of Head Checks on the Gauge Corners of Rails: Recent Results*. in *PROCEEDINGS OF THE INTERNATIONAL CONFERENCE AND EXHIBITION RAILWAY ENGINEERING 2003, HELD LONDON, UK, 30 APRIL-1 MAY 2003-CDROM*. 2003.

78. Papaelias, M., *An integrated strategy for efficient non-destructive evaluation of rails* in *Fault Detection: Classification, Techniques and Role in Industrial Systems*, U. Fausto Pedro García Márquez and Mayorkinos Papaelias (Birmingham University, Editor. 2013.

79. Zumpano, G. and M. Meo, *A new damage detection technique based on wave propagation for rails.* International journal of solids and structures, 2006. **43**(5): p. 1023-1046.

80. Popović, Z., et al., *Rail inspection of RCF defects.* Metalurgija, 2013. **52**(4): p. 537-540.

81. Drinkwater, B.W. and P.D. Wilcox, *Ultrasonic arrays for non-destructive evaluation: A review.* Ndt & E International, 2006. **39**(7): p. 525-541.

82. Wilcox, P., et al. *Long range inspection of rail using guided waves*. in *AIP Conference Proceedings*. 2003. AIP.

83. University of Warwick *Rail Inspection*. [online] 2010 [cited 2018 04/01]; Available from: https://warwick.ac.uk/fac/sci/physics/research/ultra/research/rail_inspection/.

84. Topp, D., *Recent developments and applications of the acfm inspection method and ASCM stress measurement method.* NON DESTRUCTIVE TESTING AUSTRALIA, 2005. **42**(5): p. 143.

85. Tsunashima, H., et al., *Condition monitoring of railway track using in-service vehicle*, in *Reliability and safety in railway*. 2012, InTech.

86. Schöbel, A. and T. Maly, *Operational fault states in railways.* European transport research review, 2012. **4**(2): p. 107-113.

87. Zhang, T., J. Andrews, and R. Wang, *Optimal scheduling of track maintenance on a railway network.* Quality and Reliability Engineering International, 2013. **29**(2): p. 285-297.

88. Vrije Universiteit Brussel. *acoustic emission testing* [online] Unknown; Available from: http://mech.vub.ac.be/teaching/info/Damage_testing_prevention_and_detection_in_aeronautics/PDF/acoustic-emission.pdf.

89. Unnþórsson, R., *Hit Detection and Determination in AE Bursts*. 2013: INTECH Open Access Publisher.

90. Mistras Group Inc. *Acoustic Emission Technology*. [Online] 2014 11/06/2015];

Available from: http://www.mistrasgroup.com/products/technologies/acousticemission.aspx.

91. Physical Acoustics Corporation. *Acoustic Emission Technology*. [online] 2010; Available from: http://www.pacndt.com/index.aspx?go=technologies&focus=acoustic%20emission.htm.

92. NDT Resource Centre. *Introduction to Acoustic Emission Testing*. 2014; Available from: https://www.nde-ed.org/EducationResources/CommunityCollege/Other%20Methods/AE/AE_Intro.htm.

93. Vallen, H., *AE testing fundamentals, equipment, applications*. Journal of Nondestructive Testing(Germany), 2002. **7**(9): p. 1-30.

94. Scruby, C., *An introduction to acoustic emission.* Journal of Physics E: Scientific Instruments, 1987. **20**(8): p. 946.

95. Beck, P., *Quantitative damage assessment of concrete structures using Acoustic Emission*. 2004, Cardiff University.

96. Smith, S.W., *The scientist and engineer's guide to digital signal processing*. 1997.

97. Christian U. Grosse, L.M.L., *Signal-Based AE Analysis*, in *Acoustic Emission Testing*, C.U. Grosse, Ohtsu, Masayasu Editor. 2008, Springer-Verlag Berlin Heidelberg.

98. Grosse, C.U., et al., *Signal conditioning in acoustic emission analysis using wavelets*. NDT. net, 2002. **7**(9): p. 1-9.

99. Kaphle, M., et al., *Identification of acoustic emission wave modes for accurate source location in plate-like structures*. Structural control and health monitoring,

2012. **19**(2): p. 187-198.

100. Rose, J.L., M.J. Avioli Jr, and Y. Cho. *Elastic wave analysis for broken rail detection*. in *Quantitative Nondestructive Evaluation*. 2002. AIP Publishing.

101. Kaiser, J., *An investigation into the occurrence of noises in tensile tests, or a study of acoustic phenomena in tensile tests.* Technische Hochschule, 1950.

102. Tensi, H.M. *The Kaiser-effect and its scientific background*. in *26th European conference on acoustic emission testing*. 2004.

103. Waller, J., et al. *Use of acoustic emission to monitor progressive damage accumulation in Kevlar® 49 composites*. in *Aip Conference Proceedings*. 2010.

104. NDT Resource Center. *Theory-AE Sources*. [Online] Unknown; Available from: https://www.nde-ed.org/EducationResources/CommunityCollege/Other%20Methods/AE/AE_Theory-Sources.htm.

105. Sinclair, A., D. Connors, and C. Formby, *Acoustic emission analysis during fatigue crack growth in steel.* Materials Science and Engineering, 1977. **28**(2): p. 263-273.

106. Moorthy, V., T. Jayakumar, and B. Raj, *Influence of micro structure on acoustic emission behavior during stage 2 fatigue crack growth in solution annealed, thermally aged and weld specimens of AISI type 316 stainless steel.* Materials Science and Engineering: A, 1996. **212**(2): p. 273-280.

107. Raj, B., et al. *Acoustic Emission Technique for Characterizing Deformation and Fatigue Crack Growth in Austenitic Stainless Steels*. in *AIP Conference Proceedings*. 2003. AIP.

108. Ennaceur, C., et al., *Monitoring crack growth in pressure vessel steels by the*

acoustic emission technique and the method of potential difference. International Journal of Pressure Vessels and Piping, 2006. **83**(3): p. 197-204.

109. Roberts, T. and M. Talebzadeh, *Acoustic emission monitoring of fatigue crack propagation.* Journal of Constructional Steel Research, 2003. **59**(6): p. 695-712.

110. Yu, J., et al., *Prediction of fatigue crack growth in steel bridge components using acoustic emission.* Journal of Constructional Steel Research, 2011. **67**(8): p. 1254-1260.

111. Aggelis, D.G., E.Z. Kordatos, and T.E. Matikas, *Monitoring of metal fatigue damage using acoustic emission and thermography.* Journal of Acoustic Emission, 2011. **29**: p. 113-122.

112. Bassim, M., S.S. Lawrence, and C. Liu, *Detection of the onset of fatigue crack growth in rail steels using acoustic emission.* Engineering Fracture Mechanics, 1994. **47**(2): p. 207-214.

113. Bruzelius, K. and D. Mba, *An initial investigation on the potential applicability of Acoustic Emission to rail track fault detection.* NDT & E International, 2004. **37**(7): p. 507-516.

114. Kostryzhev, A., C. Davis, and C. Roberts, *Detection of crack growth in rail steel using acoustic emission.* Ironmaking & Steelmaking, 2013. **40**(2): p. 98-102.

115. KORENSKA, M., et al., *Experimental Study of the Potential Usage of Acoustic Emission to Railway Track Faults Detection.*

116. Murav'ev, V., M. Murav'ev, and T. Murav'ev, *The possibilities of acoustic emission testing of rails during exploitation.* Russian Journal of Nondestructive Testing, 2008. **44**(1): p. 33-40.

117. Zhang, J., et al., *Defect detection and location in switch rails by acoustic emission*

and Lamb wave analysis: A feasibility study. Applied Acoustics, 2016. **105**: p. 67-74.

118. Johnson, K., *Acoustic and auditory phonetics.* Phonetica, 2004. **61**(1): p. 56-58.

119. Al-Balushi, K. and B. Samanta, *Gear fault diagnosis using energy-based features of acoustic emission signals.* Proceedings of the Institution of Mechanical Engineers, Part I: Journal of Systems and Control Engineering, 2002. **216**(3): p. 249-263.

120. Jemielniak, K. and O. Otman, *Tool failure detection based on analysis of acoustic emission signals.* Journal of Materials Processing Technology, 1998. **76**(1): p. 192-197.

121. Suzuki, H., et al., *Wavelet transform of acoustic emission signals.* Journal of Acoustic Emission, 1996. **14**: p. 69-84.

122. Polikar, R., *The wavelet tutorial.* 1996.

123. Tan, C.K. and D. Mba, *Limitation of acoustic emission for identifying seeded defects in gearboxes.* Journal of Nondestructive Evaluation, 2005. **24**(1): p. 11-28.

124. Ametek. *Definition : Crest Factor*. [online] Unknown [cited 2018 06/01]; Available from: http://www.programmablepower.com/support/FAQs/DF_Crest_Factor.pdf.

125. Stoica, P. and R.L. Moses, *Spectral analysis of signals*. 2005: Pearson/Prentice Hall Upper Saddle River, NJ.

126. Welch, P.D., *The use of fast Fourier transform for the estimation of power spectra: A method based on time averaging over short, modified periodograms.* IEEE Transactions on audio and electroacoustics, 1967. **15**(2): p. 70-73.

127. DeCarlo, L.T., *On the meaning and use of kurtosis.* Psychological methods, 1997.

2(3): p. 292.

128. Kannatey-Asibu, E. and D. Dornfeld, *A study of tool wear using statistical analysis of metal-cutting acoustic emission.* Wear, 1982. **76**(2): p. 247-261.

129. Lokajíček, T. and K. Klima, *A first arrival identification system of acoustic emission (AE) signals by means of a high-order statistics approach.* Measurement Science and Technology, 2006. **17**(9): p. 2461.

130. Dwyer, R.F. *Detection of non-Gaussian signals by frequency domain kurtosis estimation*. in *Acoustics, Speech, and Signal Processing, IEEE International Conference on ICASSP'83.* 1983. IEEE.

131. Ottonello, C. and S. Pagnan, *Modified frequency domain kurtosis for signal processing.* Electronics Letters, 1994. **30**(14): p. 1117-1118.

132. Pagnan, S., C. Ottonello, and G. Tacconi. *Filtering of randomly occurring signals by kurtosis in the frequency domain*. in *Pattern Recognition, 1994. Vol. 3-Conference C: Signal Processing, Proceedings of the 12th IAPR International Conference on*. 1994. IEEE.

133. Antoni, J., *The spectral kurtosis: a useful tool for characterising non-stationary signals.* Mechanical Systems and Signal Processing, 2006. **20**(2): p. 282-307.

134. Shinde, S., et al., *WAVELET BASED DENOISIONG OF ACOUSTIC SIGNAL.*

135. Eftekharnejad, B., et al., *The application of spectral kurtosis on acoustic emission and vibrations from a defective bearing.* Mechanical Systems and Signal Processing, 2011. **25**(1): p. 266-284.

136. Sawalhi, N. and R.B. Randall. *The application of spectral kurtosis to bearing diagnostics*. in *Proceedings of ACOUSTICS*. 2004.

137. TABATABAEI, A.M. *FRACTURE AND FATIGUE CRACK GROWTH*

CHARACTERIZATION OF CONVENTIONAL AND HEAD HARDENED RAILWAY RAIL STEELS [online] 2014; Available from: http://etd.lib.metu.edu.tr/upload/12616888/index.pdf.

138. Vallen. *Acoustic Emission Preamplifiers Specification*. [online] 2017; Available from: http://www.vallen.de/fileadmin/user_upload/Pre.pdf.

139. Mistras Group Inc. *Product Data Sheet: WD Sensor*. [online] 2011; Available from: http://www.physicalacoustics.com/content/literature/sensors/Model_WD.pdf.

140. Mistras Group Inc. *Product Data Sheet: R50α Sensor*. [online] 2011; Available from: http://www.physicalacoustics.com/content/literature/sensors/Model_R50a.pdf.

141. National Physical Laboratory. *Guide on Acoustic Emission Sensor Couplants*. [online] 2012 [cited 2017 23/10]; Available from: http://www.npl.co.uk/ultrasound-and-underwater-acoustics/ultrasonics/research/guide-on-acoustic-emission-sensor-couplants.

142. ASTM E650, *Standard Guide for Mounting Piezoelectric Acoustic Emission Sensors*. 2017: ASTM International, West Conshohocken, PA.

143. Grosse, C. *Acoustic Emission (AE) Hsu-Nielsen source*. [online] 2002 [cited 2018 05/10]; Available from: https://www.ndt.net/ndtaz/content.php?id=474.

144. British Standards Institution, *Method for the determination of the rate of fatigue crack growth in metallic materials -Part 1: Fatigue crack growth rates of above 1028 m per cycle*. 1998.

145. McEvily, A.J. and J. Kasivitamnuay, *Metal failures: mechanisms, analysis,*

prevention. 2013: John Wiley & Sons.

146. Pluvinage, G., *Notch effects in fatigue and fracture*. 2001: Springer.

147. Barile, C., et al., *Acoustic Emission Analysis of Aluminum Specimen Subjected to Laser Annealing*, in *Residual Stress, Thermomechanics & Infrared Imaging, Hybrid Techniques and Inverse Problems, Volume 8*. 2014, Springer. p. 309-315.

148. Evans, A., *Residual stress measurement using acoustic emission.* Journal of the American Ceramic Society, 1975. **58**(5-6): p. 239-243.

149. Shi, S., *Evaluating the structural integrity of high strength low alloy steels considered for shipbuilding using acoustic emission*. 2015, University of Birmingham.

150. Han, Z., et al., *Acoustic emission monitoring of brittle fatigue crack growth in railway steel*, in *Advances in Acoustic Emission Technology*. 2017, Springer. p. 371-382.

151. Shi, S., et al., *Quantitative monitoring of brittle fatigue crack growth in railway steel using acoustic emission.* Proceedings of the Institution of Mechanical Engineers, Part F: Journal of Rail and Rapid Transit, 2017: p. 0954409717711292.

152. Fowler, T., et al., *The MONPAC system.* Journal of acoustic emission, 1989. **8**(3): p. 1-8.

153. Bulmer, M.G., *Principles of statistics*. 1979: Courier Corporation.

154. Antoni, J. and R. Randall, *The spectral kurtosis: application to the vibratory surveillance and diagnostics of rotating machines.* Mechanical Systems and Signal Processing, 2006. **20**(2): p. 308-331.